Experimental Studies of Selective Catalytic Reduction of NO_x with NH_3 on Cu-ZSM-5 Foam Catalysts

A thesis submitted

in partial fulfillment for the award of the degree of

Doctor of Philosophy

by

Risha Raju

Department of Aerospace Engineering

Indian Institute of Space Science and Technology

Thiruvananthapuram, India

June 2023

Certificate

This is to certify that the thesis titled ***Experimental Studies of Selective Catalytic Reduction of NO_x with NH_3 on Cu-ZSM-5 Foam Catalysts*** submitted by **Risha Raju**, to the Indian Institute of Space Science and Technology, Thiruvananthapuram, in partial fulfillment for the award of the degree of **Doctor of Philosophy** is a bonafide record of the original work carried out by him under my supervision. The contents of this thesis, in full or in parts, have not been submitted to any other Institute or University for the award of any degree or diploma.

Dr A. Salih
Professor
Dept. of Aerospace Engineering

Dr. Kuruvilla Joseph
Professor
Dept. of Chemistry

Dr. Deepu M
Professor & Head
Dept. of Aerospace Engineering

Place: Thiruvananthapuram
Date: June 2023

Declaration

I declare that this thesis titled ***Experimental Studies of Selective Catalytic Reduction of NO_x with NH_3 on Cu-ZSM-5 Foam Catalysts*** submitted in partial fulfillment for the award of the degree of **Doctor of Philosophy** is a record of the original work carried out by me under the supervision of **Dr. A. Salih**, and co-supervision of **Dr. Kuruvilla Joseph** has not formed the basis for the award of any degree, diploma, associateship, fellowship, or other titles in this or any other Institution or University of higher learning. In keeping with the ethical practice in reporting scientific information, due acknowledgments have been made wherever the findings of others have been cited.

Place: Thiruvananthapuram
Date: June 2023

Risha Raju
(SC16D037)

Acknowledgements

I would like to thank my advisors, Professor A. Salih and Professor Kuruvilla Joseph, for their guidance, strong support, and motivation throughout my PhD. It was an honor and privilege to work under supervision. I thank them for giving me the freedom to conduct this independent research. I would like to thank Gomathi N, Associate Professor, of Chemistry, for evaluating the publications and providing great support. I thank Professor Prabhakaran K for giving me the opportunity to be part of his laboratory. I thank Professor Aravind Vaidyanathan for providing the opportunity to work as a part of his team. I would like to thank Dr. Prathap C and Dr. Rajesh Sadananthan for their support throughout this research. I would like to thank Professor Niket Kaisare and Professor Preeti Aghalayam (Indian Institute of Technology, Madras) for their contributions to the initial discussion. I am thankful to the members of my dissertation committee, Professor Deepu M, Dr. Anil Lal, and Dr. Jobin Cyriac.

I would like to thank the technical team of the Aerospace department, Mr Vinil Kumar R and Mr Sujin Raj for the assistance in the laboratory, Mr Prakash S and Virosh M for the test rig fabrication, Mr Dinesh D and Mr Bibin D for the instrument demonstration, Mr Rijas A and Mr Satheesh V for the structural analysis of catalyst. I am grateful to Dr. Sujith Vijayan and Dr. Praveen Wilson (Department of Chemistry) for their support in the catalyst development and characterization. I would like to thank my dear friend, "Rajesh Natarajan, " for the advice, help, and support in tackling my tough times. I would like to thank Dr. Jishnu Chandran R and Dr. Arun Govind Neelan for their immense support and for being the best labmates. I am grateful to my colleagues Dr. Dhanesh Ayyappan and Swetha S Menon for their support and motivation. I would like to thank Ms Anagha P, Ms Minha M, Ms Neethu M, Ms Sharon Vargheese and Ms Swathi V V for filling my research life with lots of love and fun. I am fortunate to have met these amazing personalities during my PhD. I am grateful to have "POMY" on my side on the long lonely experiment days where I realized and enjoyed another dimension of myself. I thank my colleagues, hostel mates, and friends for their support throughout my research. Last but not least, I thank my family, whose sacrifice, patience, and motivation helped me tackle difficult times.

”

Risha Raju

Abstract

Selective Catalytic Reduction (SCR) is one of the most promising technologies for reducing after-exhaust NO_x emissions. Cu zeolites generally provide high SCR conversion rates at temperatures $\lessapprox 350°C$. The limitations associated with powdered catalysts, such as low mass diffusion and high pressure drop, can be minimized to a certain extent by replacing them with structured catalysts. The foam catalysts exhibit superior characteristics, such as a high surface-to-volume ratio, porosity, and tortuosity, which improve the mass diffusion and lower the pressure drop.

In this study, α-alumina foam was prepared using a thermo-foaming technique. The procedure followed during this research for the preparation of the Cu-ZSM-5 zeolite coating over alumina foam through in situ hydrothermal and dip-coating methods is also presented in detail. A self-supporting foam catalyst of Cu-ZSM-5 is prepared using a freeze-casting emulsion method.

A comprehensive experimental study was conducted to understand the mass transfer and pressure drop characteristics of the foam catalysts. Correlations for the mass transfer coefficient and friction factor were derived for the foam catalyst and validated against the available data in the literature reviewed. A detailed investigation of key SCR reactions, such as the standard SCR, fast SCR, slow SCR, NO oxidation, NH_3 oxidation, and NO_2 decomposition, was also carried out in this research. The inhibitory effects of the feed reactants were studied by varying the feed concentration. A detailed investigation of the impact of the inhibition effect of NO_2 and NH_3 on the SCR reaction at low temperatures is also presented. Numerical analysis of real engine catalytic convertor is explored to conclude the inferences from SCR chemistry.

Contents

List of Figures

List of Tables

Nomenclature

A_p = Droplet surface area (m^2)
A_c = Area of cross section
A = Reaction pre-exponent factor
$B_{m,i}$ = Spalding mass transfer number
$B_{T,i}$ = Spalding heat transfer number
C_P = Specific heat capacity of bulk gas ($J.kg^{-1}.K^{-1}$).
$C_{p_{BL}}$ = Specific heat capacity of fluid near solid boundary ($J.kg^{-1}.K^{-1}$)
C = Species concentration
d_p = Droplet diameter (mm)
D_i = Species molecular diffusivity (m^2/s)
E_a = Activation energy ($J.kmol^{-1}.K^{-1}$)
$h_{vap,i}$ = Latent heat of vaporization of species i ($J.kg^{-1}$)
h = Convective heat transfer coefficient ($W.m^{-2}.K^{-1}$)
K_C = Mass transfer coefficient (m/s)
K_T = Heat transfer coefficient (m/s)
λ = Bulk gas thermal conductivity ($Wm^{-1}K^{-1}$)
λ_S = Solid thermal conductivity ($Wm^{-1}K^{-1}$)
m_p = Mass of the particle (kg)
m_{vap} = Mass vaporized
N_{SP} = Number of chemical species
Pr = Prandtl number
P_t = Total vapor pressure
P_i = Partial pressure of species i
Re_d = Reynolds number based on the particle diameter and the relative velocity
R = Gas constant
ρ_i = Density of species i (kg/m^3)
ρ_G = Density of bulk gas ($kg.m^{-3}$)

ρ_{BL} = Density of fluid near solid boundary (kg.m^{-3})

Sh = Sherwood number

Sc = Schmidt number

S_V = Geometric surface area to bed volume (m^{-1})

S_{VC} = Active catalytic surface to void volume (m^{-1})

$\dot{S}$ = Species production rate by surface reaction (kmol.m^{-2}.s-1)

T_p = Temperature of the droplet

T_G = Bulk gas temperature (K)

T_S = Solid temperature (K)

V = Interstitial velocity (m/s)

$\overrightarrow{v}$ = velocity of flow (m/s)

W = Molar mass (kg$_i$.kmol^{-1})

x_i = Volume fraction of component in the droplet

$Y_{i,s}$ = Vapor mass fraction at surface

$Y_{i,\infty}$ = Vapor mass fraction at the bulk gas

T_∞ = Local temperature of the continuous phase (K)

Y_u = Mass fraction of urea

Y_G = Bulk mass fraction (kg$_i$.kg$_{total}{}^{-1}$).

Y_{BL} = Mass fraction of species near solid boundary (kg$_i$.kg$_{total}{}^{-1}$)

ϵ = Porosity

η = Viscosity (kg.m^{-1}s^{-1})

Chapter 1

Introduction

The combustion of automobile fuels produces a substantial amount of gases such as CO, CO_2, NO_x, hydrocarbons, and SO_2. These gases pose a significant threat to the environment, and must be turned harmless before venting into the atmosphere. The US Environmental Protection Agency has incorporated certain policies to minimize the emission of these gases, paving the way for the development of exhaust after-treatment systems for automobiles. Exhaust after-treatment along with inline cylinder NO_x control is required to meet emission standards. NO_x emission standards have become stringent over the past few decades, which has led to research on new NO_x reduction technologies. NO_x was formed by the reaction between N_2 and O_2 during combustion at an elevated temperature of approximately 1100°C. Selective Catalytic Reduction (SCR) is an effective technology for NO_x emission control applications globally, in response to increasing NO_x emissions from industries, marine applications, and automobiles. Liquefied ammonia is directly used for selective catalytic reduction in stationary industrial applications; however, it poses difficulties in terms of storage, transportation, handling, and toxicity in automobile installations. Urea, which can directly produce ammonia, is chosen as a precursor due to its ease of storage and low cost. In automobile applications, urea-water solution-based SCR is a promising technology for NO_x reduction. The urea–water solution sprayed into the hot exhaust stream broke into smaller droplets. The turbulent exhaust gas flow heats these droplets to form gaseous urea, which undergoes thermal decomposition to ammonia and isocyanic acid in the mixing chamber. Isocyanic acid is hydrolyzed to produce ammonia and CO_2. The produced ammonia undergoes a catalytic chemical reaction to reduce NO_x in the catalytic converter. The distribution of ammonia at the inlet of the catalytic converter is a crucial criterion, as ammonia acts as a reducing agent in SCR (NH_3 SCR). The main challenges in the urea water solution injection system are the incomplete decomposition of urea and uniform distribution of ammonia upstream of the SCR unit. The performance of

an SCR system depends on the nature of the flow and the heat and mass transfer between spray droplets and exhaust gases.

1.1 Motivation

1. The current selective catalytic reduction methods are predominantly based on urea SCR. However, there is a potential for NH_3 slip, which refers to the unreacted NH_3 in the SCR catalyst. Therefore it is vital to develop an efficient catalyst for urea SCR due to the above limitation.

2. The non-uniformities of NH_3 in the SCR feed produced by the decomposition of urea-water solution injection and feed conditions in the mixing chamber have to be optimized for the improved performance of the Urea SCR.

3. Zeolites have been applied widely to industrial processes mainly in adsorption and catalysis due to their high surface area, and ion-exchange capacity and are hydrothermally stable and highly active at high temperatures. These diverse properties combined with their unique highly ordered crystalline nature, which enables high performance of zeolites. It is crucial to investigate the ionic exchange level of the Cu^{2+} species on ZSM-5 and Si/Al ratio, which drives the specific activity of Cu-ZSM-5.

4. The NH_3 SCR process is mass transfer limited within 150-550°C. This hurdle can be overcome using a structured catalyst. Cu-ZSM-5 wash-coated monolith catalysts are widely used in the SCR process whereas Cu-ZSM-5 with foam structure is a new aspect explored in this study. The tortuous flow field developed in the foam system favors both the axial and radial dispersion of heat and mass, generating a more homogeneous distribution of temperature and gas concentration, resulting in a higher temperature, faster kinetics, and higher conversion.

1.2 Scope of work

1. Foam catalyst by three different processing methods are prepared

   (a) Supported foam catalysts

   - Cu-ZSM-5 dip-coated on α alumina foam
   - Cu-ZSM-5 hydrothermally coated on α alumina foam

(b) Self-supporting foam catalysts by freeze casting

2. Experimental investigation of SCR reaction chemistry

3. Experimental investigation of mass transfer and pressure drop studies

4. Numerical analysis of NH_3 SCR reactor

   - Numerical analysis of mixing chamber
   - Numerical analysis of SCR converter

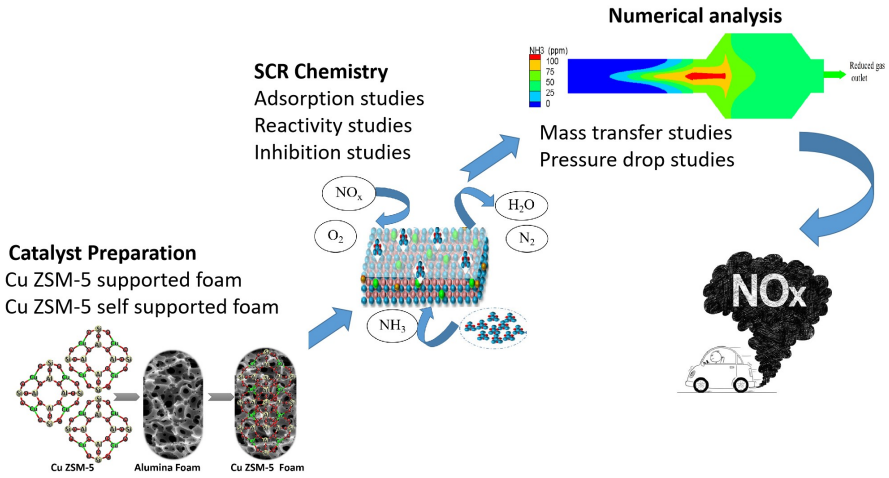

Figure 1.1: Thesis objective and outline

1.3 Thesis outline

The overall objective of this study is to develop and test a foam-supported catalyst for the after-emission reduction of NO_x. The objective and outline of thesis is shown in Figure 1.1. The Cu-ZSM-5 supported foam catalyst was prepared by in situ hydrothermal coating and dip coating on α alumina foam, and the self-supported foam catalyst was prepared using the freeze-casting method. The $DeNO_x$ experimental test rig was assembled and set up in a laboratory. Steady-state and transient experiments on SCR reactions were performed to elucidate a better understanding of SCR chemistry. NH_3 and NO_x uptake, NO oxidation, NH_3 oxidation, Standard SCR, Fast SCR, and NO_2 SCR were investigated. The effect of ammonium nitrates on the standard SCR reaction and NO oxidation under different operating conditions was studied. The inhibitory effects of NH_3 were investigated in this

study. The remainder of this paper is organized as follows. Chapter 1 provides a brief introduction to NO_x emission reduction by NH_3 SCR. Chapter 2 provides background on emissions, emission reduction techniques, SCR catalysts, catalyst supports and processing methods, and catalyst preparation processes. Chapter 3 describes the experimental setup, catalyst synthesis, and characterization techniques. Chapter 4 presents a comprehensive experimental study on the steady-state and transient kinetics of various SCR reactions on Cu-ZSM-5 dip-coated α alumina foams. Chapter 5 focuses on the preparation and characterization of in situ hydrothermal synthesised Cu-ZSM-5 on alumina foam. The performance of the lab-synthesized Cu-ZSM-5 was investigated using steady-state and transient NO_x reduction experiments. Chapter 6 presents a self-supporting Cu-ZSM-5 foam catalyst designed to enhance NO_x removal efficiency over a short reactor length. Chapter 7 discusses the numerical analysis of mixing chamber non-uniformities and feed conditions for the optimal performance of the urea SCR. The major conclusions drawn from this study are summarized in Chapter 8.

Chapter 2

Literature Review

2.1 Background on Emissions

The primary sources of energy, fossil fuels in the form of coal and crude oil, have a significant impact on the development of industries. Statistics indicate that 80% of energy demand depends on fossil fuels. The increased dependence on the limited resources of fossil fuels as a source of energy results in a high risk of the depletion of these resources in the near future. The combustion of fossil fuels results in the release of volatile organic compounds (VOC), carbon monoxide (CO), carbon dioxide (CO_2), nitric oxide (NO), nitrogen dioxide(NO_2), hydrocarbons (HC), and sulfur dioxide (SO_2). These gases pose a significant threat to the environment and must be turned harmless before venting into the atmosphere. The US Environmental Protection Agency has incorporated certain policies to minimize the emission of these gases, paving the way for the development of exhaust after-treatment systems. The National Emissions Ceilings Directive (NECD) recognizes and stresses the control of four main air pollutants: NO_x, SO_x, non-methane volatile organic compounds (NMVOCs), and ammonia (NH_3). The statistics clearly show that the NO_x emission limits appear to be the greatest challenge.

The combustion of fossil fuels in automobile engines is widely used in stationary power plants, industrial installations, and light- and heavy-duty vehicles because of its high efficiency, durability, and reliability.

A gasoline engine uses a spark plug to ignite an air-fuel mixture. The combustion of fuel emits CO, HC, NO_x and SO_x. A three-way catalytic converter (TWC) was installed in the tailpipe to reduce the emission of harmful gases into the atmosphere. The TWC uses precious metals such as Pt and Pd to reduce HC and CO emissions, and Rh, which reduces NO_x emissions. When the engine is operated at a stoichiometric air-to-fuel ratio, which is the amount of fuel required to oxidize the fuel of λ 1, all HC, CO, and NO_x are

converted simultaneously. During rich operations, higher emissions of CO and HC with lower NO_x are released during incomplete combustion. Lean operation leads to complete combustion of fuel, resulting in lower HC, CO, and higher NO_x. The three-way catalysts are comprised–0.1-0.15% precious metals, 10-20% CeO_2 and the remainder is the γ-Al_2O_3 washcoat [1]. Diesel engines are lean-burn engines that utilize excess air. A diesel engine uses the heat of compression to initiate ignition to burn the fuel, which is called compression ignition. This compression process results in incomplete combustion and high emissions [2]. Unburned fuel and lubricating oil form volatile organic fractions (VOF), particulate matter (PM) forms solid emissions, and HC, CO NO_x and SO_x form gas-phase emissions from diesel engines. Therefore, diesel engines require exhaust after-treatment systems. Although diesel engines produce high emissions, they are still widely used because of their high fuel efficiency, long life, durability, reliability, and low gas phase emissions. The overall NO_x produced in a diesel engine is higher than that produced in gasoline engines, which reduces the NO_x in the TWC. Therefore, various NO_x technologies have been developed and commercialized to meet the stringent emission standards. The NO_x emission limits for diesel and petrol engines is summarized in Table 2.1.

Table 2.1: Euro NO_x emission standards

Euro standard	Introduction year	Petrol NO_x (g/km)	Diesel NO_x (g/km)
Euro 1	1992	0.97	0.97
Euro 2	1997	0.5	0.9
Euro 3	2000	0.15	0.5
Euro 4	2005	0.08	0.25
Euro 5	2009	0.06	0.18
Euro 6	2015	0.06	0.08
Euro 7	2025	0.03	0.04

2.2 NO_x Reduction Technologies

NO_x is formed by the reaction between N_2 and O_2 during combustion at an elevated temperature of approximately 1100°C. Nitrogen oxides include mainly nitric oxide (NO) and nitrogen dioxide (NO_2). NO_x in the presence of sunlight, NO_x reacts with volatile organic compounds to form ground-level ozone. Ground-level ozone harms humans and depletes the stratospheric ozone layer. NO_x reacts with water vapor to form an acid rain. Therefore, NO_x is a major air pollutant that adversely affects human health. Hence, the EPA stan-

dard for NO_x emissions is very stringent, and various technologies have been developed to minimize NO_x emissions.

2.2.1 Direct decomposition of NO

The decomposition of nitric oxide to N_2 and O_2 is thermodynamically favored at diesel exhaust pressures and temperatures. The rate of the spontaneous reaction was zero because the activation energy for this reaction was high. In the 1990s, Iwamoto reported that copper ion-exchanged ZSM 5 zeolites are highly active catalysts for the direct and continuous decomposition of nitrogen monoxide [3]. Although the Cu-ZSM-5 catalyst is promising, the reaction was inhibited by H_2O and O_2. SO_2 in the feed gas poisons the catalyst, thereby reducing the rate of the reaction. Studies have been conducted to enhance the direct decomposition of NO_x over different catalysts. The activity and selectivity of Cu-ZSM-5 are unsatisfactory for commercializing the technology for NO_x reduction in diesel engines.

2.2.2 Exhaust Gas Recirculation (EGR)

NO_x is formed by the reaction between N_2 and O_2 during the combustion process at an elevated temperature of about 1100°C. NO_x formation can be reduced by decreasing the flame temperature. In this technology, a portion of the exhaust gas is recirculated back to the engine, thereby reducing the air available for combustion. Because the amounts of fuel and air in the inlet are constant, the exhaust gas is recirculated to the engine and operates at a lower air-to-fuel ratio. This lowers the flame temperature and, in turn, the NO_x emissions during the combustion. This technique lowers engine durability because it affects the engine cooling. The cooler inlet air is mixed with hot recirculated exhaust gas, increasing the demand for excess inlet cooler air, which can damage the engine. The reduced temperature results in incomplete combustion of fuel in the engine. A diesel particulate filter requires elevated temperatures to regenerate and oxidize accumulated soot [4]. However, owing to EGR, the exhaust temperature decreases and the formation of soot increases, which affects the efficiency of the DPF. These drawbacks have limited the use of EGR in commercial applications.

2.2.3 NO_x absorber catalyst

NO_x absorber catalysts are also known as NO_x storage-and-reduction (NSR) or Lean NO_x trap (LNT) catalysts. This technology is mainly used in light-duty diesel engine vehicles

and lean-burn gasoline engine vehicles. In NSR catalysts, NO_x is absorbed and stored in lean cycles, and the absorbed NO_x is released and reduced in the subsequent fuel-rich cycle by hydrocarbons in the fuel. In the fuel-rich cycle, the NSR catalyst was regenerated. The lean NO_x trap is a bifunctional catalyst composed of precious metals (Pt, Pd, and Rh) and alkaline earth metals (Ba and K) in the form of oxides or carbonates. Precious metal catalysts oxidize NO to NO_2 and are stored as metal nitrates. LNT catalysts have been successfully used in stationary power and natural gas turbine post-treatment systems for several years. Toyota laboratories have introduced the concept of NSR in automobile applications. This technology has been adapted and commercialized worldwide for automobile applications, as it does not require any additional infrastructure because it uses HC as the reductant in fuel. The major challenge in this technique is the development of adaptive control techniques for lean and rich diesel engine operations, and the cost of precious metals (Pt, Pd, and Rh). NSR catalysts are susceptible to sulfur poisoning, and the desulfation of these catalysts leads to sintering of Pd and Pt. These disadvantages make NSR suitable for application in diesel engines. Ammonia is an attractive fuel candidate that can reduce fossil fuel consumption and CO_2 emissions owing to its reliable combustion properties. Recent studies on mitigating NO_x emissions from different ammonia combustion processes were explored in a review by Park et al. [5].

2.2.4 Selective Catalytic Reduction (SCR)

Selective catalytic reduction was developed in the 1970s in Japan for application in thermal power plants. Selective Catalytic Reduction (SCR) is an effective technology for NO_x emission control applications globally, in response to increasing NO_x emissions from industries [6], marine applications [7] [8], and automobiles. SCR technology finds widespread application in NO_x control in coal-fired power plants, refinery heaters, boilers, furnaces, coke ovens, etc.. SCR technology is one of the most promising technologies that can meet NO_x emission standards. The application of selective catalytic reduction (SCR) technology to mobile vehicles has gained attention in recent years. The first commercial SCR application for diesel trucks was launched in 2004 by Nissan Diesel in Japan and Daimler Chrysler in Europe. SCR technology has emerged as an efficient method for NO_x reduction. There are two types of SCR technologies: HC SCR and NH_3 or urea SCR. HC SCR uses the HC present in exhaust diesel engines as the reducing agent for NO_x reduction. In 1984, Konig et al. used this technology for light passenger vehicles using a Cu-exchanged zeolite mordenite catalyst. This group studied HC SCR activity in different metal zeolites

including Cu, Cr, Fe, Mn, V, Co, Ni and Cu was found to be the most effective metal. Iwamoto further investigated HC SCR over Cu-ZSM-5. Smedler et al. found Ag/Al_2O_3 to be an effective catalyst for reducing NO_x at 400°C, using propane, propene, or alkenes as reducing agents. However, Ag/Al_2O_3 exhibited a low SCR activity at low temperatures. Pd and Pt/O_3 catalysts perform well at low temperatures but produce a high amount of N_2O, which is a greenhouse gas that leads to ozone depletion [9].

Table 2.2: NO_x reduction technologies

NO_x reduction technologies	Conversion
Direct decomposition of NO	>50%
Exhaust gas recirculation	20-60%
Lean NO_x trap	30-50%
Selective catalytic reduction	>90%

Liquefied ammonia is used directly for SCR in stationary industrial applications; however, it poses difficulties in terms of storage, transportation, handling, and toxicity in automobile installations. Urea, which can directly produce ammonia, is chosen as a precursor due to its ease of storage and low-cost [10]. In automobile applications, urea-water solution (diesel exhaust fluid)-based selective catalytic reduction (SCR) is a promising technology for NO_x reduction [11]. The urea–water solution sprayed into the hot exhaust stream broke down into smaller droplets, and the turbulent exhaust gas flow heated these droplets. The urea-water solution evaporates to form gaseous urea, which undergoes thermal decomposition to ammonia and isocyanic acid in the mixing chamber. Isocyanic acid is hydrolyzed to produce ammonia and CO_2 [12](Table 7.1. The produced ammonia undergoes a catalytic chemical reaction to reduce NO_x in the catalytic converter. The distribution of ammonia at the inlet of the catalytic converter is a crucial criterion, as ammonia acts as a reducing agent in NH_3 SCR. The main challenges in the urea water solution injection system are the incomplete decomposition of urea and the uniform distribution of ammonia upstream of the SCR unit. Certain studies [13, 14] have reported that these challenges can be resolved to an extent by using mixers of different designs and by optimizing the dimensions of the mixing chamber so that the spray mixture achieves sufficient mixing and reaction time before entering the SCR unit. The performance of an SCR system depends on the nature of the flow and the heat and mass transfer between spray droplets and exhaust gases.

Table 2.3: Kinetic parameters for Urea decomposition

Reactions	Rate kmol/m^{3}s	A	E_a (J/kmol)
Thermolysis			
NH_2CONH_2->NH_3+HNCO	$A_1 e^{-\frac{E_1}{RT}} C_{\text{Urea}}$	2.0×10^3	2.3×10^7
Hydrolysis			
HNCO+H_2O->NH_3+CO_2	$A_2 e^{-\frac{E_2}{RT}} C_{\text{HNCO}}$	2.5×10^5	6.2×10^7

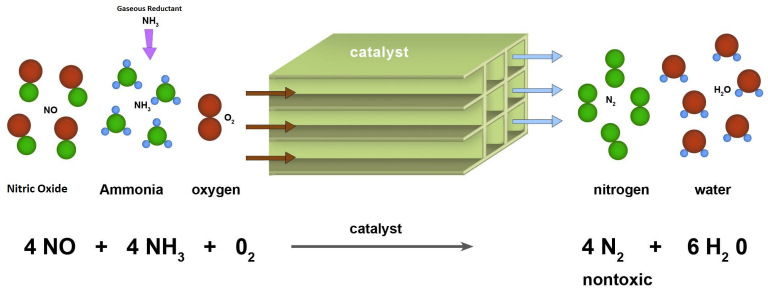

Figure 2.1: Representation of SCR system. [15]

2.3 SCR Applications

SCR has been used to control emissions from fossil fuel-fired stationary sources since the 1970s. They are widely used in utility and industrial boilers, process heaters, gas turbines, internal combustion engines, chemical plants, and steel mills. NO_x reduction technologies and their efficiency is summarized in Table 2.2. The potential of SCR for NO_x removal in vehicular applications was realized in the 1990s, and has gained considerable attention in the last few years. The first commercial SCR application for diesel trucks was launched in 2004 by Nissan Diesel in Japan and by Daimler Chrysler in Europe. SCR is widely used in industrial, marine and automobile applications.

2.4 SCR Chemistry

Selective catalytic reactions involve the following sets of reactions [16]:

1. Standard SCR reaction: This reaction involves NO and NH_3 reacting in the presence

of O_2.

$$4NH_3 + 4NO + O_2 \rightarrow 4N_2 + 6H_2O \quad \Delta H = -4.07 \times 10^5 J/molNH_3 \quad (2.1)$$

2. Fast SCR reaction : When NO and NO_2 in feed react simultaneously to form N_2 and H_2O. This reaction is faster than standard SCR

$$2NH_3 + NO + NO_2 \rightarrow 2N_2 + 3H_2O \quad \Delta H = -3.78 \times 10^5 J/molNH_3 \quad (2.2)$$

3. NO_2 SCR Reaction

$$4NH_3 + 3NO_2 \rightarrow 3.5N_2 + 6H_2O \quad \Delta H = -3.41 \times 10^5 J/molNH_3 \quad (2.3)$$

4. Ammonia oxidation is the key side reaction where NH_3 is selectively oxidised to N_2

$$4NH_3 + 3O_2 \rightarrow 2N_2 + 6H_2O \quad \Delta H = -3.12 \times 10^5 J/molNH_3 \quad (2.4)$$

$$2NH_3 + 2O_2 \rightarrow N_2O + 3H_2O \quad \Delta H = -2.76 \times 10^5 J/molNH_3 \quad (2.5)$$

$$4NH_3 + 5O_2 \rightarrow 4NO + 6H_2O \quad \Delta H = -2.27 \times 10^5 J/molNH_3 \quad (2.6)$$

$$4NH_3 + 7O_2 \rightarrow 4NO_2 + 6H_2O \quad \Delta H = -2.84 \times 10^5 J/molNH_3 \quad (2.7)$$

5. NO is oxidised to NO_2 at a temperature above 150^0C and NO_2 is more effectively reduced by NH_3 than NO.

$$NO + 0.5O_2 \rightleftarrows NO_2 \quad \Delta H = -5.7 \times 10^4 J/molNH_3 \quad (2.8)$$

6. NO_2 complicate the reaction by the formation of ammonium nitrate, which on decomposition at a temperature above 200^0C leads to the formation of N_2O

$$2NH_3 + 2NO_2 \rightarrow NH_4NO_3 + N_2 + 2H_2O \quad \Delta H = -2.91 \times 10^5 J/molNH_3 \quad (2.9)$$

$$NH_4NO_3 \rightarrow N_2O + 2H_2O \quad \Delta H = -3.66 \times 10^4 J/molNH_3 \quad (2.10)$$

The above-mentioned reaction network complicates the kinetic analysis of the SCR. The NH_3 oxidation, NO oxidation, fast SCR, and slow SCR affect the standard SCR rate at different temperatures and concentrations of NH_3, NO, NO_2, O_2 and H_2O. The representation of SCR is shown in Figure 2.1.

At low temperatures, both L–H mechanism and E-R mechanism participated in SCR reactions, but L–H mechanism was the main mechanism for low-temperature de-NOx [17].

Copper-based zeolites exhibit the best activity for the direct decomposition of NO [18] [3] [19] [20]. Mechanistic aspects of NH_3 SCR over various catalysts have been reported in the literature. Brandenberger et al. reviewed the NH_3-SCR reaction chemistry, mechanisms and kinetics on the metal-exchanged zeolite catalysts [21]. AV Salkar et al prepared metal zeolites (Cu, Cr and Fe from H ZSM-5) by wet impregnation and concluded that Cu-ZSM-5 showed better catalytic activity with water and was superior to other catalysts. The study also concluded that the presence of O_2 helps adsorb more NO over Cu-ZSM-5 [22]. Yaxin Xu prepared Hydrothermal synthesis of FER zeolites for selective catalytic reduction of NO_x by methanol [23]. Rahkamaa et al studied the effect of NO_2 in SCR chemistry and concluded that the presence of NO_2 in the inlet flow enhances the catalytic activity of fresh and hydrothermally aged zeolite catalysts. The study also suggests that the oxidation of NO to NO_2 is the rate-determining step [24]. Koebel investigates reaction pathways in the SCR process with NO and NO_2 at low temperatures. The study revealed that the rate of fast SCR is 10 times higher than that of the standard SCR. At temperatures above 200°C, fast SCR dominates, whereas at lower temperatures, ammonium nitrate is formed in the reaction of NO_2 with NH_3 and is analogous to a NO_x storage-reduction catalyst [25] [26]. Si et al. found that the number of Lewis acid sites increased monotonically with the Cu loading increased, while the number of Brønsted acid sites decreased. Cu occupies the Brønsted acid sites in the pores and produces more Lewis acid sites. The NO conversion efficiency increased with the increase of Lewis acid sites at low temperatures, indicating that Lewis acid sites play a key role in the low-temperature SCR activity [27]. Despres et al. studied the adsorption and desorption of NO and NO_2 on Cu-ZSM-5 and concluded that NO is stored in Cu ZMS-5 as NO_2 therefore, NO oxidation is a key reaction. The study also concluded that water inhibits NO_2 storage in Cu-ZSM-5 because it competes with nitrate formation [28]. Komatsu et al compared the selectivity of N_2 in Cu morderite, Cu-Y and Cu-ZSM-5 and concluded Cu-ZSM-5 to be most active due to oxygen bridged Cu^{2+} ions [29]. Wallin et al studied the effect of ammonia on SCR of NO_x over H-ZSM-5 [30]. It is well documented that Cu-zeolites are far superior to Fe-zeolites at NO_2/NO_x ratios below 0.5 at low temperatures [31] [32]. Krishna Kamasundaram et al studied NH_3 SCR of NO_x

on Fe-Cu Zeolite at transient and steady-state and concluded that Fe-zeolite catalyst can achieve higher NO_x conversion levels at lower surface coverage, than Cu-Zeolite catalyst at optimal NO_2/NO_x ratios, due to the differences in their ammonia storage characteristics [33]. Sjovall et al. presented a global kinetic model for the SCR reaction over Cu-ZSM-5 [34], [35]. Olsson et al. performed kinetic studies of wash-coated monoliths. They eliminated the mass transfer diffusion by maintaining a constant space velocity [36]. Kwak et al. reported that Cu-ZSM-5 and Cu-SSZ-13 catalysts exhibit very high selectivity for NH_3 oxidation [37].

2.5 Catalyst for SCR

The SCR technology uses three different types of catalysts: noble metals, metal oxides, and metal-exchanged zeolites.

2.5.1 Noble metal-based catalysts

Noble metal catalysts are usually applied to reducing NO_x from moving sources but are limited in stationary sources due to the shortcomings of high costs, narrow working temperature window, oxygen inhibition effect and sensitivity to SO_2 and other gases. Noble metals such as Pt, Rd, and Pd were active in the SCR of NO_x. Of the three catalysts, platinum is most active for the oxidation of saturated hydrocarbons, palladium for the oxidation of carbon monoxide and unsaturated hydrocarbons and rhodium for NO_x removal. Rhodium is the most expensive catalysts, while palladium is the cheapest. However, at high temperatures, the Pt catalyst loses its selectivity for the NO_x reduction reaction owing to ammonia oxidation. The NH_3 oxidation rate is lower and the selectivity to N_2 is greater for Rh and Pd than for Pt. Owing to these limitations, the catalyst has not yet been commercialized for SCR using NH_3 [38].

2.5.2 Metal oxide based catalyst

Vanadia supported on titania and promoted with tungsten was found to be a promising deNO_x NH_3 SCR catalyst among metal oxides. Vanadium V_2O_5-based catalysts operate over a wide temperature range–250-400°C. Different metal oxide mixtures are used with vanadium, which has different roles in SCR. V_2O_5 is responsible for NO_x reduction and oxidation of SO_2. Tungsten trioxide (WO_3) is the most frequently used stabilizer for SCR

vanadia/titania formulations, and it improves thermal stability up to 700°C. These catalysts have significant resistance to sulfur poisoning and hence can be used in high-sulfur diesel fuels. Several studies have focused on vanadia-based catalysts for understanding the kinetics and mechanisms of SCR chemistry [39] [40] [41] [42]. BASF was the first to describe vanadia as an active component for SCR and TiO_2-supported vanadia for treatment of exhaust gases were developed in Japan [42] [43] [44]. This catalyst has been effective and popular in stationary SCR applications since the 1980s but has not been widely used for mobile applications because of its toxicity concerns related to the volatility of vanadia above 650°C. Mn-based catalysts supported on Al2O3, TiO2, CeO2, activated carbon fibers, and carbon nanotubes were reviewed by Zhiqing Zhang [45] [46] [47]. The effect of ceria modification on the low-temperature activity of the V2O5-WO3/TiO2 catalyst was evaluated for the selective catalytic reduction of NO with NH3 (NH3-SCR) is widely studied [48] [49] [50] [51].

2.5.3 Zeolite based catalysts

Zeolites are a class of aluminosilicates constructed from SiO_4 and AlO_4 tetrahedrons linked by oxygen to form a three-dimensional open-framework crystalline structure with channels and interconnected voids or cages. Zeolites carry a negative framework charge due to the lower charge of Al^{3+} compared to Si^{4+}, which is compensated by the incorporation of additional cations or the presence of hydroxyl moieties in the void spaces of the structures. This makes zeolites more active for catalytic processes. Zeolites have been applied widely to industrial processes mainly in adsorption and catalysis due to their high surface area, ion exchange capacity and regular arrays of channels and cavities. Zeolites are highly active, highly selective towards N_2, cheap, and nontoxic. Thus, metal-based zeolites have been commercially used in mobile emission applications. Barrer and Miller used FAU zeolites for Fluid Catalytic Cracking in the 1960s. leading to 30% gasoline yield (2013 33-35). Zeolites have applications in multiple processes, such as refinery operations (zeolite Y in FCC plants), cleaning of exhaust streams (zeolite Cu-ZSM-5/ zeolite Cu-CHA), and softening of water (zeolite A).

Various metal-exchanged zeolites, namely Cu, Fe, Cr, Ce, and Ag, have been investigated for NH_3 SCR. They exhibited excellent stability and selectivity for NH_3 SCR. Cu and Fe are the most widely studied NH_3 SCR catalysts, owing to their availability and high activity. The presence of transition metal ions provides a redox center for the internal surface area of the zeolite structure. Cu Zeolites are active at a lower temperature of 250°C whereas

Fe zeolites are active at higher temperatures of 300°C. In Fe ZSM-5 the conversion of NO to NO_2 on Fe^{3+} is the rate-determining step [52]. NH_3 reduced Fe^{3+} to below 300°C, and the conversion of Fe^{2+} to Fe^{3+} occurred only above this temperature. Therefore, the catalyst was only active above this temperature. It was seen that medium pore zeolites such as ZSM-5 (MFI framework), ferrierite or mordenite(MOR framework) were more active compared to zeolites with larger pores, zeolite Y (FAU framework), USY, and beta (BEA framework). Most recently, small-pore zeolites with CHA frameworks have gained attention in NH_3 SCR [53] [54] [55] [56]. The diverse properties offered by zeolites combined with their unique highly 'ordered' crystalline nature, enables the high performance of zeolites.

In heterogeneous catalysis, the pore diameter, morphology The number of acidic groups on the zeolite surface determines the reactivity of the catalyst. In the 1970s, zeolites were recognized as effective catalysts for the selective catalytic reduction of nitrogen oxides with ammonia. Metal-exchanged zeolites with Fe and Cu are highly effective for SCR reactions over a wide temperature range and have high tolerance to sulfur. The zeolite structure and composition directly impact the NO_x reduction activity, NH_3 storage capacity, and durability of the catalyst. Zeolites with small pores (chabazite CHA, SAPO-34) with 8-membered ring pore opening of 0.3-0.45 nm, medium pore zeolites like ZSM-5 with a 10-membered ring with a pore opening of 0.45-0.6 nm and large pore 12 membered ring zeolites with a pore opening of 0.7-0.8 nm, such as BEA or mordenite, are used as catalysts for NO_x reduction by NH_3 SCR [20] [57]. The active sites of these microporous zeolites become inaccessible to the reactants with sizes greater than the dimensions of the pores, this leads to strong diffusion limitation. This diffusion limitation increases the possibility of coking, which deactivates the catalysts and shortens the catalytic life [58].

Table 2.4: Performance of different catalysts for NH_3 SCR

Catalyst	Metal loading (wt%)	Method	Reaction conditions	Reaction temperature (∘C)	NO_x conversion (%)	Space velocity GHSV	Reference
Cu-ZSM-5	2	Liquid ion exchange	500ppm NH3, 500ppm NO, 7% O2	300-350	85	12000h^{-1}	[59] [60] [61] [62]
Cu FER	1.1	Liquid ion exchange	1000ppm NH_3, 1000ppm NO, 8%H_2O,10% O_2	350-400	75	25000h^{-1}	[59] [60]
Cu beta	1.6	Liquid ion exchange	1000ppm NH_3, 1000ppm NO, 8%H_2O,10%	300-350	69	25000h^{-1}	[59] [60]
Cu Y	0.7	Liquid ion exchange	1000ppm NH_3, 1000ppm NO, 8%H_2O,10% O_2	300-400	45	25000h^{-1}	[63] [59] [64]
Fe ZSM-5	0.7	Liquid ion exchange	1000ppm NH_3, 1000ppm NO, 8%H_2O,10% O_2	350-550	73	25000h^{-1}	[61] [59]
Cu SSZ-13	3.8	one pot hydrothermal	1000ppm NO, 1000ppm NH_3, 5% O_2	300-300	>95	20000h^{-1}	[65] [66]
Cu SAPO-34	1.7	Liquid ion Exchange	500ppm NH_3, 500ppm NO, 5% O_2	320-580	>95	12000h^{-1}	[67] [68]
Mn ZSM-5	5	Impregnation	500ppm NH_3, 450ppm NO, 5%O_2	300-400	>93	18000h^{-1}	[61] [62]
Ni ZSM-5	5	Impregnation	500ppm NH_3, 450ppm NO, 5%O_2	450	90	18000h^{-1}	[61] [62]
Zn ZSM-5	1.1	one step hydrothermal	800ppm NH_3, 800ppm NO and 5% O_2	350-500	>90	4800h^{-1}	[69]
Pd ZSM-5	0.7	Impregnation	500ppm NH_3, 700ppm NO, 2.6% O_2	200	90	20000h^{-1}	[70]
Ni ZSM-5	0.7	Impregnation	500ppm NH_3, 700ppm NO, 2.6% O_2	400	>85	20000h^{-1}	[70]
Ag ZSM-5	0.7	Impregnation	500ppm NH_3, 700ppm NO, 2.6% O_2	250-400	>73	20000h^{-1}	[70]
Fe Cu-ZSM-5	4	Solid state ion exchange	1000ppm NH_3, 1000ppm NO, 3%O_2	200-470	>90	45000h^{-1}	[71]

Noble metal catalysts have good activity at low temperatures, but they are not widely

used because of their poor anti-SO_2 poisoning ability, relatively high cost, and narrow operating windows [38]. The transition metal oxide catalysts have the advantages of high thermal stability and low cost, but their activity was lower than that of noble metals [72]. Therefore, the search for Green and efficient SCR catalysts have attracted considerable attention from researchers. Copper zeolite catalysts as the low-temperature NH3-SCR catalysts have broad application prospects to remove NO_x because they have better thermal stability, broad temperature windows, and special active sites of isolated ions [73]. The active substances of copper zeolite catalysts include Cu^{+}, Cu^{2+}, CuO, Cu_2O and other forms of copper oxide, which are essential for driving the nitrogen cycles. It can be found that the copper zeolite catalysts have better de-NO_x performance at low temperatures. Copper zeolite catalysts suitable for low temperatures include Cu-ZSM-5, Cu-BEA, Cu-MOR, Cu-FER, Cu-SSZ-13 and Cu-SAPO-34. Panahi et al. studied transition metal oxides (Co, Mn, Cr, Cu and Fe), and found that Cu/ZSM-5 was the most active catalyst in the presence of oxygen [74]. The performance of the zeolite catalysts for NH_3-SCR is presented in Table 2.4 [75] [76]. .

The most useful properties of Cu-substituted ZSM-5 catalysts are their low-temperature SCR activity, (200°C and below) high efficiency of standard SCR in a wide temperature window and high selectivity to N_2. The literature shows that higher the Cu loading in Cu-ZSM-5, the higher the NO–NH_3 SCR activity at low temperature. Komatsu with co-authors concluded that the active site of Cu-ZSM-5 zeolites for NO–NH_3 SCR is a pair of copper ions (dimer) connected by bridging oxygen, and their fraction increases with the copper loading [56]. Choi et al. supposed that NH_3 was strongly adsorbed on Bronsted acid sites and interacted with NO, which was weakly adsorbed on isolated copper ions, thus ensuring high NO reduction [77].

2.6 Catalyst Support

In gas-solid catalysis in automotive catalysis, the reactant gases are transported axially by convention, and the catalyst diffuses to the surface of the catalyst where the reaction occurs and products diffuse back to the gas phase. In exothermic reactions, the generated heat increases the overall catalyst temperature. Therefore, the material used for the catalyst supports should provide high thermal resistance with a low thermal expansion coefficient, which minimizes any change in the dimensions of the support. Ceramic or cordierite and metal monoliths are usually used as catalytic supports. Metal monoliths are expensive and are rarely used in commercial applications. A patent on the production of structured ce-

ramic articles by Corning, submitted in September 1958, refers to the use of honeycomb monolithic structures as catalyst supports for emission control [78]. Wash-coated monolithic catalysts are commonly used in exhaust after-treatment systems for stationary and automobile applications.

In a catalytic reactor, the optimum flow resistance plays an important role along with transport limitations. High flow resistance at a high flow rate increases the cost of reactor maintenance. Therefore, a balance between flow resistance and transport must be maintained for catalyst reactor optimization. A packed bed leads to high mass transfer at the expense of a high-pressure drop, whereas monoliths provide high low flow resistance but low heat and mass transfer.

The main drawbacks of these monolith-channelled structures are their Low interphase mass transfer rates suppressed radial mixing and improper washcoating. These channels have limited applications for dust-laden gases, such as emissions from coal boilers, because dust can block the opening of the channel and shorten the catalyst life. Metal wire mesh honeycombs have three-dimensional openings that provide a non-blocking network and permit free radial flow. These supports permit a rapid mixing of the gas flow and enhance interphase mass transfer rate to reduce reactor size [79].

2.6.1 Monolith supports

Monolith structures are usually cordierite magnesium Aluminium silicate, in the form of honeycomb-like structures with well-defined geometry of straight parallel channels of square, triangular, hexagonal, or sinusoidal cross-sections. The straight parallel channels have large open frontal areas and hence provide an unrestricted flow. Monoliths have been proposed as suitable catalyst supports for the production of synthesis gases (CO and H2) and dehydrogenation of ethylbenzene. Monolith catalysts have attractive applications in the selective hydrogenations of C2-C4 streams from steam crackers or post-reactors in selective oxidation processes. Monolith catalysts are commonly used for exhaust after treatment in automobile applications because they can be conveniently placed in exhaust pipes. High flow rates of gases from a diesel engine can pass through the monolith support with a minimal pressure drop, which reduces the back pressure and hence minimizes the engine load. Monoliths can be fabricated with different cell sizes and surface areas depending on the application. In exothermic reactions, ceramic or cordierite monoliths provide a high mechanical strength and high thermal resistance. The uniform flow distribution in the monolith reduces the formation of hotspots and provides high mass transfer rates.

Monolith catalysts face various challenges, such as the manufacturing cost, loading, packaging, and sealing of monolithic reactors. The pressure drop in a packed bed for the same geometric surface area may be two or three orders of magnitude greater than that of the monolith.

Ceramic monoliths are advantageous over metallic monoliths as they posses better porosity, good coating adherence, and thermal stability, whereas metallic monoliths have better heat transfer, pressure drop, mechanical stability, wall thickness and the overall volume [80]. Ceramic monoliths have good thermal stability due to a low thermal Howeveron coefficient however, the expansion coefficient could still crack with significant temperature changes.

2.6.2 Foam Supports

Open-cell foams contain cells with interconnected void regions and struts with interconnected solid matrices. Foams are low-density materials with high specific strength, high surface area, low thermal conductivity and controlled permeability. Because of their low-pressure drop, low density, high geometric surface area, high convective heat transfer, and radial mixing due to turbulent flow, foams can replace packed beds of particles in environmental catalysis. Foam-based reactors operating at a high space velocity with a low-pressure drop shorten the reactor length, simplify the loading procedure, and lower the overall installation costs. The structural morphology and specific surface area of the foam are responsible for its performance. Tortuous flow paths through the porous matrix are expected to enhance the gas/solid heat and mass transfer rates, and high surface-to-volume ratios would yield high activity per unit reactor volume. Foams are expected to minimize the occurrence of hot spots in the catalyst when highly exothermic reactions are performed while avoiding mechanical strength and thermal shock limitations. The porosity of the structure favours turbulent flow, which enhances mass transfer when compared to cordierite. The convection of heat through the pores results in good radial mixing and, hence, improved heat transfer [81]. Ceramic foams are used in molten metal filters and high-temperature thermal insulations. Metal foams are used in light constructions, as elements of aircraft, and as absorbers of energy in heat exchangers or recuperators. Metal foams have struts of less than one millimetre, larger specific surface area and higher porosity in compared to the ceramic ones. Moreover, metal foams show good mechanical properties, high thermal conductivity and resistance to thermal and mechanical shocks. The structure can improve the intraparticle reactions and external mass transport, leading to a

more controlled catalytic behavior and lower pressure drop obtained by random heterogeneous particles and pellets of catalysts. Structured catalysts are generally prepared by depositing an active material on an inert mechanical structure. Structured zeolites have some issues due to low zeolite loading or loss of the active phase due to poor adhesion and unmatched thermal expansion behavior with the monolithic substrate. The first work to synthesis zeolite on porous ceramics can be traced back to attempts to synthesisdensely layers of zeolite A or silicalite on α-Al_2O_3 in membrane applications [78]. Nova et al [82] investigated the influence of the substrate properties on the NH_3-SCR of NO_x for commercial cordierite honeycomb monoliths wash coated with Cu-exchanged zeolite. The study concluded that for catalysts with identical overall washcoat loads, a change in monolith cell density had a detrimental effect on ammonia conversion, with internal and external diffusional limitations caused by a thicker zeolite layer and larger channel hydraulic diameter, respectively. Ceramic or metallic foams offer the additional advantages of radial mixing within the body and enhanced mass and heat transfer owing to the turbulence of the flow and higher specific surface areas at the expense of only slightly increased pressure drops. Lee et al [83], [84] developed self-supporting ZSM-5 zeolite monolith foams (ZMFs) by introducing a solution of zeolite precursor within pre-shaped polymeric templates, followed by hydrothermal synthesis. Self-supported foam catalysts have increased active phase load in the structured reactor without additional weight, reactor volume, or pressure drops. The successful development of self-supported the catalyst could provide a ready-to-use material without the necessity of washcoating steps. Foam catalysts provide superior mass transfer, large surface area and short diffusion length within a catalytic layers of a few micrometers [85].

Foams have already been proposed as catalyst supports the oxidation of organic compounds like alcohols [86], hydrocarbons, ammonia, methane or the CO_2 reformation. Catalysts based on silver and copper foams have been studied for the partial oxidation of methanol, ethanol, and ethylene glycol [86]. Zeolites coated on SiC foams are used as environmental catalysts, which helps in process intensification [87]. Alumina foam catalysts support industrial steam reforming processes [88] [89]. The mass transport and kinetics in a structured steel foam reactor with a wash-coated Cu-ZSM-5 catalyst for the SCR of NO_x with ammonia was studied by Kryca et al. [90, 91]. Seijger et al. [92, 93] discuss the in-situ hydrothermal synthesis of binder-less ZSM-5 on ceramic foam support and its application to SCR.

The irregular, higher void fraction, and tortuous structure of foam catalysts provide well-mixed flow with back diffusion of heat transfer in all catalytic domains, providing in-

creased residence time and temperature, and consequently increasing reaction kinetics and conversion. The tortuosity provided by the struts of the foam disturbs the flow field, which induces dispersion in both the axial and radial directions [94]. Foams have higher porosity ranging from to 70-95%, and therefore possess a low-pressure drop and a higher geometric surface area than pellets [95]. The pressure drop in foams increases with decreasing porosity. The high porosity of foams makes it preferable for heat and mass transfer applications [96]. These structured catalysts showed the same catalytic activity as that of the powdered catalysts. But due to the higher amount of catalyst per unit volume of the reactor, its excellent mass transfer coefficient and low internal diffusion limitations, they could ensure to improve the NO conversion rate. The mass transfer coefficient and friction factor for cordierite monolith, packed bed and foam reactors reported in the literature are tabulated in Table 2.5

Table 2.5: Geometric characteristics of the samples and correlations for mass transfer and friction factor [97], [90].

Material type	Cell Density	Porosity	Dpore (m)	Sv [m^2/m^3]	Mass transfer correlations	friction factor
Cordierite monolith	400cpsi	0.85	1.16e-3	2709	$Sh = 3.608[1+0.095Re.Sc(d/L)]^{0.45}$ [98]	$fRe = 14.23/Re(1+0.045/(L/Dh.Re))^{0.5}$
Packed bed	-	0.4	0.3e-3	12000	$Sh=2+0.6Re^{0.5}Sc^{1/3}$	Ergun Equation
FeCrAl foam	20PPI	0.94	1.10e-3	1400	$Sh = 0.55Re^{0.5864}Sc^{1/3}$	f = 11.12/Re + 0.16
FeCrAl foam	30 PPI	0.96	0.9e-3	2100	$Sh = 0.41Re^{0.6147}Sc^{1/3}$	f = 6.66/Re + 0.11
Al foam	10 PPI	0.92	1.2e-3	1800	$sh = 1.13Re^{0.467}Sc^{1/3}$	f = 10.5/Re + 0.13
Al foam	20 PPI	0.92	0.8e-3	2153	$Sh = 0.68Re^{0.355}Sc^{1/3}$	f = 3.66/Re + 0.08
Al foam	40 PPI	0.94	0.7e-3	4300	$sh = 0.37Re^{0.398}Sc^{1/3}$	f = 3.08/Re + 0.08

The major development in this research area is contributed by the research groups summerized in the Table 2.6. Most of the literature works monolith as the support, whereas this study introduce and explore the supremacy of foam catalysts in NH_3 SCR. The performance of zeolite catalyst for NO_3 reduction is given by Figure 2.2

2.7 Processing Methods of Foam Supports

2.7.1 Sacrificial template method

In the sacrificial template method, a pore-filling agent is dispersed homogeneously in the ceramic slurry. The slurry containing the template was cast and placed in a mold. The pore-forming agents are divided into synthetic organic matters, natural organic matters and metallic and inorganic matters [99] [100] [101]. The pore-forming agent was removed by evaporation, pyrolysis, and leaching using acids or bases. The porosity, pore size, and pore morphology depend on the nature of the pore-filling agent. Li et al fabricated porous silicon

Table 2.6: Literature review

Author	Year	Scientific Contributions	Scientific Group
Saurabh Y. Joshi Ashok Kumar Krishna Kamasamudram Neal W. Currier	2015-present	Experimental and kinetic modelling of NH_3 SCR on commercial Cu-Fe zeolite catalyst under standard SCR reaction	Corporate Research and Technology, Cummins Inc.
Pranit Subhash Metkar Michael P. Harold Vemuri Balakotaiah	2013-present	Experimental and kinetic modelling of NH_3 SCR of NO_x on Fe-Cu zeolites wash coated on the monolith.	University of Houston Ford motors
Louise Olsson Hanna Sjovall Xavier Auvray	2015-present	Selective catalytic reduction of NO_x with NH_3 over Cu-ZSM-5 wash coated on monolith	Chalmers University of Technology & General Motors
Joanna Kryca J. Łojewska A. Kołodziej	2013-present	Experimental study of NH_3 SCR for NO_x reduction Cu Zeolites coated on metallic foams.	Polish Academy of Sciences
Isabella Nova Enrico Tronconi	2013-present	Experimental study of NH_3 SCR for NO_x reduction Cu Zeolites coated on Monolith.	University of Milan Rolls-Royce
Niket Kaisare Divesh Bhatia Preeti Aghalayam	2014-Present	Selective catalytic reduction of NO_x on powdered Au/Al_2O_3	IITM IITD Cummins Inc

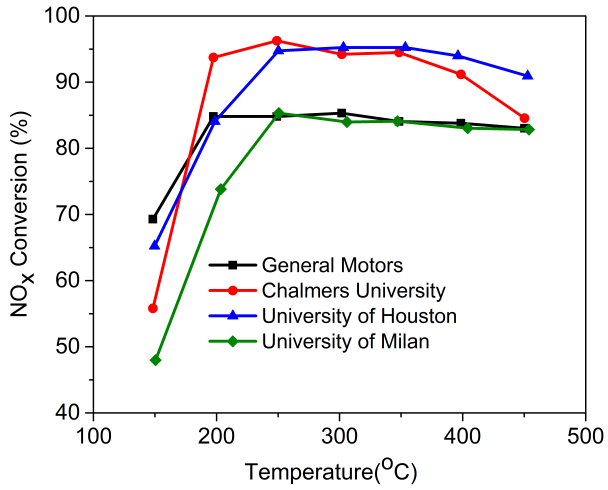

Figure 2.2: Reported literature zeolite performance

nitride with fibrous β-grain structure, using naphthalene powder as the pore-forming agent and gas-pressure sintering at temperatures above 1700°C [102]. Prabhakaran et al [103] used wheat particles as both a pore-forming agent and gelling agent for the preparation of macroporous alumina ceramics with pore sizes ranging from 20 to 800 μ m. Zhang et al [104], [100] produced porous alumina ceramics with unidirectionally aligned continuous pores via the slurry coating of mercerised cotton threads. Although the sacrificial template method offers better tailoring ability in terms of porosity, pore size distribution, and pore

morphology, the main disadvantage of this process is the time-consuming step required to remove the sacrificial phase either by heat treatment or sublimation.

2.7.2 Replication technique

Replication techniques were used to prepare reticulated ceramic foams. Replication techniques use porous templates such as wood, corals, and sea sponges. The presence of oriented vessels in the structure of wood enables the preparation of macroporous ceramics with highly anisotropic aligned pores, which cannot be achieved using other replica techniques. The carbon pre-form prepared by heating at 600-1800°C is infiltrated with gaseous or liquid ceramic precursors at high temperatures to obtain the macroporous ceramic. Similar approaches of impregnating pine wood using low-viscosity alumina, titania, and zirconia sols has been adopted in the literature [105] [106] [107]. Polymeric foams, such as polyurethane, are used as synthetic templates. The polyurethane foams are impregnated with ceramic slurry. The excess slurry is then drained by centrifugation or roller compression. The slurry-impregnated templates are dried and then pyrolyzed to decomposes organic sponges. After the pyrolysis, the ceramic layers are sintered at high temperatures for densification [108] [109]. The disadvantage of the replication technique is that struts of the structure are often prone to flaws, such as cracks and pores, during the burning step of the replica materials, leading to degraded mechanical properties [110].

2.7.3 Freeze casting

Freeze casting or ice templating technique is used to make homogenous cellular and unidirectional Lamellar microstructured foams. freeze casting method is simple, inexpensive, and environmentally friendly method capable of producing ceramic pieces with high porosity (25% to 90%) and with the possibility to control the morphology of these bodies compared with that of the methods. The formation of crystalline ice causes the substances originally dispersed in the aqueous medium to be expelled to the boundaries between the adjacent ice crystals. It does not require the addition of special templates, which usually lead to high production costs and require severe removal process [111]. The ceramic powder suspension was cast in a mold by freezing the dispersion medium. The dispersion medium during sintering was removed and the pores were left behind. There are four major steps in the freeze-casting process: preparation of the slurry, controlled solidification of the slurry, sublimation of the solvent and finally sintering of the green body. Zhang et al prepared novel graded porous Si_3N_4 ceramics by an aqueous freeze casting method [112].

Many studies have been carried out using additives such as polyvinyl alcohol (PVA), glycerol and gelatin to adjust the pore morphology and microstructures of the porous ceramics prepared by freeze-casting. Zuo et al used PVA to modify the pore morphology and structure of hydroxyapatite ceramics [113] [114]. Zhang et al used gelatin as an additive for the preparation of porous hydroxyapatite ceramics [115] [116]. Araki and Halloran studied the use of camphene as a solvent for the preparation of porous alumina ceramics via freeze casting [117] [118]. Tang et al prepared alumina ceramics with unidirectionally aligned gradient pore structure by freeze casting using a TBA-water system [119].

2.7.4 Emulsion templating

Emulsion templating was used for the preparation of the macroporous ceramics. An emulsion is a two-phase mixture of immiscible fluid phases in which one phase is dispersed in the other in the form of droplets. In oil and water emulsions, the oil phase is an organic solvent while the continuous phase is water, whereas in water-in-oil emulsions, the aqueous solution is the droplet phase with an organic solvent as the continuous phase. An emulsifier was used to stabilize the droplets dispersed in the continuous phase. A structure-directing agent was added to generate mesopores. The emulsion structure is maintained during polymerization, and upon the removal of the emulsion phase, a closed-cell macroporous structure is produced [111]. For the preparation of ceramic foams, this method uses oil droplets as a template and disperses them in a ceramic powder suspension or sol using an emulsifying agent. The emulsion was formed by the slurry and oil phases, and the oil phase was removed by drying after gelation. The oil-removed emulsion bodies were sintered to produce ceramic foams. The void spaces created by the removal of the emulsion droplet from the gel remain as macropores. The emulsion templates prevented large shrinkage and reduced cracks during sintering. The size of the emulsion droplets can be adjusted by changing the composition of the emulsifier, and can be easily removed by evaporation, extraction, and calcination. This method yields pores of various ranges from to 50-600μm. Vitorino et al reported the preparation of alumina foams by emulsion templating method using liquid paraffin for the oil phase [120]. Vijayan et al reported the alumina foam preparation with hydrogenated vegetable oil as the oil phase [121]. A method based on high alkane phase emulsions (HAPES) using decane as the oil phase has been studied for the preparation of macroporous ceramics [122]. The main disadvantages of emulsion templating technique are the long solidification process (24–48 h) and the requirement of development of emulsions with high stability that maintains its shape until

solidification [123].

2.7.5 Direct foaming

In direct foaming techniques, unidirectional channels are formed by stabilizing the air or gas in a ceramic powder suspension. A surfactant is used to stabilize the gases which have the property of adsorbing onto the surfaces or interfaces of the system and of altering to a marked degree the surface or interfacial free energies of surfaces [124]. Wang et al. studied the microstructure control in ceramic foams using a mixture of cationic cetyltrimethylammonium bromide (CTAB), and anionic surfactant sodium dodecyl sulfate (SDS) [125]. Although the direct foaming method is simple, inexpensive, and environmentally benign, owing to the nature of the introduced pores, the pore morphologies are typically spherical.

2.7.6 Gel casting

In gel casting techniques in situ polymerization of the organic monomer and cross-linker added in the ceramic powder, the suspension is the commonly used methods for preparing foamed ceramic powder suspensions. The wet foams removed from the mould after gelation are subsequently dried, and the binder is removed and sintered to produce ceramic foams. Zhou et al prepared pore-gradient Al2O3 foams by gel casting using the epispastic polystyrene (EPS) sphere template using acrylamide (AM) as the monomer and N, N'-methylene bisacrylamide (MBAM) as the cross linker. [126]. Biopolymers such as gelatin, proteins like ovalbumin and bovine serum albumin, agar, starch, and wheat particles are used as non-toxic gelling agents for fabricating ceramic foams. Lyckfeldt and Ferreira used starch as both pore former and consolidating agents for the preparation of porous alumina ceramics [127]. Mouazer et al prepared SiC foams by gel casting using agar as the gelling agent [128]. Lemos and Ferreira et al prepared porous hydroxyapatite bioceramics by a new direct consolidation method using fresh egg white [129].

2.7.7 Particle stabilized foams

In the particle-stabilization method, colloidal particles were used to stabilize the oil droplets in the emulsion. Studart et al reported the processing routes for the macroporous ceramics from particle-stabilized foams and emulsions [99]. Binks and Horozov et al reported the case of aqueous foams stabilized solely by silica nanoparticles [130]. Gonzenbach et al reported the preparation of macroporous alumina ceramics from particle-stabilized wet

foams [131]. Chuanuwatanakul et al produced porous cellular alumina ceramic green bodies by combining the particle-stabilized foam method using gel casting [132].

2.8 Introduction of Alumina as Supports

Supported catalysts can provide the same catalytic effects as a reduced amount of powdered catalyst owing to the advantages of the support geometry. Alumina is widely used as a catalytic support owing to its ability to disperse the supported phase, high thermal stability, and low availability. The ability to disperse is associated with the acid–basic character of the Al_2O_3 surfaces. Alumina, with its very stable surface OH groups, its Lewis acidity and the very high polarity of the surface acid–base pairs provide specific sites for anchoring cationic, anionic, and metallic species [133]. Aluminas can be used as a washcoat, a high-surface-area layer that gives the geometrical framework a suitable morphology to support and disperse the catalytically active phase, or they can be used as a primer, an intermediate layer between the geometrical support and the washcoat that acts as a glue between the two layers [134].

The majority of emissions in automobiles occur during the cold start of the engine, where the catalyst surface is not heated to the reaction temperature. A close-coupled catalytic converter near the engine manifold reduces the time the catalyst reaches the light-off temperature, thus reducing emissions. The close coupled converter near the exhaust manifold exposes it to a a more severe environment of 650°C, increasing the risk of catalyst or support sintering. α Al_2O_3 is the most thermodynamically stable polymorph of alumina, and is composed of octahedral Al cations. It possesses high mechanical, chemical, and high-temperature stabilities. The converter with α Al_2O_3 can be placed near the engine manifold in a close-coupled position, reducing cold start emissions, and also that thermal deactivation of the converter owing to support sintering is minimized. The temperature of a catalytic converter cycles between ambient and over 1000°C, α Al_2O_3 based converter was able to withstand temperatures greater than 1200°C and melt at 2072°C, under which the commercial cordierite converter experienced meltdown at 1450°C [135].

2.9 Catalyst Preparation Process

2.9.1 Wash coating

In washcoating techniques, the catalyst powder can be easily coated on the supports in the form of thin layers. The accessibility of the catalyst to the reaction increased, which enhanced the performance of monolithic catalysts. The washcoat thickness was varies from to 10-60μm. The catalyst support was pretreated with a secondary washcoat before washing the catalyst. Secondary support can provide better adherence and improved dispersion of active sites. Typically, γ-alumina is used as a secondary support owing to its high surface area. The methods adopted for the secondary coating of γ-alumina on metal and ceramic catalyst supports differ because of the different levels of adhesion [136]. Methods used for coating γ-alumina on ceramic coating are ceramic structures colloidal coating, sol-gel, and slurry coating. The secondary coating on the catalyst support involves repeated dipping of the support in a slurry or solution mixture, removing the excess liquid by compressed air followed by calcination. This process was repeated until the desired amount of coating was achieved. The open frontal area, geometric surface area and hydraulic diameter will be affected by the coating thickness. The coating of metallic substrates can be achieved by slurry coating, chemical vapor deposition, and anodization of Aluminium.

Zeolites are coated on monoliths by slurry coating or in-situ synthesis. In slurry coating, the particle size and slurry concentration influence adherence. Binder materials such as silica and $Al(NO_3)_3$ are used to improve the adhesion, but they reduce the catalytic activity by increasing the diffusional distance.

2.9.2 In-situ hydrothermal coating

In situ coating involves nucleation and growth of zeolites on the monolith channels, which results in chemical interaction of the zeolite layer with the surface of the monolith, leading to superior mechanical strength. In situ synthesis is divided into direct synthesis and direct synthesis with seeding or secondary growth. A zeolite seed layer was deposited on the substrate before hydrothermal treatment using a secondary growth technique [137] [138]. The formation of the precursor gel from the zeolite solution is crucial for coating in both the seeded and unseeded methods. The monolith was placed vertically in a mixture containing alumina precursor, silica precursor, and base. The precursor gel along with the monolith was heat treated in an autoclave and rinsed. sonicated, dried, and calcined. The Si/Al ratio, amount of water in the precursor solution, crystallization time, and temperature affect

nucleation, morphology, crystallinity, orientation on the surface of the channel, and adhesion to the surface. Zeolites grown onto monoliths also can lead to a better adhesion to the monolith surface compared to slurry coating [139]. The performances of Cu zeolites with supports for NO reduction by NH_3 SCR reported in the literature are presented in Table 2.7.

Table 2.7: Performance of Cu zeolites with supports for NO reduction by NH_3 SCR

Catalyst	Support	Method	CPSI	Compressibility MPa	Reaction condition	NO conversion (%)	Temperature (∘C)	Reference
Cu-ZSM-5	Polyether Urethane Foam	Hydrothermal	50	0.31	400ppm NH_3, 40ppm NO,6%O_2	86	250	[85]
Cu-ZSM-5	Nanosheet	Hydrothermal			1000ppm NH_3, 1000ppm NO, 8%O_2, 5%H_2O	>99	130-450	[68]
Cu-ZSM-5	Geo Polymer	3D printing	-	0.45	400ppm NH_3, 40ppm NO,6%O_2	>98	130-350	[140]
Cu SSZ-13	Honeycomb Monolith	3D Printing	-	2.54	500ppm NH_3, 500ppm NO, 5%O_2	>80	165-550	[141]
Cu CHA	Honeycomb Monolith	Washcoating	400	-	750ppm NH_3, 750ppm NO, 6%O_2	90	220-320	[142]
Cu BETA	Honeycomb Monolith	Washcoating	400	-	400ppm NH_3, 40ppm NO,6%O_2	60	260	[142]
Cu-ZSM-5	Honeycomb Monolith	Washcoating	400	-	400ppm NH_3, 40ppm NO,6%O_2	85	200	[142]
Cu SSZ-13	Honeycomb Monolith	Washcoating	400	-	500ppm NH_3, 500ppm NO, 5%O_2		250-450	[142] [143]
Cu-ZSM-5	Honeycomb Monolith	Washcoating			500ppm NH_3, 500ppm NO, 8%O_2	98	200-250	[144]
Cu-ZSM-5	Kanthal foam	Dip coating	20PPI	-	2000ppm NH_3, 2000ppm NO, 5% O_2	50	450	
Cu SSZ-13	Kanthal foam	hydrothermal	30PPI	-	2000ppm NH_3, 2000ppm NO, 5% O_2	96	250	[34]
Cu-ZSM-5	Honeycomb Monolith	Washcoating	400	-	500ppm NH_3, 500ppm NO, 8%O_2, 2%H_2O	98	250	[145]
Cu-CHA	Honeycomb Monolith	Washcoating	400	-	500ppm NH_3, 500ppm NO, 5%O_2	>98	250-300	[145]

Chapter 3

Experimental Details

3.1 Materials

Alumina powder (A16SG grade) of average particle size 0.34μm and specific surface area 10.4 m^2/g is procured from ACC Alcoa, Kolkata. Analytical reagent-grade sucrose and acetone were procured from Merck India Ltd. (Mumbai, India). Tetraethylorthosilicate aluminium isopropoxide ($Al(O\text{-}i\text{-}Pr)_3$), sodium hydroxide(98%), PAOH (20 wt

Ammonium zeolite ZSM-5 with SiO_2/Al_2O_3 of 23 with a specific surface area of 425 m^2/g used is procured from Alfa Aesar. The food grade HVO (Dalda, Bunge India Pvt. Ltd., India) was procured from a local market with a melting temperature range of 40–41°C. Analytical reagent grade sodium dodecyl sulphate (Merck India Ltd., Mumbai) and carrageenan (Sigma–Aldrich, USA) is used as an emulsifying agent and gelling agent, respectively. 35 wt% aqueous ammonium poly acrylate solution (Darvan 821A, Vanderbilt Company Inc., Norwalk, CA, USA) was used as dispersant. Distilled water is used to prepare ZSM-5 powder suspensions. Analytical reagent-grade toluene was procured from Merck India Ltd., Mumbai. Aluminium Oxide, 20% in H_2O, colloidal dispersion was procured from Alfa Aesar.

3.2 Experimental Set up

The experimental setup consists of a flow panel, reactor system, and gas analyzer system. The gas cylinders clamped to the walls were mounted with double-stage special SS regulators, and the gas lines were removed from the cylinder with $\frac{1}{4}$ inch SS tubes with ferrule fittings to the flow-panel arrangement. Special care was taken while fixing the regulator to the cylinder to ensure that there was no gas leakage in the connection with the help of

the ferrule fitting. The gases passed from the gas cylinder to the gas line at a pressure of 2 bar. The gas line from the cylinder enters the ball valve for sudden closure and opening of the gas line. The gas line was then connected to a pressure gauge, where a line pressure of 2 bar was rechecked and verified. Thus, the gases flowed through the MFC at a flow rate of 0.2 SLPM each. An MFC with a maximum flow rate of 1 SLPM and sensors resistant to corrosive gases were used. The flow was then passed through a check valve (3.5 bar to avoid backflow of the gases). Five similar gas lines are provided for NO, NO_2, N_2 O_2 and NH_3. These gases were mixed in the gas line and entered the reactor (vertical split tube furnace), where the NO_x gases were reduced to harmless gases N_2 and H_2O. The reactor consisted of a quartz tube of 1200 mm long with an inner diameter of 8 mm and an outer diameter of 12 mm. The reactor had a cylindrical catalyst core sample (Cu-ZSM-5, 25 mm long and 7 mm in diameter) cut from the prepared catalyst sample and wrapped with fiber-glass insulation tape to avoid gas bypassing the catalyst. The wrapped core sample was loaded into an 8 mm diameter quartz tube reactor. The reactor was filled with 3 mm quartz beads upstream to increase the heat transfer to the inlet gas stream and improve temperature uniformity. The quartz tube was fitted with graphite ferrules and custom stainless-steel end capes that connected the reactor gas in lines and provided inlet ports for thermocouples, pressure transducers, and sampling lines. The ferrule fittings in the quartz tube prevented any leakage in the quartz tube connection. The reduced gases from the reactor were analyzed using a Testo 350 flue gas analyzer for NO_x and an ammonia analyzer for NH_3 exiting the reactor. A K-type thermocouple was placed in the reactor and connected to a PID controller to control the temperature. The gas flow was controlled by Alicat's mass flow controller series, using Alicat's Flow Vision Software. A stainless-steel poppet check valve was used to avoid backflow of the gases. A digital absolute piezoresistive pressure sensor LEO-3 with a pressure range of 0-4 bar and a digital display were used to measure the pressure drop in the reactor. The reduced gases were vented using a blower the atmosphere. The experimental setup was a closed system with gas inlets from the cylinders and gas outlets vented into the atmosphere using a blower. All fittings and connections were ferrule fittings to avoid leakage in the system. A schematic and the components of the experimental setup are shown in Figure 3.1 and Figure 3.2.

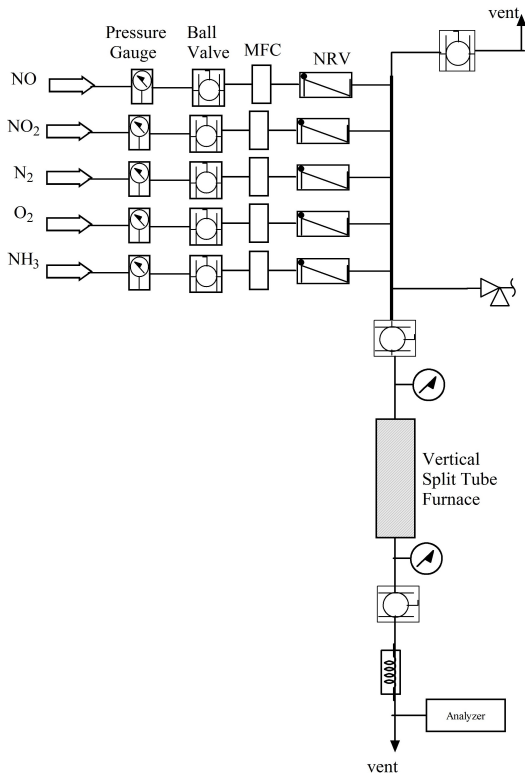

Figure 3.1: Schematic of the experiment set up

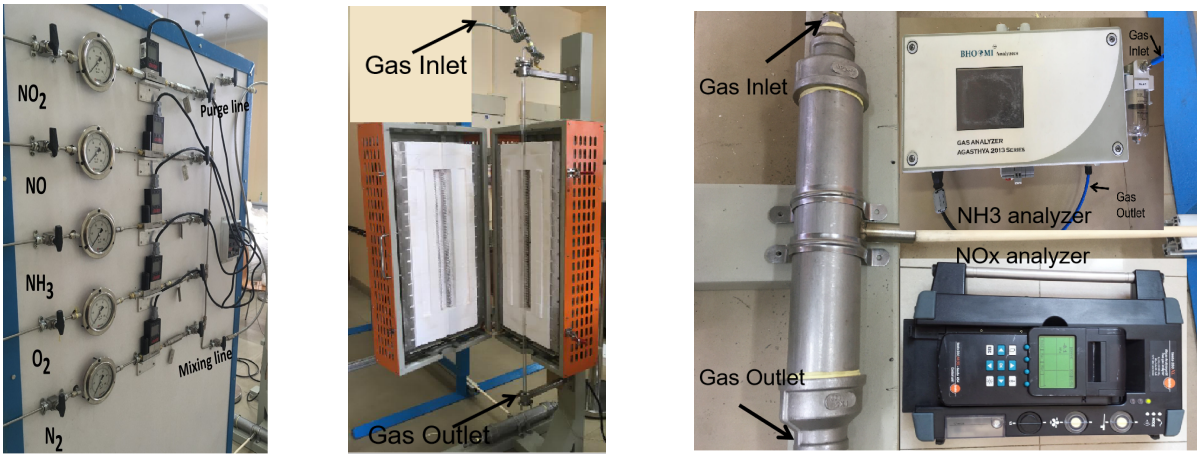

(a) Flow Panel **(b)** Reactor **(c)** Analyzer setup

Figure 3.2: Components of the experimental setup

3.2.1 Flow panel system

3.2.1.1 Mass flow controller

The mass flow controllers Alicat's MCS series for corrosive gases in the range of 0-1 SLPM were controlled automatically by Alicat's Flow Vision Software.

3.2.1.2 Check valve

Stainless Steel Poppet Check Valve, Adjustable Pressure, 1/4 in. Swagelok Tube Fitting, 3–50 PSIG (0.21 to 3.5 bar). Ensure that the valve is connected to the correct flow direction.

3.2.1.3 Pressure transducer

A digital absolute piezoresistive pressure sensor with a digital display is used to measure the pressure drop in the reactor.

3.2.2 Reactor system

A vertical split tube furnace was used as the reactor, where the reactants reacted with the catalyst and were reduced to harmless gases N_2 and O_2. The reactor consists of a 1200 mm long vertical quartz tube with an inner diameter of 8 mm and wall thickness of 2 mm. The quartz tube was filled with 3 mm quartz beads to improve the temperature and flow uniformity. A K-type thermocouple was placed in the reactor and connected to a PID controller to control the temperature.

3.2.3 Gas analysis system

3.2.3.1 Ammonia analyzer

An ammonia analyzer was used to quantify the amount of unreacted ammonia at the reactor outlet. NH_3 slip is considered to be very low at higher temperatures.

3.2.3.2 Flue gas analyzer

Testo 350 flue gas analyzer box with (O_2, CO, NO_{low}, NO_2, HC, fresh air valve, and Peltier chiller) test 350 analyzer box equipped with O_2, an incl. differential pressure sensor, temperature probe input Type K NiCr-Ni, and Type Pt 10Rh-Pt.

3.3 Experiment Section

3.3.1 Characterization and measurement

Powder X-ray diffraction (XRD) patterns of the synthesized zeolite samples were recorded using a Bruker D8 Advance powder diffractometer with Cu K radiation. The morphology of the foam catalyst samples was examined using scanning electron microscopy (SEM, FEI-Quanta FEG 200F). The samples were sputter-coated with gold prior to SEM analysis. The textural properties of the foam catalyst were obtained from N_2 adsorption-desorption measurements using a surface area analyzer (Micromeritics Tristar II, USA). The samples were degassed at 300°C for 12 h under flowing N_2 before the analysis. The BET–Emmett–Teller (BET) method was used to calculate the surface area. The total pore volume is estimated from the amount of N_2 adsorbed at a relative pressure of 0.99. The micropore volume was obtained using the t-plot method for N_2 adsorption at -196°C. The pore size distribution (PSD) was calculated using density functional theory (DFT). The particle size of the foam catalyst was determined using a Mastersizer 2000 instrument (Malvern Instruments, UK). The chemical state of the Cu ions was determined by X-ray Photoelectron spectroscopy (XPS) using an Omicron Nanotech. A Bruker Advance-300 nuclear magnetic resonance (NMR) spectrometer was used to collect the ^{27}Al NMR and ^{29}Si NMR spectra. The reducibility of the catalyst was analyzed by hydrogen temperature-programmed reduction (H_2-TPR) using a chemisorb 2750 (Micromeritics). H_2 TPR was performed with 500 mg of the catalyst sample preheated at 150°C by passing high-purity helium (25 cm^3/min) for 1 h. The gas was switched to 5% H_2 in Ar at 25cm^3/min at room temperature until the baseline was stable. The TPR was then started from room temperature to 900°C at a rate of 10°C/min. The acidity and activity of the catalysts were studied by ammonia temperature-programmed desorption (NH_3-TPD) experiments conducted using a Chemisorb 2750 instrument (Micromeritics). In NH_3-TPD, 500 mg of the catalyst sample was heated to 150°C under a high-purity helium flow (10 ml/min) for 30 min. Subsequently, 10% NH_3 in helium gas was passed through the sample at a flow rate of 30 ml/min for 30 min. NH_3-TPD is carried out from 100 to 600°C with a hold of 10 minutes at each temperature. The compressive strength of the alumina foams was measured in a Universal Testing Machine (Instron 5500, Instron USA) at a loading rate of 0.5 mm/min. The foam catalysts were designated as Cu-ZSM-5-x, where x represents the SiO_2 to Al_2O_3 mole ratio.

3.3.2 Mass transfer and pressure drop studies

Mass transfer studies have been performed on catalysts with particular dimensions. The mass transfer coefficient of the Cu-ZSM-5 foam catalyst for SCR was evaluated using activity tests. The average diameter of the cells was used as the characteristic length. Standard SCR of NO over the Cu-ZSM-5 catalyst by NH_3 was performed with a feed gas composition of 250 ppm NO, 250 ppm NH_3 and 8% O_2 at 450°C. The mass transfer coefficients K_m were measured from steady-state NO conversion under diffusion-controlled conditions under the assumption of isothermal plug flow behavior and irreversible reactions [146]. The balance of the mass transfer rate with the catalytic reaction rate and the assumption of negligible surface concentration yields the mass transfer coefficient K_m (m/s), as given by equation 3.4 [147] [148].

$$F\frac{dX}{dV} = -r = KC(1-X) \tag{3.1}$$

By integrating and rearranging Equation 3.1, the first-order rate constant (K) based on the reactor volume is given by Equation 3.2.

$$K = -\frac{Fln(1-X)}{CV} \tag{3.2}$$

The first-order kinetic constant is proportional to the mass transfer coefficient K_m and specific surface area S_v [149], assuming a cubic cell.

$$K = K_m S_v \tag{3.3}$$

The mass transfer coefficient K_m

$$K_m = -\frac{ln(1-X)}{\frac{S_v V}{Q}} \tag{3.4}$$

$$S_v = \frac{4(1-\epsilon)}{d_s} \tag{3.5}$$

where V is the volume of foam (m^3), X is NO conversion and Q is volumetric flow (m^3/s). F is the molar flow rate(mol/s), V is the reactor volume(m^3), r is the reaction rate (mol/m^3s), K is the rate constant and C is the NO concentration (mol/m^3) and d_s is

the struct diameter.

The pressure drop across the reactor was determined at different reactant gas flow rates. A digital absolute piezoresistive pressure sensor LEO 3 with a digital display of range 0-4 bar was used to measure the pressure drop in the reactor. A pressure transducer (Keller), connected to the inlet and outlet of the reactor, was used to measure the flow pressure. A schematic of the pressure-drop experiment is shown in Figure 3.3. Groppi et al. [150]

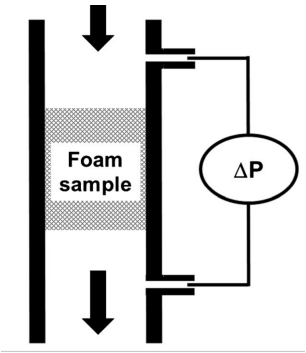

Figure 3.3: schematic of pressure drop experiment

determined the correlation for both metallic and ceramic foams with a pore density of 5-15 PPI for Re-up to 200, and Garrido et al. [146] studied the influence of topology on the mass transfer parameters and developed a correlation for ceramic foams (10–45 PPI) within the range of Re from 7 to 1100.

$$\frac{\Delta P}{L} = \frac{2f}{a}\rho u^2 \tag{3.6}$$

The pressure drop in foams, packed beds of pellets or monoliths are described by Giani et al. [148] as given by equation 3.6, where f is a friction factor and a is the characteristic length, specific to each support. where ΔP is the pressure drop across the foam (kPa), L is the reactor length, and u is the superficial velocity (m/s). The friction coefficient of the foam catalyst was derived from Equation 3.6. The geometric characteristics of the samples and correlations for the mass transfer and friction factor reported in the literature are listed in Table 3.1.

3.3.3 Experiment Protocol

In standard SCR, NO_x is reduced by NH_3 in the presence of O_2 in the active sites of Cu-ZSM-5. The activity of Cu-ZSM-5 foam catalyst to standard SCR reaction is studied from 200-550°C. Initially, 250 ppm NH_3 was passed over the catalyst until saturation. Subsequently, 250 ppm NO and 8% O_2 were fed to the reactor simultaneously at a particular

Table 3.1: Geometric characteristics of the samples and correlations for mass transfer and Fanning friction factor [97], [90].

Material type	Cell Density	Porosity	Dpore (m)	Sv [m^2/m^3]	Mass transfer correlations	Fanning friction factor
FeCrAl	20PPI	0.94	1.10e-3	1400	Sh = $0.55Re^{0.5864}Sc^{1/3}$	f = 11.12/Re + 0.16
FeCrAl	30 PPI	0.96	0.9e-3	2100	Sh = $0.41Re^{0.6147}Sc^{1/3}$	f = 6.66/Re + 0.11
Al	10 PPI	0.92	1.2e-3	1800	sh = $1.13Re^{0.467}Sc^{1/3}$	f = 10.5/Re + 0.13
Al	20 PPI	0.92	0.8e-3	2153	Sh = $0.68Re^{0.355}Sc^{1/3}$	f = 3.66/Re + 0.08
Al	40 PPI	0.94	0.7e-3	4300	sh = $0.37Re^{0.398}Sc^{1/3}$	f = 3.08/Re + 0.08

temperature.

$$4NH_3 + 3O_2 => 2N_2 + 6H_2O \tag{3.7}$$

$$4NH_3 + 5O_2 => 4NO + 6H_2O \tag{3.8}$$

$$4NH_3 + 7O_2 => 4NO_2 + 6H_2O \tag{3.9}$$

The activity of Cu-ZSM-5 for NH_3 oxidation was studied by exposing the catalyst to over 250 ppm NH_3 and 8% O_2. Steady-state experiments were conducted in the temperature range of 200-550°C with a hold of 30 min at each temperature and a ramp of 5°C/min.

The NO_x adsorption study quantified the storage of NO and NO_2 in the Cu-ZSM-5 foam catalyst. NO_x adsorption experiments were performed with a feed NO_x concentration of 250 ppm, along with inert gas at 150°C. During NO_x uptake, NO_x was fed into the catalyst for 30 min until saturation. The NO_2 gas was switched off, and the inert gas was allowed to flow for 10 min to desorb the loosely bound NO_x. A temperature ramp of 5°C/min was applied from to 150-500°C to desorb the stored NO_x. In the transient experiments, 250 ppm NH_3 was introduced into the reactor along with inert gas at 150°C, 250°C, and 350°C. The ammonia feed was switched off once the catalyst was saturated with ammonia gas (1800 s). The inert gas flowed over the catalyst for 600 s to release the loosely bound ammonia. feed with 250 ppm NO_x and 8% O_2 was then introduced into the reactor. The effect of the NH_3 feed gas concentration on the SCR reaction was studied by varying the feed concentration from 100-500 to, ppm at intervals of 30 min. The concentration of NO was maintained at 250 ppm and that of O_2 at 8% at a feed flow rate of 1000 ml/min. The effect of the NO concentration in the feed gas was studied over a Cu-ZSM-5 foam catalyst with feed gas concentrations of 250 ppm NH_3, 100-500 ppm NO, and 8% O_2 at 200°C and 250°C. The NO concentration was maintained for 30 min at each concentration. The

influence of the O_2 concentration on the feed gas composition was studied by varying the concentration of O_2 from to 4-12% for 30 min at each concentration, while maintaining a constant concentration of other feed gases at 250 ppm of NO and 250 ppm of NH_3 at 200°C and 350°C. The effect of the NO_2 concentration on the feed composition was studied by varying the concentration of NO_2 from 100-500 to, ppm and keeping 250 ppm NO, 250 ppm NH_3 and 8% O_2 constant. NH_3 inhibition is evident in the study of variable NH_3 in the SCR reaction. A transient experiment was carried out to investigate NH_3 inhibition in standard SCR with feeds of 250 ppm NO_x, 250 ppm NH_3 and 8% O_2. The feed was passed over the catalyst for 30 minutes at 200°C. Once the reactants are saturated, NH_3 is suddenly switched off, and the transient NO and NO_2 outlet concentration responses are monitored. It is important to investigate the effect of the NO_2/NO_x feed ratio on NO oxidation and standard SCR, owing to the formation of nitrates. The effect of the NO_2/NO_x feed ratio on NO oxidation was studied at different temperatures of 200°C and 350°C, with the NO_2/NO_x ratio varied from 0 to 0.75, by maintaining the NO_x concentration at 250 ppm.

Chapter 4

Experimental Investigation of Mass Transfer and Kinetics of NH_3 SCR Over Cu-ZSM-5 dip-coated on α Alumina Foam

4.1 Introduction

Nitrogen oxides (NO_x), which originate from various combustion processes, are major air pollutants harmful to humans and the environment. This is a major component of fossil-fuel combustion. These pollutant gases must be removed before the flue gas is vented into the atmosphere, because nitrogen oxides are major contributors to greenhouse gases. Selective Catalytic Reduction (SCR) is the major technique used for NO_x emission reduction by NH_3 the catalysts used for SCR include metal oxides, noble metals, and zeolites. Zeolites are widely used as SCR catalysts owing to their high selectivities. The alumina sites in the framework structure of the zeolite carry negative charge, and the structure-directing agent often acts as a counterion in the framework to maintain the electroneutrality of zeolites. Barrer et al. [151] discovered that the presence of organic cations along with alkali provides more open crystal structures, which improves the accessibility of the active sites. The drawbacks of zeolite powders with high mass-transfer limitations and pressure drops can be further improved by introducing catalytic supports. Powdered zeolite catalysts are coated on substrates using dip coating, spin coating, in-situ crystallization, and secondary growth techniques. The catalyst support was pretreated with a secondary washcoat before the catalyst was washed. This secondary support can provide better adherence and improved dispersion of the active sites. In the slurry coating, the particle size and slurry concentration influence adherence. Binder materials such as silica and $Al(NO_3)_3$ are used

to improve adhesion, but they reduce the catalytic activity by increasing the diffusional distance. Washcoating on substrates has the disadvantages of low catalyst loading per unit volume of the system and loss of the active phase owing to poor adhesion and unmatched thermal expansion with the substrate.

The literature reveals several 1D kinetic models for NH_3-based SCR in monolithic reactors based on the single-channel assumption. Chatterjee et al. [152] developed a kinetic model for titania-vanadia catalyst, which was validated using experimental data from diesel engine bench tests. Their model showed that the reduction efficiency of NO_x increases in the presence of NO_2 in the feed. Olsson et al. [35] developed a kinetic model for Cu-ZSM-5 catalyst and estimated the kinetic parameters by performing experiments for a wide range of operating conditions. Pant and Schmieg [153] examined the performance of a Cu-ZSM-5 catalyst, which showed a reduction in NO_x conversion due to NH_3 oxidation at high temperatures. To account for this behavior, they suggested that the rate expressions in the model given by Olsson et al. [154] for the standard SCR reaction and ammonia oxidation reaction should be of the second order in the NH_3 concentration. A combination of the models given by Olsson et al. [34] and Wang et al. [155] was proposed by Metkar et al. [156], which considers the effect of washcoat diffusion. They studied the activities of dual-layered Cu- and Fe-zeolite catalysts. They found higher performance for a broader range of operating conditions in dual catalysts than in individual catalysts. Dong fang Wu et al. studied the mechanical stability of ZSM-5 wash coated on monolith [157]. Landong et al. synthesized Cu-ZSM-5, Cu-Titanium silicate, and Ir ZSM-5 on honeycomb cordierite monolith and studied SCR of NO_x from automobile exhaust [158] [159]. Kryca et al. compared the heat and mass transfer properties and pressure drops of packed-bed reactors, Kanthal foam, monoliths, and honeycomb reactors. They concluded that packed bed reactors offer high mass transfer with a high-pressure drop, whereas monolithic reactors possess a low-pressure drop but poor mass transfer [90]. Kryca et al. studied NO_x SCR by NH_3 and concluded that the structure of the support significantly affects catalyst performance, even for a highly active catalyst. They also confirm that the reduction of NO is a diffusion-limited process and the optimization of support geometry may lead to further enhancement of catalytic performance.

In this study, a Cu-ZSM-5 catalyst was dip-coated onto a macroporous cylindrical α alumina foam support. The activities and performances of the catalysts were evaluated using a dip-coated system.

Experimental Details

4.2 Preparation of Cu-ZSM-5 dip-coated on α alumina foam

4.2.1 Preparation of Alumina Foam

Figure 4.1: Schematic for thermo-foaming of alumina [160]

The thermo-foaming method reported by Vijayan et al. was used for the preparation of alumina foam because it is environmentally benign and can produce alumina foam bodies of diverse shapes [160] as shown by Figure 4.1. Accordingly, a mixture of 100 g of alumina powder and 100 g of sucrose was prepared by planetary ball milling in an acetone medium, followed by drying in an air oven. The alumina powder-sucrose mixture was heated in a borosilicate tray at 185°C to melt the sucrose and thoroughly mixed with a wooden ladle to form an alumina powder dispersion in molten sucrose. The alumina powder dispersion in the molten sucrose was heated in an air oven at 140°C for 72 h to achieve foaming and setting. Cylindrical samples with a diameter of 10 mm and a length of 25 mm were prepared by cutting the foamed body using a stainless steel tube. The cylindrical bodies

were heated in an electrically heated furnace to 1600°C. A heating rate of 30°C/h was used from room temperature to 600°C, and 120°C/h from 600°C to 1600°C with a holding time of 2 h at 600°C and 1600°C. The volume shrinkage of the bodies was calculated from their initial and final dimensions. The density of the alumina foam body was calculated by using the weight and dimensions obtained after sintering.

4.2.2 Preparation of dip-coated Cu-ZSM-5 on α alumina foam

The Ammonium ZSM-5 powder was ion-exchanged with Na ZSM-5 using $NaNO_3$ for 48 h and calcined at 500°C for 5 h. The Na-ZSM-5 foam catalysts were ion-exchanged with 50 ml of 0.02 M copper acetate solution at 50°C for 72 h. The Cu-exchanged zeolites were then dried at 120°C for 2 h. A thin layer of 5wt% binder, Aluminium oxide, 20% in H_2O, colloidal dispersion with distilled water and ethanol (50:50) was wash-coated on alumina foam to generate an improved zeolite surface. This sample was then calcined for 1 h at 550°C before the introduction of the zeolite layer. Alumina foams (7.8 mm in diameter and 17 mm in length) were dip-coated with a slurry of 20 g of Cu-ZSM-5 along with 25 g Al_2O_3, 50 g ethanol, and 30 ml H_2O. 1.1 wt% of Cu-ZSM-5 was obtained by dip-coating each alumina foam sample. The Cu-ZSM-5 foam catalyst prepared by dip coating method have compressive strength of 6 MPa.

Results and Discussions

4.3 Characterization and measurements

4.3.1 BET surface area analysis

The N_2 adsorption-desorption isotherms of the foam catalysts are shown in Figure 4.2. The isotherms of the Cu-ZSM-5 foam samples exhibit a continuous increase in the adsorbed nitrogen volume with P/P_0 and a small hysteresis branch corresponding to adsorption-desorption. The Cu-ZSM-5 foam catalysts exhibit type 1 hysteresis associated with porous materials consisting of well-defined cylindrical pore channels or agglomerates of approximately uniform mesopores. The enhanced uptake of nitrogen at P/P_0 greater than 0.8 shows the presence of macropores. The plateau region at P/P_0 was less than 0.5, indicating the presence of micropores, which is beneficial for an excellent pore structure and large BET surface area. The pore size distribution is important for determining the accessibility of

active sites to reactants and the extent of dispersion of the active metals within the catalyst. The BJH analysis of the Cu-ZSM-5 foam samples exhibited a broad distribution of pore sizes in the range of 2–20 nm, with a maximum at 10 nm, as shown in the inset of Figure 4.2. The surface area of the Cu-ZSM-5 foam catalyst is 172 m^2/g. The chemical composi-

Table 4.1: Surface area analysis

Sample	S_{BET} m^2/g	S_{micro} m^2/g	$S_{external}$ m^2/g	V_{total} cm^3/g	Cu %	Al %
Cu-ZSM-5	172	122	48	0.14	6.7	2.4

tion of the foam catalyst, as determined by ICP, is presented in Table 4.1. The Cu content of the Cu-ZSM-5 foam catalyst is 6.7

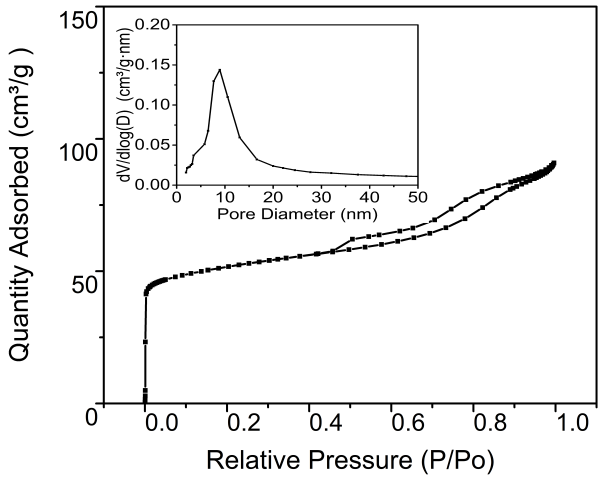

Figure 4.2: N_2 adsorption isotherm of Cu-ZSM-5 foam catalysts

4.3.2 Transition electron microscopy analysis

The distribution of copper species on the catalyst was analyzed using HR-TEM. Figure 4.3 shows the distribution of copper species as dark spots. The insert in the Figure 4.3 shows The interplanar spacing of the small dark spots was 0.23 nm, which corresponds to CuO.

4.3.3 Scanning electron microscopy analysis

The SEM micrograph of the fractured surface of the alumina foam support in Figure 4.4 shows an interconnected cellular structure, with cell sizes ranging from 25 to 170 μm. The circular cell windows connecting the cells had sizes in the range of 50–2500 μm.

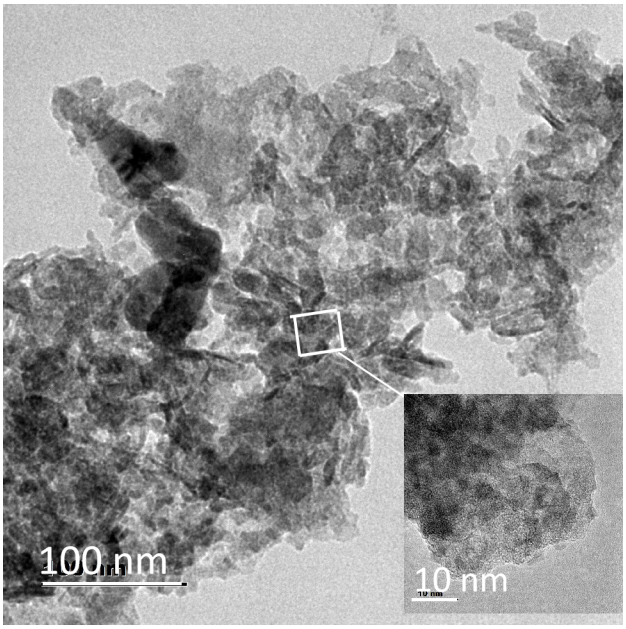

Figure 4.3: TEM micrograph of Cu-ZSM-5 foam catalyst

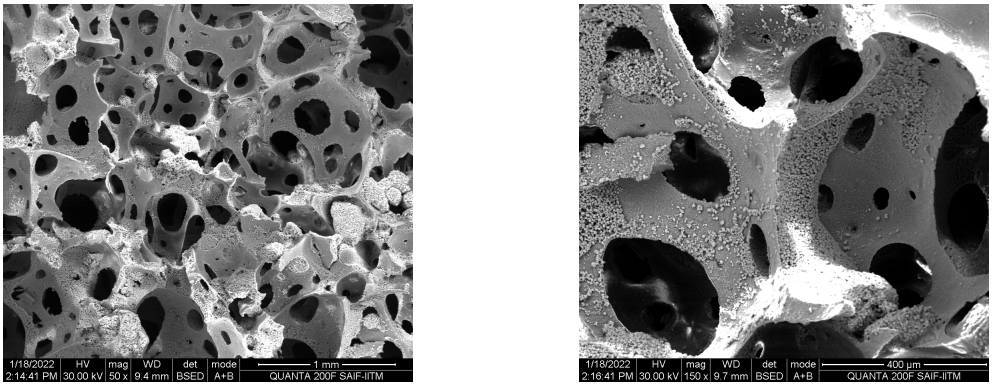

(a) **(b)**

Figure 4.4: SEM micrograph of Cu-ZSM-5 foam catalyst

The interconnected cellular structure provides a large area for the deposition of the ZSM-5 catalyst and a tortuous path for NO_x leading to a higher NO_x reduction efficiency. An SEM micrograph of alumina foam is shown in Figure 4.4a. The deposition of Na-ZSM-5 crystals on the cell wall surface of the support foam is shown in Figure 4.4b. It was found that the cell wall surfaces of the alumina foam were almost completely covered by Na-ZSM-5 crystals during in situ hydrothermal synthesis. The high-magnification SEM image shows the macroporous irregular morphology of the catalyst coated on the alumina cell wall surfaces. Figure 4.4b shows a high-magnification image of the catalyst coating on the alumina foam surface. The macropores present in the catalyst support would facilitate

the diffusion of gas molecules to access the active sites of the catalyst.

4.3.4 Ammonia temperature programmed desorption

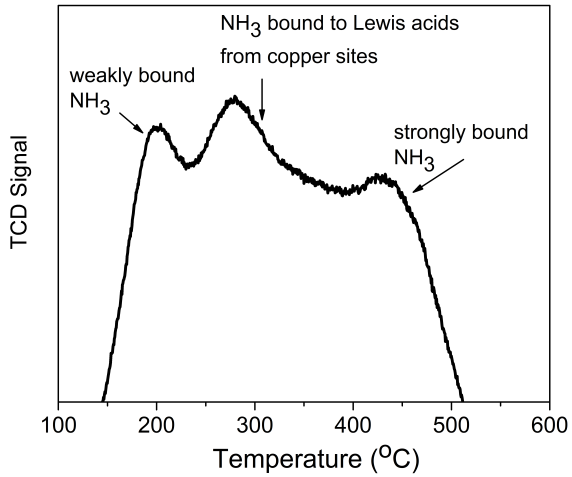

Figure 4.5: Ammonia temperature programmed desorption of Cu-ZSM-5 foam catalyst

Table 4.2: NH_3-TPD data of Cu-ZSM-5 foam catalysts

Samples	Tpeak (^{o}C)			Acid amount (μmol/g)		
	Peak 1	Peak 2	Peak 3	Weak acidity	Lewis acidity	Strong acidity
Cu-ZSM-5	190	279	444	59	36	107.5

The ammonia temperature programmed desorption (TPD) curves of the Cu-ZSM-5 foam catalysts are shown in Figure 4.5. The area under the ammonia-TPD graph was directly proportional to the number of acidic sites in the zeolite. Ammonia TPD curves of the zeolite showed three desorption peaks.

The desorption peak at a lower temperature of approximately 190°C corresponds to physisorbed ammonia in weak acid sites or NH_3 adsorbed on weak acid sites on surface hydroxyls [161].

The desorption peak centered at 280°C was assigned to NH_3 released from Lewis acid sites originating from the copper species [162]. The high-temperature desorption peak at 444°C is related to the presence of strongly acidic hydroxyl groups as the sorption sites.

The NH_3-TPD peaks and acidity of the Cu-ZSM-5 foam are listed in Table 4.2. The total acidity of Cu-ZSM-5 foam catalyst is 202 μmol/g,

4.3.5 X-ray photoelectron spectroscopy

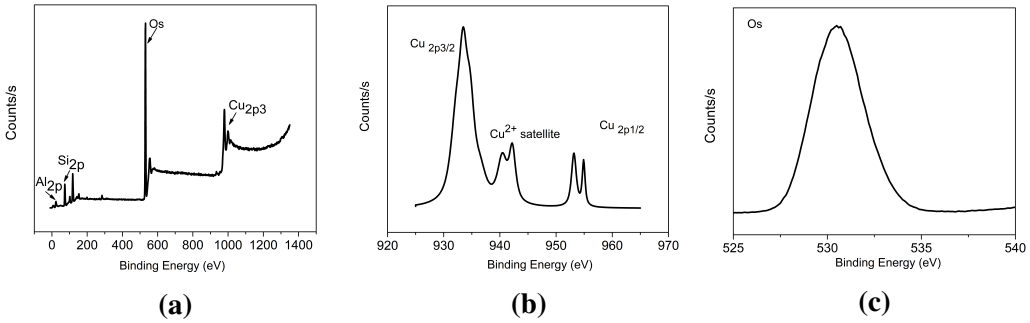

Figure 4.6: X-ray photoelectron spectroscopy of Cu-ZSM-5 foam catalyst (a) XPS Survey (b) Cu_{2p} Scan (c) O1s Scan

X-ray photoelectron spectroscopy revealed the elemental composition and chemical state of Cu in Cu-ZSM-5 zeolite. The number of electrons and elements is given by the area under the curve. Figure 4.6a shows XPS survey scans of the Cu-ZSM-5 foam catalysts. Figure 4.6b shows the binding energies of 933.4 eV for Cu $2p_{3/2}$ and 946.3 eV for Cu $2p_{1/2}$ with satellite peaks around 940 eV, which correspond to Cu^{2+} in CuO. The binding energy of 935.1 eV and 955 eV corresponds to isolated Cu^{2+} [163] [161] [164]. The XPS peak at 932.5 eV corresponds to Cu^{+} in Cu-ZSM-5. XPS analysis gives a ratio of isolated Cu^{2+} to CuO of 1.01. O1s peak at 532.4 ev in Figure 4.6c is assigned to the surface adsorbed oxygen and the peak at 530.6 eV on O1s spectra is assigned to oxygen in CuO. The peak centred at around 531.6 eV is attributed to lattice oxygen species (Cu-O-Cu and isolated Cu^{2+}) and the peak located at 532.6 eV could be assigned to the surface chemisorbed oxygen species [165]. Surface-chemisorbed oxygen species are more reactive than lattice oxygen species in oxidation reactions because of their higher mobility [166].

4.4 Mass transfer and pressure drop studies

In environmental catalysis, a trade-off between the mass transfer and pressure drop performance of the catalyst is advisable. Kycra et al. reported that packed bed reactors offer a high mass transfer at the expense of a high pressure drop. Monolith reactors offer a low-pressure drop, but with low mass transfer [97]. An ideally structured catalyst should yield very high conversions under diffusion-controlled conditions to meet the required emission limits while keeping the pressure drop as low as possible to reduce energy costs. Foam reactors provide high mass transfer with a low-pressure drop compared to existing monolith

reactors for NO_x reduction by NH_3 SCR. Mass transfer studies were carried out in hierarchical Cu-ZSM-5 foam of 7.8 mm diameter and length of 17 mm. The flow velocity was varied from 0.4 m/s to 5.4 m/s. The mass transfer coefficient of the Cu-ZSM-5-20 foam catalyst for standard SCR was evaluated using activity tests. The average cell diameter was used as the characteristic length. Microscopic imaging revealed that the average pore size and strut diameter were 2.5 mm and 0.89 mm, respectively. The estimated porosity was 70%, and the specific surface area was 3362 m^2/m^3. The standard SCR of NO over the Cu-ZSM-5 catalyst by NH_3 was performed with a feed gas composition of 250ppm NO, 250ppm NH_3 and 8% O_2 at 450°C. The rate constant remains approximately the same for temperatures above 350°C at 80,000 h^{-1}, which suggests the onset of full external mass transfer control. The mass-transfer coefficient was evaluated from the activity test using Equation 3.4 [146].

Figure 4.7a shows the estimated mass transfer coefficient of the Cu-ZSM-5 foam catalyst plotted against feed flow rate. Figure 4.7a shows that the mass transfer coefficient increases with increasing feed flow rate for the Cu-ZSM-5 foam catalyst [90] [146] [81]. In heterogeneous reactors, external mass transport can be increased by better fluid mixing. The tortuous flow path in the foam catalysts increased mixing and enhanced external mass transfer. A higher flow rate leads to a reduction in boundary-layer thickness and contributes to better mixing. This reduces the mass transfer resistance and promotes the transport of more reactants to the surface.

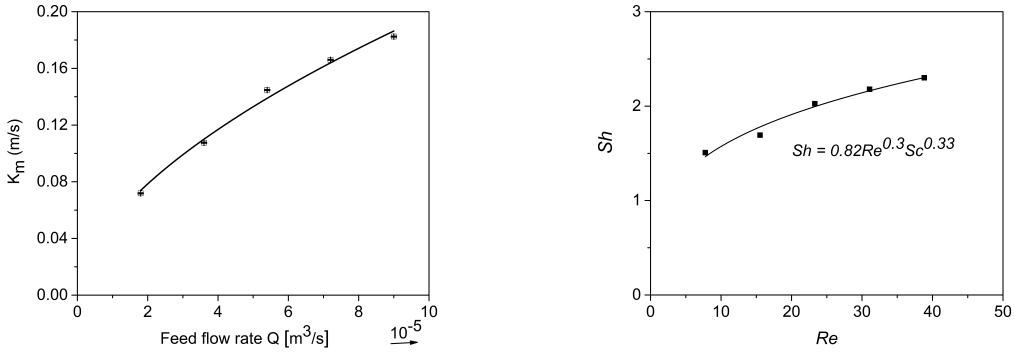

Figure 4.7: (a)Mass transfer coefficient evaluated at a feed flow rate of $1.8e^{-5}$ to $1xe^{-4}$ m^3/s for Cu-ZSM-5 foam catalyst. (b) Correlation between Sherwood number and Reynolds number

The mass transfer data were fitted to be expressed as a correlation using non-dimensional quantities of the Sherwood number, Schimidt number, and Reynolds number. Figure 4.7b

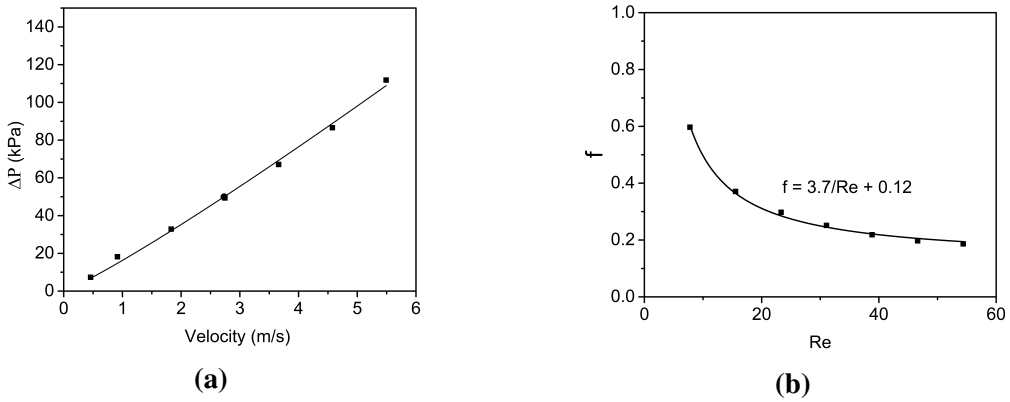

Figure 4.8: (a) Pressure drop across the Cu-ZSM-5 foam catalyst for a velocity of 0.4 to 5.4 m/s (b)Friction factor vs Reynolds number for Cu-ZSM-5 foam catalyst

shows the data fitted to a single correlation represented by

$$Sh = 0.82Re^{0.3}Sc^{1/3} \;\; Re < 50 \tag{4.1}$$

The developed mass transfer correlation was well aligned with the correlations reported in the literature [150].

Pressure drop studies conducted on the Cu-ZSM-5-20 foam catalyst and blank alumina foam with feed flow velocity of 0.4 to 5.4 m/s are shown in Figure 4.8a. From Figure 4.8a it is observed that the pressure drop increases with an increase in flow velocity. The pressure drop across the Cu-ZSM-5-20 foam catalyst support was a minimum of 7.3 kPa at the lowest velocity of 0.4 m/s, with a linear increase in the pressure drop to 112 kPa at 5.4 m/s.

$$f = \frac{3.7}{Re} + 0.12 \;\; Re < 50 \tag{4.2}$$

The friction factor coefficient evaluated from equation 4.2 was fitted, as shown in Figure 4.8b for the Cu-ZSM-5 foam catalyst. The correlation obtained by curve fitting is a Forchheimer-type equation with a viscous term and inertial term.

The experimental Sh and friction factor values were in excellent agreement with those predicted in previous studies [90].

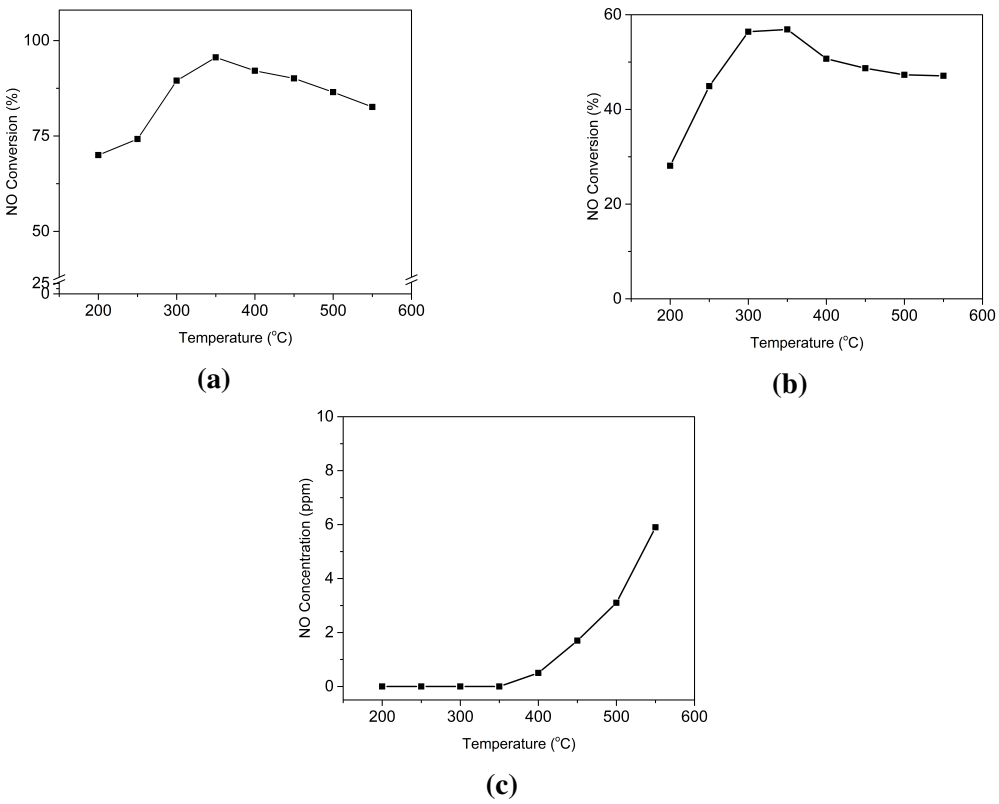

Figure 4.9: (a) NO conversion for NH_3 oxidation over Cu-ZSM-5 foam catalyst exposed over 250 ppm NH_3 and 8% O_2 (b) NO conversion in Cu-ZSM-5 foam catalyst exposed over 250 ppm NO and 8% O_2 (c) NO outlet concentration for NH_3 oxidation over Cu-ZSM-5 foam catalyst exposed over 250 ppm NH_3 and 8% O_2

4.5 SCR Reaction Chemistry

4.5.1 Selective catalytic reduction of NO with NH_3

In standard SCR, NO_x is reduced by NH_3 in the presence of O_2 in the active sites of Cu-ZSM-5. The activity of Cu-ZSM-5 foam catalyst to standard SCR reaction is studied from 200-550°C. Initially, 250 ppm NH_3 was passed over the catalyst until saturation. Subsequently, 250 ppm NO and 8% O_2 were fed to the reactor simultaneously at a particular temperature. Figure 4.9a shows the steady-state NO_x conversion at different temperatures over the Cu-ZSM-5 foam catalyst measured from the outlet NO concentration. As shown in Figure 4.9a, the NO conversion of 70% at 200°C increased with an increase in temperature, with a maximum at 350°C. The highest conversion of 95% was observed at 350°C, beyond which the conversion slightly decreased. The conversion decreased at temperatures above

400°C owing to the unavailability of NH_3 for reduction.

NO oxidation is an important reversible side reaction. This reaction is kinetically controlled at low temperatures and equilibrium at higher temperatures. At lower temperatures, NO oxidation leads to the production of NO_2 whereas at higher temperatures, NO_2 decomposes into NO. NO oxidation is desirable because of the high SCR rate in the presence of NO_2. NO oxidation was studied with a feed of 250 ppm NO and 8%O_2 in the temperature range of 200-550°C, with a hold of 30 min at each temperature and a ramp of 5°C/min. Figure 4.9b shows NO conversion at different temperatures. NO conversion increased from 28% at 200°C to a maximum of 56% at 350°C. NO conversion decreased beyond this temperature to 47% at 550°C, which can be attributed to the decomposition of NO_2 to NO. Ammonia oxidation is a side reaction during NH_3 SCR. This reaction is crucial because it limits the ammonia available for the NO_x reduction. The oxidation of NH_3 leads to the following reactions.

$$4NH_3 + 3O_2 => 2N_2 + 6H_2O \tag{4.3}$$

$$4NH_3 + 5O_2 => 4NO + 6H_2O \tag{4.4}$$

$$4NH_3 + 7O_2 => 4NO_2 + 6H_2O \tag{4.5}$$

The activity of Cu-ZSM-5 for NH_3 oxidation was studied by exposing the catalyst to over 250 ppm NH_3 and 8% O_2. Steady-state experiments were conducted in the temperature range of 200-550°C, with a hold of 30 min at each temperature and a ramp of 5°C/min. Figure 4.9c shows the NO concentration at different temperatures. It was observed that the NO formed is negligible during NH_3 oxidation. No NO_2 was reported in the NH_3 oxidation. Therefore, we concluded that Cu-ZSM-5 is more selective for the oxidation of NH_3 to N_2 [53]. Komatsu et al. [29] observed that NO yields less than 1% during ammonia oxidation and confirmed that the ammonia oxidation to N_2 is highly catalysed by Cu-ZSM-5 [167] .

4.5.2 Adsorption Study

NO_x Adsorption Study

A NO_x adsorption study quantified the storage of NO and NO_2 in the Cu-ZSM-5 foam catalyst. NO_x adsorption experiments were performed with a feed NO_x concentration of 250ppm along with inert gas at 150°C. During the NO_x uptake, NO_x was fed into the

catalyst for 30 min until saturation. NO_2 gas was switched off, and the inert gas was allowed to flow for 10 min to desorb the loosely bound NO_x. A temperature ramp of 5°C/min was applied from to 150-500°C to desorb the stored NO_x.

For the NO adsorption study, 250ppm of NO was adsorbed onto the catalyst for 30 min at 150°C. Once NO saturation was achieved, loosely bound NO was removed using an inert gas for 10 min. A temperature ramp of 14°C/min was applied at 150° C. Figure 4.10a shows the NO uptake and outlet concentrations during the TPD. Initially, the NO outlet concentration approached the feed value, indicating weak adsorption of NO. The NO desorbed during the temperature ramp was also very low and was obtained at approximately 311°C [168].

$$3NO_2 + [Cu - O] -> Cu(NO_3)_2 + NO \tag{4.6}$$

$$Cu(NO_3)_2 -> 2NO_2 + [Cu - O] + 0.5O_2 \tag{4.7}$$

$$Cu(NO_3)_2 + NO -> 3NO_2 + [Cu - O] \tag{4.8}$$

The species [Cu-O] would represent half of the dimer species involved.

The storage capacity of NO_2 on the catalyst was investigated using 250 ppm NO_2 and inert gas in the feed at 150°C, followed by a temperature ramp of 10°C/min. The outlet concentrations of NO and NO_2 are recorded. Figure 4.10b compares the NO and NO_2 outlet concentrations in NO_2 uptake and desorption experiments. During the temperature ramp, a large amount of NO_2 was observed, unlike in NO TPD. The formation of NO during NO_2 adsorption is likely because the stored species formed during adsorption are nitrates bound to copper cations on copper dimers, as is evident from the XPS analysis of the catalyst (Reaction 4.6). The ratio of NO formed to NO_2 consumed was 1:3, which confirms the disproportionation reaction [169] [36]. NO_2 desorbed of 9.5mmol/g by the decomposition of these nitrates at a high temperature of 273°C shows the high storage capacity of the catalyst and high thermal stability of the nitrates formed by the disproportionation reaction (Reaction 4.7). The small NO peak observed during the temperature ramp confirmed the decomposition of NO_2. Because the temperature in the experiment was high, there was no adsorption of NO_2 on weakly adsorbed sites. A negligible amount of NO was adsorbed by the Cu-ZSM-5 catalyst, whereas NO could be stored in the catalyst by oxidation to NO_2 [170].

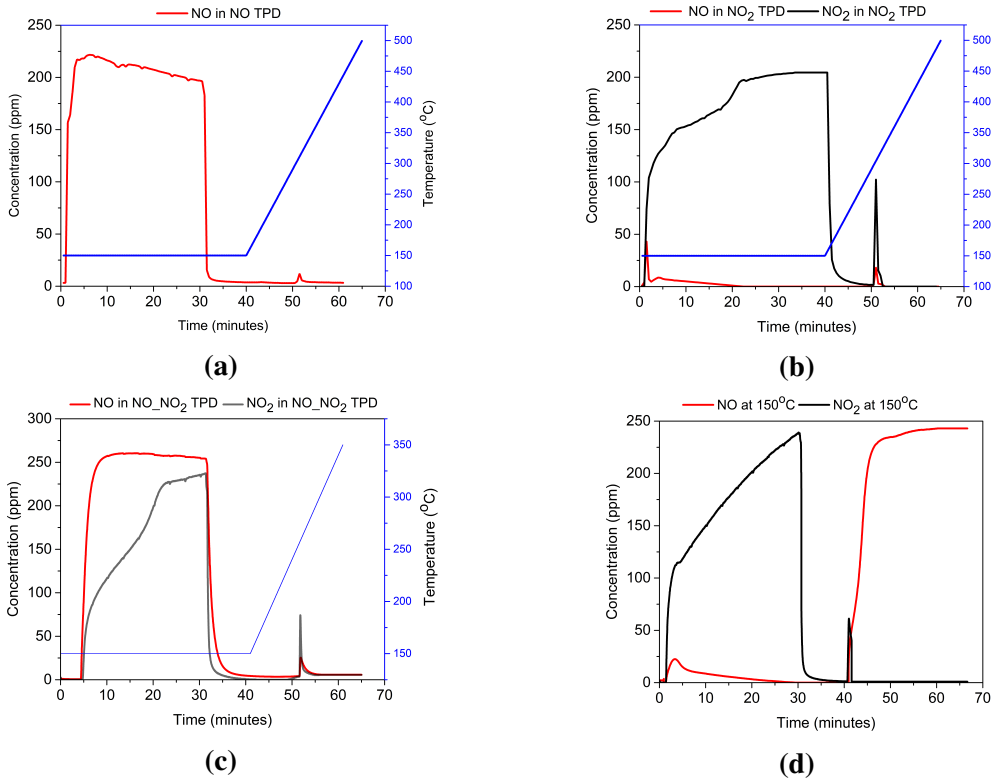

Figure 4.10: (a)NO outlet concentrations for NO TPD with a feed of 250 ppm NO. (b) NO and NO_2 outlet concentrations for NO_2 TPD with a feed of 250 ppm NO_2. (c) NO, and NO_2 outlet concentrations for NO-NO_2 TPD with a feed of 250 ppm NO, 250 ppm NO_2. (d) NO and NO_2 outlet concentrations for 250 ppm NO_2 followed by 250 ppm NO.

To understand the influence of NO on the storage of NO_2, a desorption study was conducted by adding NO to NO_2 during adsorption. 250 ppm NO and 250 ppm NO_2 with inert gas were allowed to adsorb onto the catalyst for 30 min, followed by TPD at a heating rate of 10° C/min. Figure 4.10c shows the concentrations of outlet NO and NO_2 during TPD. As shown in Figure 4.10c, the amount of NO_2 desorbed during TPD significantly decreased to 51 ppm in the presence of NO. NO_2 adsorbed on the catalyst forms nitrates, whereas NO reacts with the formed nitrates, which in turn limits the storage of NO_2 in the presence of NO. It is observed that the nitrates were less stable in the presence of NO in the feed. Figure 4.10c also shows that it took some downtime for NO to reach a steady state during uptake. The activity of NO in reducing surface nitrates is very strong even at a low temperature of 50°C [171] [168]. The high reactivity of NO with nitrates at low temperatures has a strong influence on the stability of the nitrates formed during the adsorption of NO_2. The maximum decomposition rate was observed at 188°C in the presence of NO and 273°C, in the absence of NO respectively. The effect of NO on the desorption of the stored NO_2

was investigated at 150°C. The catalyst was initially saturated with 250 ppm of NO_2 for 30 min. After the uptake, the NO_2 feed was switched off, the sample was stabilized for 10 min with inert gas, and then 250 ppm NO was introduced into the sample. The amount of NO and NO_2 at the outlet was monitored and recorded. As shown in Figure 4.10d the NO_2 outlet concentration increased slowly to reach a steady state during adsorption. Upon the introduction of NO, a strong peak of NO_2 of 61 ppm was observed, which was attributed to the decomposition of nitrates by NO (Reaction 4.8). A downtime of 6 min was required for the NO to reach the feed concentration. NO reacts with stored NO_2 in the form of nitrates and releases NO_2.

4.5.3 Reactivity study : NO/NO_2–NH_3–O_2 reacting system

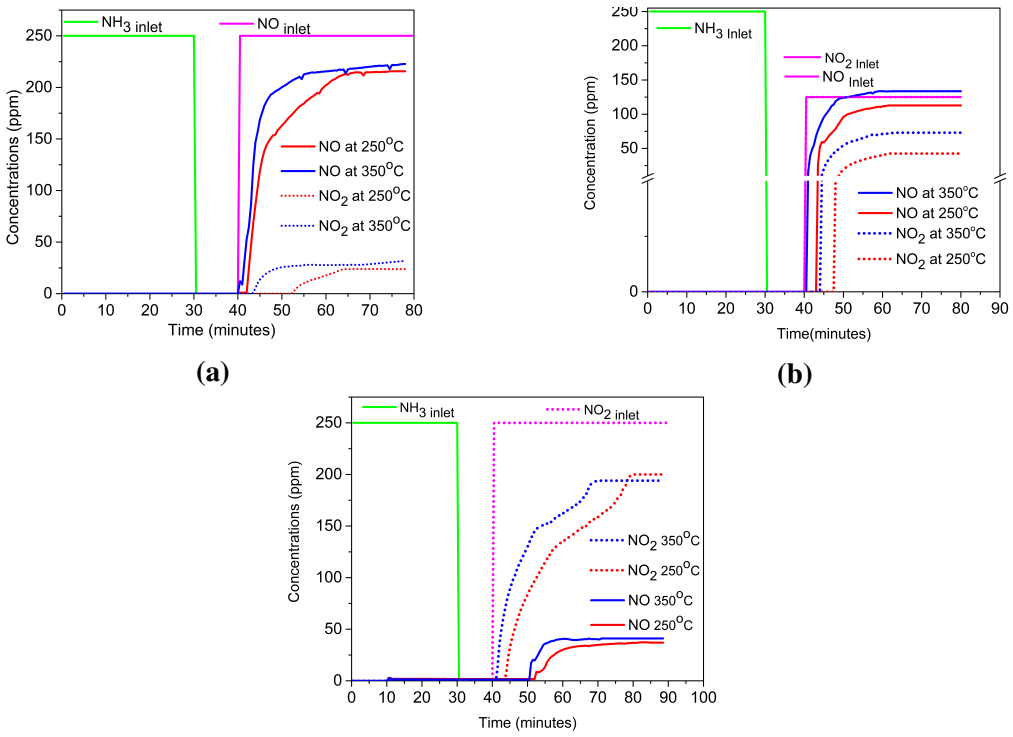

Figure 4.11: (a) NO and NO_2 outlet concentration for a feed of 250 ppm NO and 8% O_2 on 250 ppm preadsorbed NH_3. (b) NO and NO_2 outlet concentrations for a feed of 125 ppm NO, 125 ppm NO_2 and 8% O_2 at 250 pre-adsorbed NH_3. (c) NO_2 outlet concentration for a feed of 250 ppm NO_2 and 8% O_2 at 250 ppm preadsorbed NH_3.

4.5.3.1 NO Feed (NO/NO_2 = 1/0)

In the transient experiments, 250ppm NH_3 was introduced into the reactor along with inert gas at 350°C. The ammonia feed was switched off once the catalyst was saturated with ammonia gas (1800 sec). The inert gas flowed over the catalyst for 600 s to release the loosely bound ammonia. feed with 250ppm NO and 8% O_2 was then introduced into the reactor.

The reactivity of NO on pre-adsorbed ammonia in the presence of O_2 was studied by passing 250 ppm NO and 8% O_2 onto a saturated catalyst with 250 ppm NH_3. The transient responses of the NO and NO_2 outlet concentrations are shown in Figure. 4.11a. Figure 4.11a shows a NO concentration of 80 ppm, 47 min after the introduction of NO and O_2 gas at 250°C. The NO outlet concentration never reached the feed concentration owing to the absence of oxidation. NO oxidation begins at 55 min, when most of the stored NH_3 is depleted. The NO outlet concentration reached a steady-state concentration of 213ppm after 70 min. The standard SCR reaction on the catalyst takes 7 min to completely consume the stored NH_3. At 350°C, an NO concentration of 47 ppm was observed at 43 min of the experiment, with a steady-state concentration of 213 ppm at 55 min. The NO_2 concentration was observed 46 min after the onset of NO oxidation. The SCR catalyst takes 7 min and 3 min to consume stored NH_3 which can reduce 170 ppm and 203 ppm of NO_x at 250°C and 350°C, respectively, under standard SCR conditions. The rate of the standard SCR reaction increases with increasing temperature.

4.5.3.2 Equimolar Feed (NO/NO_2 = 1/1)

The reactivity of equal concentrations of NO and NO_2 of 125 ppm and 8% O_2 over the NH_3 preadsorbed catalyst was studied in this experiment. Figure 4.11b shows the transient outlet NO and NO_2 concentrations. At 250°C, an NO concentration of 60 ppm was observed at 44 min, which reached a steady-state concentration of 125 ppm at 61.5 min. NO_2 concentration was obtained at 49 min and reached a steady state of 43 ppm at 67 min. At 350°C, an NO concentration of 38 ppm was observed at 41.5 min, which reached a steady-state concentration of 134 ppm at 58 min. The NO_2 concentration was observed at 49 min, with a steady-state concentration of 73 ppm at 65 min. It is concluded that the reactivity of NO_2 lasts for a longer duration than that of the NO NO_2 outlet concentration, which appears at a later stage than that of the NO concentration, as shown in Figure 4.11b. It was also concluded that SCR duration was almost the same at all temperatures in this study. The presence of NO_2 enhanced the rate of consumption of pre-adsorbed ammonia

compared with only NO in the feed. The SCR durations are 4 min and 1.5 min with NO reductions of 190 ppm and 212 ppm at 250°C and 350°C, respectively. Temperature had a less significant effect on fast SCR.

4.5.3.3 NO_2 Feed ($NO/NO_2 = 0/1$)

The reactivity of NO_2 with NH_3 in the presence of O_2 was studied by passing 250ppm NO_2 and 8% O_2 over a foam catalyst saturated with 250ppm NH_3. Figure 4.11c shows the NO_2 outlet concentration on the preadsorbed NH_3. At 250°C, NO_2 was observed at 56 min, and reached a steady state of 200 ppm at 79 min. At 350°C, NO_2 was observed at 52 min, and reached a steady state of 192 ppm at 68 min. The SCR duration was extended to 16 min and 12 min at 250°C and 350°C, respectively.

4.5.4 Effects of feed gas composition in NH_3 SCR

4.5.4.1 Effect of NH_3 feed concentration

The effect of the NH_3 feed gas concentration on the SCR reaction was studied by varying the feed concentration from 100-500 to,ppm at intervals of 30 min. The concentration of NO was maintained at 250 ppm and that of O_2 at 8% at a feed flow rate of 1000 ml/min. Figure 4.12a shows the outlet concentrations of NO and NO_2 for different NH_3 feed concentrations at temperatures of 200°C and 350°C.

Figure 4.12a shows that at 200°C, the outlet NO concentration decreased from 250 to 178ppm for an NH_3 feed concentration of 100 ppm. Increasing the NH_3 feed to 200 ppm and 300 ppm reduced the NO concentrations to 152 and 140ppm, respectively. Further increasing the NH_3 concentration in the feed increases the NO outlet concentration. This shows that an increase in the NH_3 concentration inhibits NO_x reduction in the standard SCR. At 350°C, the NO concentration drops to 120ppm for an NH_3 feed concentration of 100 ppm. The NO concentration did not change with increasing NH_3 concentration at a high temperature of 350°C. It is also evident that NH_3 inhibition is higher at 200°C than at 350°C.

Initially, the NO_2 outlet concentration in Figure 4.12a decreases from 70 to 35 ppm as the NH_3 feed concentration increases from 100 ppm to 200ppm. NO_2 was only observed in the gas phase by NO oxidation when all NH_3 was consumed in the standard SCR reaction. This is attributed to the fact that all NH_3 in the feed is consumed until the feed NH_3 concentration is 300 ppm. Increasing the NH_3 concentration in the feed gradually decreases the

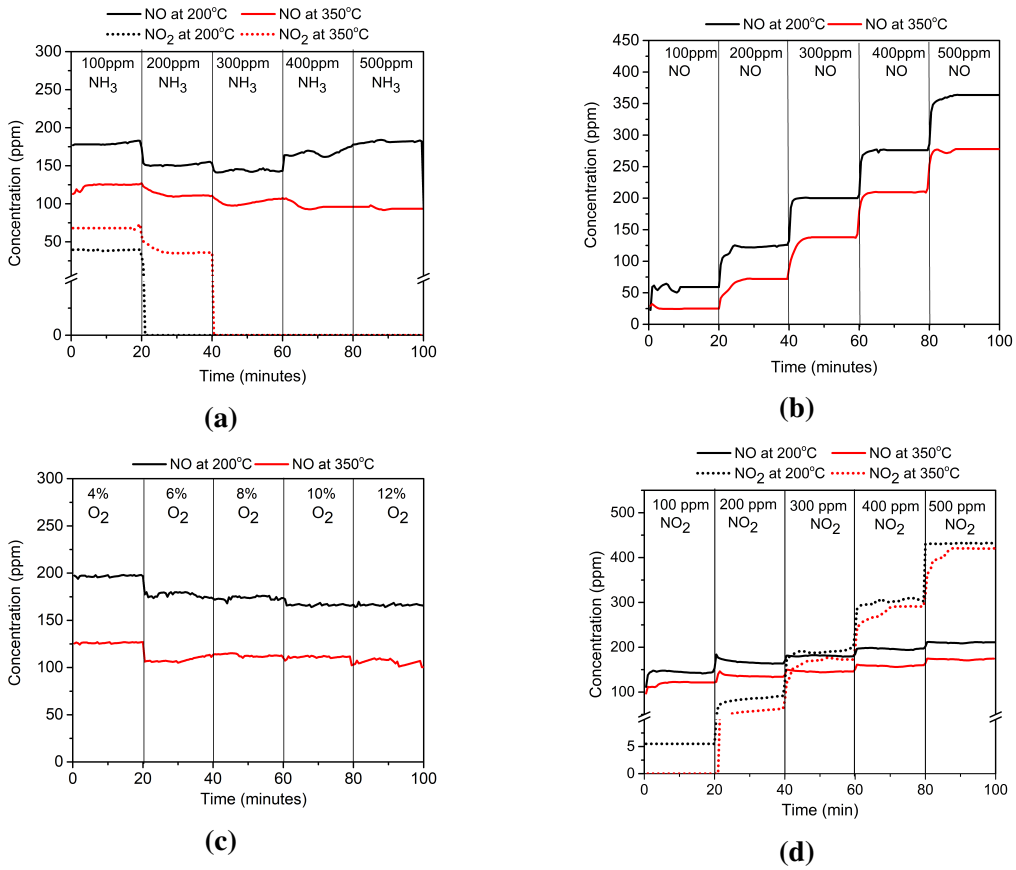

Figure 4.12: (a)NO and NO_2 outlet concentrations at 200°C and 350°C for catalyst is exposed to feed concentration (a)100-500 ppm NH_3, 250 ppm NO, and 8% of O_2. (b) 100-500 ppm NO, 250 ppm NH_3, and 8% of O_2. (c) 4% - 12% of O_2. 250 ppm NO, and 250 ppm NH_3. (d)100-500 ppm NO_2, 250 ppm NO, 250 ppm NH_3, and 8% of O_2.

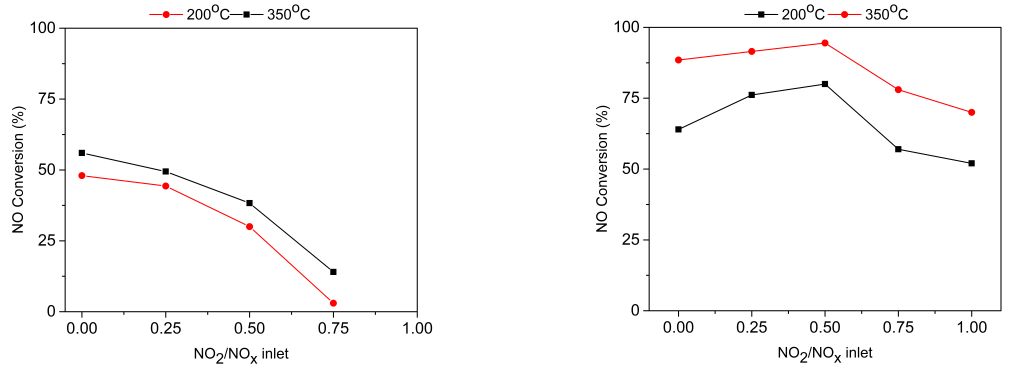

Figure 4.13: Effect of NO_2/NOx feed ratios on (a) NO oxidation at 200°C and 350°C (b) Standard SCR at 200°C and 350°C

NO_2 concentration at the outlet. This indicates that excess ammonia in the feed inhibited NO oxidation. It is inferred that NH_3 inhibits the standard SCR reaction by blocking the sites required for NO oxidation via strongly bound NH_3 [16]. NO_x reduction is inhibited by NH_3 at lower temperatures because of ammonia oxidation.

4.5.4.2 Effect of NO feed concencentration

The effect of NO concentration in the feed gas was studied over a Cu-ZSM-5 foam catalyst with feed gas concentrations of 250 ppm NH_3, 100-500 ppm NO, and 8% O_2 at 200°C and 250°C. The NO concentration was maintained for 30 min at each concentration. Figure4.12b shows the outlet concentrations of NO at different feed concentrations. At 200°C, it can be observed from Figure 4.12b that the NO outlet concentration drops to 55 ppm for an NO feed concentration of 100 ppm. It was also observed that the NO outlet concentration increased to 134 and 195 with an increase in the NO feed concentration to 200 and 300 ppm, respectively. Upon further increasing the NO feed concentration to 500 ppm, the NO outlet concentration increased to 356ppm at 200°C, and 278 ppm at 350°C. As the ammonia in the feed remains the same with an increase in the NO feed concentration, NO reduces until the ammonia available for reduction is consumed to such an extent that NO oxidation dominates, as evidenced by the increase in the NO_2 concentration. NO concentrations exceeding the ammonia concentrations could not be reduced. At 200°C, NO conversion showed the same trend but lower conversions than at 350°C.

4.5.4.3 Effect of O_2 feed concentration

The influence of the O_2 concentration on the feed gas composition was studied by varying the concentration of O_2 from to 4-12% for 30 min at each concentration, while maintaining a constant concentration of other feed gases at 250ppm of NO and 250ppm of NH_3 at 200°C and 350°C. Figure 4.12c shows the outlet concentrations of NO and NO_2 for different O_2 feed concentrations. At 200°C, the NO concentration decreased to 195 ppm with an O_2 feed gas concentration of 4%. The outlet NO concentration increased to 179 and 175ppm for feed O_2 concentrations of 6% and 8%, respectively. With an increase in the feed O_2 concentration to 10%, the outlet NO concentration reaches 165 ppm. The NO outlet concentration decreases with an increase in the O_2 feed concentration. An increase in the O_2 concentration in the feed offers higher NO conversion, which can be attributed to the reaction of O_2 with NO to form active nitrites and nitrate intermediate species. Increase in O_2 in the feed promotes the reuse of Cu^{2+} ions by oxidizing the Cu^{+} [2]. At 350°C, the

decrease in NO conversion can be attributed to NH_3 scarcity for the reaction owing to NH_3 oxidation with an increase in the O_2 concentration.It is observed that at 200°C, the increase in the NO conversion O_2 feed is significant compared to that at 350°C [16].

4.5.4.4 Effect of NO_2 feed concentration

The effect of the NO_2 concentration on the feed composition was studied by varying the concentration of NO_2 from 100-500 to,ppm and keeping 250 ppm NO, 250 ppm NH_3 and 8% O_2 constant. Figure 4.12d shows the NO and NO_2 concentrations for different NO_2 feed gas compositions at 200°C and 350°C. At 200°C, the NO_2 concentration decreased to 6 ppm for a NO_2 feed concentration of 100 ppm, and increased to 277 ppm for the 300 ppm feed. Thereafter, with an increase in the NO_2 feed concentration, NO_2 drastically increased because of the lower NH_3/NO_x feed ratio and the formation of ammonium nitrates. NO_2 was more reactive than NO with NH_3. The NO concentration increased slightly with increasing NO_2 feed concentration. At 350°C, the NO concentration decreases marginally from 144ppm for 100ppm NO_2 in the feed to 180ppm for 300ppm NO_2 in the feed. At 350°C, the increase in NO concentration was higher than that at 200°C because ammonium nitrates were stable up to 200°C and further blocked NO_x reduction.

4.5.4.5 Effects of NO_2/NO_x feed ratio

4.5.4.6 Effects of NO_2/NO_x feed ratio on NO oxidation

It is important to investigate the effect of the NO_2/NO_x feed ratio on NO oxidation because this reaction is the rate-determining step in standard SCR. The effect of the NO_2/NO_x feed ratio on NO oxidation was studied at different temperatures of 200°C and 350°C with the NO_2/NO_x ratio varied from 0 to 0.75 by maintaining the NO_x concentration at 250 ppm. The NO conversions for different NO_2/NO_x feed ratios at 200°C are shown in Figure 4.13a. It is evident from Figure 4.13a that increasing the NO_2/NO_x ratio decreases the NO oxidation. For the pure NO feed, 48% of NO is oxidized to NO_2, with the introduction of 44 ppm NO_2 in the oxidized NO feed reduced to 48%. An increase in the NO_2/NO_x ratio above 0.5 leads to a further decrease in NO oxidation to 30%, which is attributed to the disproportionation reaction (Reaction:8), as evidenced by TPD studies. It can be inferred that the nitrate formed by NO_2 adsorption blocks NO oxidation by increasing the NO_2 concentration. The inhibition of NO oxidation by NO_2 was more pronounced beyond a NO_2/NO_x ratio of 0.5. NO_2 inhibition of the NO oxidation reaction can be due to the competitive adsorption of NO_2 and blockage of NO oxidation sites. NO_2 is a stronger oxidizing agent

than O_2 and can oxidize the metal sites and prevent the adsorption of O_2 [172] [173] [174]. Figure 4.13a shows the NO oxidation at 350°C for NO_2/NO_x ratios from 0 to 0.75. It is evident from the Figure 4.13a that at 350°C for a pure NO feed, approximately 56% of NO is oxidized, which is higher than that at 200°C. With the introduction of 62.5 ppm NO_2, the NO oxidation was reduced to 48%. At 350°C, NO oxidation follows the same trend as that at 200°C with NO_2/NO_x ratio but with higher NO oxidation. It can be inferred that the nitrates deposited on the NO oxidation sites decomposed at a higher temperature of 350°C.

4.5.4.7 Effects of NO_2/NO_x feed ratio on standard SCR

The effect of the NO_2/NO_x feed ratio on the standard SCR was investigated using 250 ppm NH_3, 8% O_2 and 250 ppm NO_x. The NO_2/NO_x ratio is varied from 0 to 1 at intervals of 30 min at temperatures of 200°C and 350°C. Figure 4.13b shows the NO conversions at different NO_2/NO_x ratios. At 200°C, for the pure NO feed, 62% of NO is reduced, whereas with increasing NO_2 concentration to 62.5 ppm NO conversion increases to 75%. NO conversion increased from 75% to 80% with an increase in the NO_2/NO_x feed ratio from 0.25 to 0.5. The increased No conversion at NO_2/NO_x ratio of 0.5 is attributed by the fast SCR.NO conversion decreased to 57% with further increases in the NO_2/NO_x ratio above 0.5. For NO_2/NO_x ratio above 0.5 , part of the NO_x reacts by fast SCR reaction where as the remaining NO_2 reacts by slower NO_2 SCR reaction.This decrease in NO conversion is also also due to the deposition of nitrates on the active sites by the disproportionation reaction, which blocks NO oxidation, which is the rate-determining step in standard SCR.The Figure 4.13b shows an NO conversion of 88% for a NO_2/NO_x ratio of 0 at 350°C, which is higher than the rate at 200°C. For a NO_2/NO_x ratio of 0.25, the NO conversion was 91%, which increased to 94% for a NO_2/NO_x ratio of 0.5. The increased NO reduction at high temperatures is due to the decomposition of nitrates deposited in the active sites. NO follows the same trend of decreased conversions for NO_2/NO_x ratios above 0.5, as that at 200°C, but with higher conversions.

4.6 Summary

The Cu-ZSM-5 dip-coated on α alumina foam catalyst was prepared with a surface area of 172 m^2/g and mesoporosity of 10 nm. The Cu-ZSM-5 foam catalyst achieved Lewis acidity of 36 μmol/g and Brønsted acidity of 107.5 μmol/g. The distribution of Cu species from the XPS analysis indicated that the ratio of isolated Cu^{2+} to CuO was 0.55.

The interaction of reactant NO_x gases with Cu-ZSM-5 was studied using adsorption and temperature-programmed desorption. NO_x adsorption and TPD studies have concluded that NO_2 can be stored in the form of nitrates. The high reactivity of NO with nitrates at low temperatures has a strong influence on the stability of the nitrates formed during the adsorption of NO_2. The desorption of nitrates was observed at 200°C, with 4.7 mmol/g NO_2 desorbed in the presence of NO and 300°C in the absence of NO at 9.5 mmol/g NO_2. The standard SCR duration is 7 min and 3 min with NO reductions of 170 ppm and 203 ppm at 250°C and 350°C, respectively. The fast SCR duration is 4 min and 1.5 min with NO reductions of 190 ppm and 212 ppm at 250°C and 350°C, respectively. Temperature had a less significant effect on the fast SCR. The slow SCR duration was extended to 16 min and 12 min at 250°C and 350°C, respectively.

An investigation of the effect of reactant gases on the standard SCR reveals that an increase in the NH_3 concentration in the feed decreases the NO_x reduction. At low temperatures, NH_3 in the feed gas inhibits the SCR reaction and complicates the SCR catalyst design in automotive applications. In standard SCR, excess NH_3 blocks the adsorption of NO on Cu sites through an oxygen atom and reduces $DeNO_x$ activity. It is also inferred that a NO concentration that exceeds the NH_3 feed concentration cannot be reduced. A study on the effect of the NO_2/NO_x ratio on NO oxidation concluded that nitrates formed on increasing the NO_2 concentration block NO oxidation, which is the rate-determining step in standard SCR at low temperatures, whereas the deposited nitrates decompose at a higher temperature of 350°C and increase the NO_x reduction.

Chapter 5

Experimental Investigation of Mass Transfer and Kinetics of NH_3 SCR Over In-situ Hydrothermal synthesised Cu-ZSM-5 on α alumina Foam

5.1 Introduction

Selective catalytic reduction (SCR) of NO_x with NH_3 is considered the most promising technology to meet the stringent EPA standards for NO_x emissions from heavy-duty vehicles. Different catalysts for the SCR of NO_x with ammonia have been reported in literature. These catalysts can be divided into three groups according to the temperature at which they are active. Noble metals such as platinum are active for the SCR of NO_x at lower temperatures ranging from 225-250°C. However, at high temperatures, the Pt catalyst loses its selectivity for the NO_x reduction reaction. The second group of catalysts is metal oxide mixtures, among which vanadia supported on titania is commonly used in SCR [175]. These catalysts are active in the temperature range of 250–450°C, and at temperatures above this range, selectivity is lost because of the enhanced oxidation of ammonia. Metal oxide catalysts are also found to have low stability at high temperatures, and the toxicity of vanadium has raised public health concerns. Recent research has focused on metal-exchanged zeolites for applications over a wide temperature range.

Among these, Fe ZSM-5 and Cu-ZSM-5 catalysts have been widely studied for the SCR of NO_x with ammonia, NO decomposition, and SCR with hydrocarbons [16] [176] [29]. Cu-ZSM-5 has higher activity at lower temperatures, whereas Fe ZSM-5 has higher ac-

tivity at higher temperatures [29]. Different types of Cu-zeolites have been studied extensively in the SCR literature and these catalysts mainly include Cu-MOR, 4 Cu-BEA, Cu-ZSM-5, Cu-Y, Cu-NaY, Cu-Ferrierite and Cu-FAU. Cu-ZSM-5 has been widely used for NH_3 SCR owing to its high activity at 200-400°. Iwamoto et al performed pioneering research on Cu-ZSM-5 activity in deNOx efficiency and proposed the surface reaction mechanism [3]. Olsson and coworkers carried out a global and detailed kinetic modelling study of NH_3 SCR reactions on Cu-ZSM-5. The active sites of these microporous zeolites become inaccessible to reactants with sizes greater than the pore dimensions, which leads to a strong diffusion limitation. This diffusion limitation increases the possibility of coking, which deactivates the catalysts and shortens their catalytic life [58]. Researchers focused on the introduced hierarchical porosity to zeolite structures to solve the diffusion and mass transfer limitations resulting from microporous zeolites. Hierarchical porosity refers to the introduction of a secondary pore system, typically in the mesopore range, to intrinsic zeolite microporosity. The main challenge in the development of hierarchical zeolites is to facilitate the access of bulky reactants to active sites while preserving the acidity and crystallinity of the original zeolites [58] [177]. In recent years, many strategies have been introduced for the synthesis of hierarchical zeolites with microporous, mesoporous, or macroporous structures. Templating methods are most effective as they add mesoporosity to zeolite crystals during their synthesis and control the crystallization process, resulting in intercrystalline mesoporosity [178]. The template or surface-directing agent SDA may be in the form of either organic or inorganic cations. Since the alumina sites in the framework structure of the zeolite carry a negative charge, the structure-directing agent often acts as a counterion in the framework to maintain the electroneutrality of the zeolite. Barrer et al. [151] discovered that the presence of organic cations along with alkali leads to more open crystal structures, thus improving the accessibility of active sites. The drawbacks of zeolite powders with higher mass transfer limitations and pressure drops can be overcome by introducing catalytic supports. There are many approaches to the incorporation of zeolites on catalyst substrates, such as dip coating, spin coating, in-situ crystallization, and secondary growth techniques. In in situ hydrothermal synthesis, the supports can act as initial nutrients for the growth of the zeolitic framework, if the support has activated silica or alumina atoms, and a chemical bond between the crystals and substrate layer is formed, thus ensuring strong adherence of zeolite to the support and providing high vibration resistance [158]. Main differences in synthesis methods are manifested in intercrystalline porosity, molecular accessibility of inter crystal micropores, the orientation of the crystals to the support, bonding strengths between crystals and support, uniformity, degree of cover-

age, and coating thickness [92]. In situ crystallization is also capable of coating substrates of complex shapes and sizes in a confined space. It is a one-step process in which the need for the preparation of seed crystals, use of a binder, and subsequent dip and spin coating are eliminated, providing a higher active load per gram of coating [179]. Monolayer films of ZSM-5 synthesized on stainless steel and aluminium alloy by in-situ hydrothermal crystallization were studied by Zhengbao et al [180]. The optimization process for the H-ZSM-5 honeycomb monolith by extrusion is developed by Aranzabal et al [181]. Wang et al studied the in-situ hydrothermal synthesis of Cu-ZSM-5 on honeycomb cordierite for the reduction of NO_x [182]. Landong et al. synthesized Cu-ZSM-5, Cu-titanium silicate, and Ir ZSM-5 on a honeycomb cordierite monolith, and studied the SCR of NO_x from automobile exhaust [158] [159]. Kryca et al. compared the heat and mass transfer properties and pressure drops of packed bed reactors, Kanthal foam, monoliths, and honeycomb reactors. They concluded that the packed bed reactor offers high mass transfer but with a high-pressure drop, whereas monolithic reactors possess a low-pressure drop but with a poor mass transfer [90]. Kryca et al. studied NO_x SCR by NH_3 and concluded that the structure of the support significantly affects catalyst performance, even for a highly active catalyst. They also confirm that the reduction of NO is a diffusion-limited process and the optimization of support geometry may lead to further enhancement of catalytic performance. Mass transport and kinetics in a structured steel foam reactor with a Cu-ZSM-5 catalyst for the SCR of NO_x with ammonia were studied by Kryca et al. [90], [91]. Seijger et al studied the insitu synthesis of binderless ZSM-5 on ceramic foam support and its application in SCR [92] [93].

In response to the increasing levels of NO_x emission across the globe from different industrial, marine, and automobile applications, Selective Catalytic Reduction (SCR) is considered an effective technology for controlling the NO_x emission in such varied applications. In automobile applications, urea-water solution-based SCR is a promising technology for NO_x reduction [11]. The urea-water solution sprayed into the hot exhaust stream was decomposed into ammonia and iso-cyanic acid in the mixing chamber. Isocyanic acid is further hydrolyzed to ammonia and CO_2 [12]. NH_3 SCR in stationary applications operates at temperatures ranging from 280°C to 400°C, whereas in mobile applications, where ammonia is formed by the decomposition of urea, it operates at a wider temperature window of 150°C to 550°C. The main challenges in urea SCR are the incomplete decomposition of urea to NH_3 and their subsequent non-uniform distribution at the SCR inlet.

Metal-exchanged zeolites with Fe and Cu have been recognized as effective catalysts for the selective catalytic reduction of nitrogen oxides with ammonia.

The dynamic behaviour of zeolite catalysts is largely dominated by the balance between rates of the NH_3 adsorption, desorption, and surface reactions with NO_x. Copper zeolite catalysts can adsorb and store reactant gases, NH_3 and NO_2 on Cu sites [168]. The redox state of the Cu zeolites plays a crucial role in the storage and thermal stability of NO_2 and NH_3. Colombo et al. concluded that the pre-reduced Cu zeolites give higher NO_2 storage compared to pre-oxidized catalyst [183] but are highly unstable. In a pre-oxidized catalyst, it is very difficult to maintain equal amounts of NO and NO_2 reactant gases for the SCR reaction due to thermodynamic restrictions. The effect of various NO/NO_2 feed ratios on the SCR activity at different temperatures has been discussed in many studies [184] [16]. In mobile applications that operate at low temperatures of 150°C, it is important to understand the effect of NH_3 formed from urea decomposition in SCR chemistry. There should be enough ammonia present on the catalyst to reduce all NO_x, but at the same time, there must be no excess ammonia to prevent slippage from automobiles. The activity and mechanism of the NO/NO_2–NH_3 SCR system have been reported in the literature [185] [186] [154] [34] [155] [156] [152] [187]. Nova et al. proposed an analogy of metal-based zeolites with vanadium-based catalysts in which NH_3 adsorbs on the non-reducible acidic sites of the zeolites, and the NO-NH_3 reaction is activated at the redox sites [188]. The standard and fast SCR involves a reaction between adsorbed NH_3 and gas-phase NO and NO_2(Eley Rideal mechanism) [39] [189]. The role of NO_2 in NH_3 SCR catalytic chemistry has been studied in detail by Tronconi et al. [174]. Ruggeri et al. provided evidence of nitrite formation in the oxidative activation of NO and its role in SCR reactions [190].

Ammonia inhibition at low temperatures is critical for simulating the highly transient operation of onboard SCR converters for exhaust after-treatment. At low temperatures, onboard SCR converters for vehicles involve fast dynamics associated with urea dosage. The SCR performance under such highly transient conditions is governed by the same dynamic features during the NH_3 shut-off experiments. Therefore the inclusion of NH_3 distribution and interaction in SCR chemistry to develop a kinetic model is relevant for the industrial implementation of SCR technology for vehicles. These effects of transient NH_3 supply on the selective catalytic reduction of zeolites with a step and pulse feed of NH_3 have been reported [191] [192] [171] [193] [194].

This study focuses on the performance of a hierarchical Cu-ZSM-5 catalyst coated on α alumina foam substrate for the standard SCR of NO_x by NH_3. This work is also aimed at mass transfer and pressure drop studies on hierarchical Cu-ZSM-5 foam catalysts. The objective of this study was to conduct differential and integral flow reactor experiments on the NH_3 SCR of NO on a Cu-ZSM-5 foam catalyst. Most of the previous studies involved

powder catalysts and catalysts coated on monoliths, and only a few studies have reported their kinetics.The storage capacity of the reactant gases NO and NO_2 with Cu-ZSM-5 was analyzed by NO_x uptake and TPD studies. Transient effects of feed gases NO, NH_3 and O_2 on SCR activity at different temperatures. The reactivities of feed NO and NO_2 on preadsorbed NH_3 in the presence of O_2 were studied at different temperatures to elucidate the fast dynamics of SCR chemistry. NH_3 inhibition effects on SCR reactions were studied to understand the complex SCR chemistry in real exhaust gas after-treatment systems for vehicles.

.

Experimental Details

5.2 In-situ hydrothermal synthesis of ZSM-5 on α alumina foam

The compositions used for the in situ hydrothermal synthesis of the ZSM-5 catalyst on the alumina foam support are given in Table 5.1. The initial zeolite building blocks were formed by the hydrolysis of TEOS and $Al(O\text{-}i\text{-}Pr)_3$. Alumina and silica building blocks were prepared by stirring the respective precursors separately in water containing TPAOH for 24 h using a magnetic stirrer. Sodium hydroxide in the form of a 1 M solution was added to the alumina precursor solution. The amounts of water and TPOH were equally distributed between the alumina and silica building-block solutions. The obtained alumina and silica building block solutions were then mixed and stirred for 8 h. The mixed alumina and silica building blocks were transferred to the Teflon vessel of a hydrothermal reactor. The reactor was properly sealed after adding the alumina foam support, prepared as described in 4.2.1. The hydrothermal reactor with the contents was heated in an air oven at 150°C for 72 hours. The reactor was allowed to cool and open after it reached room temperature. The ZSM-5 coated alumina foams and ZSM-5 powder settled at the bottom of the reactor were collected. The ZSM-5 coated alumina foams were subjected to ultrasonication to remove loosely bound ZMS-5 on the foam surface and then washed several times with distilled water. The ZSM-5 coated foams and ZSM-5 powders were dried at 110°C for 1 h, and then calcined at 550°C for 16 h in a muffle furnace at a heating rate of 5°C/min.

Table 5.1: Chemical composition of Na-ZSM-5 sample mixture

Si/Al ratio	AIP(g)	TEOS (g)	NaOH(g)	TPAOH (g)	H_2O(g)
10	1	5.1	0.039	0.59	52.35
20	1	10.2	0.039	0.59	52.35
50	0.2	5.1	0.039	0.59	52.35

5.2.1 Ion Exchange of ZSM-5 Foam

The Na-ZSM-5 coated alumina foams were ion-exchanged with 50ml of a 0.02 M solution of copper acetate at 50°C for 72 h. The Cu-exchanged zeolites were dried at 120°C for 2 h.

Results and Discussion

5.3 Characterisation and measurements

In the in-situ hydrothermal synthesis of Na-ZSM-5, the organic template TPAOH acts as a hydroxyl ion donor because of its basicity and forms a cation. This accelerates the hydrolysis and condensation of TEOS and $(Al(O\text{-}i\text{-}Pr)_3$ to form precursor sols. During hydrothermal treatment, the precursor sol particles dissolve in water, and the soluble aluminosilicate forms regroups around the cation to form the nuclei of the ordered zeolite. The Al atoms of the alumina foam in contact with the basic aluminosilicate solution act as nucleation sites for the crystallization of zeolites [92]. In other words, the Aluminium atoms at the nucleation sites may become part of the zeolite structure. Negatively charged aluminosilicates can interact directly with excess organic cations in the template to form mesoporous channels [195]. During the ion exchange of the Na-ZSM-5 foam, the dissolution of copper acetate in water produces hydrated ions, hexaaqua complex $[Cu(H_2O)_6]^{2+}$ and their hydrolysis products, such as $Cu(H_2O)_5OH]^{+}$ and $[Cu_2(OH)_2(H_2O)_8]^{2+}$. A blue color slowly developed on the ZSM-5 coated alumina foam when immersed in a copper acetate solution. This was due to the exchange of Na ions in the zeolite framework with copper. This blue color turned to light green upon drying at 120°C for 2 h owing to dehydration and the formation of oxygen-bridged $[Cu\text{-}O\text{-}Cu]^{2+}$ complexes. A photograph of the alumina foam substrate before sintering and zeolite-coated alumina foam and zeolite-coated alumina foam after copper exchange is shown in Figure 5.1. We obtained alumina foam with 70% porosity and 30 PPI using a thermoforming method. The amount of ZSM-5 coated on α alumina foam are 2.9wt %, 3.2wt %, and 1.9 wt% for Cu-ZSM-5-10, Cu-ZSM-5-20, and

Cu-ZSM-5-50 respectively by hydrothermal synthesis.

(a) (b) (c)

Figure 5.1: a) Foam obtained before sintering. b) Foam after in-situ hydrothermal synthesis. c) Foam obtained after ion exchange with copper acetate.

5.3.1 BET surface area analysis

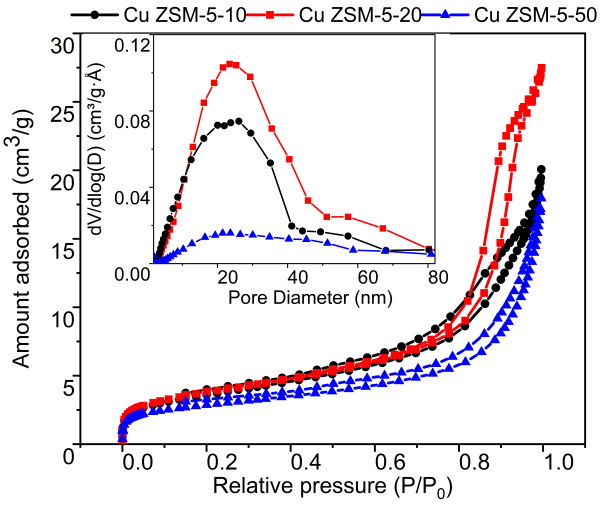

Figure 5.2: N_2 adsorption isotherm of Cu-ZSM-5 foam catalysts

The N_2 adsorption-desorption isotherms of the foam catalysts are shown in Figure 5.2. The isotherms of the hierarchical Cu-ZSM-5 foam samples exhibit a continuous increase in the adsorbed nitrogen volume with P/P_0 and a small hysteresis branch corresponding to adsorption-desorption. The Cu-ZSM-5 foam catalysts exhibit type 1 hysteresis, which is characteristic of materials with a narrow distribution of uniform mesopores. The enhanced uptake of nitrogen at P/P_0 greater than 0.8 shows the presence of macropores. The plateau region at P/P_0 was less than 0.5, indicating the presence of micropores, which is beneficial for the excellent pore structure and large BET surface area. Cu-ZSM-5-20 has type

Table 5.2: Surface area analysis

Sample	S_{BET}	S_{micro}	$S_{external}$	V_{total}	Average Particle size	Cu	Al
	m^2/g	m^2/g	m^2/g	cm^3/g	nm	%	%
Cu-ZSM-5-10	45	15	30	0.1	393.5	0.9	5.3
Cu-ZSM-5-20	55	20	35	0.2	311.8	0.8	2.7
Cu-ZSM-5-50	14	6	8	0.03	678.4	0.7	1.4

1 hysteresis associated with porous materials consisting of well-defined cylindrical pore channels or agglomerates of approximately uniform size, whereas Cu-ZSM-5-50 and Cu-ZSM-5-10 have slit-shaped pores. The pore size distribution is important for determining the accessibility of active sites by reactants and the extent of dispersion of active metals within the catalyst. The BJH analysis of the Cu-ZSM-5 foam samples with SiO_2/Al_2O_3 ratios of 10, 20, and 50 exhibited a broad distribution of pore sizes in the range of 2–50 nm with a maximum at 25 nm, as shown in the inset of Figure 5.2. The surface area of ZSM-5-10, ZSM-5-20, and ZSM-50 powders are 285 m^2/g, 310 and 158 m^2/g, respectively. They showed a marginal decrease in surface area after Cu exchange. The surface area of Cu-ZSM-5-10, Cu-ZSM-5-20, and Cu-ZSM-5-50 were 266, 287, and 149 m^2/g, respectively. The Cu-ZSM-5 foam catalysts exhibited a lower surface area, although they retained a similar trend as the SiO_2 to Al_2O_3 ratio. The surface areas of the Cu-ZSM-5-10, Cu-ZSM-5-20, and Cu-ZSM-5-50 foam catalysts are 45, 55, and 14 m^2/g, respectively. The low value observed for the foam catalyst was due to the presence of a large amount of alumina foam with a lower surface area of 1 m^2/g. The textural properties of the Cu-ZSM-5 foam catalysts at various SiO_2/Al_2O_3 ratios of Cu-ZSM-5 foam catalyst are given in Table 5.2. The average particle sizes of the powder catalysts with SiO_2 to Al_2O_3 ratios of 10, 20, and 50 were 393.5 nm, 311.8 nm, and 678 nm, respectively. The lower average particle size of Cu-ZSM-5-20 resulted in a high surface area.

The chemical composition of the foam catalyst, determined by ICP, is presented in Table 5.2. The copper contents (%) observed in the Cu-ZSM-5-10, Cu-ZSM-5-20, and Cu-ZSM-5-50 powder catalysts were 8.8, 7.9, and 4.7%, respectively. It was observed that the capacity to introduce copper on exchangeable sites decreases with an increase in the SiO_2/Al_2O_3 ratio owing to the unavailability of Al atoms. The lower surface area of Cu-ZSM-5-10 can also be attributed to the blockage of pores due to the high copper loading.

5.3.2 Transition electron microscopy analysis

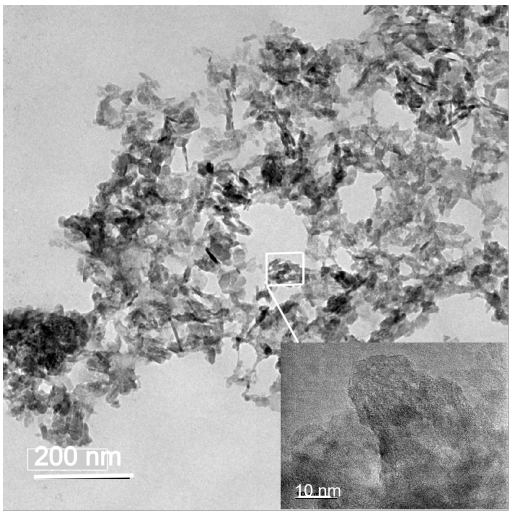

Figure 5.3: TEM micrograph of Cu-ZSM-5 foam catalyst

The distribution of the copper species on the catalyst was analyzed using HR-TEM. Figure 5.3 shows the distribution of copper species as dark spots. The insert of the figure shows The interplanar spacing of the small dark spots is 0.23 nm, which corresponds to CuO.

5.3.3 Scanning electron microscopy analysis

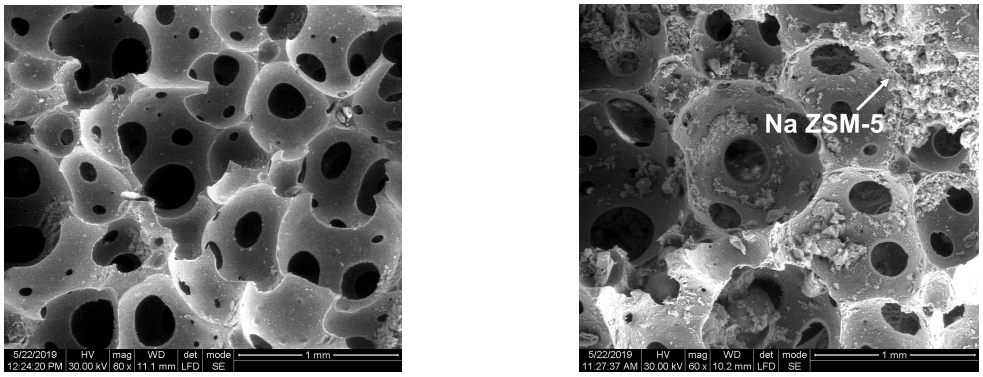

(a) **(b)**

Figure 5.4: SEM micrograph of Cu-ZSM-5 foam catalyst (a) alumina foam (b) In-situ coated Cu-ZSM-5-20 on α alumina foam

The SEM micrograph of the fractured surface of the alumina foam support in Figure

5.4 shows an interconnected cellular structure with cell sizes ranging from 17 to 132 μm. The circular cell windows connecting the cells have sizes in the range of 90–1120 μm.

The interconnected cellular structure provided a large area for the deposition of the ZSM-5 catalyst and a tortuous path for NO_x leading to a higher NO_x reduction efficiency. An SEM micrograph of the alumina foam is shown in Figure 5.4a. The deposition of Na-ZSM-5 crystals on the cell wall surface of the support foam is shown in Figure 5.4b. It was found that the cell wall surfaces of the alumina foam were almost completely covered by Na-ZSM-5 crystals during the in-situ hydrothermal synthesis. The high-magnification SEM image shows the macroporous irregular morphology of the catalyst coated on the alumina cell-wall surfaces. A high-magnification image of the catalyst coating on the alumina foam surface is shown in Figure 5.4b. The macropores present in the catalyst support would facilitate the diffusion of gas molecules to access the active sites of the catalyst.

5.3.4 X-ray diffraction analysis

The crystallinity and structure of the catalysts were studied using XRD. Figure 5.5 shows the XRD pattern of Na-ZSM-5-20 coated alumina foam, Cu-ZSM-5-20 coated alumina foam, and Cu-ZSM-5-20 powder. The hexagonal structure with the R3c space group of alpha-alumina foam has a = 4.758A, b =,4.409A and c = 12.991 A (volume 254A3 JCPDS International Center for Diffraction Data 10-0173). Na-ZSM-5 has an orthorhombic Pnma space group a = 20.09A, b = 19.738A, and c = 13.1420A (volume 5211.3A3) [196]. No distinct peaks for ZSM-5 were observed in the XRD spectrum of the Na-ZSM-5 foam catalyst because of the small amount of zeolite coating compared to the alumina foam substrate. However, a shift in the diffraction angle was observed after copper exchange. The shoulder peaks in Figure 5.5 at 35.5° and 38.1° observed for Cu-ZSM-5 are characteristic of the monoclinic CuO phase [197].

5.3.5 Ammonia temperature programmed desorption

The ammonia Temperature Programmed Desorption (TPD) curves of the Cu-ZSM-5 foam catalysts are shown in Figure 5.6. The area under the ammonia-TPD graph is directly proportional to the number of acidic sites in the zeolite. The ammonia TPD curves of zeolite showed two desorption peaks, indicating the existence of two types of acidic sites. Bronsted acid sites are formed by Al atoms connected to Si by bridging oxygen, where the negative charge is compensated by a proton. Lewis acid site is composed of Cu ions and extra framework aluminium ions. The interaction of bases with acid sites in zeolites accounts

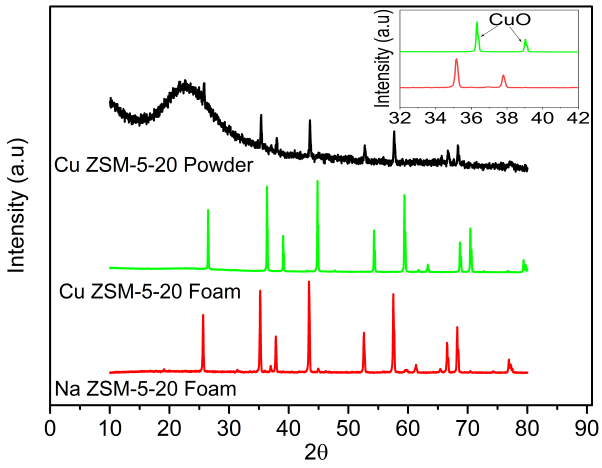

Figure 5.5: X-ray diffraction analysis of a) Na ZSM- foam, Cu-ZSM-5 foam and Cu-ZSM-5 powder

for the confinement effect arising from van der Waals interactions, which was monitored in this study at different temperatures [198]. The desorption peak at a lower temperature of approximately 220°C was attributed to NH_3 desorbed from the extra framework Al and Cu [161] [199]. The high-temperature desorption peak centered at 350°C is assigned to NH_3 released from the Brønsted acid sites (Si-(OH)-Al) [162]. The high-temperature desorption peak was related to the presence of strongly acidic hydroxyl groups as sorption sites. The area under the ammonia TPD was directly proportional to the number of acidic sites in the zeolite.

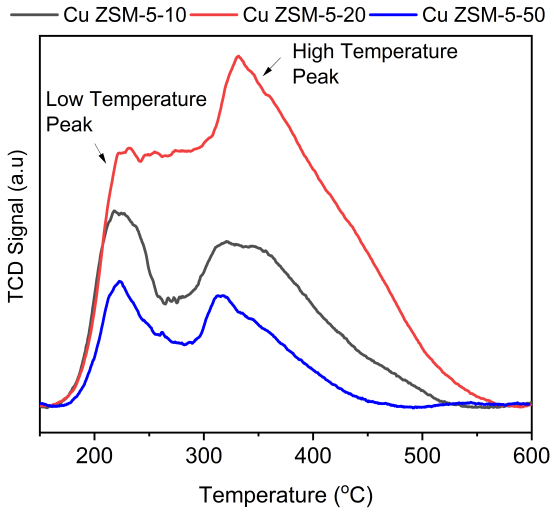

Figure 5.6: Ammonia temperature programmed desorption of Cu-ZSM-5 foam catalyst

The NH_3-TPD peaks and acidity of the Cu-ZSM-5 foam are tabulated in Table 5.3. The

number of weakly acidic sites increased with an increase in copper loading in Cu-ZSM-5-10, Cu-ZSM-5-20, and Cu-ZSM-5-50 to 47, 37, and 33 μmol/g, respectively. However, the amount of strong acidity was highest in Cu-ZSM-5-20 at 222 μmol/g, followed by Cu-ZSM-5-10 at 150 μmol/g, and Cu-ZSM-5-50 at 140 μmol/g. This indicates that the number of Brønsted acid sites was high in Cu-ZSM-5-20. A high copper loading leads to a decrease in the number of Brønsted acid sites, as Lewis acid sites are formed by the substitution of protons of (Si-(OH)-Al) by Cu $^{2+}$ions. An increase in the high-temperature shoulder peak was observed with an increase in the copper loading in Cu-ZSM-5-10 [200].

Table 5.3: NH_3-TPD data of Cu-ZSM-5 foam catalysts

Samples	Tpeak (^{o}C)		Acid amount (μmol/g)		
	LT peak	HT peak	Weak acidity	Strong acidity	Total acidity
Cu-ZSM-5-10	218.1	345.9	47	150	190
Cu-ZSM-5-20	221.7	332.3	37	222	259
Cu-ZSM-5-50	223.9	318.6	33	140	170

5.3.6 Nuclear magnetic resonance spectroscopy

Solid-state NMR allows the investigation of the local structure of the nuclei in solid catalysts. This is an important method for the investigation of oxygen coordination, local symmetry, and concentration of aluminium species in the framework and extra framework positions in Cu-ZSM-5. The ^{27}Al NMR and ^{29}Si NMR studies analyzed the coordination and acidity of the Cu-ZSM-5 20. Copper-exchanged zeolites are attractive acidic catalysts, because of the presence of Lewis acid sites of Cu ions and extraframework Aluminium species, as well as the Brønsted acid sites formed by water dissociation. Water molecules dissociate in the electronic field of the metal cations, and the hydroxyl protons are bound to the oxygen-bridged aluminosilicate framework. These bridging hydroxyl Si–(OH)–Al groups act as catalytically active Brønsted acid sites [201]. The ^{27} Al NMR spectrum in Figure 5.7b shows two resonance chemical shifts. The resonance with a peak at 56ppm is associated with the four-fold coordinated Aluminium framework. These tetrahedrally coordinated aluminium frameworks compensate for their negative charge due to the hydroxyl protons of the Si-(OH)-Al groups. The resonance chemical shift peak at 13 ppm is associated with six-fold coordinated extra-framework Aluminium [202]. Cationic extraframework aluminium species coordinated to framework oxygen atoms near bronsted acid sites may cause a polarizing effect and stabilized the deprotonated zeolite. This could lead to an enhanced acid strength of bridging OH groups in zeolites. This peak can also

be associated with octahedrally coordinated aluminium atoms in neutral extra-framework Aluminium oxide clusters [202].

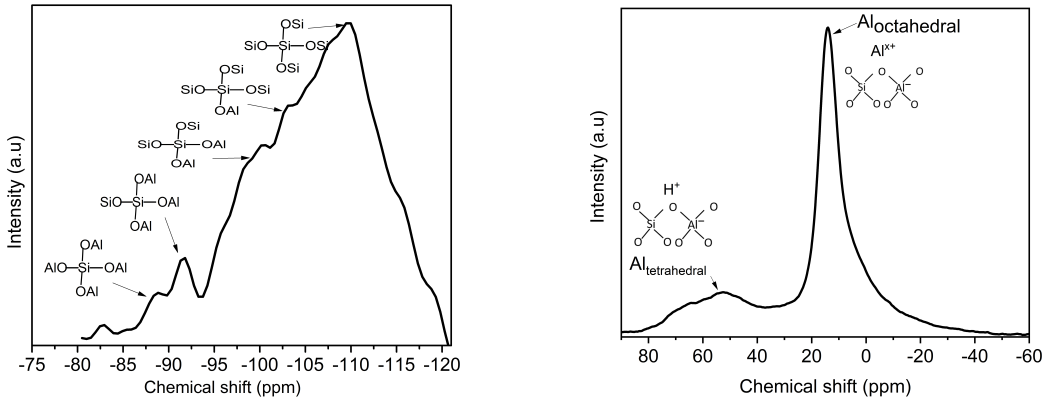

Figure 5.7: Nuclear magnetic resonance spectroscopy of (a) ^{27}Al of Cu-ZSM-5-20 (b) ^{29}Si NMR of Cu-ZSM-5-20

The ZSM-5 framework consists of a TO_4 tetrahedral structure with silicon and Aluminium at the center T positions. ^{29}Si NMR spectrum in Figure 5.7a shows five different peaks corresponding to the coordination of Al with Si. In ^{29}Si NMR, the chemical shift from -100 to -120 ppm is attributed to silicon connected to four neighboring silicon atoms (Si(0 Al)). The resonance with a chemical shift of-92 to -110ppm corresponds to Si connected to a 1 Al atom (Si(1 Al)). The resonance peak between -90 and -100ppm represents silicon tetrahedra connected to two Al atoms (Si(2 Al)). The silicon connected to 3 Al is represented by a resonance shift of -85 to -95 ppm (Si(3 Al)). Silicon atoms with four neighboring Aluminium atoms were represented by a chemical shift between -80 and -90 ppm (Si(4 Al)) [203]. The Si coordination in Cu-ZSM-5 affects the acidic strength in the following order: Si(0Al) $\leq$ Si(4Al) $\leq$ Si(3Al) $\leq$ Si(2Al) $\leq$ Si(1Al). The characterization results revealed 60% Si(0 Al), 16% Si(1 Al), 14% Si(2 Al), 1.8% Si(3 Al), and 7% Si(4 Al) in the Cu-ZSM-5-20 foam catalyst. Si(1Al) and Si(2Al) contributed more to the acidity and activity of the catalyst. The high-intensity band at approximately - -103 ppm can be assigned to Si atoms close to the Brønsted acid sites of Si(1OH,1Al,2Si). The results reveal that the synthesized Cu-ZSM-5-20 foam catalyst is highly acidic and active because most of the silicon atoms are connected to the Brønsted acid site. The Cu-ZSM-5-20 samples have a high number of Brønsted acid sites and extra-framework Aluminium atoms coordinated to the framework oxygen.

5.3.7 Ultraviolet visible spectroscopy

The presence and coordination of the metal species in the samples were studied using UV-vis-DR spectroscopy. Figure 5.8 shows the presence of three intense bands at 200-250 nm, 300-380 nm, and 600-800 nm. Itho et al. reported that the band around 212 nm was associated with the framework ZSM-5 structure [204]. The peak at approximately 250 nm in Cu-ZSM-5 was assigned to the presence of Cu^{+} ions. The band between 300-380 nm is related to Cu^{2+} interacting with the framework oxygen. This band corresponds to a charge transfer transition from oxygen to metal involving an isolated framework Cu^{2+} and oxocations (Cu^{2+}-O^{2-}-Cu^{2+}) [205]. The broadband between 600-800 nm is related to d-d transitions of Cu^{2+} in octahedral oxygen coordination, which is attributed to the dispersed surface CuO particles [161] [197]. It was concluded from the literature that CuO is formed on the external surface with an increase in copper loading [200]. Figure 5.8

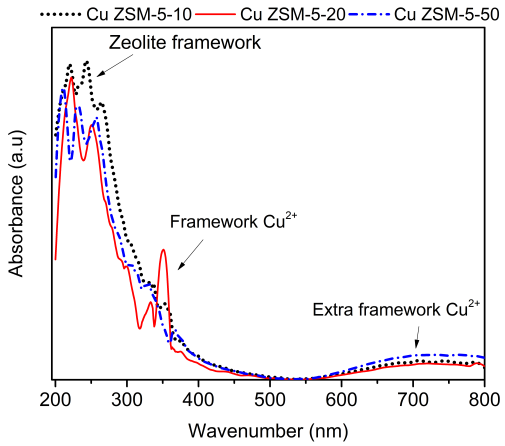

Figure 5.8: Ultraviolet–visible spectroscopy of Cu-ZSM-5 foam catalyst

reveals Cu-ZSM-5-20 has the highest Cu^{2+} ions with a sharp band at 348 nm followed by Cu-ZSM-5-10 and Cu-ZSM-5-50.

5.3.8 Electron paramagnetic resonance

The identification of Cu ions in the Cu-ZSM-5 foam was performed using electron paramet-ric resonance. Figure 5.9 shows the EPR spectrum of the Cu-ZSM-5-20 foam catalyst. The spectrum shows an axially symmetric species with EPR parameters $g = 2.05$, $A = 145G$. These values agree well with the literature values for octahedral copper complexes con-taining hydroxyl groups [206]. The EPR parameter was identified as $[Cu(H_20)_6]^{2+}$ located

at the intersection of the two channels of the structure [207]. The hydrolysis of the hexaaqua copper complex loses water during calcination and forms oxygen bridged [cu-O-cu]$^{2+}$ dimer. The green color of the calcined sample indicates the presence of an oxygen-bridged copper dimer. Because the Cu^{2+} ions in dimers and CuO are EPR-inactive because of the paired electrons, the EPR spectra can be assigned to isolated Cu^{2+} [197], [207].

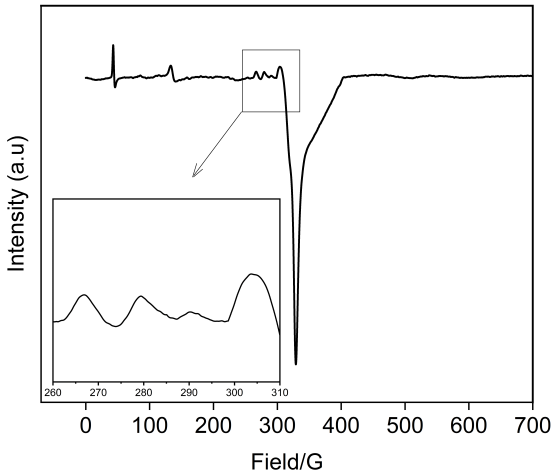

Figure 5.9: Electron Paramagnetic Resonance analysis of Cu-ZSM-5-20 foam catalyst

5.3.9 X-ray photoelectron spectroscopy

X-ray photoelectron spectroscopy revealed the elemental composition and chemical state of copper in the Cu-ZSM-5 zeolite. Figure 5.10a shows XPS survey scans of the Cu-ZSM-5 foam catalysts. Figure 5.10b shows the binding energies of 933.4 eV at Cu $2p_{3/2}$ and 943.3 eV at Cu $2p_{1/2}$ with shakeup satellite peaks at approximately 961.6 eV corresponding to Cu^{2+} in CuO. The binding energies of 935.1 eV and 956 eV correspond to isolated Cu^{2+} [163] [161] [164]. XPS analysis showed the highest CuO content in Cu-ZSM-5-10 (51%), followed by Cu-ZSM-5-50 (41%), and Cu-ZSM-5-20 (29%). O1s peak at 532.4 ev in Figure 5.10c is assigned to surface-adsorbed oxygen, and the peak at 530.6 eV is assigned to oxygen in CuO. The peak centred at around 531.6 eV is attributed to lattice oxygen species (Cu-O-Cu and isolated Cu^{2+}) and the peak located at 532.6 eV could be assigned to the surface chemisorbed oxygen species [165]. Surface-chemisorbed oxygen species are more reactive than lattice oxygen species in the oxidation reaction because of their higher mobility [166]. The peaks corresponding to lattice oxygen species and surface chemisorbed oxygen were more dominant in the analyzed samples.

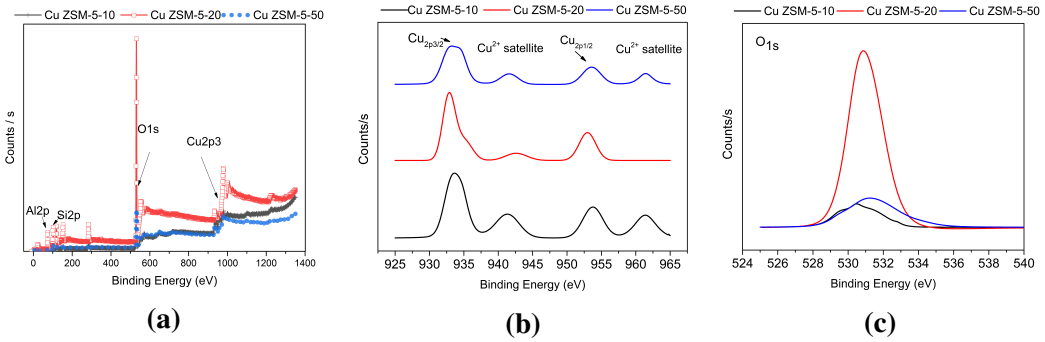

Figure 5.10: X-ray photoelectron spectroscopy of Cu-ZSM-5 foam catalyst (a) XPS Survey (b) Cu_{2p} Scan (c) O1s Scan

5.3.10 H_2 Temperature Programmed Reduction

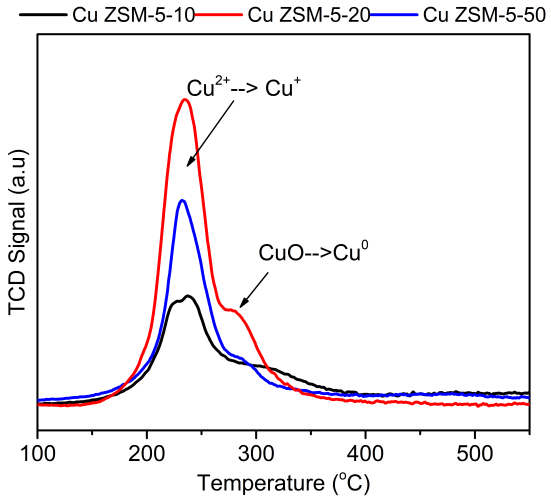

Figure 5.11: H_2 temperature-programmed reduction of Cu-ZSM-5 foam catalyst

Table 5.4: H_2 TPR of Cu-ZSM-5 foam catalysts

Samples	Tpeak (°C)		H_2 consumption (μmol/g)	
	LT peak	HT peak	LT consumption	HT consumption
Cu-ZSM-5-10	233	286	333	47
Cu-ZSM-5-20	234.3	272.2	612.1	19
Cu-ZSM-5-50	232.3	279.6	381	33.5

The redox properties and dispersion of Cu ions in Cu-ZSM-5 were obtained using H_2 TPR. Two reduction peaks are observed in the H_2-TPR profile of the Cu-ZSM-5 foam catalyst, as shown in Figure 5.11.

Table 5.5: Quantification of Cu dispersion in Cu-ZSM-5 foam catalysts

Samples	Volume Adsorbed (ml/g)	Metal loading (%)	No of moles of metal on the surface (μmoles/g)	Total moles of metal on the catalyst (μmoles/g)	Metal Dispersion (%)	Active metal surface area (m^2/g)
Cu-ZSM-5-10	8.56	0.9	152	142	10	1.5
Cu-ZSM-5-20	16.92	0.8	204	126	16	2
Cu-ZSM-5-50	8.52	0.7	126	110	12	1.3

Cu-ZSM-5-10, Cu-ZSM-5-20, and Cu-ZSM-5-50 show two reduction peaks in the H_2-TPR peaks as tabulated in Table 5.4. The peaks observed at approximately 240 and 290°C were assigned to the reduction of isolated Cu^{2+} to Cu^{+} and CuO to Cu° respectively. This reveals that the Cu^{+} produced in the Cu-ZSM-5-10, Cu-ZSM-5-20, and Cu-ZSM-5-50 foam catalysts were more stable in the studied temperature range. This is advantageous because the oxidation of Cu^{+} to Cu^{2+} is easier than the oxidation of elemental copper to Cu^{2+} during the regeneration of the catalyst. This would lead to enhanced catalyst life. The percentages of reducible Cu^{2+} and CuO in the foam catalyst were determined from the area under the corresponding peaks in the H_2-TPR graph. The Cu in Cu-ZSM-5-10 was in the form of 34% reducible isolated Cu^{2+} and 66% CuO. On the other hand, Cu-ZSM-5-20 contains 76.2% isolated Cu^{2+} and 23.7% CuO and Cu-ZSM-5-50 have 43% reducible isolated Cu^{2+} sites and 56% CuO. Cu-ZSM-5-20 shows the highest active metal surface area of 2 m^2/g of catalyst and copper dispersion of 16% as given in Table 5.5. The copper dispersion, which is the ratio of the number of moles on the surface of the catalyst to the total number of moles, was the highest for Cu-ZSM- 5-20 as evidenced in Table 5.5.

5.4 Mass transfer and pressure drop studies

Mass transfer studies are carried out in hierarchical Cu-ZSM-5 coated on alumina foam of 7.8 mm diameter and 22 mm long. The standard SCR reaction was carried out in a tubular reactor with a diameter of 8 mm and a length of 1200mm. The flow velocity was varied from 0.4 of 2 m/s. The mass transfer coefficient of the Cu-ZSM-5-20 foam catalyst for the standard SCR was evaluated by activity tests. The average diameter of the cells was used as the characteristic length. Microscopic imaging revealed that the average pore size and struct diameter were 1 mm and 0.36 mm, respectively. The estimated porosity was 70% and the specific surface area was 3362 m^2/m^3. Standard SCR of NO over the Cu-ZSM-5 catalyst by NH_3 was performed with a feed gas composition of 250ppm NO, 250ppm NH_3

and 8% O_2 at 450°C. The rate constant remains approximately the same for temperatures above 350°C, which suggests the onset of full external mass transfer control. The mass transfer coefficient was evaluated from the activity test using Equation 3.4 [146].Figure 5.12 shows the estimated mass transfer coefficients for the blank alumina foam and Cu-ZSM-5 foam catalyst plotted against the feed flow rate. Figure 5.12 shows that the mass transfer coefficient increases with an increase in the feed flow rate for both the Cu-ZSM-5 foam catalyst and blank alumina foam [90] [146] [81]. In heterogeneous reactors, the external mass transport can be increased by better fluid mixing. The tortuous flow path in the foam catalysts increases mixing and enhances external mass transfer. A higher flow rate leads to a reduction in the boundary-layer thickness and contributes to better mixing. This reduced the mass transfer resistance and promoted the transport of more reactants to the surface. The mass transfer coefficient decreases beyond a flow rate of $3.5x10^{-5}$ owing to the lower residence time available for the reaction. The reaction rate becomes limited beyond this flow rate.

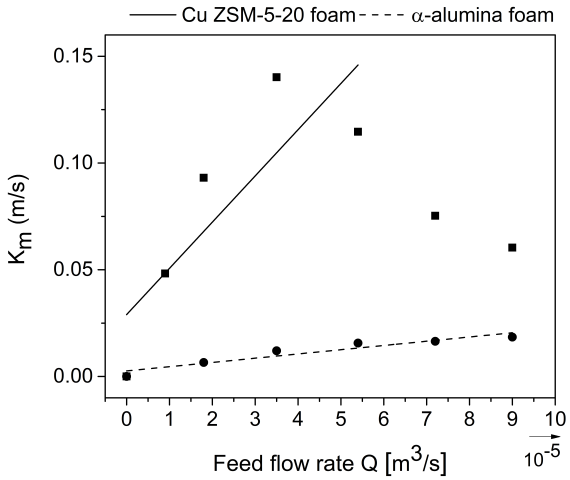

Figure 5.12: Mass transfer coefficient evaluated at a feed flow rate of $0.9e^{-5}$ to $9e^{-5}$ m^3/s for Cu-ZSM-5 foam catalyst

The mass transfer data are fitted to be expressed as a correlation using the non-dimensional quantities of the Sherwood number, Schmidt number, and Reynolds number. Figure 5.14 shows the data fitted to a single correlation represented by

$$Sh = 0.9Re^{0.4}Sc^{1/3} \;\; Re < 50 \tag{5.1}$$

The developed mass transfer correlation is well aligned with the correlations reported in the literature [150].

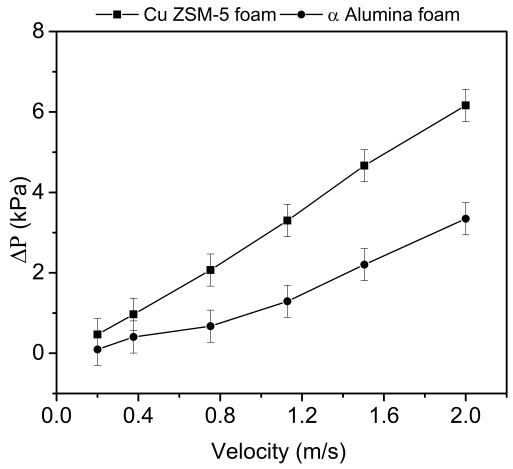

Figure 5.13: Pressure drop across the Cu-ZSM-5 foam catalyst for a velocity of 0.2 to 2 m/s

Pressure drop studies carried out on the Cu-ZSM-5-20 foam catalyst and blank alumina foam with a feed flow velocity of 0.2 2 m/s are shown in Figure 5.13. Figure 5.13 shows that the pressure drop increases with an increase in the flow velocity. The pressure drop across the alumina foam catalyst support was a minimum of 0.1 kPa at the lowest velocity of 0.2 m/s, with a linear increase in pressure drop to 3.3 kPa at 2 m/s. The pressure drop across the Cu-ZSM-5-20 foam catalyst was a minimum of 0.4 kPa at the lowest velocity of 0.2 m/s, with a linear increase in pressure drop of 6.5 kPa at 2 m/s.

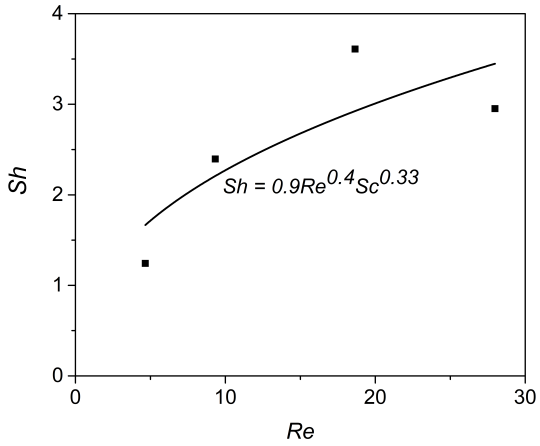

Figure 5.14: Correlation between Sherwood number and Reynolds number

The macroporous structure and porosity of the foam catalyst led to a low pressure drop. The surface area of α alumina foam of 1 m^2/g increases to 55 m^2/g on coating Cu-ZSM-5-20 on alumina foam, which results in a slight increase in the pressure drop due to the

deposition of catalysts that resist the flow [208].

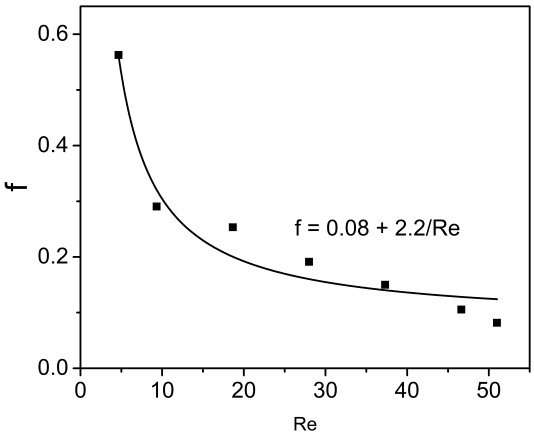

Figure 5.15: Friction factor vs Reynolds number for Cu-ZSM-5 foam catalyst

$$f = \frac{2.2}{Re} + 0.08 \;\; Re < 50 \tag{5.2}$$

The friction factor coefficient evaluated from equation 5.2 was fitted as shown in Figure 5.15 for the Cu-ZSM-5 foam catalyst. The experimental Sh and friction factor values were in excellent agreement with the values predicted in previous studies [90]. Mass transfer and pressure drop increased with an increase in the mass flow rate of the reactants. The mass transfer of the foam reactor increased at the expense of pressure drop. The tradeoff between mass transfer and pressure drop reveals the overall performance of the catalyst. A higher trade-off index for the catalyst support yields a higher conversion with a smaller pressure drop [148] [208]. The trade-off calculations for this foam catalyst at 450°C showed the highest trade-off index at Re = 18.

5.5 SCR Reaction Chemistry

5.5.1 Standard SCR of NO_x by NH_3

The standard SCR of NO over the Cu-ZSM-5 foam catalyst by NH_3 was performed with a feed gas composition of 250 ppm NO, 250 ppm NH_3 and 8% O_2 in the temperature range–200-550°C. Figure 5.16 shows the NO conversion efficiency as a function of temperature for different Cu-ZSM-5 foam catalyst samples, calculated from the measured NO outlet concentrations. Figure 5.16 shows the highest NO conversion efficiency for Cu-ZSM-5-20 at 98% at 350°C. In contrast, Cu-ZSM-5-10 and Cu-ZSM-5-50 exhibited con-

version efficiencies of 93% and 85%, respectively, at 350°C. The SCR activity depends on the acidity and amount of exchanged cations on the surface [209]. It is observed that NO reduction increases from a lower temperature and reaches a maximum conversion of approximately 350°C. The increase in NO conversion at low temperatures was attributed to the oxidation of NO.

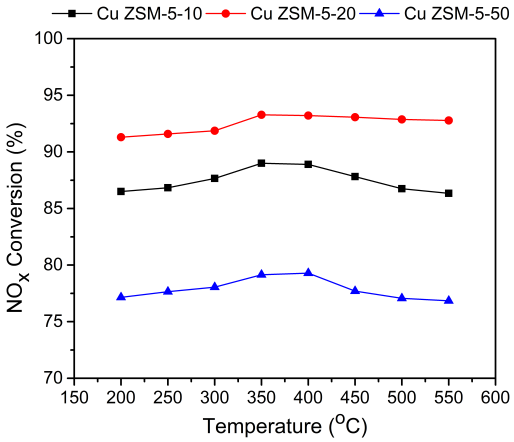

Figure 5.16: Steady-state NO_x conversion at temperatures from 200°C to 550°C over Cu-ZSM-5 foam catalysts with different silica-to-alumina ratios. The catalysts were exposed to 250 ppm NO, 250 ppm NH_3 and 8% O_2.

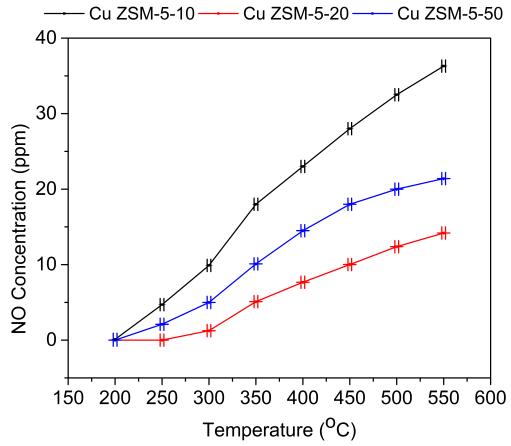

Figure 5.17: Steady-state NO outlet concentration (solid lines) and NO_2 outlet concentration (dash lines) at temperatures from 200°C to 550°C for NH_3 oxidation over Cu-ZSM-5 foam catalyst with different silica to alumina ratios. The catalysts were exposed to 250 ppm NH_3 and 8% O_2.

The oxidation of NO to NO_2 is highly important in the selective catalytic reduction of nitric oxides because NO_2 is more reactive than NO by reaction (**??**). Thus, NO_2 can enhance the reduction of NO at lower temperatures. A steady-state experiment was performed

using a feed composition of 250ppm NO and 8% O_2 over the Cu-ZSM-5 foam catalyst to study the oxidation of NO to NO_2. Figure 5.18 shows the concentrations of NO and NO_2 at the outlet for temperatures ranging from 200-550°C subjected to NO oxidation. Figure 5.18 shows that NO oxidation increases from 200-450°C and then declines at the higher temperature. Figure 5.18 reveals that NO oxidation is highest in Cu-ZSM-5-10, which can be attributed to the high CuO content in the sample [210]. In the Cu-ZSM-5-10 sample, NO oxidation reached equilibrium at 450°C and then decreased because of NO_2 decomposition. NO oxidation was reduced at higher temperatures owing to the decomposition of NO_2 to NO.

NO_2 decomposition on foam catalyst samples was analyzed by passing 250ppm NO_2 over the foam catalyst samples. Figure 5.19 shows NO_2 decomposition over the Cu-ZSM-5 foam catalyst. Figure 5.19 reveals that NO_2 decomposition initiates at 400°C and increases with increasing temperature. Higher NO_2 decomposition was observed for Cu-ZSM-5-20, which can be ascribed to the amount of isolated Cu^{2+} as evident from NH_3-TPD [211].

In Figure 5.16 Cu-ZSM-5-20 shows a slight decrease in NO conversion at temperatures above 350°C, whereas in Cu-ZSM-5-50 and Cu-ZSM-5-10, the NO conversion efficiency decreases drastically owing to NH_3 oxidation. A steady-state experiment was carried out to determine the NH_3 oxidation performance of the Cu-ZSM-5 foam catalyst samples exposed to over 250 ppm NH_3 and 8% O_2. NH_3 oxidizes to NO, NO_2 and N_2 according to equations (**??**), (**??**), and (**??**), respectively. Figure 5.17 shows the NH_3 oxidation for Cu-ZSM-5 samples with different silica-alumina ratios at temperatures from 200°C to 550°C. Figure 5.17 reveals that NO formation by NH_3 oxidation gradually increases from to 350-550°C. The high NH_3 oxidation in Cu-ZSM-5-10 was attributed to the high CuO content in the sample. Surface CuO favors the low-temperature SCR reaction by NO oxidation, while inhibiting high-temperature SCR because of its high activity towards ammonia oxidation [210]. Lei wang et al. reported that isolated copper ions are active for SCR reaction and CuO promotes NH_3 oxidation before SCR reaction at higher temperatures above 350°C [212]. It appears that the Cu-ZSM-5-20 foam catalyst does not favor ammonia oxidation even at higher temperatures. The low NH_3 oxidation in Cu-ZSM-5-20 was due to the high NH_3 adsorption on the strongly acidic sites of the sample. NH_3 adsorbed on the Cu sites forming copper ammonia complexes is an active site for SCR reactions, whereas the bronsted acid serves as ammonia storage [209] [213]. The acid sites can stabilize adsorbed ammonia at high temperatures and effectively inhibit NH_3 oxidation [199]. Jun Wang et al [212]. reported that Cu structures with extra lattice oxygen are more active in ammonia oxidation and selective for the formation of NO at temperatures above 400°C. It was also

observed that the Cu-ZSM-5 samples exhibited higher selectivity for N_2 by NH_3 oxidation. Sullivan et al. [167] also reported N_2 formation during ammonia oxidation. Yashnik et al. reported that NH_3 oxidation was faster when the feed contained NO due to the ability of NO to catalyze NH_3 oxidation [209]. It can be concluded from NH_3-TPD that strong acid sites and isolated Cu ions are the sources of ammonia for the SCR reaction, resulting in higher NO reduction at higher temperatures. NH_3 oxidation follows the same trend as the CuO content in the sample, as revealed by H_2 TPR and XPS.

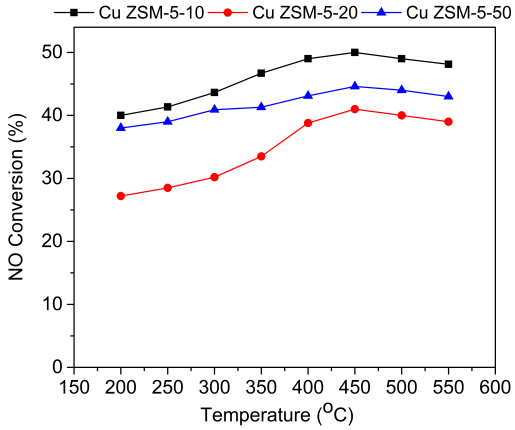

Figure 5.18: Steady-state NO conversion at temperatures from 200°C to 550°C for NO oxidation over Cu-ZSM-5 foam catalyst with different silica to alumina ratios. The catalysts were exposed to 250 ppm NO and 8% O_2.

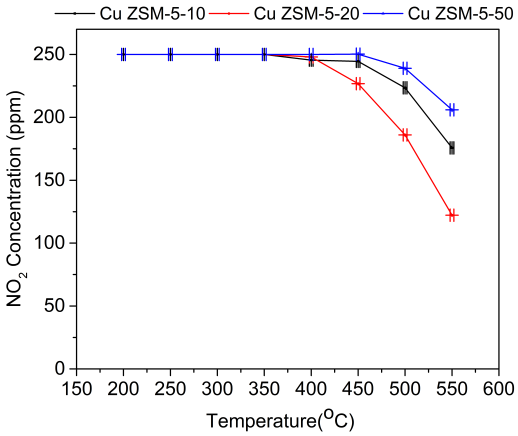

Figure 5.19: Steady-state NO_2 concentration at temperatures from 200°C to 550°C for NO_2 decomposition over Cu-ZSM-5 foam catalyst with different silica to alumina ratios. The catalysts were exposed to 250 ppm NO_2

Sjovall et al. reported that 1 g of Cu-ZSM-5 wash-coated on a monolith with a surface area of 299 m^2/g and Cu loading of 2 wt% yields NO conversion of 98% at 250°C, which

drops to 60% at 500°C for a space velocity of 18400 h $^{-1}$ [16]. Metkar et al. reported 25 g of Cu-ZSM-5 catalyst coated on monolith with a surface area of 350m^2/g and Cu loading of 2.5% yields a NO_x conversion of 95% at 350°C, which drops to 70% at 500°C for a space velocity of 57000hr^{-1} [156]. The present study concludes that hydrothermal coating of 3.2 wt% of Cu-ZSM-5 on alumina foam with a surface area of 55 m^2/g and copper loading of 0.8 wt% exposed to a standard SCR feed could achieve a conversion of 98% at 350°C, which dropped to 97% at 500°C for a space velocity of 80000hr^{-1}. The comparison of rate constants from the literature tabulated in Table 5.6 reveals that Cu-ZSM-5 foam catalyst with the present reaction conditions is more efficient than the Cu-ZSM-5 coated on monolith as reported by Sjovall et al. [16]. The majority of the reported catalysts

Table 5.6: Comparison of rate constants

NO conversion (%)	Space Velocity (h^{-1})	Temperature (°C)	Concentration (ppm)	Rate constant (s^{-1}	References
98	18400	250	500	2.89e-5	[34]
95	57000	350	500	11.67e-5	[145]
98	80000	350	250	6.27e-5	Present study

show maximum NO conversion efficiency at 250–350°C, followed by a rapid decline due to ammonia oxidation. The more or less steady NO conversion efficiency exhibited by the Cu-ZSM-5-20 foam catalyst in the temperature range of 400 to 550°C shows diffusion limitation in the catalyst.

5.5.2 NO_x adsorption study

The NO_x adsorption study was carried out using NO and NO_2 uptake, followed by temperature-programmed desorption. 250 ppm NO_x with inert gas was passed over the catalyst for 30 min, followed by the removal of loosely bound NO_x. Subsequently, a temperature ramp was implemented to desorb the stored NO_x. The outlet NO_x concentration is monitored and recorded. For the NO adsorption study, 250ppm NO was adsorbed onto the catalyst for 30 min at 150°C. Once NO saturation was obtained, loosely bound NO was removed by inert gas for 10 min. A temperature ramp of 14°C/min was applied at 150°C. Figure 5.20a shows the NO uptake and outlet concentrations during TPD. Initially, the NO outlet concentration almost reached the feed value, which indicated the weak adsorption of NO. The NO desorbed during the temperature ramp was also very low and was obtained at

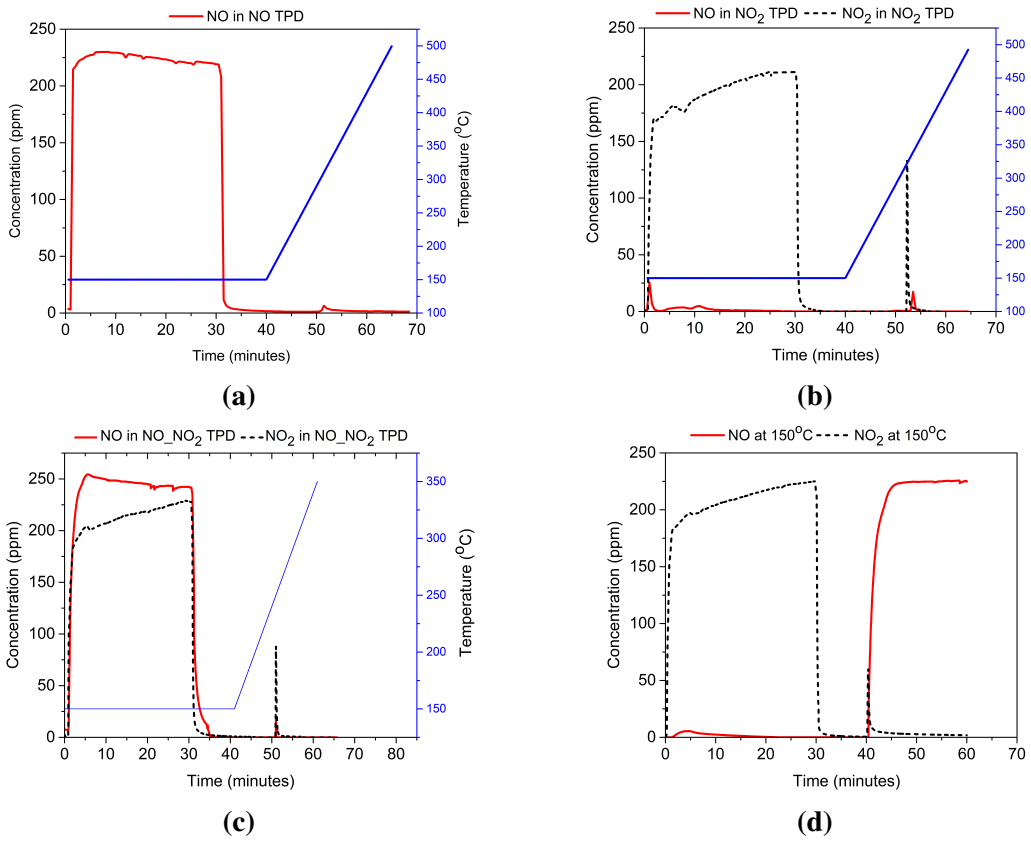

Figure 5.20: (a)NO outlet concentrations for NO TPD with a feed of 250 ppm NO at 150°C. (b) NO and NO_2 outlet concentrations for NO_2 TPD with a feed of 250 ppm NO_2 at 150°C. (c) NO, and NO_2 outlet concentrations for NO-NO_2 TPD with a feed of 250 ppm NO, 250 ppm NO_2 at 150°C. (d) NO and NO_2 outlet concentrations for 250 ppm NO_2 followed by 250 ppm NO at 150°C.

approximately 320°C [168].

$$3NO_2 + [CuO] -> Cu(NO_3)_2 + NO \tag{5.3}$$

$$Cu(NO_3)_2 -> 2NO_2 + [CuO] + 0.5O_2 \tag{5.4}$$

$$Cu(NO_3)_2 + NO -> 3NO_2 + [CuO] \tag{5.5}$$

The storage capacity of NO_2 on the catalyst was investigated using 250 ppm of NO_2 and inert gas in the feed at 150°C, followed by a temperature ramp of 14°C/min. The outlet concentrations of NO and NO_2 are recorded. Figure 5.20b compares the NO and NO_2

outlet concentrations in NO_2 uptake and desorption experiments. During the temperature ramp, a large amount of NO_2 was observed, unlike in the NO TPD. The formation of NO during NO_2 adsorption is likely because the stored species formed during the adsorption are nitrates bound to copper cations on copper dimers in the catalyst (Reaction 5.3). The ratio of NO formed to NO_2 consumed is 1:3, which confirms the disproportionation reaction [169] [36]. The large amount of NO_2 released by the decomposition of these nitrates at a high temperature of 360°C shows the high storage capacity of the catalyst and high thermal stability of the nitrates formed by the disproportionation reaction (Reaction 5.4). The small NO peak observed during the temperature ramp confirms the decomposition of NO_2. Because the temperature in the experiment was high, there was no adsorption of NO_2 on the weakly adsorbed sites. It was observed that a negligible amount of NO was absorbed by the Cu-ZSM-5 catalyst, whereas NO could be stored in the catalyst by oxidation to NO_2 [170].

To understand the influence of NO on the storage of NO_2, a desorption study was conducted by adding NO to NO_2 during the adsorption process. 250 ppm NO and 250 ppm NO_2 with inert gas were allowed to adsorb on the catalyst for 30 min, followed by TPD at a heating rate of 10° C/min. Figure 5.20c shows the concentrations of outlet NO and NO_2 during TPD. It can be observed from Figure 5.20c that the amount of NO_2 desorbed during TPD decreases significantly in the presence of NO. The NO_2 adsorbed on the catalyst forms nitrates, whereas NO reacts with the formed nitrates, which in turn limits the storage of NO_2 in the presence of NO. It is observed that the nitrates were less stable in the presence of NO in the feed. It is also observed from Figure 5.20c that it took some downtime for NO to reach a steady state during uptake. The activity of NO in reducing surface nitrates is very strong even at a low temperature of 50°C [171] [168]. The high reactivity of NO with nitrates at low temperatures has a strong influence on the stability of the nitrates formed during the adsorption of NO_2. The maximum decomposition rate was observed at 250°C in the presence of NO and at 360°C in the absence of NO.

The effect of NO on the desorption of stored NO_2 was investigated at 150°C. The catalyst was initially saturated with 250 ppm of NO_2 for 30 min. After the uptake, the NO_2 feed was switched off and the sample was stabilized for 10 min with inert gas, and then 250 ppm NO was introduced to the sample. The amounts of NO and NO_2 at the outlet were monitored and recorded. As shown in Figure 5.20d the NO_2 outlet concentration increased slowly to reach a steady state on adsorption. Upon the introduction of NO, a strong peak of NO_2 is observed, which is attributed to the decomposition of nitrates by NO (Reaction 5.5). Downtime was observed for NO to reach the feed concentration. NO reacts with

stored NO_2 in the form of nitrates and releases NO_2.

5.5.3 Effects of feed gas composition in NH_3 SCR

5.5.3.1 Effect of NH_3 feed concentration

The effect of the NH_3 feed gas concentration on the SCR reaction was studied by varying the feed concentration from 100-500 to,ppm at intervals of 30 min. The concentration of NO was maintained at 250 ppm and that of O_2 at 8% with a feed flow rate of 1000ml/min. Figure 5.21a shows the outlet concentrations of NO and NO_2 for different NH_3 feed concentrations at temperatures of 150°C and 250°C.

Figure 5.21a shows that at 250°C, the outlet NO concentration drops from 250 to 150ppm for an NH_3 feed concentration of 100 ppm. An equal amount of NO is consumed with 100 ppm of NH_3, which reveals the dominance of the standard SCR reaction. Increasing the NH_3 feed to 200 and 300ppm reduced the NO concentration to 120 and 100 ppm, respectively. Further increasing the NH_3 concentration in the feed increases the NO outlet concentration. This shows that an increase in the NH_3 concentration inhibits NO_x reduction in the standard SCR. It is also evident that NH_3 inhibition was higher at 150°C than at 250°C.

Initially, the NO_2 outlet concentration in Figure 5.21a increased as the reaction proceeded, reaching a maximum at 300 ppm NH_3 feed concentration. Increasing the NH_3 concentration in the feed beyond this value gradually decreased the NO_2 concentration at the outlet. This indicated that excess ammonia in the feed inhibited NO oxidation. The NO_2 concentration in the outlet predicts simultaneous NO oxidation with standard SCR. It is inferred that NH_3 inhibits the standard SCR reaction by blocking the sites required for NO oxidation by strongly bound NH_3 [16]. NO_x reduction was inhibited by NH_3 at higher temperatures because of ammonia oxidation.

5.5.3.2 Effect of NO feed concencentration

The effect of the NO concentration in the feed gas was studied over a Cu-ZSM-5 foam catalyst with feed gas concentrations of 250 ppm NH_3, 100-500 ppm NO, and 8% O_2 at 150°C and 250°C. The NO concentration was maintained for 30 min at each concentration. Figure 5.21b shows the outlet concentrations of NO for different NO feed concentrations. At 250°, it can be observed from Figure 5.21b that the NO outlet concentration drops to 25 ppm for an NO feed concentration of 100 ppm. It was also observed that the NO outlet concentration increased to 70 and 120 with an increase in the NO feed concentration to

200 ppm and 300 ppm, respectively. Upon further increasing the NO feed concentration to 500 ppm, the NO outlet concentration increased further to 230 ppm at 250°C and 380 ppm at 150°C. The NO_2 outlet concentration increased from 12 ppm to 70 ppm upon increasing the feed NO concentration to 100 ppm to 300 ppm. Further increasing the NO concentration increased the NO_2 outlet concentration to 150 ppm at 250°C and 38 ppm at 150°C. As the ammonia in the feed remains the same with an increase in NO feed concentration, NO is reduced until the ammonia available for reduction is consumed, beyond which NO oxidation dominates, as evidenced by the increase in NO_2 concentration. NO concentrations exceeding the ammonia concentration cannot be reduced. At 150°C, the NO conversion showed the same trend but lower conversions than at 250°C.

5.5.3.3 Effect of O_2 feed concentration

The influence of the O_2 concentration on the feed gas composition was studied by varying the concentration of O_2 from to 4-10% for 30 min at each concentration while maintaining the concentration of other feed gases constant at 250 ppm of NO and 250 ppm of NH_3 at 150°C and 250°C. Figure5.21c shows the outlet concentrations of NO and NO_2 for different O_2 feed concentrations. At 250°C, the NO concentration decreased to 118ppm with an O_2 feed gas concentration of 4%. The outlet NO concentration increased to 132 and 138ppm for feed O_2 concentrations of 6% and 8%, respectively. With an increase in the feed O_2 concentration to 10%, the outlet NO concentration increased to 142ppm. The NO outlet concentration increased slightly with an increase in the O_2 feed concentration. This increase in NO conversion can be attributed to NH_3 scarcity for the reaction due to NH_3 oxidation with the increase in the O_2 concentration. The high rate of NH_3 oxidation leads to less availability of NH_3 gas for NO reduction. Figure 5.21c also shows that the NO_2 concentration increased from 8 to 14 ppm as the O_2 feed concentration increased from 4% to 8% at 250°C. The increase in the NO_2 concentration implies that NO oxidation increases the O_2 feed concentration because of the high availability of Cu^{2+} ions [2]. It is observed that at 250°C, the decrease in NO conversion is significant compared to that at 150°C [16].

5.5.4 Effects of NO_2/NO_x feed ratio

5.5.4.1 Effects of NO_2/NO_x feed ratio on NO oxidation

It is important to investigate the effect of the NO_2/NO_x feed ratio in NO oxidation as this reaction is the rate-determining step in standard SCR. The effect of the NO_2/NO_x feed ratio on NO oxidation was studied at different temperatures of 150°C and 350°C with

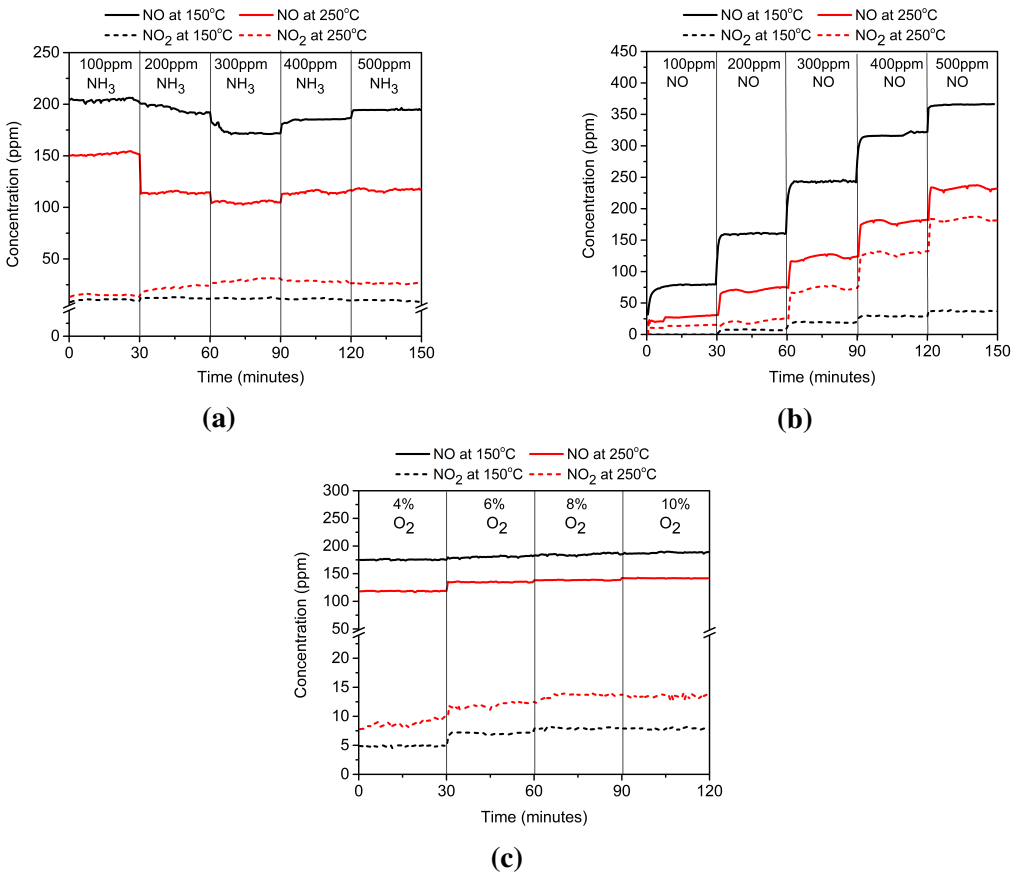

Figure 5.21: NO and NO_2 outlet concentrations at 150°C and 250°C for catalyst is exposed to feed concentration (a)100-500 ppm NH_3, 250 ppm NO, and 8% of O_2. (b) 100-500 ppm NO, 250 ppm NH_3, and 8% of O_2. (c) 4% - 10% of O_2. 250 ppm NO, and 250 ppm NH_3.

the NO_2/NO_x ratio varied from 0 to 1 by keeping the NO_x concentration at 250 ppm. The outlet concentrations of NO for different NO_2/NO_x feed ratios at 150°C are shown in Figure 5.22a. It is evident from Figure 5.22a that for pure NO feed, 45 ppm NO was oxidized to NO_2, with the introduction of 62.5 ppm NO_2 in the feed 14.5 ppm of NO was oxidized. It is observed that an increase in the NO_2/NO_x ratio above 0.5 leads to an increase in the outlet NO concentration due to the disproportionation reaction (Reaction:5.3). We can infer that the nitrate formed by NO_2 adsorption blocks NO oxidation by increasing the NO_2 concentration. The inhibition of NO oxidation by NO_2 is more pronounced beyond the NO_2/NO_x ratio of 0.5. NO_2 inhibition on NO oxidation reaction can be due to competitive adsorption of NO_2 and blockage of NO oxidation sites. NO_2 is a stronger oxidizing agent than O_2 and can oxidize metal sites and prevent the adsorption of O_2 [172] [173] [174]. Figure 5.22b shows the NO oxidation at 350°C for NO_2/NO_x ratios from 0 to 1. It is evident from the Figure 5.22b that at 350°C, for a pure NO feed, approximately 115 ppm of NO

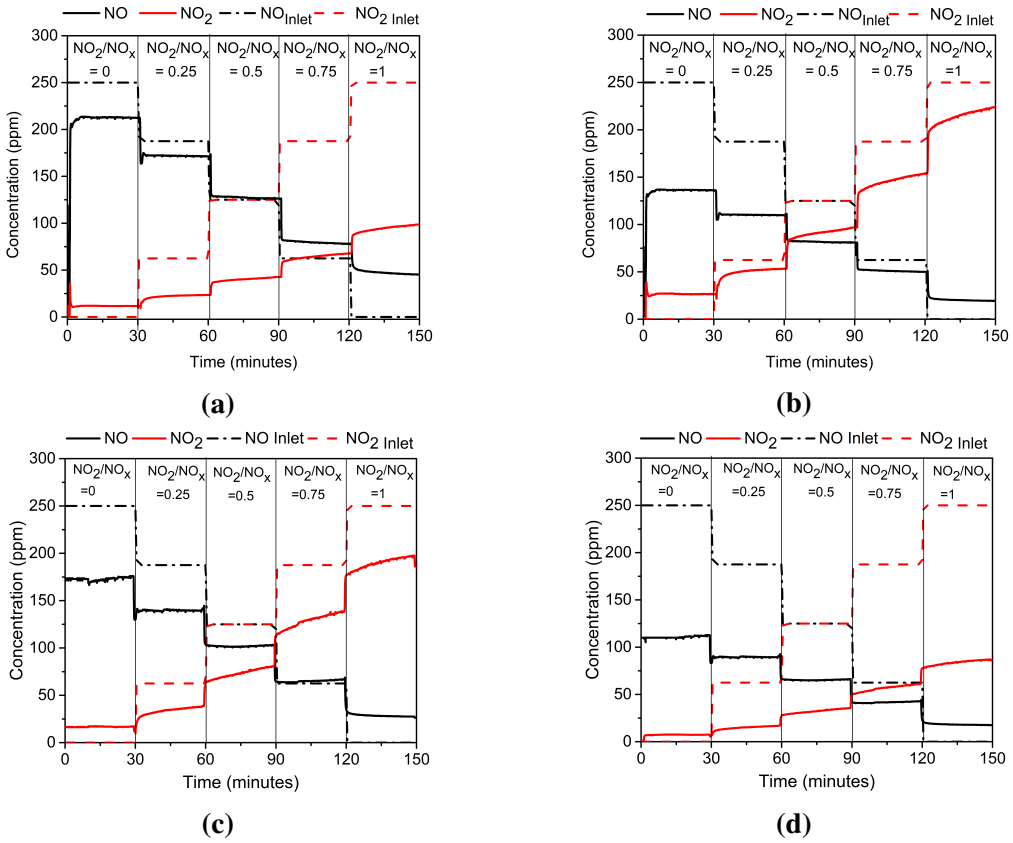

Figure 5.22: Effect of NO_2/NOx feed ratios on (a) NO oxidation at 150°C (b) NO oxidation at 350°C (c) Standard SCR at 150°C (d) Standard SCR at 350°C

is oxidized, which is approximately 60% higher than that at 150°C. With the introduction of 62.5 ppm NO_2, 77 ppm of NO was oxidized, which decreased with an increase in the NO_2/ NO_x ratio. At 350°C, NO oxidation follows the same trend as that at 150°C with NO_2/NO_x ratio but with lower nitrate storage. We can infer that the nitrates deposited on the NO oxidation sites decomposed at a higher temperature of 350°C.

5.5.4.2 Effects of NO_2/NO_x feed ratio on standard SCR

The effect of NO_2/NO_x feed ratio on standard SCR is investigated with 250 ppm NH_3, 8% O_2 and 250 ppm NO_x. The NO_2/NO_x ratio was varied from 0 to 1 at intervals of 30 min at temperatures of 150°C and 350°C. Figure 5.22c shows the outlet NO and NO_2 concentrations for different NO_2/NO_x ratios. At 150°C, for the pure NO feed, 77 ppm of NO is reduced, whereas with increasing NO_2 concentration to 62.5 ppm, the NO concentration decreases to 45 ppm. The NO concentration increased further with an increase in the NO_2/NO_x feed ratio above 0.5. This decrease in NO conversion is due to nitrates deposited

on the active sites by the disproportionation reaction, which blocks NO oxidation, which is the rate-determining step in standard SCR. The Figure 5.22c shows a reduction of 140 ppm of NO for a NO_2/NO_x ratio of 0 at 350°C, which is approximately 45 % higher than that at 150°C. For NO_2/NO_x ratios of 0.25, 98 ppm, NO was reduced. The increased NO reduction at high temperatures is due to the decomposition of nitrates deposited in the active sites.

5.5.4.3 Reactivity study : NO/NO_2–NH_3–O_2 reacting system

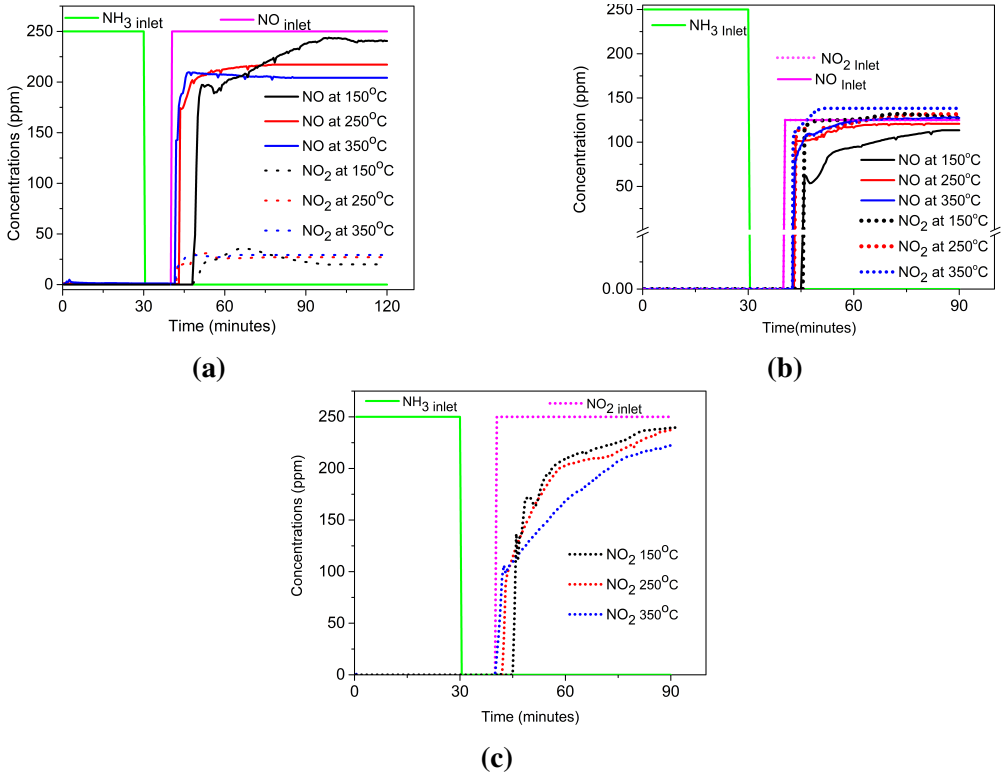

Figure 5.23: (a) NO and NO_2 outlet concentration for a feed of 250 ppm NO and 8% O_2 on 250 ppm preadsorbed NH_3. (b) NO and NO_2 outlet concentrations for a feed of 125 ppm NO, 125 ppm NO_2 and 8% O_2 at 250 ppm pre-adsorbed NH_3. (c) NO_2 outlet concentration for a feed of 250 ppm NO_2 and 8% O_2 at 250 ppm preadsorbed NH_3.

In mobile applications that operate at low temperatures of 150°C, it is important to know the effect of the distribution of NH_3 formed from urea dosing in SCR chemistry. Transient experiments were performed to elucidate the practical conditions for the SCR of NO_x. The catalyst was preadsorbed with NH_3 at 150°C, 250°C, and 350°C for 30 min with inert gas. The NH_3 gas in the feed was switched off once NH_3 was saturated and inert gas

was passed over the catalyst to remove loosely bound ammonia. NO_x gas is passed over the catalyst at different NO/NO_2 ratios along with O_2. The total flow rate was kept constant at 1000 ml/min. The catalyst was pretreated with 8% O_2 at 500°C for 30 min prior to each experiment. The transient outlet concentrations of NO and NO_2 were recorded to study the reactivity of NO, NO_2 and O_2 on preadsorbed NH_3 at different temperatures.

5.5.4.4 NO feed (NO/NO_2): (1/0)

The reactivity of NO on pre-adsorbed NH_3 in the presence of O_2 was studied in this experiment. Feed with 250 ppm NH_3 and inert gas was fed for 30 min at 150°C. Then, NH_3 was switched off and inert gas was passed over the catalyst for 10 min. 250 ppm NO and 8% O_2 were passed over the catalyst simultaneously. Transient NO and NO_2 outlet concentrations were recorded. This procedure was repeated for 250°C and 350°C. The Figure 5.23a shows the transient NO and NO_2 outlet concentration at 150°C, 250°C and 350°C. Figure 5.23a shows that the SCR duration is 11.2 min from the NO feed at 150°C. It takes 56.15 minutes to reach a steady NO concentration of 244 ppm from 197 ppm obtained after Standard SCR reaction. The NO_2 breakthrough occurs at 24.7 min from the NO feed owing to NO oxidation. At 250°C, the SCR reaction occurs for 3.2 min, which is almost 3.5 times that at 150°C. It takes 20.13 min for the NO concentration to reach a steady concentration of 213 ppm from 204 ppm after the SCR reaction. NO_2 breakthrough occurred 12.5 min from the NO feed. At 350°C, the SCR duration is 1.8 min, which is 6.2 times the duration at 150°C. A steady NO concentration of 209.7 ppm is obtained at 6.7 minutes from NO feed. An early breakthrough of NO_2 was observed at 5.4 minutes of NO feed.

Therefore, it can be concluded that SCR duration depends on the adsorption temperature of NH_3. The SCR reaction duration decreased with increasing temperature. The NO reduction rate was high at high temperatures and the NO concentration reached a steady state in a short time. At high temperatures, the amount of NO reduction was low owing to the short SCR duration.

The standard SCR reaction lasted for 11.2 min, 3.2 min, and 1.8 min with 53 ppm, 40 ppm, and 38 ppm NO reduced at 150°C, 250°C, and 350°C, respectively. The high SCR reaction rate at higher temperatures resulted in the faster consumption of stored NH_3 and led to the early breakthrough of NO_2 by NO oxidation.

5.5.4.5 NO/NO_2 feed (NO/NO_2): (1/1)

The reactivities of equimolar NO and NO_2 on preadsorbed NH_3 in the presence of O_2 were analyzed in this experiment. 250 ppm NH_3 is preadsorbed in the presence of inert gas for 30 min. Once the catalyst surface was saturated by NH_3, NH_3 gas was switched off, and inert gas was allowed to pass through the catalyst to remove loosely bound NH_3 on the catalyst. 125 ppm NO, 125 ppm NO_2 and 5% O_2 were simultaneously passed over the catalyst, and the NO and NO_2 outlet concentrations were monitored at regular intervals. Figure 5.23b shows the NO and NO_2 outlet concentrations at different intervals in the transient experiments.

Figure 5.23b shows that at 150°C, the NO concentration suddenly peaks after 5 min of the SCR reaction with a concentration of 86 ppm and reaches a steady state of 113.6 ppm after 30 min. At 250°C, the NO concentration peaked after 3 min of the SCR reaction which was 1.67 times that at 150°C. The NO concentration reached a steady state of 129 ppm at 27.35 min from a peak NO concentration of 116ppm. At 350°C, an NO concentration of 122 ppm was achieved after 1.7 min of the SCR reaction which is 1.76 times that at 250°C. The NO concentration reaches a steady state of 125 ppm after 14 min. It was observed that the SCR duration for NO/NO_2 feed conditions in fast SCR had a less significant impact on the temperature. The amount of NO reduction was 64 ppm, 22 ppm, and 15 ppm at 5 min, 3 min,minutes and 1.7 min for 150°C, 250°C, and 350°C, respectively. The reaction times were almost the same for both the standard and fast SCR at 250°C and 350°C.

5.5.4.6 NO_2 feed (NO/NO_2): (0/1)

The reactivity of NO_2 on preadsorbed NH_3 in the presence of O_2 was studied by passing 250 ppm NH_3 through inert gas for 30 min. After saturation of the catalyst surface with NH_3, NH_3 gas was switched off, and inert gas was passed to remove loosely bound NH_3. NO_2 (250 ppm NO_2 and 8% O_2 were passed over the catalyst, and the NO_2 outlet concentration was recorded. Figure 5.23c shows the NO_2 outlet concentration on preadsorbed NH_3. The NO_2 feed led to a slow SCR reaction with a duration of 7 min with an outlet NO_2 concentration of 137 ppm at 150°C and reached a steady state after 41 min with a NO_2 concentration of 240 ppm. At 250°C, the slow SCR lasts for 4.7 minutes with a NO_2 peak concentration of 112 ppm after 20 min with a steady NO_2 concentration of 203 ppm. At 350°C, slow SCR lasts for 2.2 minutes with an outlet NO_2 concentration of 106 ppm and reaches a steady state after 36 min with a steady-state NO_2 concentration of 208 ppm. The long duration to reach steady-state NO_2 concentration at high temperatures is due to

NO_2 decomposition. The SCR duration and NO_2 peak value decreased with increasing temperature.

5.5.4.7 Ammonia inhibition effect in SCR reactions

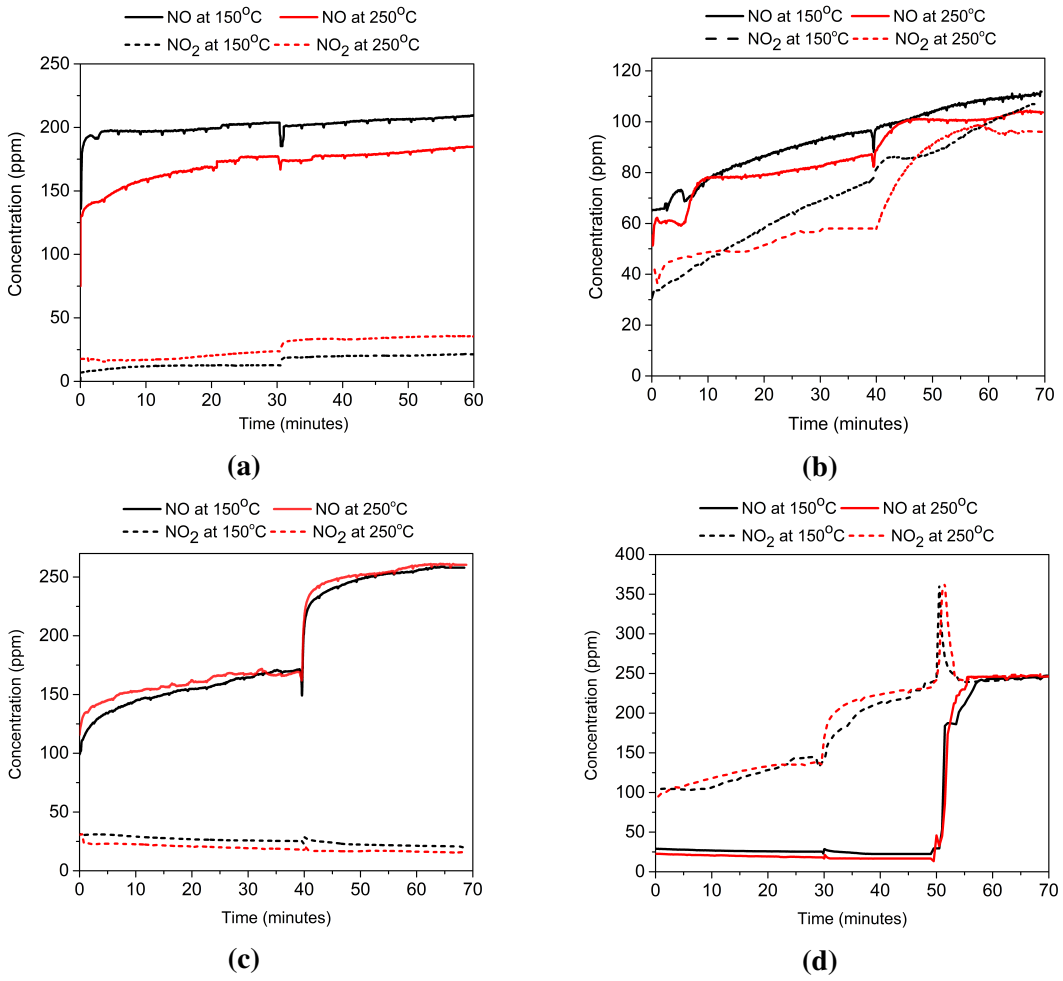

Figure 5.24: (a) NO and NO_2 outlet concentration for a feed of 250 ppm NH_3 250 ppm NO, and 8% O_2 at 150°C and 250°C. (b) NO and NO_2 outlet concentration for a feed of 250 ppm NH_3, 125 ppm NO, 125 ppm NO_2 and 8% O_2 at 150°C and 250°C. (c) NO and NO_2 outlet concentration for a feed of 250 ppm NH_3, 250 ppm NO_2 at 150°C and 250°C. (d) NO and NO_2 outlet concentration for a feed of 250 ppm NH_3 250 ppm NO_2, 250 ppm NO_2 at 150°C and 250°C.

NH_3 has strong interactions with Cu-ZSM-5 compared with other reactants in SCR chemistry, which is evident from NH_3 TPD [214].

Cu atoms are coordinated to oxygen atoms in Si-O-Al bridges to form $[Cu(OH)]^+$ via ion exchange [215] [216]. Cu-NH_3 interactions are dependent on the nature of Cu ions

(Cu^{2+}, $[Cu(OH)]^{+}$, Cu+), local environment of the Cu ions, gas composition and temperature. C.Paolucci et al stated that $[Cu(OH)]^{+}$ is more reducible by NH_3 than other Cu^{2+} ions [217]. The Cu-NH_3 interactions and their blocking effects are discussed in this section.

5.5.4.8 NH_3 inhibition in standard SCR

A transient experiment was carried out to investigate NH_3 inhibition in standard SCR with a feed of 250ppm NO, 250ppm NH_3 and 8% O_2. The feed was passed over the catalyst for 30 minutes at 150°C. Once the reactants are saturated, NH_3 is suddenly switched off, and the transient NO and NO_2 outlet concentration responses are monitored. The experiment was repeated at 250°C. Figure 5.24a shows the transient NO and NO_2 responses at 150°C and 250°C. Figure 5.24a shows a dip in the NO concentration on NH_3 shut-off, which goes through a minimum and then increases as a result of the consumption of adsorbed NH_3. During the transient shut-off of NH_3, only the adsorbed NH_3 reacted with the NO feed, which enhanced NO reduction. The enhanced NO reduction on NH_3 shut-off confirms the inhibitory effect of NH_3 gas in the feed. At 250°C, a long downtime for the NO outlet concentration to reach a steady state was observed, which shows high NH_3 adsorption and reaction. The dip at 250°C is less than that at 150°C, indicating that ammonia inhibition is less evident at high temperatures.

A standard SCR reaction occurs via the reduction and oxidation of metal ions using three active reactants. Cu(I) is oxidized to Cu(II) during the redox cycle and is limited by the activation of O_2 at low temperatures. It is evident from literature that low-temperature O_2 activation requires two Cu(I) sites [218] [217]. Gao et al. proposed from DFT studies that two NH_3 ligands of Cu(I) activate the O_2 in the oxidation half cycle of Standard SCR (Reaction 5.6)

$$2[Cu(NH_3)_2]^{+} + O_2 => [Cu(NH_3)2]^{+} - O_2 - [Cu(NH_3)_2]^{+} \tag{5.6}$$

In the reduction half-cycle of Standard SCR, NO adsorbed on the Cu site by an oxygen atom. NO is oxidized to NO_2 and facilitates Cu(I) oxidation, according to equation 5.7.

$$\begin{aligned}[Cu(NH_3)_2]^{+} - O_2 - [Cu(NH_3)_2]^{+} + NO => \\ [Cu(NH_3)_2]^{2+} - O^{2-} - [Cu(NH_3)_2]^{2+} + NO_2\end{aligned} \tag{5.7}$$

In the presence of excess NH_3, NH_3 blocks the adsorption of NO on the Cu sites through an oxygen atom and reduces DeNO_x activity. Cu ions are heavily ligated with NH_3 in

the low-temperature regime (Reaction (5.7), (5.6)). Therefore, excess ammonia blocks the reoxidation of redox sites and prevents NO oxidation, which is the rate-limiting step in Standard SCR [219] [220]. A standard SCR reaction by the oxidative adsorption of NO with stronger non-dissociative adsorption of NH_3 on Cu sites has been reported for Cu-ZSM-5, Cu-SAPO-34, and Cu-SSZ-13 [221] [222] [223]. There is a possibility of adsorption of excess ammonia on the already adsorbed sites, forming dimeric species at high ammonia coverage and may block the activation of NH_3 and its interaction with NO, which may suppress the SCR activity.

5.5.4.9 NH_3 inhibition in fast SCR

The inhibiting effects of NH_3 on fast SCR were analyzed with feed gases of 125 ppm NO, 125 ppm NO_2 and 250 ppm NH_3 at 150°C and 250°C. The feed gas was passed over the catalyst for 40 min until saturation was reached. NH_3 gas was switched off when all reactants were saturated, and the concentrations of NO and NO_2 were monitored. Figure 5.24b shows the transient NO and NO_2 response on NH_3 shut-off in the fast SCR reaction at 150°C and 250°C. Figure 5.24b shows a dip in the NO concentration on NH_3 shut-off, which reaches a minimum and then increases to a steady state with time. The decrease in NO concentration is due to the reaction of NO with nitrates formed upon the reaction with NH_3 and NO_2. It is also observed that the dip decreases with an increase in temperature, as NH_4NO_3 formed decomposes with an increase in temperature. Initially, the NO_2 concentration was lower than that of NO because of the reaction of NH_3 and NO_2 to form ammonium nitrate, nitrogen, and water (Reaction 5.9). The NO_2 concentration slowly increased with a decrease in the number of available active sites as the reaction proceeded. It is observed that at 150°C, the NO_2 concentration shows a peak in the removal of NH_3 which is attributed to NO_2 formation during the reaction of NO with nitrates, beyond which the outlet concentration increases and finally reaches a steady state (Reaction 5.8). Grossale et al. [171] reported that the most stable nitrate species formed reacts with NO at 50°C in the absence of NH_3 whereas NO does not react with nitrates in the presence of NH_3. It was observed that there is a short-lived increase in the consumption of NO and the formation of NO_2 as NH_3 is consumed through the reaction. In other words, NO_x reduction could be accelerated by decreasing the ammonia in the feed [187] [192].

$$NH_4NO_3 + NO => NO_2 + N_2 + 2H_2O \tag{5.8}$$

$$2NH_3 + 2NO_2 => NH_4NO_3 + N_2 + H_2O \tag{5.9}$$

The Fast SCR mechanism follows a redox reaction scheme similar to that of the Mars-Van Krevelen scheme. It has been proposed that for Cu zeolites, in the reduction half-cycle, Cu^{2+}-NH_3 ligands activate NO and are reduced to Cu^{+} (Reaction 5.10) [218] [224] [221]. The nitrosoamide intermediate formed during the reduction half-cycle is highly unstable and decomposes to N_2 and H_2O even at 100°C [218] [224] [225]. During oxidation, half-cycle Cu^{+} reacts with NO_2 to form nitrates and nitrite species, which decompose to N_2 and H_2O at high temperatures.

$$Cu^{2+} - NH_3 + NO => Cu^{+} - NH_2NO + H^{+} \tag{5.10}$$

$$Cu^{+} + NO_2 => Cu^{2+} - NO_2 \tag{5.11}$$

$$Cu^{2+} - NO_2 + NH_3 + H^{+} => Cu^{2+} - NH_4NO_3 \tag{5.12}$$

It is argued that NH_3 is adsorbed on the acidic sites of the zeolite, and NO_2 interacts with the Cu site to form nitrates. The formed nitrates interact with neighboring ammonia sites, or ammonia can spill over the formed nitrates to form ammonium nitrates (Reaction 5.12) [175] [226] [227]. Ammonium nitrate is thermally stable below 250°C, and can potentially deactivate low-temperature NO_x reduction. The strong interaction of ammonia with nitrates blocks the reduction of nitrate species by NO. Therefore, the removal of ammonia from the feed enhances the SCR reactivity. Grossale et al. reported that the reduction of surface nitrates by NO is the rate-determining step for Fast SCR. The NH_3 blocking effect on Fast SCR is not due to the competitive chemisorption of ammonia on the catalytic sites, but by the capture of surface nitrates by ammonia in an unreactive form [171] [185].

5.5.4.10 NH_3 inhibition in slow SCR

NH_3 inhibition on slow SCR was investigated with feeds of 250 ppm NO_2 and 250 ppm NH_3. The feed gas was passed through the catalyst for 40 min. NH_3 is suddenly switched off once the gases are saturated and NO_2 is passed over the catalyst. Figure 5.24c shows the transient outlet NO_2 response over a catalyst. The outlet NO_2 concentration initially decreased because of the reaction of NO_2 with NH_3 to form ammonium nitrate (Reaction 5.9). The NO_2 concentration shows a small dip when NH_3 is shut off, which is attributed

to the NO_2 reacting with the adsorbed NH_3 sites. The rate of ammonium nitrate formation increases with NH_3 coverage. Thus, the rate of ammonium nitrate formation decreases upon NH_3 shut-off, and the outlet NO_2 concentration suddenly increases to a steady state [228]. The reduction of nitrates by NH_3 determines the rate of the NO_2 SCR reaction mechanism [229]. At low temperature, ammonium nitrate forms and gets deposited on the catalyst, it inhibits the reaction of NO_2 with NH_3 either by blocking the active sites or by reducing the accessibility of pore structure [171]

NH_3 inhibition of the SCR reaction is relevant at low temperatures and complicates SCR catalyst design in automotive applications. NH_3 inhibition in Cu-ZSM-5 is less significant, but understanding the distribution and inhibition of NH_3 is relevant in mobile automobile applications, where NH_3 is produced by urea dosing [36] [16] [230] [214]. Thus, it can be concluded that the NH_3 inhibition in slow SCR is low compared to that in Standard SCR and Fast SCR.

$$3NH_4NO_3 + 2NH_3 => 4N_2 + 9H_2O \tag{5.13}$$

The reactivity of NO towards nitrate adsorbed species were analyzed in the presence of pre-adsorbed ammonia. 250 ppm NO_2 and 250 ppm NH_3 are simultaneously fed to the reactor for 30 min. NH_3 is suddenly switched off when the reactants are saturated on the catalyst, and NO_2 is passed over the catalyst for another 20 min. Once NO_2 was saturated over the catalyst, NO_2 was shut off, and 250 ppm NO was passed over the catalyst. Transient outlet NO and NO_2 concentrations were recorded. Figure 5.24d shows the transient responses of NO and NO_2 at 150°C and 250°C. Initially, when NH_3 and NO_2 were fed to the reactor, the outlet NO_2 concentration increased with the formation of ammonium nitrate (Reaction 5.9). When NH_3 is shut off, the NO_2 concentration exhibits a dip and increases to the NO_2 feed concentration with time. At 50 min of the experiment, when NO was introduced over the catalyst, we observed a significant peak in the NO_2 outlet concentration, which reached a steady state with time. The peak of the NO_2 concentration is attributed to the reaction of ammonium nitrates with NO (Reaction 5.8). The downtime observed in the NO outlet concentration to reach its steady state indicates the reaction of NO with ammonium nitrate to form NO_2, N_2 and H_2O. Figure 5.24d shows a steady initial NO concentration due to the adsorption of NO_2 on the catalyst by the disproportionation reaction (Reaction 5.3), which reaches a steady state.

5.6 Summary

Cu-ZSM-5 catalysts synthesized with different SiO_2/Al_2O_3 ratios of 10, 20, and 50 were deposited on an alumina foam support by an in situ hydrothermal process followed by copper exchange for the SCR of NO_x by NH_3. It is concluded that hydrothermal coating of 3.2 wt% of Cu-ZSM-5-20 on alumina foam with a surface area of 55 m^2/g and copper loading of 0.8 wt% exposed to a standard SCR feed could achieve a conversion of 98% at 350°C, which dropped to 96% at 500°C for a space velocity of 80000hr^{-1}. The more or less steady NO conversion efficiency exhibited by Cu-ZSM-5-20 foam catalyst in the temperature range of 200 to 550°C is advantageous in NO_x reduction from high-temperature exhaust gases. It is inferred from the H_2 TPR that surface CuO inhibits high-temperature SCR because of its high activity towards ammonia oxidation, whereas it promotes low-temperature SCR by NO Oxidation. NH_3 adsorbed on the Cu sites forming copper ammonia complexes is an active site for SCR reactions, whereas the Brønsted acid serves as ammonia storage. The interaction of reactant NO_x gases with Cu-ZSM-5 is studied by adsorption and temperature-programmed desorption. NO_x adsorption and TPD studies concluded that NO can be stored in the catalyst by oxidizing to NO_2 as a negligible amount of NO is absorbed by the Cu-ZSM-5 catalyst, whereas NO_2 can be stored in the form of nitrates. The high reactivity of NO with nitrates at low temperatures has a strong influence on the stability of the nitrates formed during adsorption of NO_2. The desorption of nitrates was observed at 250°C in the presence of NO and at 360°C in the absence of NO. An investigation of the effect of reactant gases on the standard SCR reveals that an increase in the NH_3 concentration in the feed decreases NO_x reduction by inhibiting NO oxidation. It is also inferred that NO concentration that exceeds the NH_3 feed concentration cannot be reduced. The study on the effect of NO_2/NO_x ratio on NO oxidation concludes that nitrates formed on increasing NO_2 concentration block NO oxidation which is the rate-determining step in standard SCR at low temperatures, whereas the deposited nitrates get decomposed at a higher temperature of 350°C and increase the NO_x reduction.

The reactivity of NO and NO_2 on the preadsorbed NH_3 in the presence of O_2 at different temperatures elucidates the fast dynamics of SCR chemistry. The study revealed a high reaction rate at a high temperature of 350°C over a short duration. The reactivity of NO on pre-adsorbed NH_3 in the presence of O_2 decreases with increasing temperature, whereas the reactivity of equimolar NO and NO_2 has a less significant impact on temperature. The reactivity of NO_2 on pre-adsorbed NH_3 in the presence of O_2 decreased with an increase in temperature. At low-temperature NH_3 in the feed gas inhibits SCR reaction and

complicates the SCR catalyst design in automotive applications. In standard SCR, excess NH_3 blocks the adsorption of NO on Cu sites through an oxygen atom and reduces $DeNO_x$ activity, whereas in fast SCR, excess NH_3 masks the reaction of surface nitrates with NO, which is the rate-determining step. In slow SCR, ammonium nitrates are deposited on the catalyst and block active sites. Therefore the inclusion of NH_3 distribution and interaction in SCR chemistry to develop a kinetic model is relevant for the industrial implementation of the SCR technology on vehicles.

Chapter 6

Experimental Investigation of Mass Transfer and Kinetics of NH_3 SCR Over Self-Supporting Cu-ZSM-5 Foam

6.1 Introduction

Nitrogen oxides originating from various combustion processes are major air pollutants and are harmful to humans and the environment. These gases contribute as a major source of the formation of photochemical smog, acid rain, ozone depletion and greenhouse effects. The selective catalytic reduction of NO_x with ammonia (NH_3 SCR) in the presence of excess oxygen has emerged as $DeNO_x$ processes for both stationary and mobile sources. Researches are focused on meeting the stringent US EPA by introducing highly efficient metal-based zeolites for the amendment of NO_x. In diesel engines, the exhaust gas temperature downstream of the diesel oxidative catalysis unit is around 600°C due to cyclic regeneration in the upstream of the diesel particulate filter. Therefore the high hydrothermal stability of SCR catalyst is advisable [231]. Cu zeolites possess high hydrothermal stability, lower susceptibility to poisoning by long-chain hydrocarbons, and outstanding efficiency in oxidizing NH_3 slip to N_2 than Fe zeolite [232].

Zeolites are microporous fine powders which lead to high diffusion limitation and pressure drop over the reactor. Recently, research is focused on the development of novel structured catalyst systems to improve the mechanical strength, diffusion and heat transport properties of the zeolites. Zeolite-based structured catalysts can promote high flow transfer while reducing the pressure drop in catalytic reactions.

Packed bed reactors, monoliths and foams are widely used structured reactors in in-

dustrial applications. The packed bed offers high mass transfer at the expense of a high-pressure drop. Monolithic reactors impart high mass transfer and low-pressure drop compared to packed bed reactors. Foams can replace packed beds of particles and monoliths in environmental catalysis due to low-pressure drop, low density, high geometric surface areas, high convective heat transfer and radial mixing due to turbulent flow. Foam-based reactors, operating at high space velocity with low-pressure drop will shorten the reactor length, simplify the loading procedure and lower the overall installation costs. The structural morphology of foam and its specific surface area are greatly responsible for its performance. Tortuous flow paths through the porous matrix enhance gas/solid heat and mass transfer rates, and high surface-to-volume ratios would yield high activity per unit reactor volume. Foams are expected to minimize the occurrence of hot spots in the catalyst when highly exothermic reactions are performed while avoiding mechanical strength and thermal shock limitations. The porosity of the structure favours turbulent flow, which enhances mass transfer when compared to cordierite. Convection of heat through the pores results in good radial mixing and hence improves heat transfer [81]. Foams have higher porosity ranging from 70-95% and therefore possess low-pressure drop and higher geometric surface area than pellets [95]. The pressure drop in foams increases with decreasing porosity. The high porosity of foams makes it preferable for heat and mass transfer applications [96].

Structured catalysts are generally produced by washcoating zeolite on the substrate. The mass transport and kinetics in structured steel foam reactor with wash-coated Cu-ZSM-5 catalyst for SCR of NO_x with ammonia is studied by Kryca et al [90, 91]. Seijger et al. [92, 93] discuss the in-situ hydrothermal synthesis of binder-less ZSM-5 on ceramic foam support and its application to SCR. The washcoating on substrates has the disadvantage of low catalyst loading per unit volume of the system and loss of the active phase due to poor adhesion and unmatched thermal expansion with the substrate.

Recent researches are focused on the direct synthesis of rigid, self-supporting zeolite monoliths with improved porosity created by the presence of an interconnected macropore network. Self-supported foam catalysts have increased active phase load in the structured reactor, without additional weight, reactor volume and pressure drop. The successful development of self-supported the catalyst could provide a ready-to-use material without the need of washcoating steps. Foam catalysts provide superior mass transfer, large surface area and short diffusion length within a catalytic layer of few microns [85]. Gargiulo et al. performed SCR reaction on self-supported ZSM-5 foam monoliths which are produced using polyurethane foam templates with a high mechanical strength [85]. These structured catalysts exhibited the same catalytic activity as that of powdered counterparts, but they im-

proved NO conversion due to the higher amount of catalyst per unit volume of the reactor and their superior mass transfer coefficients coupled with low internal diffusion limitations. Lee et al [83] developed self-supporting ZSM-5 zeolite monolith foams (ZMFs) by introducing a solution of zeolite precursor within pre-shaped polymeric templates, followed by hydrothermal synthesis [84].

Recently additive manufacturing or three-dimensional (3D) printing has been developed which constructs geometries with adaptability, flexibility, and complexity [233]. These catalysts hold high zeolite loading capacities of 65–90% and interconnected channels, which increase the volume efficiency of the reactor and mass transfer of the fluid. Self-supporting zeolite monoliths manufactured by 3D printing technology have superior features like high loadings of active species and tunable structures as well as functional components. These 3D printed catalysts have deficient mechanical strength as they must withstand impact of temperature, pressure, and stress changes [140]. Shuquan Ni synthesize Mn–Ce bi-oxides on 3D monolithic Ni-foam (NF) catalysts for the selective catalytic reduction of NO by NH_3 (NH_3-SCR) [234]. Rownaghi et al observed metal doped ZSM-5 monolith catalyst by 3D printing and find that incorporation of metal increases the compressive strength of zeolite monolith [235]. Wang et al. synthesized a self-supporting zeolite membrane with sponge-like architecture and zeolite microtubes have been prepared by using cellulose acetate as the template [236]. Yi Liu et al introduced an environmentally friendly process for fabricating porous and permeable zeolite block from industrial by-product fly ash [237]. A Zampieri et al. fabricated a self-supporting Biotemplating of Luffa cylindrica sponges to self-supporting hierarchical zeolite macrostructures for bio-inspired structured catalytic reactors with the biological template, luffa sponge as a macroscale sacrificial structure builder [237]. Colombo et al. reported geopolymers with high thermal stability with less structural degradation up to 800°C as amorphous analogues of zeolites for multiple applications [238]. Jia Ding et al. synthesized a series of microfibrous-structured Cu-ZSM-5/Al-fiber catalysts for SCR reaction by changing the Si/Al molar ratios [239].

In the study, a microporous self-supporting ZSM-5 foam is synthesized by freeze casting the emulsion with zeolite slurry as the water phase and hydrogenated vegetable oil (HVO) as the oil phase. The emulsion is cast into a cylindrical freeze casting the suspension medium and its sublimation creates micropores. ZSM-5 foam with unidirectionally aligned pores could be prepared by this method.

Experimental Details

6.2 Preparation of self supporting ZSM-5 by freeze casting

Ammonium ZSM-5 is ion-exchanged with 0.1 M $NaNO_3$ solution and stirred for 30 minutes. After ion exchange Na-ZSM-5 is dried at 125°C for 1 hour. The emulsion method reported by Sujith Vijayan et al. was used for the preparation of Cu-ZSM-5 foam catalyst as it is environmentally benign and capable of producing macroporous foams [240] [241]. A 10 vol% slurry was prepared by dispersing 10 g Na-ZSM-5 powder in 47.5 ml water using the ammonium polyacrylate dispersant. The amount of dispersant used is 2 wt.% of the Na-ZSM-5 powder. The slurry is ball milled in a polyethylene container using zirconia balls of 10 mm diameter for 12 h. The Na-ZSM-5 powder to the zirconia ball weight ratio used was 1 : 4. The slurry is transferred to a round bottom flask (RB flask) and heated in a water bath at 90°C for 30 minutes under constant mechanical stirring. A mechanical stirrer with speed control is used along with a Teflon paddle. Carrageenan, 1.5 wt% of H_2O present in Na-ZSM-5 slurry is added to RB flask. The oil phase is added after the carrageenan is completely dissolved in the slurry. The amount of oil phase HVO is considered to be the same amount of Na-ZSM-5 slurry. The emulsifying agent, sodium dodecyl sulphate (0.4 wt%) is dissolved in HVO at 85°C. The oil phase of molten HVO with an emulsifying agent is added to Na-ZSM-5 slurry and mechanically stirred to form a stable emulsion. The emulsions were cast in cylindrical moulds of 10 mm diameter and 30 mm length. The mould is freeze-dried at -5°C for 30 minutes. The emulsions formed from HVO to Na-ZSM-5 undergo gelation on cooling due to the solidification of HVO and physical cross-linking of carrageenan. The gelled emulsion samples removed from the moulds are dried at room temperature in an open-air atmosphere. The HVO present in the dried samples was removed by soxhlet extraction using toluene. The samples are sintered at 500°C for 4 hours with a ramp of 23°C/hr.

The Na-ZSM-5 foam catalyst after solidification is shown in Figure 6.1. The Na-ZSM-5 foam catalysts are ion-exchanged with 50 ml of 0.02 M copper acetate solution at 50°C for 72 hours. Cu exchanged zeolites are dried at 120°C for 2 hours. The self-supporting Cu-ZSM-5 foam with a porosity of 70% and 30PPI is prepared by freeze casting. The prepared self supporting Cu-ZSM-5 have high compressive strength of 0.4 MPa.

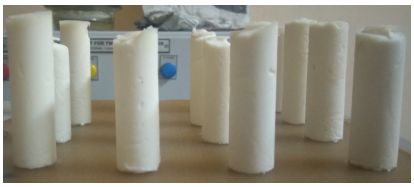

Figure 6.1: Self Suppoting Na-ZSM-5 foam catalyst after solidification in freeze casting method.

Results and Discussions

6.3 Characterization and measurements

6.3.1 BET surface area analysis

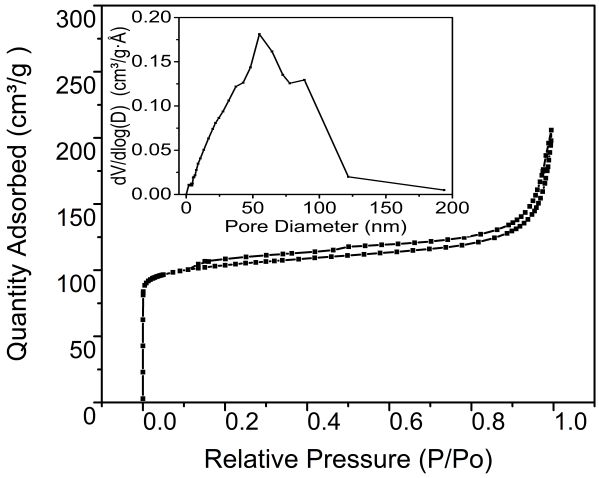

Figure 6.2: N_2 adsorption isotherm of Cu-ZSM-5 foam catalysts

The N_2 adsorption-desorptions isotherm of the foam catalysts are shown in Figure 6.1. The isotherms of the Cu-ZSM-5 foam samples exhibited a continuous increase in the adsorbed nitrogen volume with P/P_0 and a small hysteresis branch corresponding to adsorption-desorption. Cu-ZSM-5 foam catalysts exhibit type 1 hysteresis associated with porous materials consisting of well-defined cylindrical pore channels or agglomerates of approximately uniform mesopores size. The enhanced uptake of nitrogen at P/P_0 greater than 0.8 shows the presence of macropores. The plateau region at P/P_0 less than 0.5 indicates the presence of micropores, which is beneficial for the excellent pore structure and large BET surface. Pore size distribution is important to determine the accessibility of active sites by reactants and the extent of dispersion of active metals within the catalyst.

Table 6.1: Surface area analysis

Sample	S_{BET} m^2/g	S_{micro} m^2/g	$S_{external}$ m^2/g	V_{total} cm^3/g	Cu %	Al %
Cu-ZSM-5	340	260	80	0.3	6.3	4.2

The BJH analysis of Cu-ZSM-5 foam samples exhibit a broad distribution of pore sizes in the range of 2 to 150 nm with a maximum at 48 nm as shown as an inset in Figure 6.1. The surface area of Cu-ZSM-5 foam catalyst is 340 m^2/g. The chemical composition of foam catalyst determined by ICP is shown in Table 6.1. The copper content observed in Cu-ZSM-5 foam catalyst is 4.2%.

6.3.2 Transition electron microscopy analysis

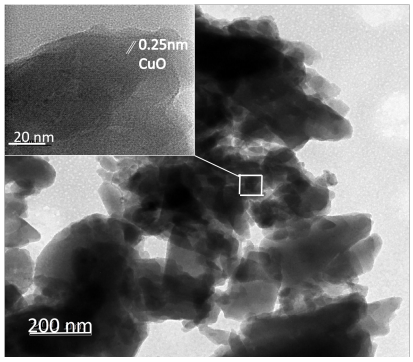

Figure 6.3: TEM micrograph of Cu-ZSM-5 foam catalyst

The distribution of copper species on the catalyst is analyzed by HR-TEM. Figure 6.3 shows the distribution of copper species by dark spots. The insert of the figure shows the interplanar spacing of the small dark spots as 0.23 nm which corresponds to CuO.

6.3.3 Scanning electron microscopy analysis

The SEM micrograph of the fractured surface of Cu-ZSM-5 foam catalyst in Figure 6.4 shows circular cell windows connecting the cells are having sizes in the range of 250 to 1500 nm. The high magnification SEM image shows the macroporous irregular morphology of the catalyst The macropores present in the catalyst facilitate the diffusion of gas molecules to access the active sites of the catalyst.

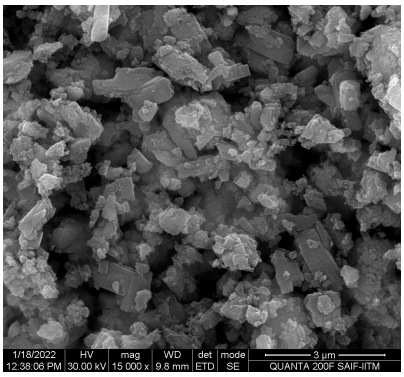

Figure 6.4: SEM micrograph of Cu-ZSM-5 foam catalyst

6.3.4 X-ray diffraction analysis

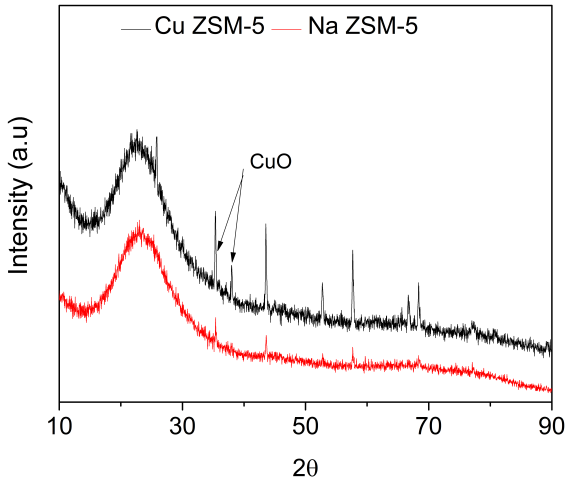

Figure 6.5: X-ray diffraction analysis of a) Na ZSM- foam, Cu-ZSM-5 foam and Cu-ZSM-5 powder

The crystallinity and structural analysis of the catalyst is studied by using XRD. Figure 6.5 shows the XRD pattern of Na-ZSM-5 and Cu-ZSM-5 powder. The Na-ZSM-5 take the structure of orthorhombic system Pnma space group a = 20.09A, b = 19.738A and c = 13.1420A (volume 5211.3A3) [196]. The peaks at 37.72°, 36.53°, 39.46°, 47.8°and 67.01°. corresponds to alumina peaks (JCPDS CARD 10-173). The peaks 21.83°,28.33°,31.29°and 36°corresponds to silica atoms (JCPDS NO 39-1425). However, a shift in the angle of diffraction is observed after the copper exchange. The shoulder peaks in Figure 6.5 at 35.5°and 38.1°observed in Cu-ZSM-5 are the characteristic of the monoclinic CuO phase [197].

6.3.5 Ammonia temperature programmed desorption

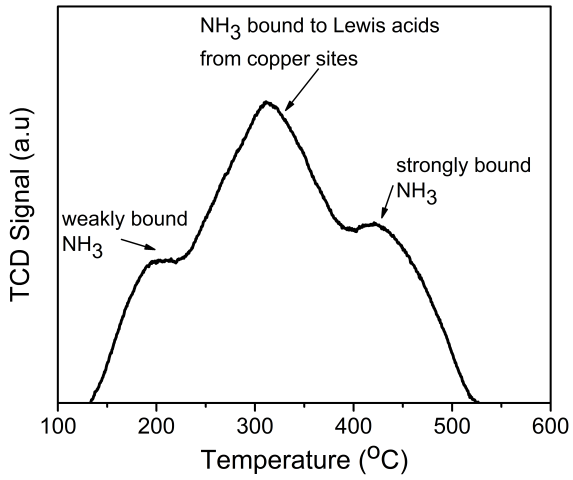

Figure 6.6: Ammonia temperature programmed desorption of Cu-ZSM-5 foam catalyst

Table 6.2: NH_3-TPD data of Cu-ZSM-5 foam catalysts

Samples	Tpeak (^{o}C)			Acid amount (μmol/g)		
	Peak 1	Peak 2	Peak 3	Weak acidity	Lewis acidity	Strong acidity
Cu-ZSM-5	188	311	448	39	225	79.5

Ammonia temperature programmed desorption (TPD) curves of Cu-ZSM-5 foam catalysts are shown in Figure 6.6. The area under the ammonia TPD graph is directly proportional to the number of acidic sites in the zeolite. Ammonia TPD curves of zeolite show three desorption peaks.

The desorption peak at a lower temperature of around 188°C is considered to be physisorbed ammonia in weak acid sites or NH_3 adsorbed on weak bronsted acid sites on surface hydroxyls [161].

The desorption peak centred at 311°C is assigned to NH_3 released from lewis acid sites originating from copper species [162]. The high-temperature desorption peak at 448°C is connected with the presence of strongly acidic hydroxyl as sorption sites.

The NH_3-TPD peaks and amount of acidity in Cu-ZSM-5 foam are tabulated in Table 6.2. The total acidity of Cu-ZSM-5 foam catalyst is 344 μmol/g,

6.3.6 X-ray photoelectron spectroscopy

X-ray photoelectron spectroscopy elucidates the elemental composition and chemical state of copper in Cu-ZSM-5. The number of electrons and the amount of element is given by

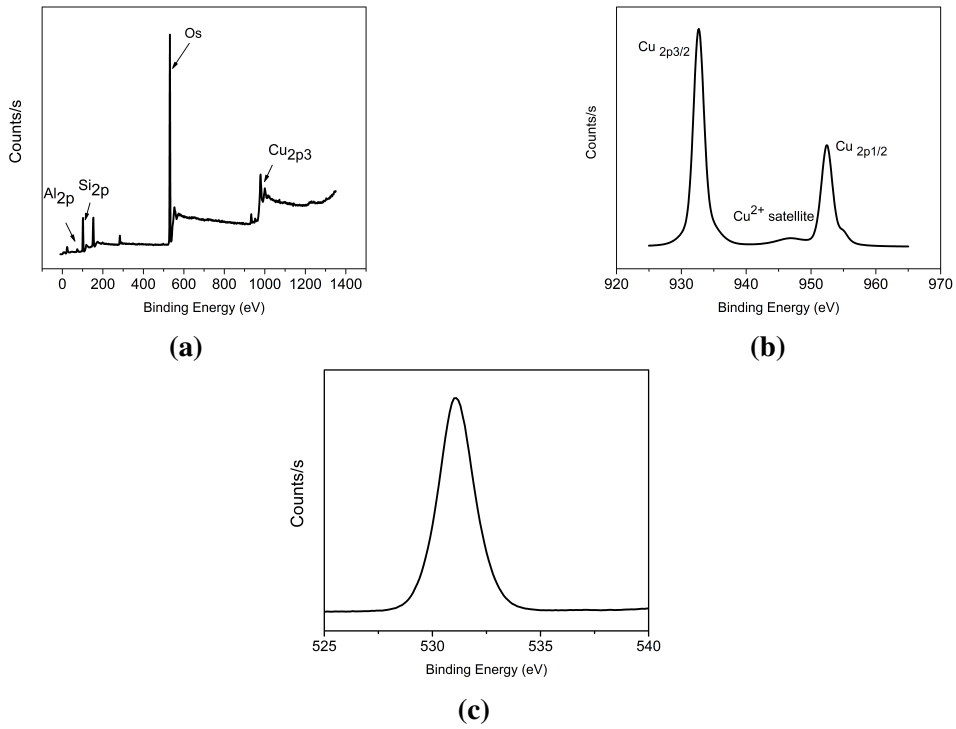

Figure 6.7: X-ray photoelectron spectroscopy of Cu-ZSM-5 foam catalyst (a) XPS Survey (b) Cu_{2p} Scan (c) O1s Scan

the area under each curve. Figure 6.7a shows the XPS survey scan of Cu-ZSM-5 foam catalysts. Figure 6.7b shows binding energy of 933.4 at Cu $2p_{3/2}$ and 946.3 eV at Cu $2p_{1/2}$ corresponds to Cu^{2+} in CuO. The binding energy of 935.1 eV and 955 eV corresponds to isolated Cu^{2+} [163] [161] [164]. The XPs peak at 932.5 eV corresponds to Cu^{+} in Cu-ZSM-5. The XPS analysis gives the isolated Cu^{2+} ions as 47% and CuO as 40%. O1s peak at 532.4 ev in Figure 6.7c is assigned to the surface adsorbed oxygen and the peak at 530.6 eV on O1s spectra is assigned to oxygen in CuO. The peak centred at around 531.6 eV is attributed to lattice oxygen species (Cu-O-Cu and isolated Cu^{2+}) and the peak located at 532.6 eV could be assigned to the surface chemisorbed oxygen species [165]. Surface chemisorbed oxygen species are more reactive than lattice oxygen species in the oxidation reaction due to their higher mobility [166]. The peaks with lattice oxygen species of 38% and surface chemisorbed oxygen of 25% are more dominant in the analyzed samples.

6.4 Mass transfer and pressure drop studies

Mass transfer studies are carried out in hierarchical Cu-ZSM-5 foam of 5 mm diameter and 11 mm long. The flow velocity is varied from 0.5 to 5 m/s. The mass transfer coefficient of Cu-ZSM-5 foam catalyst for standard SCR is evaluated from activity tests. The average diameter of the cell is adopted as the characteristic length. The microscopic imaging concludes the average pore size and struct diameter to be 0.025 mm and 0.089 mm respectively. The estimated porosity is 70% and the specific surface area is 13483 m^2/m^3. It is observed that the rate constant remains more or less the same for temperature above 350°C at 300000 hr^{-1}, which suggests the onset of full external mass transfer control. It is observed from Arrhenius plot of ln K vs 1/T for standard SCR reaction in Figure 6.8 that for Cu-ZSM-5, rate constant remains more or less the same for temperature above 350°C, which suggests the onset of full external mass transfer control. The mass transfer coefficient is evaluated from the activity test by using equation 3.4 [146].

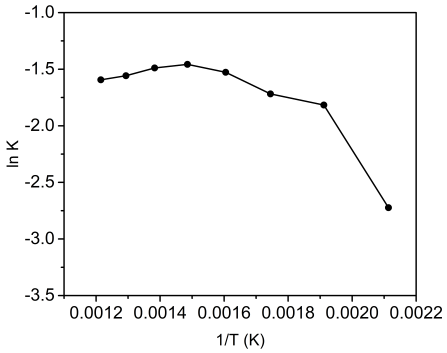

Figure 6.8: Arrhenius plot of ln K vs 1/T for standard SCR reaction

Figure 6.9a shows the estimated mass transfer coefficient Cu-ZSM-5 foam catalyst plotted against the feed flow rate. Figure 6.9a reveals that mass transfer coefficient increases with an increase in feed flow rate for Cu-ZSM-5 foam catalyst [90] [146] [81]. In heterogeneous reactors, external mass transport can be increased by a better mixing of the fluid. The tortuous path of the flow in foam catalysts increases the mixing and enhances the external mass transfer. A higher flow rate leads to the reduction of the boundary layer thickness and contributes to better mixing. This reduces the resistance of mass transfer and promotes the transport of more reactants to the surface.

The mass transfer data is fitted to be expressed as a correlation using the non-dimensional quantities of Sherwood number, Schmidt number, and Reynold number. Figure 6.9b shows

the data fitted to a single correlation represented by

$$Sh = 0.01Re^{1.5}Sc^{0.33} \;\; Re < 30 \tag{6.1}$$

The mass transfer correlation developed is well aligned to the correlations reported in the literature reviewed [150].

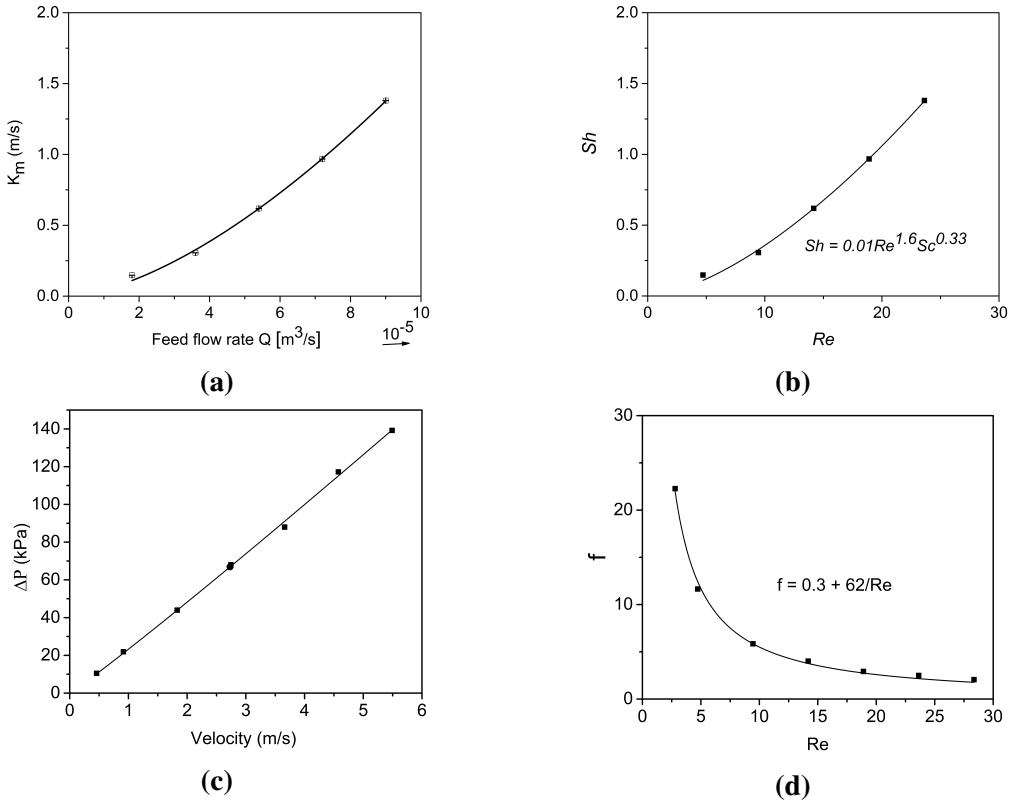

Figure 6.9: (a) Mass transfer coefficient evaluated at a feed flow rate of $1.8e^{-5}$ to $9e^{-5}$ m^3/s for Cu-ZSM-5 foam catalyst. (b) Correlation between Sherwood number and Reynolds number. (c) Pressure drop across the Cu-ZSM-5 foam catalyst for a velocity of 0.5 to 5.4 m/s. (d) Friction factor vs Reynolds number for Cu-ZSM-5 foam catalyst

Pressure drop studies carried out on Cu-ZSM-5 foam catalyst and blank alumina foam with a feed flow velocity of 0.5 to 5.4 m/s are shown in Figure 6.9c. It is observed from Figure 6.9c that pressure drop increases with an increase in flow velocity. Pressure drop across Cu-ZSM-5 foam catalyst support is a minimum of 10 kPa at the lowest velocity of 0.5 m/s with a linear increase of pressure drop to 139 kPa at 5.4 m/s.

$$f = 0.3 + \frac{62}{Re} \;\; Re < 30 \tag{6.2}$$

The friction factor coefficient evaluated from equation 6.2 is fitted as shown in Figure 6.9d for Cu-ZSM-5 foam catalyst. The correlation given by curve fitting is a Forchheimer-type equation with a viscous term and inertial term. The experimental Sh and friction factor values are in excellent agreement with the values predicted by the reported literature [90]. It is observed that the mass transfer and pressure drop increase with an increase in the mass flow rate of the reactants. The mass transfer of the foam reactor increases at the expense of pressure drop.

6.5 SCR Reaction Chemistry

6.5.1 Selective catalytic reduction of NO with NH_3

In standard SCR, NO_x is reduced by NH_3 in the presence of O_2 in the active sites of Cu-ZSM-5. The activity of Cu-ZSM-5 foam catalyst to standard SCR reaction is studied from 200-550°C. Initially 250 ppm NH_3 is passed over the catalyst until saturation. Then 250 ppm NO and 8% O_2 are fed to the reactor simultaneously at a particular temperature. Figure 6.10a shows steady state NO_x conversion at the different temperatures over Cu-ZSM-5 foam catalyst measured from the outlet NO concentration. It is observed from Figure 6.10a that NO conversion of 63% at 200°C increases with an increase in temperature with a maximum of 350°C. The highest conversion of 90% is observed at 350°C beyond which the conversion slightly decreases. The conversion decreases at a higher temperature above 400°C due to the unavailability of NH_3 for reduction.

NO oxidation is an important reversible side reaction. The reaction is kinetically controlled at low temperatures and equilibrium based at a higher temperature. At lower temperatures, NO oxidation leads to the production of NO_2 while at higher temperatures NO_2 decomposes to NO. NO oxidation is desirable due to the high rate of SCR in the presence of NO_2. The No oxidation is studied with a feed of 250 ppm NO and 8%O_2 from a temperature range of 200-550°C with a hold of 30 minutes at each temperature and a ramp of 5°C/min. Figure 6.10b shows NO conversion at different temperatures of study. NO conversion increases from 28% at 200°C to a maximum of 50% at 350°C. NO conversion decreases beyond this temperature to 43% at 550°C which can be attributed to the decomposition of NO_2 formed to NO. Ammonia oxidation is a side reaction during NH_3 SCR. This reaction is crucial as it limits the ammonia available for NO_x reduction. Oxidation of

NH_3 leads to the following reactions.

$$4NH_3 + 3O_2 => 2N_2 + 6H_2O \tag{6.3}$$

$$4NH_3 + 5O_2 => 4NO + 6H_2O \tag{6.4}$$

$$4NH_3 + 7O_2 => 4NO_2 + 6H_2O \tag{6.5}$$

The activity of Cu-ZSM-5 for NH_3 oxidation is studied by exposing the catalyst over 250 ppm NH_3 and 8% O_2. The steady-state experiments are conducted in the temperature range of 200-550°C with a hold of 30 minutes in each temperature and with a ramp of 5°/min. Figure 6.10c shows the NO concentration at different temperatures of study. It is observed that NO formed is negligible during NH_3 oxidation. There is no NO_2 reported in NH_3 oxidation. Therefore we can conclude that Cu-ZSM-5 is more selective in the oxidation of NH_3 to N_2 [53]. Komatsu et al. [29] found NO and N_2O yield less than 1% during ammonia oxidation and confirmed that the ammonia oxidation to N_2 is highly catalyzed by Cu-ZSM-5. Sullivan et al. [167] also reported N_2 formation during ammonia oxidation. NO_2 decomposition plays a vital role in high-temperature SCR reactions. The NO_2 decomposition study is investigated with a feed of 250 ppm NO_2 and inert gas from a temperature range of 200-550°C with a hold of 30 minutes at each temperature and a ramp of 5°C/min. Figure 6.10d shows NO_2 concentration at different temperatures of study. It is observed that NO_2 decomposition begins at a temperature around 350°C which becomes prominent at 550°C.

6.5.2 Adsorption Study

NO_x Adsorption Study

NO_x adsorption study quantifies the storage of NO and NO_2 in the Cu-ZSM-5 foam catalyst. NO_x adsorption experiments were carried out with a feed NO_x concentration of 250 ppm along with inert gas at 150°C. during NO_x uptake, NO_x is fed to the catalyst for 30 minutes until the saturation. The NO_2 gas is switched off and the inert gas is allowed to flow for 10 minutes to desorb the loosely bound NO_x. A temperature ramp of 5°C/min is applied from 150-500°C to desorb stored NO_x.

For the NO adsorption study, 250 ppm NO is adsorbed on the catalyst for 30 minutes at

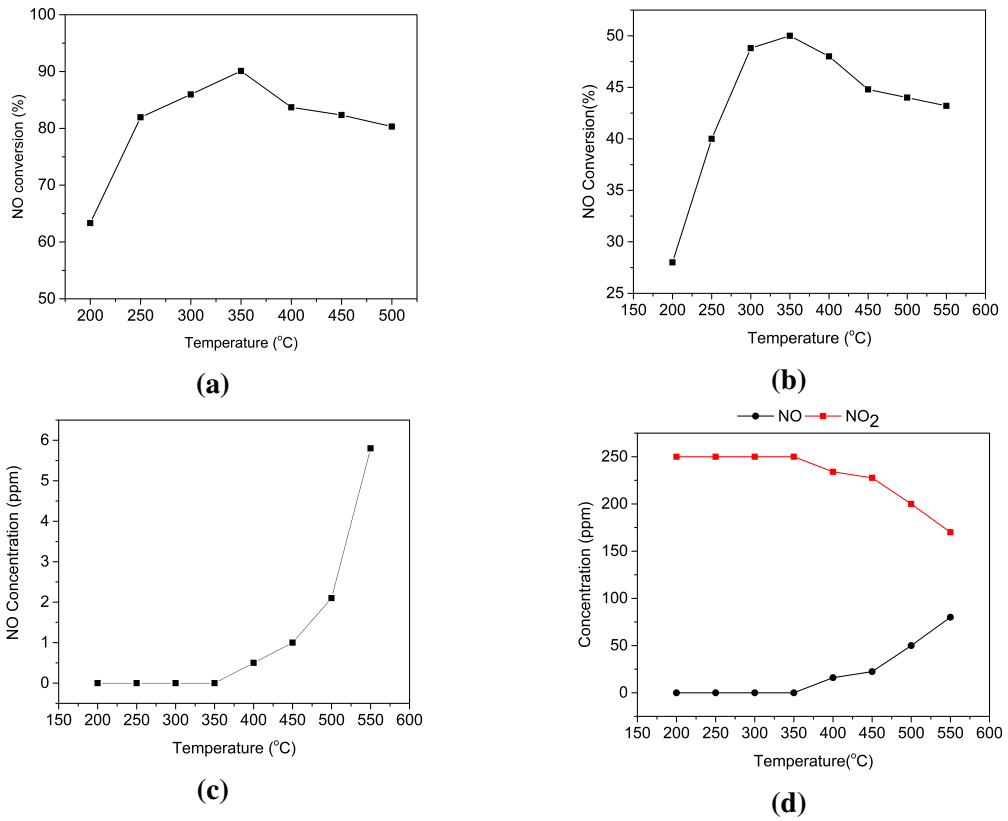

Figure 6.10: (a) NO conversion for NH_3 oxidation over Cu-ZSM-5 foam catalyst exposed over 250 ppm NH_3 and 8% O_2 (b) NO conversion in Cu-ZSM-5 foam catalyst exposed over 250 ppm NO and 8% O_2 (c) NO outlet concentration for NH_3 oxidation over Cu-ZSM-5 foam catalyst exposed over 250 ppm NH_3 and 8% O_2 (d) NO_2 decomposition reaction on Cu-ZSM-5 foam catalyst exposed over 250 ppm NO_2

150°C. Once NO saturation is obtained the loosely bound NO is removed by inert gas for 10 minutes. A temperature ramp of 14°C/min is applied at temperatures of 150°C. Figure 6.11a shows the NO uptake and NO outlet concentration during TPD. Initially, NO outlet concentration almost reaches the feed value which indicates weak adsorption of NO. NO desorbed during the temperature ramp is also very less and is obtained around 250°C [168].

$$3NO_2 + [CuO] -> Cu(NO_3)_2 + NO \tag{6.6}$$

$$Cu(NO_3)_2 -> 2NO_2 + [CuO] + 0.5O_2 \tag{6.7}$$

$$Cu(NO_3)_2 + NO -> 3NO_2 + [CuO] \tag{6.8}$$

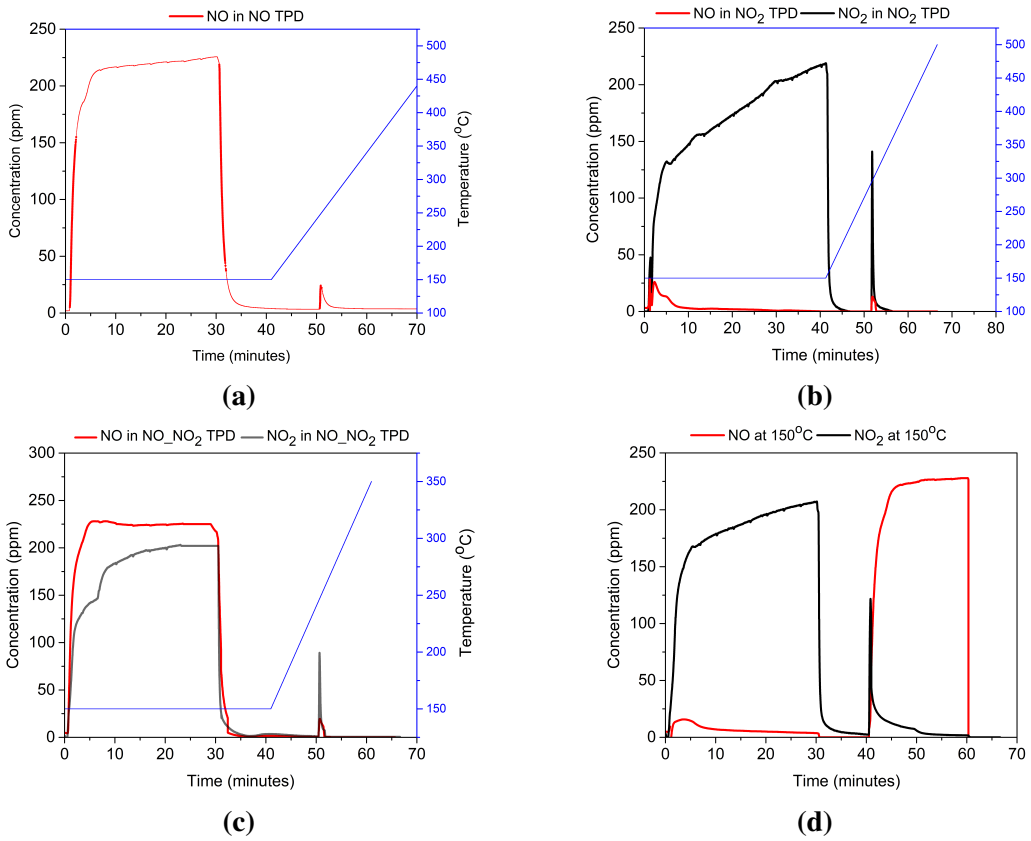

Figure 6.11: (a)NO outlet concentrations for NO TPD with a feed of 250 ppm NO at 150°C. (b) NO and NO_2 outlet concentrations for NO_2 TPD with a feed of 250 ppm NO_2 at 150°C. (c) NO, and NO_2 outlet concentrations for NO-NO_2 TPD with a feed of 250 ppm NO, 250 ppm NO_2 at 150°C. (d) NO and NO_2 outlet concentrations for 250 ppm NO_2 followed by 250 ppm NO at 150°C.

The storage capacity of NO_2 on the catalyst was investigated with 250 ppm of NO_2 and inert gas in the feed at 150°C followed by a temperature ramp of 10°C/min. The outlet concentration of NO and NO_2 is recorded. Figure 6.11b compares the NO and NO_2 outlet concentrations in NO_2 uptake and desorption experiments. During the temperature ramp, a large amount of NO_2 is observed, unlike NO TPD. The formation of NO during NO_2 adsorption is likely that the stores' species formed during the adsorption are nitrates bound to copper cations on copper dimers in the catalyst (Reaction 8). It is observed that the ratio of NO formed to NO_2 consumed is 1:3, which confirms the disproportionation reaction [169] [36]. The large amount of NO_2 of 142 ppm is released by the decomposition of these nitrates at a high temperature of 300°C shows high storage capacity of the catalyst and high thermal stability of formed nitrates by disproportionation reaction (Reaction 8.1). A small peak of NO observed during the temperature ramp confirms the decomposition

of NO_2. Since the temperature in the experiment is quite high, there was no adsorption of NO_2 on the weakly adsorbed sites. It is observed that a negligible amount of NO is absorbed by the Cu-ZSM-5 catalyst, whereas NO can be stored in the catalyst by oxidizing to NO_2 [170].

In order to understand the influence of NO on the storage of NO_2, a desorption study is conducted by adding NO along with NO_2 during the adsorption. 250 ppm NO and 250 ppm NO_2 with inert gas is allowed to adsorb on the catalyst for 30 minutes followed by TPD with a heating rate of 10°C/minute. Figure 6.11c shows the concentration of outlet NO and NO_2 during the TPD. It can be observed from Figure 6.11c that the amount of NO_2 desorbed during the TPD decreases significantly to 80 ppm in presence of NO. NO_2 adsorbed on the catalyst form nitrates whereas NO reacts with the formed nitrates, which in turn limits the storage of NO_2 in the presence of NO. It is observed that the nitrates were less stable in the presence of NO in the feed. It is also observed from the Figure 6.11c that it took some downtime for NO to reach the steady state during the uptake. The activity of NO in reducing surface nitrates is very strong even at low temperature of 50°C [171] [168]. The high reactivity of NO with nitrates at low temperatures has a strong influence on the stability of the nitrates formed during the adsorption of NO_2. The maximum decomposition rate is observed at 200°C in the presence of NO and 300°C in the absence of NO.

The influence of NO on the desorption of stored NO_2 is investigated at 150°C. The catalyst is initially saturated with 250 ppm NO_2 for 30 minutes. After the uptake, NO_2 feed is switched off and the sample is stabilized for 10 minutes with inert gas, then 250 ppm NO is introduced to the sample. The amount of NO and NO_2 in the outlet is monitored and recorded. It is observed from Figure 6.11d that NO_2 outlet concentration increases slowly to reach a steady state on adsorption. On the introduction of NO, a strong peak of NO_2 of 122 ppm is observed which is attributed to the decomposition of nitrates by NO (Reaction 8.2). There is a downtime of 5 minutes observed for NO to reach the feed concentration. NO reacts with stored NO_2 in the form of nitrates and releases NO_2.

6.5.3 Reactivity study : NO/NO_2–NH_3–O_2 reacting system

6.5.3.1 NO Feed (NO/NO_2 = 1/0)

In the transient experiments 250 ppm NH_3 was introduced to the reactor along with inert gas at 350°C. The feed ammonia is switched off once the catalyst is saturated with ammonia gas (1800sec). The inert gas is flowed over the catalyst to release loosely bound ammonia for 600 seconds. the feed with 250 ppm NO and 8%O_2 is then introduced to the reactor.

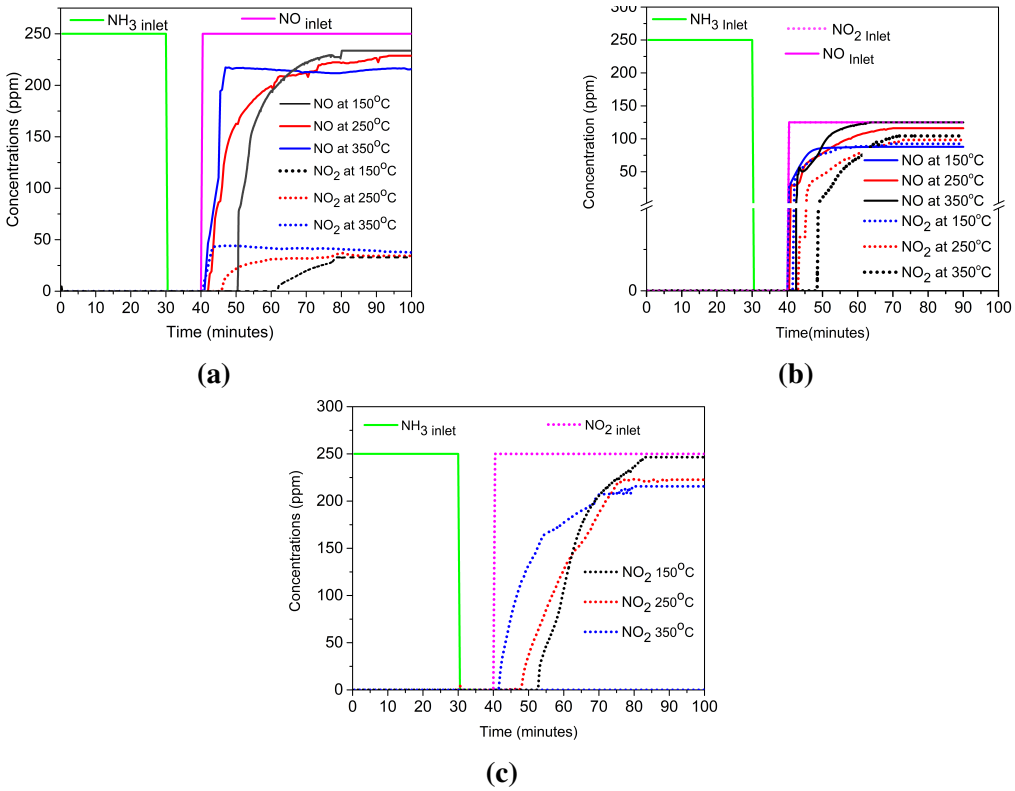

Figure 6.12: (a) NO and NO_2 outlet concentration for a feed of 250 ppm NO and 8% O_2 on 250 ppm preadsorbed NH_3. (b) NO and NO_2 outlet concentration for a feed of 125 ppm NO, 125 ppm NO_2 and 8% O_2 on 250 ppm preadsorbed NH_3. (c) NO_2 outlet concentration for a feed of 250 ppm NO_2 and 8% O_2 on 250 ppm preadsorbed NH_3.

The reactivity of NO on preadsorbed ammonia in the presence of O_2 is studied by passing 250 ppm NO and 8% O_2 onto the saturated catalyst with 250 ppm NH_3 . The transient response in the NO and NO_2 outlet concentrations are recorded as in Figure 6.12a. The Figure 6.12a shows NO concentration of 86 ppm at 50.5 minutes from the introduction of NO and O_2 gas at 150°C. It is observed that NO outlet concentration never reached the feed concentration because of No oxidation. NO oxidation begins at 62 minutes when most of the stored NH_3 is depleted. The NO outlet concentration reaches a steady state concentration of 235 ppm at 80 minutes of the study. The standard SCR reaction on the catalyst with the stored NH_3 duration was extended for 10.5 minutes on the introduction of NO and NO_2. At 250°C the NO concentration of 78 ppm is observed at 44 minutes of experiment with the steady-state concentration of 220 ppm at 73 minutes. NO_2 concentration is observed at 45 minute with the onset of NO oxidation. At 350°C NO concentration of 44 ppm is observed at 41 minutes of the experiment with a steady state value of 215 ppm observed at 45 minutes. NO oxidation onsets at 43 minutes of the experiment. The standard SCR

duration is 10.5 minutes, 4 minutes and 1 minute with NO reduction of 164 ppm, 172 ppm, and 206 ppm at 150°C, 250°C and 350°C respectively. The rate of standard SCR reaction increases with an increase in temperature. standard SCR reaction rate increases with an increase in temperature.

6.5.3.2 Equimolar Feed ($NO/NO_2 = 1/1$)

The reactivity of equal concentration of NO and NO_2 of 125 ppm and 8% O_2 over the NH_3 preadsorbed catalyst is studied in this experiment. Figure 6.12b shows the transient outlet NO and NO_2 concentrations. At 150°C, NO concentration of 56 ppm is observed at 42.5 minutes of the study which reaches a steady state concentration of 125 ppm at 61.5 minutes. NO_2 concentration is obtained at 49 minutes and reaches a steady state of 104 ppm at 72 minutes. At 250°C NO concentration of 33.25 is observed at 41 minutes which reaches the steady-state concentration of 116 ppm at 67.7 minutes. NO_2 concentration is observed at 44 minutes with a steady state concentration of 98 ppm at 67 minutes. At 350°C NO concentration of 27 ppm is observed at 40.5 minutes with a steady state concentration of 87 ppm at 48.2 minutes. NO_2 concentration is observed at 41.5 minutes and reaches a steady state of 92 ppm at 54 minutes. It is concluded that reactivity of NO_2 lasts for a longer duration as compared to NO. NO_2 outlet concentration appears in a later stage than that of NO concentration as shown in Figure 6.12b. It is also concluded that the SCR duration is almost the same for all the temperatures in the study. The presence of NO_2 enhanced the rate of consumption of preadsorbed ammonia compared to only NO in the feed. The SCR duration is 2.5 minutes, 1 minutes and 0.5 minute with NO reduction of 194 ppm, 217 ppm, and 223 ppm at 150°C, 250°C and 350°C respectively. The temperature has a less significant effect in fast SCR except at low temperatures of 150°C.

6.5.3.3 NO_2 Feed ($NO/NO_2 = 0/1$)

The reactivity of NO_2 with NH_3 in the presence of O_2 is studied by passing 250,ppm NO_2 and 8% O_2 over foam catalyst saturated with 250 ppm NH_3. The Figure 6.12c shows the NO_2 outlet concentration on preadsorbed NH_3. At 150°C NO_2 is observed at 53 minutes and reaches a steady state of 245 ppm at 67 minutes. At 250°C NO_2 is observed at 48 minutes and reaches a steady state of 225 ppm at 77 minutes. At 350°C NO_2 is observed at 42 minutes and reaches a steady state of 210 ppm at 80 minutes.The SCR duration extends to 13 minutes, 8 minutes and 2 minute at 150°C, 250°C and 350°C respectively.

6.5.3.4 Effects of feed gas composition in NH_3 SCR

6.5.3.5 Effect of NH_3 feed concentration

The effect of NH_3 feed gas concentration on SCR reaction is studied by varying its feed concentration from 100-500 ppm at an interval of 30 minutes. The concentration of NO is maintained at 250 ppm and O_2 at 8% with a feed flow rate of 1000 ml/min. Figure 6.13a shows the outlet concentrations of NO and NO_2 for different NH_3 feed concentration at a temperature of 200°C and 350°C.

Figure 6.13a shows that at 200°C, NO conversion of 60% is achieved for NH_3 feed concentration of 100 ppm. It is observed that an equal amount of NO is consumed with 100 ppm of NH_3, which reveals the dominance of standard SCR reaction. Increasing NH_3 feed to 200 ppm and 300 ppm increases NO conversion to 68% and 72% respectively. Further increasing NH_3 concentration in feed shows a slight decrease in NO conversion to 71% and 68%. This shows that an increase in NH_3 concentration inhibits the NO_x reduction in standard SCR. The Figure 6.13a shows that at 350°C the NH_3 inhibition is less evident. Therefore it can be concluded that NH_3 inhibition is high at 150°C than compared to 250°C.

6.5.3.6 Effect of NO feed concencentration

Effect of the NO concentration in the feed gas is studied over Cu-ZSM-5 foam catalyst with feed gas concentrations of 250 ppm NH_3, 100-500 ppm NO, and 8% of O_2 at 200°C and 350°C. NO concentration is maintained for 30 minutes at each concentration. Figure 6.13b shows the NO conversion for different NO feed concentrations. At 200°, it is observed from Figure 6.13b NO conversion achieved is 70% for NO feed concentration of 100 ppm. It is also observed that the NO conversion reduces to 64% and 58% with an increase in NO feed concentration of 200 ppm and 300 ppm respectively. On further increasing the NO feed concentration to 500 ppm the NO conversion reduces to 52%. At 350°C, NO conversion drops from 76% to 64% on increasing the feed NO concentration to 100 ppm to 300 ppm. Further increasing NO concentration decreases No conversion to 60% for 400 ppm NO feed and 56% for 500 ppm No feed. As the ammonia in the feed remains the same with an increase in NO feed concentration, NO reduces until the ammonia available for reduction is consumed beyond which NO oxidation dominates. NO concentration that exceeds ammonia concentration cannot be reduced.

6.5.3.7 Effect of O_2 feed concentration

The influence of O_2 concentration in the feed gas composition is studied by varying the concentration of O_2 from 4-12% for 30 minutes at each concentration while maintaining the concentration of other feed gases constant as 250 ppm of NO and 250 ppm of NH_3 at 200°C and 350°C. Figure 6.13c shows the outlet concentration of NO and NO_2 for different O_2 feed concentrations. At 200°C, the NO conversion with O_2 feed gas concentration of 4% in feed is 56%. The NO conversion decreases to 50% and 48% for feed O_2 concentration of 6% and 8% respectively. With the increase in feed O_2 concentration to 10%, the NO conversion reduces to 46% and on further increasing the feed to 12% the NO conversion reduces to 45%. At 350°C the NO conversion of 66% is achieved for 4% O_2 in the feed whereas the conversion is reduced to 65% for 12% O_2 in the feed. NO conversion slightly decreases with the increase in O_2 feed concentration. This more or less increase in NO conversion can be attributed to NH_3 scarcity for reaction due to NH_3 oxidation with the increase in O_2 concentration. The high rate of NH_3 oxidation leads to less availability of NH_3 gas for the reduction of NO.

6.5.3.8 Effect of NO_2 feed concentration

The effect of NO_2 concentration in feed composition is studied by varying the concentration of NO_2 from 100-500 ppm and by keeping 250 ppm NO, 250 ppm NH_3 and 8% O_2 as constant. Figure 6.13d shows the NO conversion with different NO_2 feed gas composition at 200°C and 350°C. At 200°C it is observed that the NO_2 conversion is 55% for a NO_2 feed concentration of 100 ppm which drops to 43% for 300 ppm feed. Thereafter with an increase in NO_2 feed concentration, NO conversion drastically decreases because of a lower NH_3/NO_x feed ratio and formation of ammonium nitrates. NO_2 is more reactive than NO with NH_3. At 350°C the NO conversion slightly drops from 62% for 100 ppm NO_2 in feed to 60% for 300 ppm NO_2 in feed. NO conversion drops on increasing NO_2 concentration as part of NO is reacted by fast SCR and the remaining NO_2 reacts by slow SCR.

6.5.4 Effects of NO_2/NO_x feed ratio

6.5.4.1 Effects of NO_2/NO_x feed ratio on NO oxidation

It is important to investigate the effect of the NO_2/NO_x feed ratio in NO oxidation as this reaction is the rate-determining step in standard SCR. The effect of NO_2/NO_x feed ratio in NO oxidation is studied at different temperatures of 150°C and 350°C with NO_2/NO_x

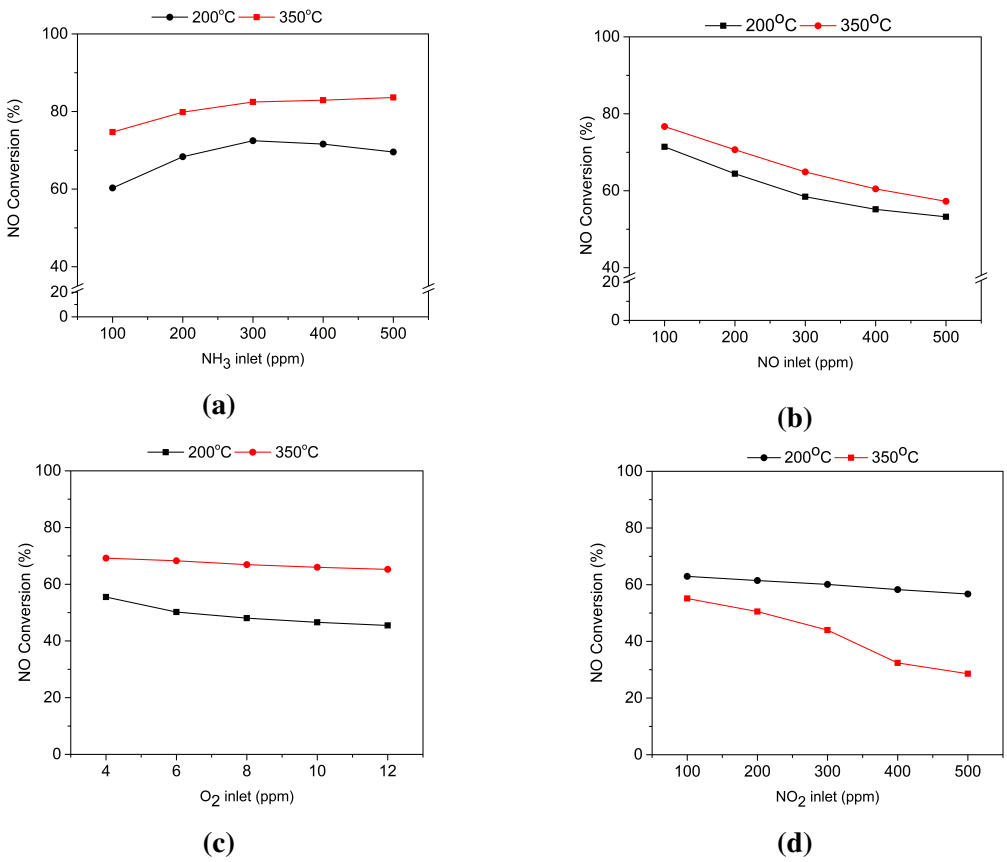

Figure 6.13: NO and NO_2 outlet concentrations at 200°C and 350°C for catalyst is exposed to feed concentration (a)100-500 ppm NH_3, 250 ppm NO, and 8% of O_2. (b) 100-500 ppm NO, 250 ppm NH_3, and 8% of O_2. (c) 4% - 12% of O_2. 250 ppm NO, and 250 ppm NH_3. (d)100-500 ppm NO_2, 250 ppm NO, 250 ppm NH_3, and 8% of O_2.

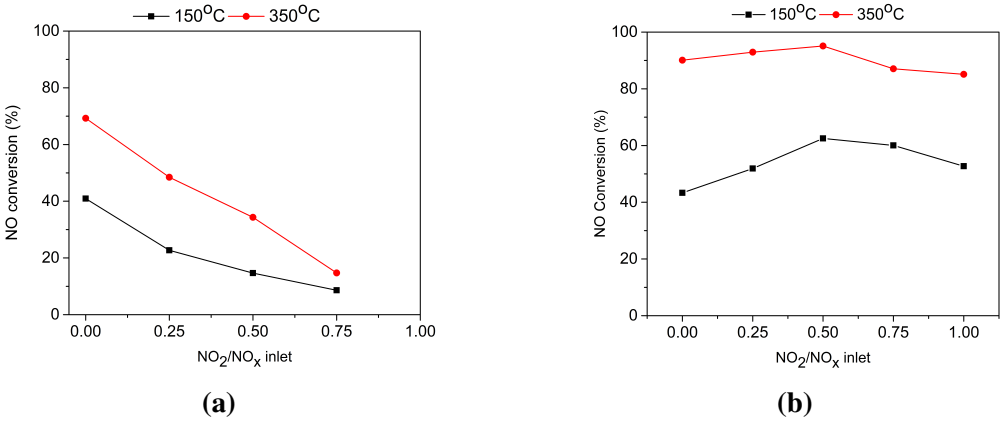

Figure 6.14: Effect of NO_2/NO_x feed ratios on (a) NO oxidation at 150°C and 350°C (b) Standard SCR at 150°C and 350°C

ratio varied from 0 to 0.75 by keeping NO_x concentration as 250 ppm. The NO conversion for different NO_2/NO_x feed ratios at 150°C is shown in Figure 6.14a. It is evident from the Figure 6.14a that increasing NO_2/NO_x ratio decreases NO oxidation. For pure NO feed, 40% NO is oxidized to NO_2, with the introduction of 62.5 ppm NO_2 in the feed NO oxidized reduces to 22%. It is observed that an increase in the NO_2/NO_x ratio above 0.5 leads to a further decrease in NO oxidation to 14% which is attributed to disproportionation reaction (Reaction:8) as evidenced by TPD studies. We can infer that nitrate formed by NO_2 adsorption blocks NO oxidation on increasing NO_2 concentration. The inhibition of NO oxidation by NO_2 is more pronounced beyond the NO_2/NO_x ratio of 0.5. NO_2 inhibition on NO oxidation reaction can be due to competitive adsorption of NO_2 and blockage of NO oxidation sites. NO_2 is strong oxidizing agent than O_2 and can oxidize the metal sites and prevent the adsorption of O_2 [172] [173] [174]. The Figure 6.14a shows the NO oxidation at 350°C for NO_2/NO_x ratio from 0 to 0.75. It is evident from the figure that at 350°C for a pure NO feed, about 70% NO is oxidized which is higher than that at 150°C. With the introduction of 62.5 ppm NO_2, NO oxidation reduces to 48.5%. At 350°C NO oxidation follows the same trend as that of 150°C with NO_2/NO_x ratio but with higher NO oxidation. We can infer that the nitrates deposited on NO oxidation sites get decomposed at a higher temperature of 350°C.

6.5.4.2 Effects of NO_2/NO_x feed ratio on standard SCR

The effect of NO_2/NO_x feed ratio on standard SCR is investigated with 250 ppm NH_3, 8% O_2 and 250 ppm NO_x. The NO_2/NO_x ratio is varied from 0 to 1 at an interval of 30 minutes at a temperature of 150°C and 350°C. The Figure 6.14b shows NO conversion at different NO_2/NO_x ratio. At 150°C, for pure NO feed, 42% of NO is reduced whereas with increasing the NO_2 concentration to 62.5 ppm NO conversion increases to 50%. The NO conversion further increases to 62% with an increase in the NO_2/NO_x feed ratio to 0.5. It is observed that the NO conversion decreases with further increases of the NO_2/NO_x ratio above 0.5. This decrease in NO conversion is due to the deposition of nitrates on active sites by disproportionation reaction, which blocks NO oxidation, which is the rate-determining step in standard SCR. The Figure 6.14b shows a NO conversion of 90% for NO_2/NO_x ratio of 0 at 350°C which is higher than at 150°C. For NO_2/NO_x ratio of 0.25, NO conversion achieved is 92% which increased to 95% for NO_2/NO_x ratio of 0.5. The increased NO reduction at high temperatures is due to the decomposition of nitrates deposited in the active sites.NO following the same trend of decreased conversions for NO_2/NO_x ratio above 0.5 as that at 150°C but with higher conversions.

In the presence of excess NH_3, NH_3 blocks the adsorption of NO on the Cu sites through an oxygen atom and reduces $DeNO_x$ activity. Cu ions are heavily ligated with NH_3 at a low-temperature regime. Therefore excess ammonia blocks the reoxidation of the redox sites and prevents NO oxidation, which is the rate-limiting step in Standard SCR (5.7), (5.6) [219] [220]. Standard SCR reaction by oxidative adsorption of NO with stronger non dissociative adsorption of NH_3 on Cu sites is reported on Cu-ZSM-5, Cu-SAPO-34 and Cu-SSZ-13 [221] [222] [223]. There is a possibility of adsorption of excess ammonia on the already adsorbed sites forming dimeric species at high ammonia coverages and may block activation of NH_3 and its interaction with NO, which may suppress the SCR activity.

6.6 Summary

Self-supporting Cu-ZSM-5 foam catalyst is prepared through emulsion method using HVO as the oil phase and Cu-ZSM-5 slurry as the water phase.The prepared self supporting Cu-ZSM-5 have high compressive strength of 0.4 MPa. The surface area of the foam is 340m^2/g with a mesoporosity of 48 nm. The Cu-ZSM-5 foam catalyst could achieve a lewis acidity of 225μmol/g and bronsted acidity of 79μmol/g. The distribution of Cu species from XPS analysis gives the ratio of isolated Cu^{2+} to CuO formed to be 0.79.

The tortuous path of the flow in foam catalysts increases the mixing and enhances the external mass transfer of the pressure drop. A higher flow rate leads to the reduction of the boundary layer thickness and contributes to better mixing. This reduces the resistance of mass transfer and promotes the transport of more reactants to the surface.

The interaction of reactant NO_x gases with Cu-ZSM-5 is studied by adsorption and temperature-programmed desorption. NO_x adsorption and TPD studies concluded that NO can be stored in the catalyst by oxidizing to NO_2 as a negligible amount of NO is absorbed by Cu-ZSM-5 catalyst, whereas NO_2 can be stored in the form of nitrates. The high reactivity of NO with nitrates at low temperatures has a strong influence on the stability of the nitrates formed during the adsorption of NO_2. The desorption of nitrates is observed at 200°C in the presence of NO and 300°C in the absence of NO. The reactivity of NO and NO_2 on the preadsorbed NH_3 in the presence of O_2 at different temperatures elucidates the fast dynamics of SCR chemistry. The study reveals a high rate of reaction at a high temperature of 350°C over a short duration of time. The reactivity of NO on preadsorbed NH_3 in the presence of O_2 decreases with an increase in temperature whereas the reactivity of equimolar NO and NO_2 has a less significant impact on temperature. The reactivity of NO_2 on preadsorbed NH_3 in the presence of O_2 decreases with an increase in temperature.

An investigation of the effect of reactant gases on standard SCR reveals that an increase in NH_3 concentration in feed decreases NO_x reduction. At low-temperature NH_3 in the feed gas inhibits SCR reaction and complicates the SCR catalyst design in automotive applications. In standard SCR excess NH_3 blocks the adsorption of NO on Cu sites through an oxygen atom and reduces DeNO_x activity. It is also inferred that NO concentration that exceeds the NH_3 feed concentration cannot be reduced. Increasing O_2 concentration in feed increases NO_x reduction. The study on the effect of NO_2/NO_x ratio on NO oxidation concludes that nitrates formed on increasing NO_2 concentration block NO oxidation which is the rate-determining step in standard SCR at low temperatures, whereas the deposited nitrates get decomposed at a higher temperature of 350°C and increase the NO_x reduction.

Chapter 7

Numerical analysis of mixing chamber non-uniformities and feed conditions for optimal performance of urea SCR

7.1 Introduction

The combustion of automobile fuels produces a substantial amount of gases, such as CO, CO_2, NO_x, Hydrocarbon, and SO_2. These gases pose a huge threat to the environment and must be turned harmless before venting into the atmosphere. The US Environmental Protection Agency has incorporated certain policies to minimize the emission of these gases, paving the way for the development of exhaust after-treatment systems for automobiles. Exhaust after-treatment along with inline cylinder NO_x control is required to meet emission standards. NO_x emission standards have become stringent over the past few decades, leading to research on new NO_x reduction technologies. NO_x is formed by the reaction between N_2 and O_2 during the combustion process at an elevated temperature of about 1100°C. Selective Catalytic Reduction (SCR) is an effective technology for NO_x emission control applications globally in response to increasing NO_x emissions from industries, marine applications, and automobiles. Liquefied ammonia is used directly for selective catalytic reduction in stationary industrial applications, but it poses difficulties in terms of storage, transportation, handling, and toxicity in automobile installations. Urea, which can directly produce ammonia, is chosen as a precursor due to its ease of storage and low-cost [10]. In automobile applications, urea-water solution-based SCR is a promising technology for NO_x reduction [11]. The urea–water solution sprayed into the hot exhaust stream breaks down into smaller droplets, and the turbulent exhaust gas flow heats these

droplets. The urea-water solution evaporates to form gaseous urea, which undergoes thermal decomposition to ammonia and isocyanic acid in the mixing chamber. Isocyanic acid is hydrolyzed to produce ammonia and CO_2 [12]. The produced ammonia undergoes a catalytic chemical reaction to reduce NO_x in the catalytic convertor. The distribution of ammonia at the inlet of the catalytic converter is a crucial criterion, as ammonia acts as a reducing agent in NH_3 SCR. The main challenges in the urea water solution injection system are the incomplete decomposition of urea and uniform distribution of ammonia upstream of the SCR unit. Certain studies [13, 14] reported that these challenges can be resolved to an extent by using mixers of different designs and by optimizing the dimensions of the mixing chamber so that the spray mixture achieves sufficient mixing and reaction time before entering the SCR unit. The performance of an SCR system depends on the nature of flow and the heat and mass transfer between the spray droplets and exhaust gases.

Urea water multicomponent spray processes involve many physical models, including droplet gas interactions, spray wall interactions, liquid wall film formation, and finite rate chemistry. In exhaust systems where the injection is not assisted by an atomizer, the impingement of droplets on the mixing chamber surface cannot be neglected owing to slow evaporation, thermolysis, and high droplet inertia. The physical mechanisms during the interaction of a spray with a wall are influenced by the droplet, fluid, and surface properties. A droplet that reaches the wall is assumed to undergo any of the following processes: it can attach to the wall in a spherical form, reflect elastically, or move tangentially along the wall with the same velocity before the impact [242]. It could attach to the wall in spherical form, it could reflect elastically, or it could move tangentially along the wall with the same velocity before the impact [242]. The droplets interact with the wall, transfer momentum, and break down into smaller particles. It can join the liquid film, which provides a longer residence time for vaporization and mixing. Therefore, the spray wall interactions and liquid film walls play a significant role in enhancing ammonia distribution. The effect on the spray wall interaction and liquid film walls is related to the evaporation and decomposition of urea droplets in the hot exhaust gas and was first modeled by Birkhold et al. [11].

Rapid Mixing (RM) model, Diffusion Limit (DL) model, and Effective Diffusion (ED) model are the proposed approaches for the evaporation of water and urea in the droplet. The RM model represents infinitely fast transport, and the DL model represents purely diffusive transport. The real characteristics of the droplet lie within these limits. The RM model approach assumes a constant temperature and species concentration throughout the droplet at a given instant of time. Birkhold et al. suggested that the RM model evaporation is accurate and requires less computational effort than the DM model [243]. Many

reviews on the decomposition temperature of urea have been reported, ranging from 407 to 533K [244–246]. These models assume that the urea-water solution evaporates and decomposes directly into NH_3 and HNCO. Frobert et al. [247] studied the effect of ammonia formation and distribution with factors such as exhaust gas temperature, mass flow rate, and NO_2 to NO_x ratio in the mixing chamber. Abidin et al. [10] studied the effect of the distance between the injector and SCR inlet on ammonia generation, uniformity index, and Ammonia to NO_x ratio.

The literature reveals several 1D kinetic models for NH_3-based SCR in monolithic reactors based on a single-channel assumption. Chatterjee et al. [152] developed a kinetic model for titania-vanadia catalyst, which was validated using experimental data from diesel engine bench tests. Their model showed that the reduction efficiency of NO_x increases in the presence of NO_2 in the feed. Olsson et al. [35] developed a kinetic model for a Cu-ZSM-5 catalyst and estimated the kinetic parameters by performing experiments for a wide range of operating conditions. Pant and Schmieg [153] examined the performance data of a Cu-ZSM-5 catalyst, which showed a reduction in NO_x conversion due to NH_3 oxidation at high temperatures. To account for this behavior, they suggested that the rate expressions in the model given by Olsson et al. [154] for the standard SCR reaction and the ammonia oxidation reaction should be second order in the NH_3 concentration. A combination of the models given by Olsson et al. [34] and Wang et al. [155] was proposed by Metkar et al. [156], which considers the effect of washcoat diffusion. They studied the activities of dual-layered Cu and Fe-zeolite catalysts. They found a higher performance for a broader range of operating conditions in dual catalysts than in individual catalysts. These models assume uniform flow, temperature, and concentration distributions in the mixing chamber. These assumptions may not be applicable in actual SCR design because of the inherent nonuniformity introduced by urea injection and decomposition [10]. Paramadayalan et al. [248] studied the effects of radial variation in flat and parabolic inlet ammonia profiles on the SCR emission performance at different temperatures.

7.2 Mathematical Formulation

This section discusses the urea SCR system modeling, which includes the urea mixing chamber and SCR converter. The first subsection discusses the 3D discrete phase mathematical modeling of the mixing chamber. In the subsequent subsection, we address 2D axisymmetric modeling of the SCR converter using a porous medium approximation.

7.2.1 Urea mixing chamber

The sprayed urea water solution (UWS) is heated by hot exhaust gas, and the droplets evaporate and decompose to form ammonia and isocyanic acid. The injected urea mass flow is extremely small, and the volume fraction of the UWS droplet to exhaust gas is expected to be small (<10%), which is a sufficient condition for using the discrete phase model [249]. The droplets are tracked by a discrete phase in a Lagrangian frame of reference, and the exhaust gas stream is tracked by a continuous phase in the Eulerian frame of reference. A rapid mixing model was used for the evaporation of droplets with the assumption of uniform spatial temperature, concentration, and fluid properties in the droplet, which only changes with time. The time variation of urea concentration of the droplet can be evaluated by

$$\frac{dY_u}{dt} = -\frac{(dm_{vap}/dt)}{m_p} Y_u \tag{7.1}$$

The rate at which the mass of the liquid in the droplet decreases is equal to the rate at which it vaporizes from the droplet surface. The convective flow of the evaporating material from the droplet surface to the bulk gas phase (Stefan flow) is important for achieving higher vaporization rates. The multicomponent droplet vaporization rate of the UWS was calculated as the sum of the vaporization rates of urea and water [250]. Convection-diffusion-controlled mass exchange was modelled at the interface. The rate of mass transfer of the evaporating material from the droplet surface to the bulk gas when the total vapour pressure at the droplet is less than the computational cell pressure is given by

$$\frac{dm_i}{dt} = K_C A_p \rho_i \ln\left(1 + B_{m,i}\right) \tag{7.2}$$

where

$$Sh = \frac{K_C\, d_p}{D_{i,m}} = 2.0 + 0.6\, \mathrm{Re}_d^{1/2}\, Sc^{1/3} \tag{7.3}$$

$$B_{m,i} = \frac{Y_{BL} - Y_G}{1 - Y_{BL}} \tag{7.4}$$

The mass transfer coefficient and Spalding mass number for species i were calculated using Eq. (7.3) and Eq. (7.4). The diffusion coefficient is defined based on the unit Lewis number.

When the total vapor pressure at the droplet surface exceeded the cell pressure, the

multicomponent droplet was in the boiling regime. The boiling rate equation is

$$\frac{dm_i}{dt} = x_i \frac{\pi d_p \lambda}{C_P} \left(2 + 0.6 \mathrm{Re}_d^{1/2} \mathrm{Pr}^{1/3}\right) \ln\left(1 + B_{T,i}\right) \tag{7.5}$$

where $B_{T,i}$ is the Spalding heat transfer number for species i given by

$$B_{T,i} = \frac{C_P \left(T_G - T_p\right)}{h_{\text{vap},i}} \tag{7.6}$$

Equation (7.5) yields the mass transfer rate for the boiling law.

$$m_p C_P \frac{dT_p}{dt} = h A_p \left(T_G - T_p\right) + \sum_i \frac{dm_i}{dt} \left(h_{vap,i}\right) \tag{7.7}$$

$$Nu = \frac{h d_p}{\lambda} = 2.0 + 0.6 Re_d^{1/2} Pr^{1/3} \tag{7.8}$$

The energy equation for a multicomponent particle obtained by neglecting the radiation heat transfer is given by Eq. (7.7), the heat transfer coefficient can be evaluated from the correlation of the Nusselt number, as given by Eq. (7.8).The heat transfer coefficient can be evaluated from the correlation for the Nusselt number as given by Eq. (7.8). Convective transport is considered by a modified Sherwood and Nusselt number using the Ranz-Marshall correlations [251]. The heat and mass lost or gained by the particle are considered as a source or sink in the continuous phase energy equation.

The vapor pressure of water is much higher than that of urea, which leads to the rapid evaporation of water from the UWS droplet. The saturation pressures for urea and water were calculated from the correlations given by Birkhold et al. [252] and Tetens [253], respectively:

$$\begin{aligned} p_{\text{sat,water}} &= 610.78\, e^{17.2694(T_p - 273.16)/(T_p - 35.86)} \\ p_{\text{sat,urea}} &= e^{29.9548 - (10876.1/T_p)} \end{aligned} \tag{7.9}$$

The total vapor pressure is computed as the sum of the partial pressures of the component i.

$$P_t = \sum P_i \tag{7.10}$$

Raoult's Law

$$C_{i,s} = \frac{p_i}{RT_G} = \frac{x_i p_{sat,i}}{RT_G} \tag{7.11}$$

The droplet interacts with the gas flow through the drag force and breakup owing to aerodynamic forces, modeled according to the correlation given by Reitz and Diwaker [251].

7.2.2 SCR converter

The transport of momentum, energy, and chemical species occurs in the stream wise and radial directions. The reactants diffuse and are adsorbed on the catalyst coated on the inner channel wall of the monolith. The reaction occurs on the surface of the inner wall, and the products are desorbed and diffused back into the bulk flow. A heterogeneous model with a porous-medium approximation was used to replicate the SCR in the monolith. The conservation equations for mass and energy in solid and fluid phases are given as follows: The fluid-phase mass balance for species i

$$\epsilon\rho_G\frac{\partial Y_{G_i}}{\partial t} = -\rho_G\overrightarrow{v}.\nabla Y_G + \nabla.(\epsilon\rho_G D\nabla Y_G) - \rho_G S_V K_C(Y_{G_i} - Y_{BL_i}) \tag{7.12}$$

Solid phase mass balance

$$0 = \rho_{BL}S_V K_C(Y_{G_i} - Y_{BL_i}) + S_{VC}\dot{S}W \tag{7.13}$$

Fluid phase energy balance

$$\epsilon\rho_G C_P\frac{\partial T_G}{\partial t} = -\rho_G C_P\overrightarrow{v}.\nabla T_G + \nabla.(\lambda\nabla T_G) - S_V K_T(T_G - T_S) \tag{7.14}$$

Solid phase energy balance

$$(1-\epsilon)\rho_{BL}C_{pBL}\frac{\partial T_S}{\partial t} = \nabla.(\lambda_S\nabla T_s) + S_V K_T(T_G - T_S) - S_{VC}\left(\sum_{k=1}^{N_{SP}} h_k\dot{S}_k\right) \tag{7.15}$$

The ideal gas law relating to the state properties completes the mathematical model of the system under investigation. All thermodynamic and transport properties of the gas were estimated as a function of the local temperature and composition. The bulk mass balance contains the terms for accumulation, convection, axial diffusion, and flux from the bulk to the surface for the molecular species NH_3, NO, NO_2, O_2, H_2O, and N_2.

7.3 Numerical Methodology

7.3.1 Urea mixing chamber model

This study attempts to investigate the effect of non-uniformity from urea water solution injection and decomposition of urea at the SCR inlet on the performance of the catalytic

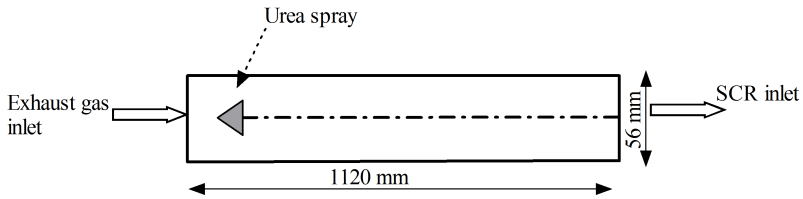

Figure 7.1: Schematic diagram of urea mixing chamber

converter. The urea–water solution injected into the hot exhaust gas atomizes the droplet, evaporates, and decomposes to form ammonia and isocyanic acid. The computation domain of the mixing chamber shown in Figure 7.1 with a diameter of 56 mm and a length of 1120 mm has 8,70,500 mesh elements. The urea-water solution was injected conically at a 20°C cone angle at the axis of the tube with an injection velocity of 10.6 m/s and a flow rate of 1×10^{-4} kg/s [11]. A hollow cone of six droplet streams with a Rosin-Rammler distribution having a mean distribution of 44 microns with a spread of 3.27 are used as the spray characteristics. The injection parameters used in the simulation of the urea mixing chamber are listed in Table 7.2. The nonuniformity at the exit of the urea mixing chamber was used as the inlet feed for the NH_3 SCR. The analysis was performed at two different urea decomposition temperatures: 486K and 523 K. The urea decomposition reactions and kinetic parameters are listed in Table 7.1.

Table 7.1: Kinetic parameters for Urea decomposition

Reactions	Rate kmol/m^{3}s	A	E_a (J/kmol)
Thermolysis			
NH_2CONH_2->NH_3+HNCO	$A_1 e^{-\frac{E_1}{RT}} C_{\text{Urea}}$	2.0×10^3	2.3×10^7
Hydrolysis			
HNCO+H_2O->NH_3+CO_2	$A_2 e^{-\frac{E_2}{RT}} C_{\text{HNCO}}$	2.5×10^5	6.2×10^7

SCR converter model

A steady-state two-dimensional geometry with an axisymmetric assumption was used to model a 3.3-liter catalytic converter. The computational domain is shown in Figure 7.2 and is divided into the inlet cone region, porous region, and outlet cone region, and contains 1,17,312 mesh elements. The governing equations are numerically integrated over an elemental volume that contains both fluids and solids [248]. The resistance coefficients in the

Table 7.2: Injection parameters for spray simulations

Injection velocity (m/s)	10.6
Injection temperature (K)	300
Injection cone angle (degrees)	20
UWS mass flow rate (kg/s)	0.0001
No. of particle streams per injection	6
Spread parameter for distribution	3.27
Mean droplet diameter (mm)	0.044
Total number of droplet diameters	10

directions perpendicular to the flow were increased by three orders of magnitude to reproduce the actual case of flow-through straight parallel channels. A 400 CPSI monolith was considered, with a geometric surface to volume ratio of 2727 m^2/m^3. The corresponding hydraulic diameter for monolith channels was 1.1 mm [248]. The 7-step kinetic model proposed by Olsson et al. [154] was adopted to study the chemistry of the urea SCR reaction, as shown in Table 7.3. Urea decomposition reactions are not included in the SCR mechanism and should be considered in future work. The surface reactions were modeled

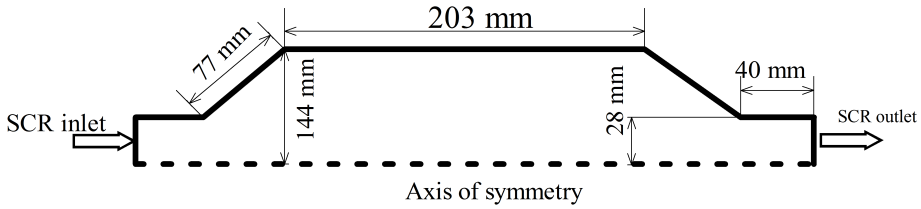

Figure 7.2: Schematic diagram of the axisymmetric catalytic converter.

Table 7.3: Urea SCR reaction mechanism proposed by Olsson et al. [35]

Urea SCR Reactions	Rate (kmol/m^2s)
NH_3+S1<=>NH_3-S1	$k_{1f}C_{NH_3}\theta_{S1-vacant}$ -$k_{1b}\theta_{NH_3-S1}$
2NH_3-S1+3/2O_2 => N_2+3H_2O+2S1	$k_2C_{O_2}\theta_{NH3-S1}$
NO+0.5O_2<=>NO_2	$k_{3f}C_{O_2}^{1/2}C_{NO}$ -$K_{3b}C_{NO_2}$
4NH_3-S+4NO+O_2 = >4N_2+6H_2O+4S1	$k_4C_{NO}\theta_{NH3-S1}$
2NH_3-S1+NO+NO_2 = >2N_2+3H_2O+2S1	$k_5C_{NO}C_{NO_2}\theta_{NH3-S1}$
4NH_3-S1+3NO_2 = >3.5N_2+6H_2O+4S1	$k_6C_{NO_2}\theta_{NH3-S1}$
2NH_3-S1+2NO_2 = >N_2+N_2O+3H_2O+2S1	$k_7C_{NO_2}\theta_{NH3-S1}$

by considering laminar finite-rate chemistry and turbulence interaction. Non-isothermal

simulations were performed, and heat loss was considered from the non-catalytic outer walls of the converter, for which the heat loss coefficient was 20 W/m^{2}K for the cone region and 10 W/m^{2}K for the monolith region [248]. A velocity-inlet boundary condition from the mixing chamber was defined. At the outlet, a pressure outlet boundary condition was imposed, with the value set to atmospheric pressure. The operating parameters for the catalytic converter simulations are summarized in Table 7.4. The single-channel model assumes that each channel in the monolith is identical to any other channel. Thus, channel-level simulations are sufficient to capture the performance of a catalytic converter. Steady-state simulations were performed with an inlet feed consisting of NH_3 from the mixing chamber with equal amounts of NO_x, 5% O_2 and 8% H_2O. The more favorable reaction is a fast SCR reaction, which requires a NO_2/NO_x ratio of 0.5. Simulations were carried out for a non-uniform profile from the mixing chamber and a uniform profile at the SCR inlet. The SCR performance was evaluated at operating temperatures of 486 and 523 .

Table 7.4: Operating parameters for catalytic converter simulations

Geometry and operating parameters	
Monolith length (m)	0.203
Monolith diameter (m)	0.144
Cell density (CPSI)	400
Channel diameter (mm)	1.1
Porosity	0.7
S/V ratio (m^2/m^3)	2727
Inertial resistance coefficient, C1 (m^{-1})	20.414
Viscous resistance coefficient, C2 (m^{-2})	3.846 x 107
Heat loss coefficient, h_{ext} (W/mK)	10 (monolith)
	20 (cone)
Ambient temperature, T_{amb} (K)	300

Solver parameters and details

The simulations for the mixing chamber and catalytic converter were performed independently using ANSYS FLUENT 19 software. The film formation on the walls of the mixing chamber by the UWS spray interaction is neglected under the assumption that the wall is at a temperature higher than the boiling point of the UWS. The spray wall interaction is considered by specifying an escape boundary condition at the walls. A two-step volumetric reaction models urea decomposition using a laminar finite rate that interacts with turbulence and chemistry. The droplet trajectories were captured using a fourth-order Runge-Kutta method. A realizable k-ϵ model with a standard wall function was used to model the turbulence. A coupled scheme was used to solve the pressure–velocity coupling. The

second-order upwind scheme solves momentum, turbulence, and species transport equations. The residual convergence criterion for the continuity, momentum, turbulence, and species energy equations is 1×10^{-6}.

Steady-state two-dimensional axisymmetric simulations of the catalytic converter were performed. A second-order upwind discretization scheme was used to solve the momentum, energy, species, and turbulence transport equations. The SIMPLE scheme was used for pressure-velocity coupling, and under-relaxation factors with default values were used. A porous-medium approximation was used to model the monolith reactor. The porous medium formulation was defined in terms of the porosity and porous resistance coefficients. The turbulence in the catalytic converter was modeled using the two-equation k–ω SST model.

The properties of the materials were determined using built-in calculation methods. For individual species, the specific heat was calculated using piecewise polynomial fits, whereas the thermal conductivity and viscosity were calculated using kinetic theory. The properties of the gaseous mixture were determined using the mass-weighted mixing law, and the mass diffusivity was calculated using the kinetic theory. The density and specific heat of the droplet mixture were calculated using the volume-weighted and mass-weighted mixing laws, respectively. For urea and water in the liquid phase, the density was assumed to be constant, and the specific heats were calculated using piecewise polynomial fits.

All the solution parameters monitored remained constant for a sufficient number of iterations, and the energy residual dropped by at least six orders of magnitude. In comparison, all other residuals decreased by at least three orders of magnitude. All results discussed were checked for grid independence.

Model validation

The experimental results of the Kim et al. [254] and Birkhold et al. [11] models were used to validate the urea mixing chamber. Table 7.5 gives the operating parameters used in the validation test case for spray in the urea mixing chamber

The exhaust gas is treated as a continuum and modeled using the Navier-Stokes equations. In contrast, the injected urea-water solution is treated as a dispersed phase by tracking a large number of droplets through the flow field. The dispersed phase exchange momentum, mass, and energy with the exhaust gas flow field [77]. We define ammonia conversion as the molar flow rate of ammonia produced in the reaction to the theoretical ammonia

produced from the injection of UWS.

$$\text{Ammonia conversion } (\%) = \frac{F_{\mathrm{NH_3,out}}}{2F_{\mathrm{urea,in}}} \times 100 \tag{7.16}$$

The residence time depends on the exhaust gas velocity and the length of the mixing chamber. It represents the time for the injected urea to get processed in the mixing chamber. The parameter uniformity index defines the degree of uniformity of ammonia concentration at the exit of the mixing chamber. The uniformity index of 1 indicates a uniform distribution of ammonia.

$$\text{Uniformity Index } = 1 - \frac{1}{2\left|C_{\text{avg}}\right| A_c} \int_{\Omega} \left|C - C_{\text{avg}}\right| d\Omega \tag{7.17}$$

where C_{avg} is the average concentration of ammonia obtained at various UWS flow rate, exhaust gas velocity, and temperature and is given by

$$C_{\text{avg}} = \frac{1}{A_c} \int_{\Omega} C d\Omega \tag{7.18}$$

The mixing chamber validation studies is as shown in Figure 7.3. Figures 7.3a and 7.3b show the comparison of the results of the present simulation model with those of Kim et al. and Birkhold et al. models, respectively. It can be seen that the amount of ammonia produced increases with a decrease in exhaust gas velocity due to increases in the residence time. The ammonia production also shows an increase with the rise in temperature, at all velocities, due to an improved rate of thermolysis reaction. The steep increase of ammonia at the entrance of the mixing chamber and a constant ammonia production after a particular length of the mixing chamber shows that an optimum mixing length exits for the mixing chamber. The present simulation model accurately replicates the results at the temperature of 573 K, whereas for the temperatures 623 K, and 673 K, the simulation results are under-predicted by this model. This variation arises from the mismatch in the activation energy range used for the validation study.

The reliability of the SCR kinetics used in this study is ensured by comparing the kinetic model with two sets of experimental data from the literature. The single-channel approximation was used for the validation study of the SCR converter. The operating conditions for the simulations are summarised in Table 7.6.

The model is able to predict the experimental data of Metkar et al. [156] and T. Paramadayalan et al. [153] [248] reasonably good as shown by Figure 7.4. The kinetic model is

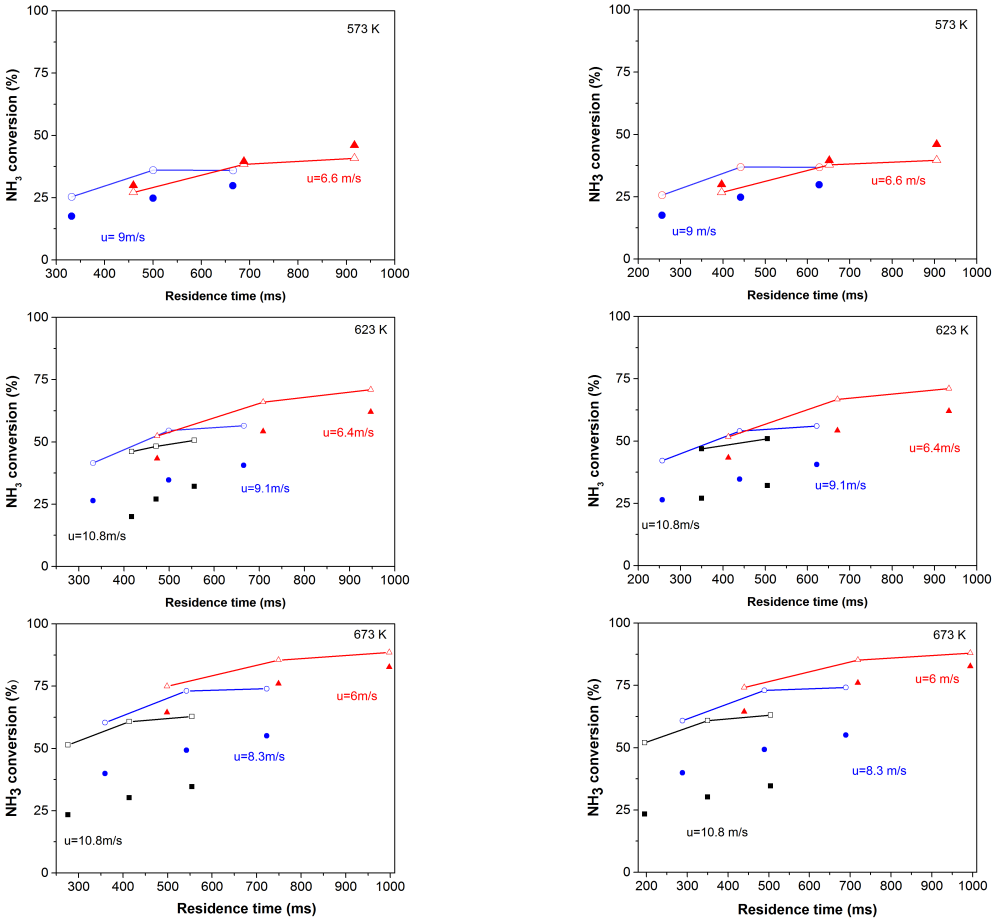

(a) Validation of present simulation model (scatter) against Kim's model (lines).

(b) Validation of present simulation model (scatter) against Birkhold model (lines).

Figure 7.3: Validation of urea water solution injection in mixing chamber

Table 7.5: Operating parameters for spray validation

Parameter	Kim et al. [254].	Birkhold et al. [11]
Length (m)	6	6
Diameter (m)	0.3	0.3
Cone angle (degree)	70	70
Urea flow rate (cc/min)	18	10
Injection velocity (m/s)	10.6	10.6
Activation energy (J/mol)	2.94×10^{7}	6.9×10^{4}

Table 7.6: Operating parameters for kinetic model validation

Parameter	Metkar et al. [145]	Pant et al. [153]
Dimension of catalyst length (mm)	20	30
Diameter (mm)	25.4	22
CPSI	400	400
Number of channels	34	188
Flow rate	57000/h	18400/h
Concentration NO (ppm)	500	500
NH_3 (ppm)	500	500
O_2 (%)	5	8
H_2O (%)	2	5

a single site mechanism and the activation energy for desorption is considered as coverage dependent. The monolith has a large amount of NH_3 adsorbed on the catalyst active site initially. The conversion of NO_x is around 100% at exhaust gas temperature of 473 - 573 K. The conversion of NO_x decreases at around 623 K due to rapid ammonia oxidation, which reduces ammonia available for NO_x reduction. At lower temperatures, the NO_x conversion is limited due to the lower rate of reaction. NO conversion is higher at a lower temperature due to NO oxidation to NO_2. The NO_2 conversion increases as the temperature increases with maximum conversion observed at around 623 K. The NO_2 decomposition occurs beyond this temperature. Therefore it is observed that NO_x reduction is highest at 523 K and then gradually decreases with temperature as reported by L.Olsson et al. [35]

7.4 Results and Discussion

The non-uniformity in ammonia distribution arising from the mixing chamber due to the factors like the location of urea injector, the temperature of exhaust gases and the residence time, influences the NO_x reduction in the SCR. An insight into the effect of non-uniformities in flow, concentration, and temperature from the mixing chamber on NO_x reduction in monolith SCR reactor has to be investigated to optimize operating parameters

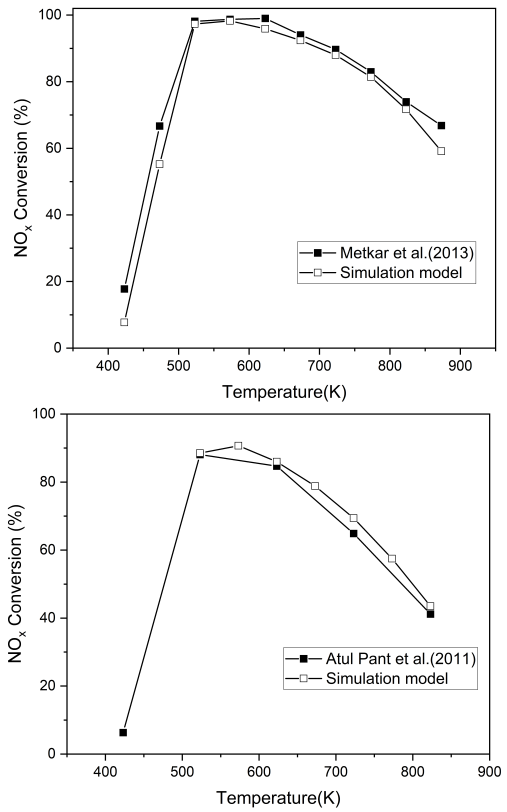

Figure 7.4: Validation: NO_x conversion for different inlet operating temperature.

of the injector and mixing chamber. In the present study, we optimize the injector flow rate and mixing chamber operating conditions to obtain higher ammonia conversion and uniform flow distribution with the help of a computational fluid dynamic analysis.

The first level of the study investigates the non-uniformity in ammonia conversion concerning the velocity and temperature of exhaust gas and the flow rate of urea solution in the injector. The second level of study investigates the effect of non-uniformities from the mixing chamber, which serves as the SCR inlet, on the rate of NO_x reduction. The study is conducted at two different exhaust gas temperature of 486 K and 523 K within which urea decomposition occurs according to Karlsson et al. [244–246]

7.4.1 Analysis of factors affecting the performance of the mixing chamber

7.4.1.1 Effect of exhaust gas velocity

The effect of exhaust gas velocity on ammonia generation and distribution in the mixing chamber is studied by considering three exhaust gas flow velocity, and the results are shown in Figure 7.5. The Figure 7.5a shows ammonia concentration at three different velocity of 4 m/s, 6 m/s and 8 m/s at the temperature of 523 K along the length of the mixing chamber for a urea-water solution flow rate of 1×10^{-4} kg/s. The figure shows that ammonia formation increases with a decrease in exhaust gas velocity throughout the mixing chamber length. The exhaust gas velocity of 4 m/s with a residence time of 0.28 second leads to an ammonia conversion of 24.6 ppm, which drops to 10.8 ppm at 6 m/s at a residence time of 0.18 second. The lowest concentration of 5.51 ppm is obtained at 8 m/s at a residence time of 0.14 second. The exhaust gas velocity determines the rate of heat transfer from the exhaust gas to the UWS droplet and the decomposition rate. The reduced exhaust gas velocity provides more residence time to exchange the heat of exhaust gas to the urea drop to evaporate and decompose. Therefore reduced velocity can enhance heat transfer and chemical reaction in urea evaporation and decomposition.

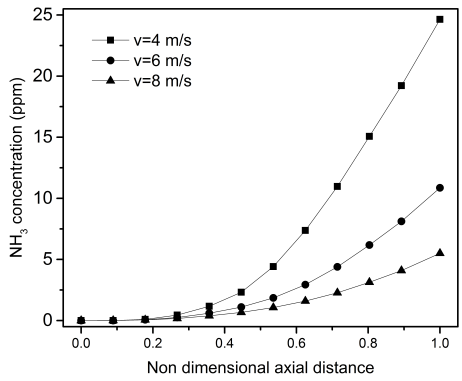

(a) NH_3 concentration along the mixing chamber length at exhaust gas velocity of 4 m/s, 6 m/s and 8 m/s.

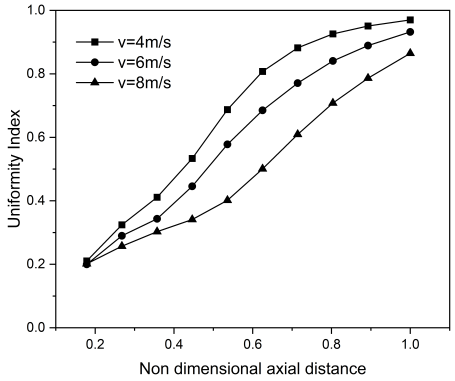

(b) Uniformity Index along the mixing chamber length at exhaust gas velocity of 4 m/s, 6 m/s and 8 m/s

Figure 7.5: Effect of exhaust gas velocity in mixing chamber

The uniformity index of ammonia produced is as shown in Figure 7.5b. Uniformity index increases along the length of the mixing chamber as the flow gets reacted and mixed in the chamber. The uniformity index at the exit for exhaust gas velocity 4 m/s is 0.98 and 0.95 for 6 m/s which drops down to 0.91 at 8 m/s. At higher velocity, the fluid will not

get enough contact with the ammonia produced to mix and form a uniform flow. A higher uniformity of ammonia produced is obtained at lower exhaust gas velocity with a higher residence time of 0.28 second.

7.4.1.2 Effect of urea flow rate

The urea flow rate on the ammonia generation and distribution in the mixing chamber are analyzed by considering three different mass flow rates of urea by keeping the other system parameters constant. The results of the study are shown in Figure 7.6. The Figure 7.6a shows the ammonia concentration along the axial distance at three different flow rate of urea water solution 5×10^{-5}, 1×10^{-4} and 2×10^{-4} kg/s at an exhaust gas velocity of 6 m/s and temperature of 486 K. The urea water solution evaporates and gets decomposed to ammonia and isocyanic acid by thermolysis. The urea thermolysis being an endothermic reaction, reduces the temperature of surrounding exhaust gas and UWS, thus slows down the urea conversion. When the urea flow rate is high, the mixture solution requires more latent heat to evaporate for the same operating conditions. A large amount of urea thermolysis requires a higher rate of heat transfer from the exhaust inflow gas. The UWS flow rate of 5×10^{-5} kg/s reaches its maximum along the length of the mixing chamber .Urea evaporation and thermolysis rate at UWS flow rate of 1×10^{-4} kg/s is very high and produces large amount of ammonia. The UWS flow rate of 2×10^{-4} has the lowest conversion because of a lack of latent heat available for evaporation. Therefore, a higher urea flow rate leads to lower urea conversion efficiency and exhaust gas temperature, which is crucial in the urea decomposition. It is observed from the Figure 7.6b that the uniformity index is 0.96 for UWS flow rate of 2×10^{-4} kg/s followed by 0.92 for 1×10^{-4} kg/s and 0.91 for 5×10^{-5} kg/s. The highest uniformity index at high UWS flow rate can be accounted for the mixing of ammonia produced with the unreacted urea which leads to a more distributed flow. The results obtained for 523K also exhibited a similar trend as observed at 486K but with a higher ammonia concentration and uniformity index ranging from 0.94 to 1. It can be concluded that the ammonia generation is higher for a low UWS flow rate, and the distribution is uniform for a high UWS flow rate. A high UWS flow rate leads to unconverted urea in the SCR inlet, which causes undesirable side reactions. Eventually, it blocks the pores, and active sites of the catalyst, thus reduce the SCR catalyst life [255]. Therefore a low UWS flow rate with a high amount of ammonia produced and distributed is preferred.

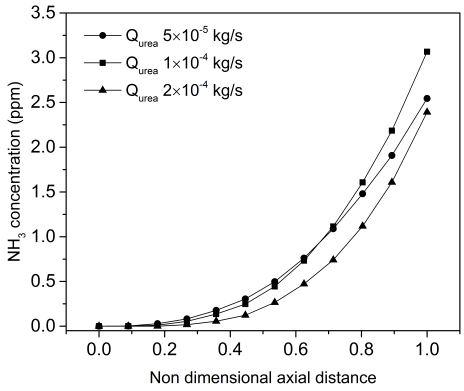

(a) NH_3 concentration at different urea water solution flow rate of 5×10^{-5}, 1×10^{-4} and 2×10^{-4} kg/s at exhaust gas velocity of 6 m/s and 486 K.

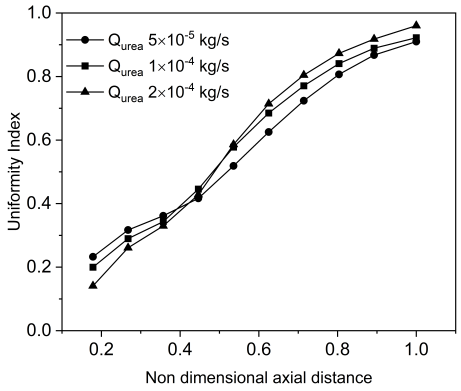

(b) Uniformity Index along the mixing chamber at urea water solution flow rate of 5×10^{-5}, 1×10^{-4} and 2×10^{-4} kg/s at exhaust gas velocity of 6 m/s and 486 K.

Figure 7.6: Effect of urea flow rate in mixing chamber

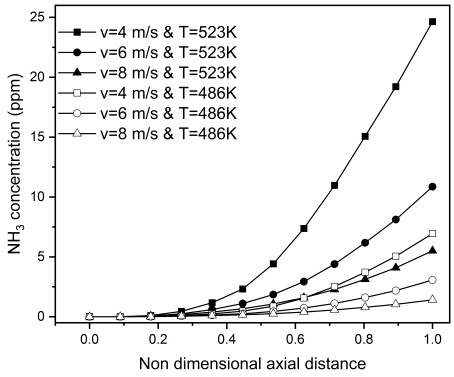

(a) NH_3 concentration along the axial distance at exhaust gas velocity of 4 m/s, 6 m/s and 8 m/s at temperatures of 486 K and 523 K.

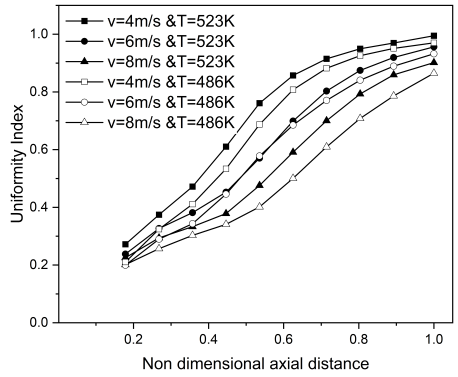

(b) Uniformity Index along the axial distance at exhaust gas velocity of 4 m/s, 6 m/s and 8 m/s at temperatures of 486 K and 523 K.

Figure 7.7: Effect of exhaust gas temperature in mixing chamber at different exhaust gas velocity

7.4.1.3 Effect of exhaust gas temperature

The effect of exhaust gas Temperature is studied by considering the exhaust gas velocity and flow rate of the urea water solution as the parameters. The result of exhaust gas temperature and velocity on ammonia concentration and its distribution is as shown in Figure 7.7. The Figure 7.7a shows the effect of exhaust gas velocity and temperature on ammonia concentration along the length of the mixing chamber. It is observed that for a particular exhaust gas velocity, a high temperature of 523 K gives increased ammonia concentration.

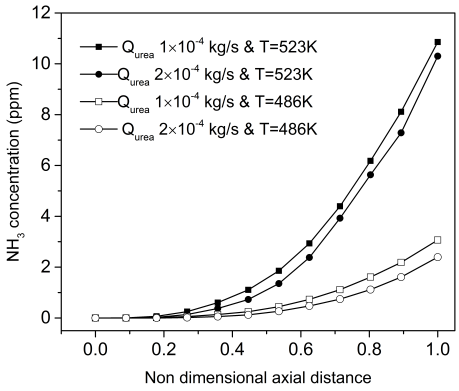

(a) NH_3 concentration along the axial distance at flow rate of urea water solution of 5×10^{-5}, 1×10^{-4} and 2×10^{-4} kg/s at temperatures of 486 K and 523 K.

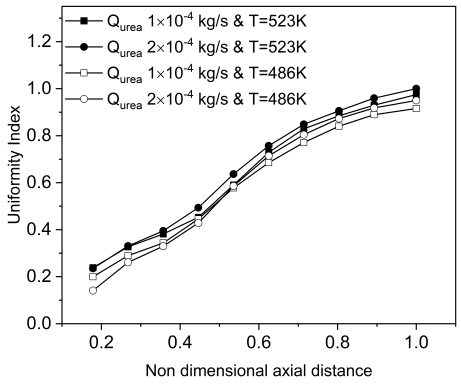

(b) Uniformity index of ammonia along the axial distance at flow rate of urea water solution 5×10^{-5}, 1×10^{-4} and 2×10^{-4} kg/s at temperatures of 486 K and 523 K.

Figure 7.8: Effect of exhaust gas temperature in mixing chamber at different urea flow rate

For a specific temperature, a higher concentration of ammonia is observed at lower exhaust gas velocities. Exhaust gas temperature and the residence time affect the heat transfer to urea droplet, causing evaporation and decomposition of urea. A higher exhaust gas temperature can promote urea conversion efficiency by accelerating evaporation and the thermolysis rate. Urea thermolysis being an endothermic reaction, reduces the temperature of the surrounding exhaust gas, thus reducing the evaporation and decomposition along the length of the reactor. A higher temperature can provide enough latent heat for UWS to evaporate and decompose. A lower exhaust gas velocity provides higher residence time and better contact with the surrounding exhaust gas and urea droplet to evaporate and decompose. Therefore urea conversion is higher at low exhaust gas velocity and high temperature.

The Figure 7.7b shows that uniformity index is higher at a lower exhaust gas velocity at a given temperature. The uniformity index increases at low exhaust gas velocity as the flow gets enough time to mix inside the chamber. The uniformity of ammonia distribution increases with temperature for a particular exhaust gas velocity. At higher temperatures, the evaporation and decomposition rate of urea increases and thereby producing higher concentration of ammonia, which further radially diffuses leading to its uniform distribution across the plane. Higher exhaust gas temperature and lower gas velocity are favorable for the generation of highly concentrated and uniformly distributed ammonia at the exit of mixing chamber.

The Figure 7.8 shows the NH_3 concentration and distribution at UWS flow rate of 1×10^{-4} and 2×10^{-4} kg/s at exhaust gas temperatures of 486 K and 523 K along the length

of the mixing chamber. A higher ammonia concentration is observed at a flow rate of 1×10^{-4} kg/s as shown in Figure 7.8a. For any given temperature, a high flow rate of urea requires a correspondingly higher quantity of latent heat for the evaporation of urea droplets, which, if insufficient, leads to a lower urea conversion rate. Exhaust gas at high temperatures could supply more latent heat for evaporation of urea droplets and, therefore, lead to the improved decomposition of urea vapors. Thus, a higher conversion of urea occurs at high exhaust gas temperatures and a low urea flow rate. The uniformity index of ammonia distribution in Figure 7.8b shows that a higher uniformity index is obtained at a higher temperature due to the higher concentration of ammonia produced for a particular UWS flow rate. The higher uniformity index observed at a higher urea flow rate could be attributed to the mixing provided by the unreacted urea with the ammonia produced in the mixing chamber. A high flow rate of UWS causes unreacted urea, which in turn leads to solid deposits in the mixing chamber. Therefore, a low flow rate of UWS and high exhaust gas temperature is favorable for a high ammonia concentration and distribution.

The simulation of the mixing chamber with a urea flow rate injected at 1×10^{-4} kg/s at 10.6 m/s and cone angle of 70° with exhaust gas velocity of 6 m/s and temperatures of 486 K and 523 K results in non-uniformity at the exit of the mixing chamber. The Figure 7.9 gives the non-uniform ammonia distribution with a maximum concentration of 105 ppm at 486 K and 350 ppm at 523 K. The ammonia concentration profile shows a maximum at the central axis due to the UWS injection at the center of the mixing chamber. An increase in the concentration near the wall is due to the reflecting boundary condition.

The non-uniform exhaust gas velocity profile along the length of the mixing chamber is, as shown in Figure 7.10. The flow profile shows that the flow gets developed along the length of the mixing chamber. Initially, the velocity profile is flat at the center with a sudden drop at the wall, which gets developed to a smooth profile along the chamber length. The flat profile is due to the inlet boundary condition, and the velocity drop at walls is due to no-slip boundary conditions at the wall. The flatness gets reduced along the length of the mixing chamber and gives almost a developed flow profile at the exit of the mixing chamber. The velocity profile shows a developing profile along the length of the mixing chamber. The exhaust gas temperature profile at the exit of the mixing chamber is shown in Figure 7.11. The exit profile shows a radial temperature variation due to symmetric injection. The exhaust gas temperature reduces along the mixing chamber's length due to the heat transfer from the exhaust gas to the urea water solution for the evaporation and decomposition.

The performance of the SCR is analyzed with the non-uniformities from the mixing

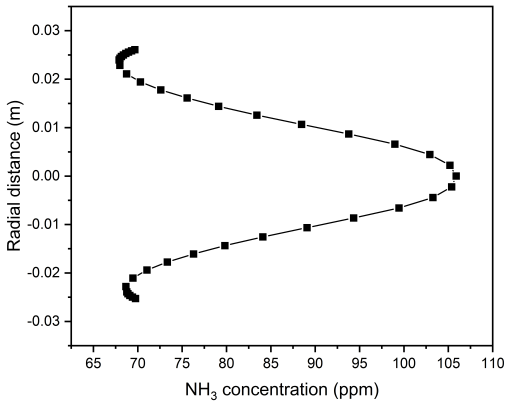

(a) NH_3 concentration profile at the exit of the mixing chamber at 486 K.

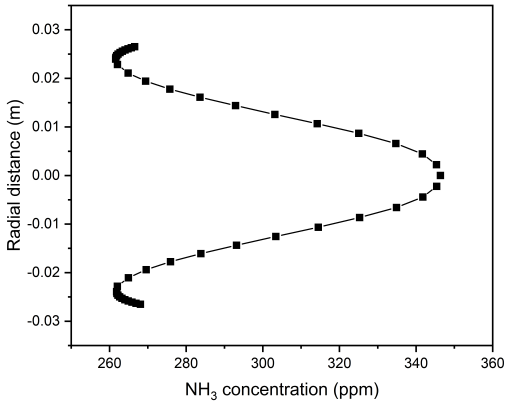

(b) NH_3 concentration profile at the exit of the mixing chamber at 523 K.

Figure 7.9: Non uniform NH_3 concentration profile at mixing chamber outlet

chamber. The distribution of NO_x, H_2O, and O_2 are assumed to be uniform at the exit of the mixing chamber.

7.4.2 Analysis of SCR performance based on inlet conditions

7.4.2.1 Effect of nonuniformity

The performance of SCR based on factors at the inlet, like non-uniform distribution of ammonia concentration, exhaust gas velocity, and temperature from the outlet of the mixing chamber in the first section, is analyzed in this section. The average concentration of ammonia produced at the exit of the mixing chamber is 75 ppm at 486 K and 275 ppm at 523 K. The NH_3-NO_x ratio in feed is maintained at 1:1 with an equimolar concentration of NO and NO_2, 5% O_2 and 8% H_2O for both temperatures. The Figure 7.12 shows that NO_x

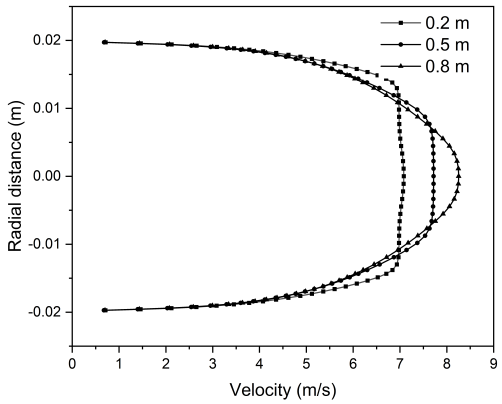

(a) Velocity profile along the length of mixing chamber at 486 K.

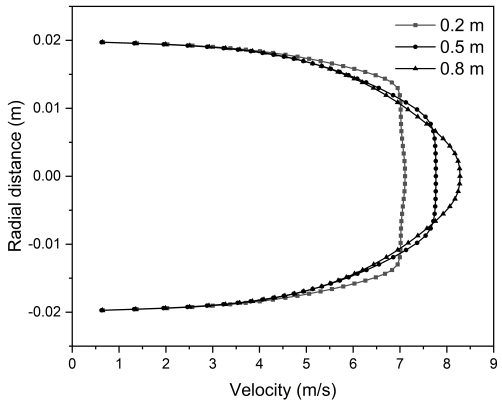

(b) Velocity profile along the length of mixing chamber at 523 K.

Figure 7.10: Non uniform exhaust gas velocity profile at mixing chamber outlet.

conversion at 486 K increases with axial distance gradually to 97% conversion. In contrast, the NO_x conversion at 523 K shows a sharp conversion to 99% at a location very close to the entry of the reactor. NH_3 gets reacted along converter length and leaves 60% unreacted ammonia at the outlet for 486 K whereas the NH_3 slip is 54% for 523 K with a sharp drop in concentration at the reactor inlet.

The contours of NH_3 and NO_x concentration along the SCR is shown in Figure 7.13 and 7.14 for two different exhaust gas temperature of 486 K and 523 K . The injector positioned at the centre in the mixing chamber shows a symmetric ammonia conversion with the highest value at the centre which enhances the availability of ammonia near the axis of the SCR. The non uniformity in temperature arising from symmetric injection and heat transfer from the exhaust gas to UWS for evaporation and decomposition leads to lower temperature at the central axis than at the walls of the mixing chamber. The non-uniformity at the mixing

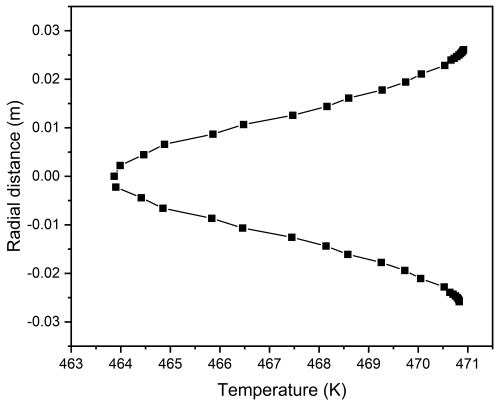

(a) Temperature profile at the exit of the mixing chamber at 486 K.

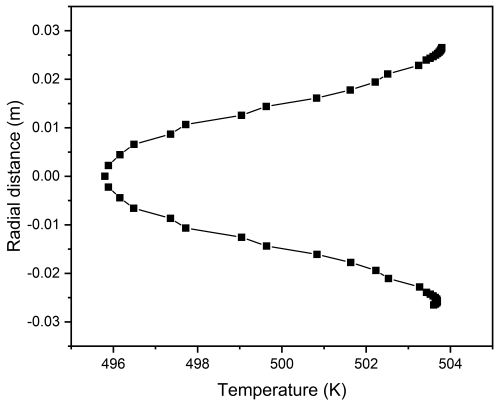

(b) Temperature profile at the exit of the mixing chamber at 523 K.

Figure 7.11: Non uniform exhaust gas temperature profile at mixing chamber outlet

chamber outlet when used as the inlet to the SCR monolith reactor results in radial variation in NO_x reduction. Figure 7.13 reveals that the NO_x concentration is high near the walls of the monolith reactor than along the central axis. The comparatively lower NO_x reduction rate near to the walls of the SCR is due to the limited availability of ammonia for reaction in this location, despite the higher temperature prevalent. It is observed that the radial variation in NO_x concentration diminishes with increase in temperature. At 523 K the radial variation in NO_x concentration decreases with respect to the distribution of NH_3 as shown in the Figure 7.14. This can be attributed to the availability of NH_3 and higher SCR reaction rate at a temperature of 523 K.

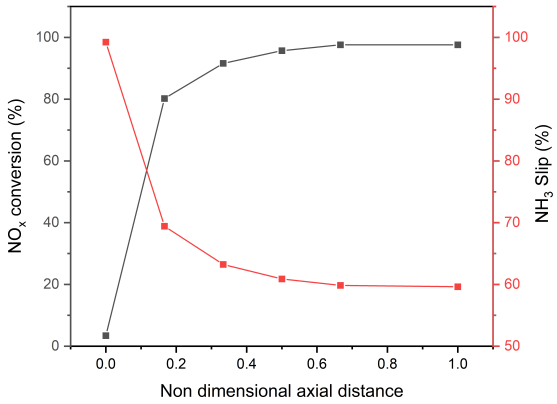

(a) NO_x conversion (%) and NH_3 slip (%) at 486 K.

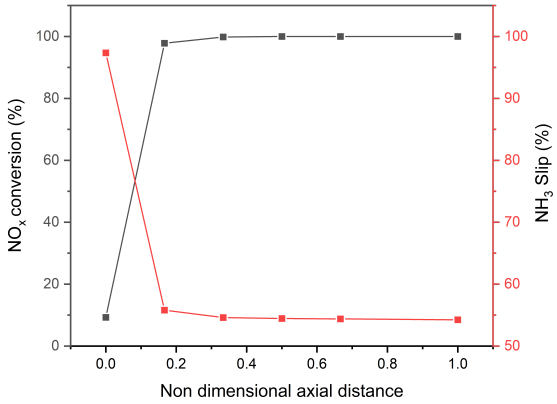

(b) NO_x and NH_3 concentration contours at 523 K.

Figure 7.12: NO_x conversion (%) and NH_3 slip (%) in the SCR reactor

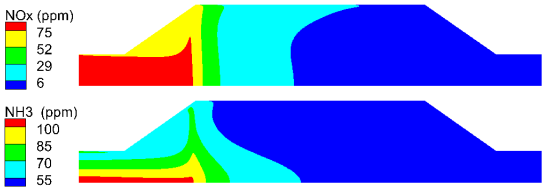

Figure 7.13: NO_x and NH_3 concentration contours at 486 K

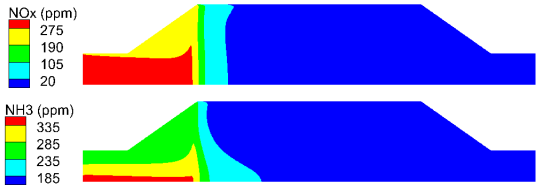

Figure 7.14: NO_x and NH_3 concentration contours at 523 K

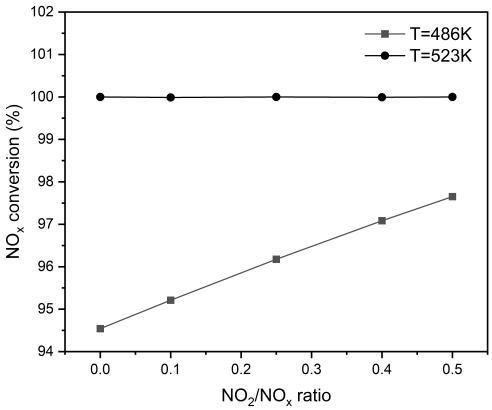

Figure 7.15: NO_x conversion at different NO_2/NO_x ratio at 486 K and 523 K

7.4.2.2 Effect of NO_x concentration in feed

The NO_x reduction with different NO_2-NO_x feed ratio is analyzed by keeping the concentration of NH_3 and NO_x as equal with 5% O_2 and 8% H_2O to study the effect of NO_x concentration in feed at two different temperature of 486 K and 523 K. A review of the literature shows that the equimolar concentration of NO and NO_2 in the feed yields higher NO_x conversion as it accelerates the standard SCR reaction. The NO_2/NO_x ratio ranges from 0 to 0.5 to study the effect of NO_x in the SCR reaction. Figure 7.15 shows that the NO_x conversion increases with an increase in NO_2/NO_x ratio at 486 K, as the availability of NO_2 increases the rate of standard SCR and fast SCR reactions. It is observed that this variation in NO_x reduction with increase in NO_2 gets diminished at an increased temperature of 523 K due to the higher reaction rate at a higher temperature. A study of uniform and non-uniform inlet profiles at the SCR inlet is made to analyze the NO_x conversion efficiency on the uniformity of feed distribution.

A uniform profile with 75 ppm NH_3, 75 ppm NO_x, 5% O_2 and 8% H_2O is fed to the reactor at 486 K with exhaust gas velocity of 6 m/s. The NO_2/NO_x ratio is varied from 0 to 0.5 to study the effect of NO_x concentration in the feed and the result of analysis is as shown in Figure 7.16. The Figure 7.16a shows that a uniform profile gives a higher conversion as compared to the non-uniform profile from the mixing chamber. It is also observed that the NO_x conversion increases sharply with the increase in NO_2/NO_x ratio in SCR with a non-uniform profile. In contrast, this increase is not that prominent in SCR with a uniform profile at 486 K. Therefore the non-uniformity in radial variation should be considered in designing the SCR. A uniform profile at the inlet can lead to an error in the actual SCR case.

The effect of NO_x concentration in feed is studied by varying the NO_2/NO_x ratio with

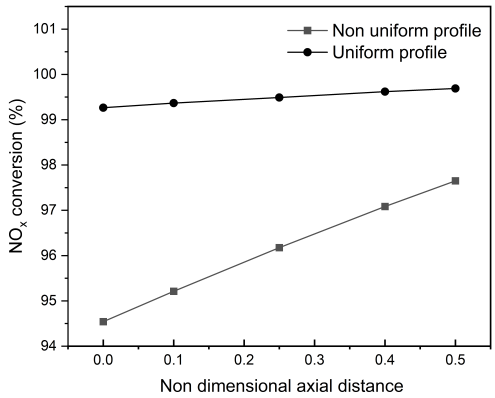

(a) NO_x conversion at different NO_2/NO_x ratio with non-uniform and uniform inlet profile at 486 K.

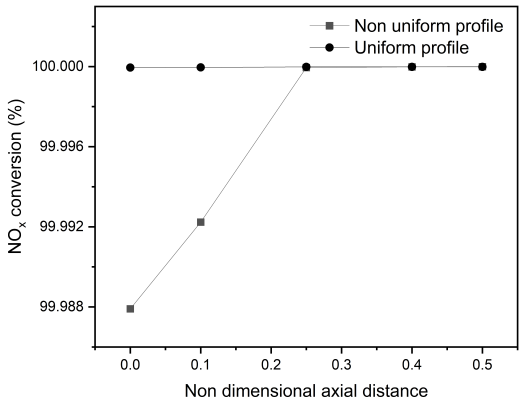

(b) NO_x conversion at different NO_2/NO_x ratio with non-uniform and uniform inlet profile at 523 K.

Figure 7.16: NO_x conversion at different NO_2/NO_x ratio with non-uniform and uniform inlet profile

275 ppm NH_3, 275 ppm NO_x, 5% O_2 and 8% H_2O with exhaust gas velocity of 6 m/s and temperature of 523 K. The uniform inlet profile gives a higher NO_x conversion compared to non-uniform inlet profiles as shown in Figure 7.16b. This difference is not that prominent at exhaust gas temperature of 523 K than at 486 K. The variation in NO_x conversion with different NO_2/NO_x ratio in uniform and non-uniform profile remains the same after a NO_2/NO_x ratio of 0.25. The difference in uniform and non-uniform profile diminishes at a higher NO_2/NO_x ratio because of the higher reaction rates at a higher temperature.

The challenge of incomplete decomposition of urea and distribution of ammonia in the SCR inlet can be improved by a low flow rate of UWS at the injector and an exhaust gas stream of high temperature and low velocity. The SCR performance with non-uniformity

from the mixing chamber can be improved by a high-temperature exhaust gas stream of 523 K, and equal concentration of NO and NO_2.

7.5 Summary

The main challenge with urea-based SCR for NO_x reduction is the incomplete decomposition of urea into ammonia in the mixing chamber and the non-uniform distribution of the feed to the SCR. The impact of these non-uniformities, as well as the relative ratio of the species in the feed to the SCR, needs to be analyzed to arrive at an optimum configuration of the system for maximizing the NO_x reduction efficiency. In the initial level of the study, the mixing chamber parameters are analyzed to maximize the urea decomposition and uniformity in feed distribution to SCR. Our analysis results reveal that lower exhaust gas velocities provide higher residence time and better contact with the surrounding exhaust gas for urea droplets to evaporate and decompose, leading to improved ammonia generation and distribution. The results also show that for a lower urea flow rate in the injector, the UWS injected in the mixing chamber gets easily atomized to urea water droplets, which readily evaporates and decomposes, resulting in high ammonia yield. It is observed that a more uniform flow of ammonia is obtained for a higher flow rate of urea, which is due to the better mixing of the ammonia generated with the unconverted urea. It concludes that a lower flow rate of urea leads to its higher conversion rate, whereas a higher urea flow rate results in better distribution of ammonia at the SCR inlet. However, high flow rates of UWS characterized by incomplete decomposition of urea causes deposit formation on the catalyst surface and eventually blocks the pores and active sites of the catalyst, due to which a low flow rate of UWS is favorable. The ammonia yield also improved at a higher temperature of exhaust gas due to the higher energy content, which is available as the latent heat for the urea-water droplets, thereby accelerating their evaporation rate. The initial level analysis suggests a lower flow rate for a urea-water solution along with an exhaust gas stream of high temperature and low velocity could maximize the ammonia generation along with a uniform distribution of the reducing agent at the SCR inlet and assures the smooth operation of the reactor.

In the second-level analysis, the relative NO_x reducing capability of the SCR is analyzed for different configurations in the inlet, like the uniformity of species distribution, NO_x concentration, and the temperature of the feed. The performance of SCR with the non-uniformities from the mixing chamber at its inlet is analyzed for the temperatures 486 K, and 523 K with an equimolar concentration of NO and NO_2. At the lower temperature, the

NO_x reduces gradually along the length of the monolith. At 523 K, the conversion reduces sharply along the length due to the improved SCR reaction rate at high temperatures. Radial variation in the NO_x and NH_3 concentrations are observed throughout the SCR length as a result of the non-uniformity arising from the mixing chamber. These variations diminish at a higher temperature. The SCR performance with a relative feed ratio of species in NO_x and non-uniformity from the mixing chamber is analyzed with NH_3 to NO_x ratio of 1. At the lower temperature, the increase in NO_2 concentration shows a linear increase in NO_x conversion. However, at a higher temperature, the variation in NO_2 concentration does not show much deviation in the NO_x conversion due to the high reaction rate. The analysis also revealed that uniformly distributed inlet profile to the SCR results in better NO_x conversion than a non-uniform inlet, due to radial variations from the mixing chamber. However, the difference in NO_x conversion based on uniform inlet profile to the SCR vanishes at a NO_2 to NO_x ratio of 0.25 for the higher exhaust gas temperature of 523 K. The second-level analysis concludes by suggesting that the improvement in NO_x conversion could be achieved in an SCR by the use of high temperature and high NO_2 concentration along with a more uniform distribution of the species at the SCR inlet. The work concludes that the non-uniformity from the mixing chamber has to be taken into account in designing an SCR system to improve the accuracy of the model.

Chapter 8

Conclusions and Recommendations for Future Work

The major industrial energy demand is met by combustion of fossil fuels. Combustion of fossil fuels emits pollutant gases that are harmful to the environment. These gases must be treated before they are vented into the atmosphere. Selective Catalytic Reduction by NH_3 has proven to be an effective catalytic process for NO_x reduction. Cu/Fe zeolites are promising catalysts for SCR. The main objective of this study is to minimize the pressure drop and diffusion limitations of microporous zeolites. The main focus of this study was the development of Cu-ZSM-5 foam catalysts. (a) Development of dip-coated Cu-ZSM-5 with in-house built α alumina foam, (b) development of in situ hydrothermally synthesized Cu-ZSM-5 foam, and (c) development of self-supported foam catalyst. The catalyst is characterised for structural properties, acid strength, types of Cu species and their reduction. These inferences are used to study the SCR chemistry of adsorption reactivity and inhibition of reactant gases.The second part of this study deals with the SCR kinetics of the developed Cu-ZSM-5 catalyst. The key reactions of the SCR chemistry, standard SCR, fast SCR, slow SCR, NO oxidation, and NH_3 oxidation were studied in detail. The third part of the study deals with the analysis of mass transfer and pressure drop over the developed catalyst. Correlations between the mass transfer coefficient and friction factor were developed. Numerical analysis of real engine catalytic convertor is explored to conclude the inferences from SCR chemistry. The mixing chamber with the UWS was simulated, and the nonuniformities from the mixing chamber were analyzed. The effect of feeding nonuniformities from the mixing chamber in an SCR converter was analyzed in this study.

The main contributions of this study include the development of a Cu-ZSM-5 foam catalyst with high mechanical strength of 0.35MPa, that provides high mass transfer and low pressure drop.

α alumina foam was prepared in-house using the thermofoaming method. Cu-ZSM-5 catalysts with Si/Al ratios of 10, 20, and 50 were synthesized and coated on α alumina foam using an in situ hydrothermal process. Mesoporosity was introduced into the Cu-ZSM-5 catalyst by the introduction of TPAOH in the precursor gel of the hydrothermal process on the coating. The maximum pore size distribution for the Cu-ZSM-5 foam samples was 25 nm. Ammonium ZSM-5 ions exchanged with Cu-ZSM-5 were dip-coated onto α alumina foam with an aluminum oxide binder.

The structural properties, acid strength, Cu active sites and their reduction analysis is characterized for three different foam catalysts and are summarized in Tables 8.1, 8.2 and 8.3. The higher activity of the catalyst is due to the low Si/Al ratio because a higher Al concentration provides more Bronsted acid sites and provides a way to introduce more Cu^{2+} ions at the exchangeable sites. However, these overloaded Cu^{2+} ions aggregate to form CuO, which blocks the zeolite pores, resulting in the deterioration of the specific activity. Therefore, Cu^{2+} ion concentration, which is a crucial factor, drives the specific activity of Cu-ZSM-5.

Table 8.1: Foam dimensions

Method	Pore size (mm)	struct diameter (mm)	Sv (m^2/m^3)	Space velocity hr^{-1}
Dip coating	2.5	0.89	1345	140000
Hydrothermal	1	0.36	3362	80000
Emulsion	0.025	0.089	13448	300000

Table 8.2: Acidity in Cu-ZSM-5 from NH_3 TPD

Methods	Acidity by extraframework Al atoms (μmol/g)	Acidity by Metal sites (μmol/g)	Acidity by bronsted sites (μmol/g)
Hydrothermal	5.7	155	254
Dip coated	59	36	108
Emulsion	39	225	80

The NO_x adsorption study summarized in Table 8.4 provides an insight into the adsorption sites of NO_2 in Cu-ZSM-5. As suggested by the NO_2 adsorption kinetics, it can be

Table 8.3: Cu ion distribution

Methods	Cu^{+}/Cu^{2+}	isolated Cu^{2+}/CuO	Cu(%)
Hydrothermal	0.18	1.01	7.9
Dip coating	0.25	0.79	1.3
Emulsion	0.45	1.18	4.4

Table 8.4: NO_x Adsorption Study

Methods	NO_2 TPD		NO-NO_2 TPD	
	NO_2 Concentration (mmol/g of catalyst)	Temperature (^{o}C)	NO_2 Concentration (mmol/g of catalyst)	Temperature (^{o}C)
Dip coated	9.2	273	4.2	188
Hydrothermal	10.5	360	5	250
Emulsion	12.6	300	4.09	200

observed from Table 8.4 that self-supported Cu-ZSM-5 can store more nitrates compared to other catalysts because of the higher number of Lewis acidic sites compared to other prepared catalysts. The high desorption temperature indicates high stability of the nitrates on the catalyst. The effect of nitrate formation in NO oxidation is explained with the help of kinetics. The first step in the Kinetics of NO oxidation is the adsorption of oxygen molecules and the dissociation of oxygen atoms on the active sites. NO reacts with oxygen active sites to form NO_2 active sites. The NO_2 active site reacted with the same oxygen active site to form nitrate.

- Kinetics of NO oxidation
- O_2 adsorption

$$O_2 + S \leftrightarrow O_2 - S$$

- O_2 dissociation

$$O_2 - S \leftrightarrow 2O - S$$

- NO Oxidation

$$NO + O - S \leftrightarrow NO_2 - S$$

- NO_2 adsorption and Nitrate formation

$$2NO_2 + S \leftrightarrow NO_2 - S$$

$$NO_2 - S + O - S \leftrightarrow NO_3 - S + S$$

$$2NO_2 - S \leftrightarrow NO_3 - S + NO + S$$

$$3NO_2 - S + O - S \leftrightarrow 2NO_3 - S + NO + 2S$$

- Nitrate decomposition

$$NO_3 - S \leftrightarrow NO_2 - S + 0.5O_2 \tag{8.1}$$

$$2NO_3 - S + NO+ \leftrightarrow 3NO_2 - S + O - S \tag{8.2}$$

S-Metal site, [O-S]- bridging metal oxide

NO_2 inhibition on NO oxidation reaction can be due to competitive adsorption of NO_2 and blockage of NO oxidation sites. NO_2 is a stronger oxidizing agent than O_2 and can oxidize the metal sites and prevent the adsorption of O_2. NH_3 reacts with active sites by different mechanism to form N_2 and H_2O in which decomposition of nitrates and nitrates are the intermediate step At high temperatures, the nitrates formed decompose from the active sites, which become available for NO oxidation. It is concluded from NO_2/NO_x studies that NO_2 is adsorbed on NO oxidation active sites and reduces the SCR reaction. The nitrates formed by NO_2 adsorption decompose at high temperatures.

Table 8.5: Reactivity of NO/NO_2-O_2-NH_3 system

Method	Temperature	NO feed		NO-NO_2 feed		NO_2 feed	
	^oC	Duration (minute)	Conversion (%)	Duration (minute)	Conversion (%)	Duration (minute)	Conversion (%)
Dip coating	250	7	68	4	24	16	50.8
	350	3	82	1.5	15	12	25.2
Hydrothermal	150	10.5	66	2.5	79	5.8	45.2
	250	4	78	1	87	4	56.8
	350	1	83	0.5	89	2.6	58.8
Emulsion	150	11.2	78	5	74	26	24.8
	250	3.2	84	3	91	20	34
	350	1.8	85	1.7	94	14	48

A comparison of the foam catalysts with respect to the reactivity of the NO/NO_2-O_2-NH_3 system is given in Table 8.5. $[Cu(OH)]^+$] is the active species in standard SCR and is

highly present in the self-supporting foam, which leads to high conversion in the catalyst compared to other prepared catalysts (Table 8.5). Isolated Cu^{2+} is the active species for fast SCR was observed for self-supported foam catalysts. Therefore, self-supporting foam catalysts possess high reactivity in fast SCR, followed by hydrothermal and dip-coated foams. In the slow SCR, NO_2 reacts with NH_3 in the Brønsted acid sites, and a higher NO_x conversion is observed in the hydrothermally coated foam than in the other foam catalysts. The NH_3 inhibition studies conclude that the self-supporting foams having high $[Cu(OH)]^+$], the active species in standard SCR adsorbs more NH_3 and gives less inhibition. In fast SCR, more isolated Cu^{2+} in the self-supporting foam catalyst forms more NH_3 active complexes that react with NO to provide less NH_3 inhibition in the reaction, whereas the bronsted acid sites with strongly bound NH_3 promote the decomposition of ammonium nitrates by proton exchange in slow SCR (Table 8.3). Therefore, NH_3 inhibition in the slow SCR was lower in Cu-ZSM-5 hydrothermally coated on the alumina foam.

In environmental catalysis, a trade-off between mass transfer and pressure drop performances of a catalyst is advisable. The ideal structured catalyst should yield very high conversions under diffusion-controlled conditions to meet the required emission limits while keeping the pressure drop as low as possible to reduce energy costs. The SCR reaction is initially dominated by kinetics at low temperature whereas with increase in temperature the molecules gets enough activation energy to react, thus the reaction rate slowly becomes very rapid and shifts to mass transfer controlled regime. It is observed from Arrhenius plot of ln K vs 1/T for standard SCR reaction in Figure 8.1 that for Cu-ZSM-5, rate constant remains more or less the same for temperature above 300°C for monolith and 350°C for, which suggests the onset of full external mass transfer control. In Monolith the reactions shifts the regime above 300°C, whereas in Cu ZSM-5 foam gives the shift above 350°C. Thus we can conclude that the Cu ZSM-5 foam can react kinetically at high temperature to give high conversion as compared to monolith. The mass transfer limitation in monolith is reduced by foam catalyst considerably.

Method	Mass transfer correlation	Friction factor correlation
Dip coating	$Sh=0.82Re^{0.3}Sc^{0.33}$	f=3.7/Re+0.12
Hydrothermal	$Sh=0.9Re^{0.4}Sc^{0.33}$	f=2.2/Re+0.08
Emulsion	$Sh=0.01Re^{1.5}Sc0.33$	f=62/Re+0.3
Cordierite monolith	$Sh = 2.696[1+0.139Re.Sc(d/L)]^{0.81}$	$f = 14.23/Re(1+0.045/(L/Dh.Re))^{0.5}$

Figure 8.2a shows the variation in the Sherwood number with Reynolds number for $Re \lessapprox 30$. It was observed that hydrothermally coated Cu-ZSM-5 gave 37% lower Sh compared to the monolith at Re = 5, whereas at a high Re of 30, Sh increased by 23% higher

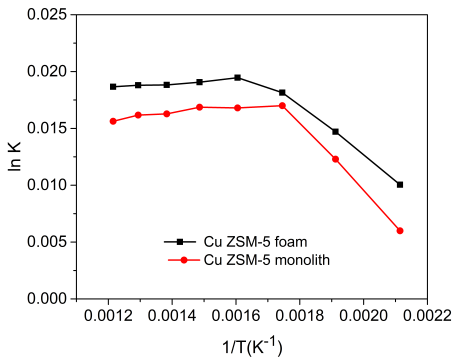

Figure 8.1: Arrhenius plot for standard SCR feed in different Cu-ZSM-5 catalyst

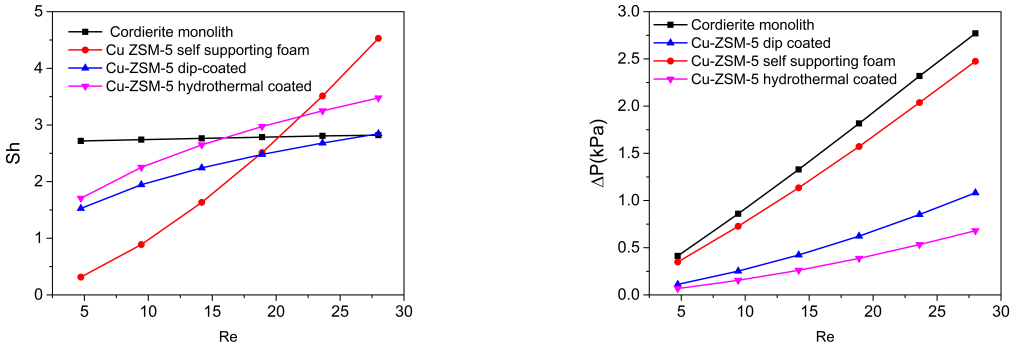

Figure 8.2: (a) Comparison of Sh of different foam catalysts with cordierite monolith. (b) Comparison of pressure drop of different foam catalysts with cordierite monolith

than that of the monolith. The dip-coated Cu-ZSM-5 exhibited a 43% higher sh at a low Re of 7. The self-supported Cu-ZSM-5 foam gave 80% higher Sh at a low Re with 60% higher Sh at a high Re of 30. Therefore, foam catalysts are recommended for use in high-flow processes. Figure 8.2b shows the pressure drops for various values of Re. This indicates that the pressure drop increases with an increase in Re. The hydrothermal-coated foam catalysts exhibit a lower pressure drop than the dip-coated foam. This was because of the resistance offered by the higher catalyst coating distributed on the same alumina foam. Hydrothermal foam catalyst could achieve 83% lower pressure drop compared to the monolith. The self-supported foam catalyst gave a 15% lower pressure drop compared to that of the monolith. The higher pressure drop in the self-supporting foam was due to the low pore size of the foam catalyst. A self-supporting foam catalyst provides a higher mass transfer than the monolith with the same pressure drop as that of the monolith at high flow rates. The hydrothermally coated catalyst provided a higher mass transfer and lower pressure drop at high flow rates.

8.1 Recommendations for future work

In the current study, a medium-pore catalyst, ZSM-5, was used for the SCR reactions. It would be interesting to observe the activity of small-pore zeolite foams such as CHA and SAPO-34. The experimental study was carried out with a flow reactor setup, where the activity was analyzed by measuring the outlet gases. The use of other experimental techniques, including Diffuse Reflectance Infrared Fourier Transform Spectroscopy (DRIFTS), is recommended to study the species formed on a surface by various surface reactions. The use of spaci-MS is recommended for future studies to resolve SCR reactions spatially.

Bibliography

[1] L. He, Y. Fan, J. Bellettre, J. Yue, and L. Luo, "A review on catalytic methane combustion at low tempetures: Catalysts, mechanisms, reaction conditions and reactor designs," *Renewable and Sustainable Energy Reviews*, vol. 119, p. 109589, 2020.

[2] B. Ashok, *NOx Emission Control Technologies in Stationary and Automotive Internal Combustion Engines: Approaches Toward NOx Free Automobiles*. Elsevier, 2021.

[3] M. Iwamoto, "Copper ion-exchanged zeolites as active catalysts for direct decomposition of nitrogen monoxide," in *Studies in Surface Science and Catalysis*. Elsevier, 1991, vol. 60, pp. 327–334.

[4] A. Jacob and B. Ashok, "An interdisciplinary review on calibration strategies of engine management system for diverse alternative fuels in ic engine applications," *Fuel*, vol. 278, p. 118236, 2020.

[5] Y.-K. Park and B.-S. Kim, "Catalytic removal of nitrogen oxides (no, no2, n2o) from ammonia-fueled combustion exhaust: A review of applicable technologies," *Chemical Engineering Journal*, vol. 461, p. 141958, 2023.

[6] F. Zheng, C. Liu, X. Ma, Z. Zhou, and J. Lu, "Review on nh3-scr for simultaneous abating nox and vocs in industrial furnaces: Catalysts' composition, mechanism, deactivation and regeneration," *Fuel Processing Technology*, vol. 247, p. 107773, 2023.

[7] Y. Zhu, W. Zhou, C. Xia, and Q. Hou, "Application and development of selective catalytic reduction technology for marine low-speed diesel engine: trade-off among high sulfur fuel, high thermal efficiency, and low pollution emission," *Atmosphere*, vol. 13, no. 5, p. 731, 2022.

[8] J. Jang, S. Ahn, S. Na, J. Koo, H. Roh, and G. Choi, "Effect of a plasma burner on nox reduction and catalyst regeneration in a marine scr system," *Energies*, vol. 15, no. 12, p. 4306, 2022.

[9] U. Deka, *Selective Catalytic Reduction of NOx over Copper-based Microporous Catalysts*. BOXpress, 2013.

[10] Z. Abidin, K. Das, and C. Roberts, "3d-semi 1d coupling for a complete simulation of an scr system," SAE Technical Paper, Tech. Rep., 2013.

[11] F. Birkhold, U. Meingast, P. Wassermann, and O. Deutschmann, "Modeling and simulation of the injection of urea-water-solution for automotive scr denox-systems," *Applied Catalysis B: Environmental*, vol. 70, no. 1-4, pp. 119–127, 2007.

[12] S. D. Yim, S. J. Kim, J. H. Baik, I.-S. Nam, Y. S. Mok, J.-H. Lee, B. K. Cho, and S. H. Oh, "Decomposition of urea into nh3 for the scr process," *Industrial & engineering chemistry research*, vol. 43, no. 16, pp. 4856–4863, 2004.

[13] X. Zhang, M. Romzek, and C. Morgan, "3-d numerical study of mixing characteristics of nh3 in front of scr," SAE Technical Paper, Tech. Rep., 2006.

[14] Y. Yi, "Development of a 3d numerical model for predicting spray, urea decomposition and mixing in scr systems," SAE Technical Paper, Tech. Rep., 2007.

[15] F. J. Janssen, F. M. Van den Kerkhof, H. Bosch, and J. R. Ross, "Mechanism of the reaction of nitric oxide, ammonia, and oxygen over vanadia catalysts. i. the role of oxygen studied by way of isotopic transients under dilute conditions," *Journal of Physical Chemistry*, vol. 91, no. 23, pp. 5921–5927, 1987.

[16] H. Sjövall, L. Olsson, E. Fridell, and R. J. Blint, "Selective catalytic reduction of nox with nh3 over cu-zsm-5—the effect of changing the gas composition," *Applied Catalysis B: Environmental*, vol. 64, no. 3-4, pp. 180–188, 2006.

[17] X. Auvray, O. Mihai, B. Lundberg, and L. Olsson, "Deactivation of cu/ssz-13 nh3-scr catalyst by exposure to co, h2, and c3h6," *Catalysts*, vol. 9, no. 11, p. 929, 2019.

[18] M. Iwamoto, S. Yokoo, K. Sakai, and S. Kagawa, "Catalytic decomposition of nitric oxide over copper (ii)-exchanged, y-type zeolites," *Journal of the Chemical Society, Faraday Transactions 1: Physical Chemistry in Condensed Phases*, vol. 77, no. 7, pp. 1629–1638, 1981.

[19] M. Iwamoto, H. Yahiro, S. Shundo, Y. Yu-u, and N. Mizuno, "Influence of sulfur dioxide on catalytic removal of nitric oxide over copper ion-exchanged zsm-5 zeolite," *Applied catalysis*, vol. 69, no. 1, pp. L15–L19, 1991.

[20] M. Iwamoto and H. Yahiro, "Zeolites in the science and technology of nitrogen monoxide removal," in *Handbook of Zeolite Science and Technology*. Marcel Dekker Inc New York, 2003, pp. 951–988.

[21] S. Brandenberger, O. Krcher, A. Tissler, and R. Althoff, "The state of the art in selective catalytic reduction of nox by ammonia using metal-exchanged zeolite catalysts," *Catalysis Reviews*, vol. 50, no. 4, pp. 492–531, 2008.

[22] A. Salker and W. Weisweiler, "Catalytic behaviour of metal based zsm-5 catalysts for nox reduction with nh3 in dry and humid conditions," *Applied Catalysis A: General*, vol. 203, no. 2, pp. 221–229, 2000. [Online]. Available: https://www.sciencedirect.com/science/article/pii/S0926860X00004890

[23] Y. Xu, D. Liu, C. Li, H. Sun, T. Duan, and H. Chen, "Hydrothermal synthesis of fer zeolites for selective catalytic reduction of nox by methanol," *Research on Chemical Intermediates*, pp. 1–15, 2023.

[24] K. Rahkamaa-Tolonen, T. Maunula, M. Lomma, M. Huuhtanen, and R. L. Keiski, "The effect of no2 on the activity of fresh and aged zeolite catalysts in the nh3-scr reaction," *Catalysis Today*, vol. 100, no. 3, pp. 217–222, 2005, catalysis for a Sustainable Future, 11th Nordic Symposium on Catalysis. [Online]. Available: https://www.sciencedirect.com/science/article/pii/S0920586104007084

[25] M. Koebel, M. Elsener, and G. Madia, "Reaction pathways in the selective catalytic reduction process with no and no2 at low temperatures," *Industrial & Engineering Chemistry Research*, vol. 40, no. 1, pp. 52–59, 2001.

[26] M. Koebel, G. Madia, and M. Elsener, "Selective catalytic reduction of no and no2 at low temperatures," *Catalysis Today*, vol. 73, no. 3, pp. 239–247, 2002, environmental Catalysis. [Online]. Available: https://www.sciencedirect.com/science/article/pii/S0920586102000068

[27] Z. Si, D. Weng, X. Wu, J. Li, and G. Li, "Structure, acidity and activity of cuox/wox–zro2 catalyst for selective catalytic reduction of no by nh3," *Journal of Catalysis*, vol. 271, no. 1, pp. 43–51, 2010.

[28] J. Despres, M. Koebel, O. Kröcher, M. Elsener, and A. Wokaun, "Adsorption and desorption of no and no2 on cu-zsm-5," *Microporous and Mesoporous Materials*, vol. 58, no. 2, pp. 175–183, 2003. [Online]. Available: https://www.sciencedirect.com/science/article/pii/S1387181102006273

[29] T. Komatsu, M. Nunokawa, I. S. Moon, T. Takahara, S. Namba, and T. Yashima, "Kinetic studies of reduction of nitric oxide with ammonia on cu2+-exchanged zeolites," *Journal of Catalysis*, vol. 148, no. 2, pp. 427–437, 1994.

[30] M. Wallin, C.-J. Karlsson, M. Skoglundh, and A. Palmqvist, "Selective catalytic reduction of nox with nh3 over zeolite h–zsm-5: influence of transient ammonia supply," *Journal of Catalysis*, vol. 218, no. 2, pp. 354–364, 2003. [Online]. Available: https://www.sciencedirect.com/science/article/pii/S0021951703001489

[31] J. M. Fedeyko, H.-Y. Chen, T. H. Ballinger, E. C. Weigert, H.-L. Chang, J. P. Cox, and P. J. Andersen, "Development of thermally durable cu/scr catalysts," SAE Technical Paper, Tech. Rep., 2009.

[32] G. Cavataio, H.-W. Jen, J. R. Warner, J. W. Girard, J. Y. Kim, and C. K. Lambert, "Enhanced durability of a cu/zeolite based scr catalyst," *SAE International Journal of Fuels and Lubricants*, vol. 1, no. 1, pp. 477–487, 2009.

[33] K. Kamasamudram, N. Currier, T. Szailer, and A. Yezerets, "Why cu-and fe-zeolite scr catalysts behave differently at low temperatures," *SAE International Journal of Fuels and Lubricants*, vol. 3, no. 1, pp. 664–672, 2010.

[34] H. Sjovall, R. J. Blint, and L. Olsson, "Detailed kinetic modeling of nh3 and h2o adsorption, and nh3 oxidation over cu-zsm-5," *The Journal of Physical Chemistry C*, vol. 113, no. 4, pp. 1393–1405, 2009.

[35] H. Sjovall, R. J. Blint, A. Gopinath, and L. Olsson, "A kinetic model for the selective catalytic reduction of nox with nh3 over an fe- zeolite catalyst," *Industrial & Engineering Chemistry Research*, vol. 49, no. 1, pp. 39–52, 2009.

[36] L. Olsson, H. Sjövall, and R. J. Blint, "Detailed kinetic modeling of nox adsorption and no oxidation over cu-zsm-5," *Applied Catalysis B: Environmental*, vol. 87, no. 3-4, pp. 200–210, 2009.

[37] J. H. Kwak, D. Tran, S. D. Burton, J. Szanyi, J. H. Lee, and C. H. Peden, "Effects of hydrothermal aging on nh3-scr reaction over cu/zeolites," *Journal of Catalysis*, vol. 287, pp. 203–209, 2012.

[38] L. Han, S. Cai, M. Gao, J.-y. Hasegawa, P. Wang, J. Zhang, L. Shi, and D. Zhang, "Selective catalytic reduction of no x with nh3 by using novel catalysts: State of the art and future prospects," *Chemical Reviews*, vol. 119, no. 19, pp. 10 916–10 976, 2019.

[39] G. Busca, L. Lietti, G. Ramis, and F. Berti, "Chemical and mechanistic aspects of the selective catalytic reduction of nox by ammonia over oxide catalysts: a review," *Applied Catalysis B: Environmental*, vol. 18, no. 1-2, pp. 1–36, 1998.

[40] L. Lietti, J. Alemany, P. Forzatti, G. Busca, G. Ramis, E. Giamello, and F. Bregani, "Reactivity of v2o5-wo3/tio2 catalysts in the selective catalytic reduction of nitric oxide by ammonia," *Catalysis today*, vol. 29, no. 1-4, pp. 143–148, 1996.

[41] N. Topsoe, J. Dumesic, and H. Topsoe, "Vanadia-titania catalysts for selective catalytic reduction of nitric-oxide by ammonia: Ii studies of active sites and formulation of catalytic cycles," *Journal of Catalysis*, vol. 151, no. 1, pp. 241–252, 1995.

[42] G. Madia, M. Elsener, M. Koebel, F. Raimondi, and A. Wokaun, "Thermal stability of vanadia-tungsta-titania catalysts in the scr process," *Applied Catalysis B: Environmental*, vol. 39, no. 2, pp. 181–190, 2002.

[43] P. Forzatti, "Environmental catalysis for stationary applications," *Catalysis Today*, vol. 62, no. 1, pp. 51–65, 2000.

[44] N. Jagtap, "Selective catalytic reduction of nox under lean burn conditions using supported metal oxide catalysts," 2009.

[45] Z. Zhang, J. Li, J. Tian, Y. Zhong, Z. Zou, R. Dong, S. Gao, W. Xu, and D. Tan, "The effects of mn-based catalysts on the selective catalytic reduction of nox with nh3 at low temperature: A review," *Fuel Processing Technology*, vol. 230, p. 107213, 2022.

[46] Y. J. Park, D. H. Kim, J.-H. Lee, H. P. Ha, and D. W. Kwon, "Unravelling the promotional effect of nb and mo on vox-based catalysts for nox reduction with nh3," *Applied Surface Science*, vol. 614, p. 156072, 2023.

[47] T. Ouyang, Y. Bai, X. Wang, X. Li, Y. Yan, Z. Wang, X. Jiang, X. Cai, J. Cai, and H. Tan, "Study on the mechanism of nox reduction by nh3-scr over znxcu1-xfe2o4 catalyst," *Physical Chemistry Chemical Physics*, 2023.

[48] Z. Ma, X. Wu, Y. Feng, Z. Si, D. Weng, and L. Shi, "Low-temperature scr activity and so2 deactivation mechanism of ce-modified v2o5–wo3/tio2 catalyst," *Progress in Natural Science: Materials International*, vol. 25, no. 4, pp. 342–352, 2015.

[49] D. W. Kwon, K. H. Park, and S. C. Hong, "Enhancement of scr activity and so2 resistance on vox/tio2 catalyst by addition of molybdenum," *Chemical Engineering Journal*, vol. 284, pp. 315–324, 2016.

[50] Y. Zhang, X. Zhu, K. Shen, H. Xu, K. Sun, and C. Zhou, "Influence of ceria modification on the properties of tio2–zro2 supported v2o5 catalysts for selective catalytic reduction of no by nh3," *Journal of colloid and interface science*, vol. 376, no. 1, pp. 233–238, 2012.

[51] Y.-J. Liao, T.-J. Huang, Y.-P. Zhang, Y.-X. Yu, and K. Shen, "Influence of ceria modification on the properties of tio2-sno2 supporting v2o5 catalysts for selective catalytic reduction of no by nh3," in *2nd Annual International Conference on Energy, Environmental & Sustainable Ecosystem Development (EESED 2016)*. Atlantis Press, 2016, pp. 63–71.

[52] D. Yu, P. Wang, X. Li, H. Zhao, and X. Lv, "Study on the role of fe species and acid sites in nh3-scr over the fe-based zeolites," *Fuel*, vol. 336, p. 126759, 2023.

[53] J. H. Kwak, R. G. Tonkyn, D. H. Kim, J. Szanyi, and C. H. Peden, "Excellent activity and selectivity of cu-ssz-13 in the selective catalytic reduction of nox with nh3," *Journal of Catalysis*, vol. 275, no. 2, pp. 187–190, 2010.

[54] I. Bull, W. Xue, P. Burk, R. Boorse, W. Jaglowski, G. Koermer, A. Moini, J. Patchett, J. Dettling, and M. Caudle, "Us patent 7,601,662, 2009," *Google Scholar There is no corresponding record for this reference*.

[55] D. W. Fickel, E. D'Addio, J. A. Lauterbach, and R. F. Lobo, "The ammonia selective catalytic reduction activity of copper-exchanged small-pore zeolites," *Applied Catalysis B: Environmental*, vol. 102, no. 3-4, pp. 441–448, 2011.

[56] S. H. Krishna, A. Goswami, Y. Wang, C. B. Jones, D. P. Dean, J. T. Miller, W. F. Schneider, and R. Gounder, "Influence of framework al density in chabazite zeolites

on copper ion mobility and reactivity during nox selective catalytic reduction with nh3," *Nature Catalysis*, vol. 6, no. 3, pp. 276–285, 2023.

[57] Y. Zhao, B. Choi, and D. Kim, "Effects of ce and nb additives on the de-nox performance of scr/cdpf system based on cu-beta zeolite for diesel vehicles," *Chemical Engineering Science*, vol. 164, pp. 258–269, 2017.

[58] K. Zhang and M. L. Ostraat, "Innovations in hierarchical zeolite synthesis," *Catalysis today*, vol. 264, pp. 3–15, 2016.

[59] K. Rahkamaa-Tolonen, T. Maunula, M. Lomma, M. Huuhtanen, and R. L. Keiski, "The effect of no2 on the activity of fresh and aged zeolite catalysts in the nh3-scr reaction," *Catalysis Today*, vol. 100, no. 3-4, pp. 217–222, 2005.

[60] J. Luo, H. Xu, X. Liang, S. Wu, Z. Liu, Y. Tie, M. Li, and D. Yang, "Research progress on selective catalytic reduction of no x by nh3 over copper zeolite catalysts at low temperature: reaction mechanism and catalyst deactivation," *Research on Chemical Intermediates*, pp. 1–37, 2022.

[61] S. S. R. Putluru, L. Schill, A. D. Jensen, and R. S. Fehrmann, "Selective catalytic reduction of nox with nh3 on cu-, fe-, and mn-zeolites prepared by impregnation: comparison of activity and hydrothermal stability," *Journal of Chemistry*, vol. 2018, pp. 1–11, 2018.

[62] C. Liu, R. Kang, F. Bin, X. Wei, K. N. Hui, S. Kasipandi, and K. San Hui, "Insights on copper, manganese, and nickel/zsm-5 catalytic mechanisms for nitric oxides selective reduction with ammonia," *Carbon Resources Conversion*, vol. 5, no. 1, pp. 15–25, 2022.

[63] P. J. Jodłowski, I. Czekaj, P. Stachurska, Ł. Kuterasiński, L. Chmielarz, R. J. Jędrzejczyk, P. Jeleń, M. Sitarz, S. Górecka, M. Mazur *et al.*, "Experimental and theoretical studies of sonically prepared cu–y, cu–usy and cu–zsm-5 catalysts for scr denox," *Catalysts*, vol. 11, no. 7, p. 824, 2021.

[64] J. Wan, H. Yang, Y. Shi, Y. Liu, J. Zhang, J. Zhang, G. Wu, and R. Zhou, "Effect of cu loading content on the catalytic performance of cu-usy catalysts for selective catalytic reduction of no with nh3," *Journal of Environmental Sciences*, vol. 126, pp. 445–458, 2023.

[65] M. S. Kumar and M. Alphin, "Influence of fe–cu-ssz-13 and hybrid fe–cu-ssz-13 zeolite catalyst in ammonia-selective catalytic reduction (nh3-scr) of nox," *Reaction Kinetics, Mechanisms and Catalysis*, vol. 135, no. 5, pp. 2551–2563, 2022.

[66] L. Xie, F. Liu, L. Ren, X. Shi, F.-S. Xiao, and H. He, "Excellent performance of one-pot synthesized cu-ssz-13 catalyst for the selective catalytic reduction of no x with nh3," *Environmental science & technology*, vol. 48, no. 1, pp. 566–572, 2014.

[67] Y. Mi, G. Li, Y. Zheng, Y. Luo, W. Liu, Z. Li, D. Wu, and H. Peng, "Insights into novel mesoporous cu-sapo-34 with enhanced denox performance for diesel emission control," *Microporous and Mesoporous Materials*, vol. 323, p. 111245, 2021.

[68] X. Wang, Y. Xu, Z. Zhao, J. Liao, C. Chen, and Q. Li, "Recent progress of metal-exchanged zeolites for selective catalytic reduction of nox with nh3 in diesel exhaust," *Fuel*, vol. 305, p. 121482, 2021.

[69] E. Yuan, W. Han, G. Zhang, K. Zhao, Z. Mo, G. Lu, and Z. Tang, "Structural and textural characteristics of zn-containing zsm-5 zeolites and application for the selective catalytic reduction of no x with nh 3 at high temperatures," *Catalysis Surveys from Asia*, vol. 20, pp. 41–52, 2016.

[70] M. Hamidzadeh, M. Ghassemzadeh, A. Tarlani, and S. S. Far, "A comparative study of m/zsm-5 (m= pd, ag, cu, ni) catalysts in the selective reduction of nitrogen (ii) oxide by ammonia," *International Journal of Scientific Research in Science and Technology Proceeding*, vol. 1, no. 4, pp. 6–11, 2015.

[71] H. Jouini, A. de Marcos-Galán, I. Mejri, R. Bensouilah, M. Mhamdi, T. Blasco, and G. Delahay, "Understanding the catalytic deactivation upon hydrothermal aging at 850° c of wo3/fe-cu-zsm-5 catalyst for selective catalytic reduction of no by nh3," *Inorganics*, vol. 10, no. 11, p. 180, 2022.

[72] J. Jang, S. Na, H. Roh, S. Ahn, and G. Choi, "Spraying and mixing characteristics of urea in a static mixer applied marine scr system," *Energies*, vol. 14, no. 18, p. 5788, 2021.

[73] G. Sun, R. Yu, L. Xu, B. Wang, and W. Zhang, "Enhanced hydrothermal stability and so 2-tolerance of cu–fe modified aei zeolite catalysts in nh 3-scr of no x," *Catalysis Science & Technology*, vol. 12, no. 12, pp. 3898–3911, 2022.

[74] P. N. Panahi, A. Niaei, D. Salari, S. M. Mousavi, and G. Delahay, "Ultrasound-assistant preparation of cu-sapo-34 nanocatalyst for selective catalytic reduction of no by nh3," *Journal of Environmental Sciences*, vol. 35, pp. 135–143, 2015.

[75] J. Li, H. Chang, L. Ma, J. Hao, and R. T. Yang, "Low-temperature selective catalytic reduction of nox with nh3 over metal oxide and zeolite catalysts—a review," *Catalysis today*, vol. 175, no. 1, pp. 147–156, 2011.

[76] Y. Pu, X. Xie, W. Jiang, L. Yang, X. Jiang, and L. Yao, "Low-temperature selective catalytic reduction of nox with nh3 over zeolite catalysts: A review," *Chinese Chemical Letters*, vol. 31, no. 10, pp. 2549–2555, 2020.

[77] C. Choi, Y. Sung, G. M. Choi, and D. J. Kim, "Numerical analysis of nox reduction for compact design in marine urea-scr system," *International Journal of Naval Architecture and Ocean Engineering*, vol. 7, no. 6, pp. 1020–1033, 2015.

[78] F. Scheffler, P. Claus, S. Schimpf, M. Lucas, and M. Scheffler, "Heterogeneously catalyzed processes with porous cellular ceramic monoliths," *Cellular ceramics: structure, manufacturing, properties and applications*, pp. 454–483, 2005.

[79] H. Sun, Y. Shu, X. Quan, S. Chen, B. Pang, and Z. Liu, "Experimental and modeling study of selective catalytic reduction of nox with nh3 over wire mesh honeycomb catalysts," *Chemical Engineering Journal*, vol. 165, no. 3, pp. 769–775, 2010. [Online]. Available: https://www.sciencedirect.com/science/article/pii/S1385894710008879

[80] V. Tomašić and F. Jović, "State-of-the-art in the monolithic catalysts/reactors," *Applied Catalysis A: General*, vol. 311, pp. 112–121, 2006. [Online]. Available: https://www.sciencedirect.com/science/article/pii/S0926860X0600473X

[81] J. Richardson, Y. Peng, and D. Remue, "Properties of ceramic foam catalyst supports: pressure drop," *Applied Catalysis A: General*, vol. 204, no. 1, pp. 19–32, 2000.

[82] I. Nova, D. Bounechada, R. Maestri, E. Tronconi, A. K. Heibel, T. A. Collins, and T. Boger, "Influence of the substrate properties on the performances of nh3-scr monolithic catalysts for the aftertreatment of diesel exhaust: an experimental and modeling study," *Industrial & engineering chemistry research*, vol. 50, no. 1, pp. 299–309, 2011.

[83] Y.-J. Lee and K. B. Yoon, "Effect of composition of polyurethane foam template on the morphology of silicalite foam," *Microporous and mesoporous materials*, vol. 88, no. 1-3, pp. 176–186, 2006.

[84] E. Verlato, S. Barison, S. Cimino, F. Dergal, L. Lisi, G. Mancino, M. Musiani, and L. Vázquez-Gómez, "Catalytic partial oxidation of methane over nanosized rh supported on fecralloy foams," *International journal of hydrogen energy*, vol. 39, no. 22, pp. 11 473–11 485, 2014.

[85] N. Gargiulo, D. Caputo, G. Totarella, L. Lisi, and S. Cimino, "Me-zsm-5 monolith foams for the nh3-scr of no," *Catalysis Today*, vol. 304, pp. 112–118, 2018.

[86] A. Petushkov, S. Yoon, and S. C. Larsen, "Synthesis of hierarchical nanocrystalline zsm-5 with controlled particle size and mesoporosity," *Microporous and mesoporous materials*, vol. 137, no. 1-3, pp. 92–100, 2011.

[87] X. Ou, F. Pilitsis, Y. Jiao, Y. Zhang, S. Xu, M. Jennings, Y. Yang, S. R. Taylor, A. Garforth, H. Zhang, C. Hardacre, Y. Yan, and X. Fan, "Hierarchical fe-zsm-5/sic foam catalyst as the foam bed catalytic reactor (fbcr) for catalytic wet peroxide oxidation (cwpo)," *Chemical Engineering Journal*, vol. 362, pp. 53–62, 2019. [Online]. Available: https://www.sciencedirect.com/science/article/pii/S1385894719300257

[88] R. Faure, F. Basile, I. Bersani, T. Chartier, A. Cuni, M. Cornillac, P. D. Gallo, G. Etchegoyen, D. Gary, F. Rossignol, and A. Vaccari, "Foam-supported catalysts tailored for industrial steam reforming processes," in *Scientific Bases for the Preparation of Heterogeneous Catalysts*, ser. Studies in Surface Science and Catalysis, E. Gaigneaux, M. Devillers, S. Hermans, P. Jacobs, J. Martens, and P. Ruiz, Eds. Elsevier, 2010, vol. 175, pp. 241–244. [Online]. Available: https://www.sciencedirect.com/science/article/pii/S0167299110750333

[89] R. Faure, F. Rossignol, T. Chartier, C. Bonhomme, A. Maître, G. Etchegoyen, P. Del Gallo, and D. Gary, "Alumina foam catalyst supports for industrial steam reforming processes," *Journal of the European Ceramic Society*, vol. 31, no. 3, pp. 303–312, 2011. [Online]. Available: https://www.sciencedirect.com/science/article/pii/S095522191000453X

[90] J. Kryca, M. Iwaniszyn, M. Pikatek, P. J. Jodlowski, R. Jkedrzejczyk, R. Pkedrys, A. Wrobel, J. Lojewska, and A. Kolodziej, "Structured foam reactor with cussz-13

catalyst for scr of nox with ammonia," *Topics in Catalysis*, vol. 59, no. 10-12, pp. 887–894, 2016.

[91] J. Kryca, P. J. Jodlowski, M. Iwaniszyn, B. Gil, M. Sitarz, A. Koodziej, T. Lojewska, and J. Lojewska, "Cu ssz-13 zeolite catalyst on metallic foam support for scr of nox with ammonia: Catalyst layering and characterisation of active sites," *Catalysis Today*, vol. 268, pp. 142–149, 2016.

[92] G. Seijger, O. Oudshoorn, W. Van Kooten, J. Jansen, H. Van Bekkum, C. Van Den Bleek, and H. Calis, "In situ synthesis of binderless zsm-5 zeolitic coatings on ceramic foam supports," *Microporous and Mesoporous Materials*, vol. 39, no. 1-2, pp. 195–204, 2000.

[93] G. Seijger, O. Oudshoorn, A. Boekhorst, H. Van Bekkum, C. Van den Bleek, and H. Calis, "Selective catalytic reduction of nox over zeolite-coated structured catalyst packings," *Chemical engineering science*, vol. 56, no. 3, pp. 849–857, 2001.

[94] V. Palma, D. Pisano, and M. Martino, "Comparative study between aluminum monolith and foam as carriers for the intensification of the co water gas shift process," *Catalysts*, vol. 8, no. 11, p. 489, 2018.

[95] R. Faure, F. Rossignol, T. Chartier, C. Bonhomme, A. Maître, G. Etchegoyen, P. Del Gallo, and D. Gary, "Alumina foam catalyst supports for industrial steam reforming processes," *Journal of the European Ceramic Society*, vol. 31, no. 3, pp. 303–312, 2011.

[96] M. Twigg and J. Richardson, "Theory and applications of ceramic foam catalysts," *Chemical Engineering Research and Design*, vol. 80, no. 2, pp. 183–189, 2002.

[97] J. Ochonska-Kryca, M. Iwaniszyn, M. Pikatek, P. J. Jodlowski, J. Thomas, A. Kolodziej, and J. Lojewska, "Mass transport and kinetics in structured steel foam reactor with cu-zsm-5 catalyst for scr of nox with ammonia," *Catalysis today*, vol. 216, pp. 135–141, 2013.

[98] M. Uberoi and C. J. Pereira, "External mass transfer coefficients for monolith catalysts," *Industrial & engineering chemistry research*, vol. 35, no. 1, pp. 113–116, 1996.

[99] A. R. Studart, U. T. Gonzenbach, E. Tervoort, and L. J. Gauckler, "Processing routes to macroporous ceramics: a review," *Journal of the American Ceramic Society*, vol. 89, no. 6, pp. 1771–1789, 2006.

[100] T. Ohji and M. Fukushima, "Macro-porous ceramics: processing and properties," *International Materials Reviews*, vol. 57, no. 2, pp. 115–131, 2012.

[101] H. Li, L. Schill, R. Fehrmann, and A. Riisager, "Recent developments of core-shell structured catalysts for the selective catalytic reduction of no x with ammonia," *Inorganic Chemistry Frontiers*, 2023.

[102] Y. Li, F. Chen, L. Li, W. Zhang, H. Yu, Y. Shan, Q. Shen, and H. Jiang, "Gas pressure sintering of arbitrary porous silicon nitride ceramics with high mechanical strength," *Journal of the American Ceramic Society*, vol. 93, no. 6, pp. 1565–1568, 2010.

[103] K. Prabhakaran, A. Melkeri, N. Gokhale, and S. Sharma, "Preparation of macroporous alumina ceramics using wheat particles as gelling and pore forming agent," *Ceramics international*, vol. 33, no. 1, pp. 77–81, 2007.

[104] G.-J. Zhang, J.-F. Yang, and T. Ohji, "Fabrication of porous ceramics with unidirectionally aligned continuous pores," *Journal of the American Ceramic Society*, vol. 84, no. 6, pp. 1395–1397, 2001.

[105] W. Wang, Y. Zhu, and J. Cao, "Evaluation of copper leaching in thermally modified southern yellow pine wood impregnated with acq-d," *BioResources*, vol. 8, no. 3, pp. 4687–4701, 2013.

[106] K. Honda, Y. Ohba, H. Yanai, H. Negishi, T. Mizutani, A. Takaoka, C. Taya, and T. Taniguchi, "Spatiotemporal regulation of myd88–irf-7 signalling for robust type-i interferon induction," *Nature*, vol. 434, no. 7036, pp. 1035–1040, 2005.

[107] M. Mizutani, H. Takase, N. Adachi, T. Ota, K. Daimon, and Y. Hikichi, "Porous ceramics prepared by mimicking silicified wood," *Science and Technology of Advanced Materials*, vol. 6, no. 1, p. 76, 2005.

[108] U. Vogt, M. Gorbar, P. Dimopoulos-Eggenschwiler, A. Broenstrup, G. Wagner, and P. Colombo, "Improving the properties of ceramic foams by a vacuum infiltration process," *Journal of the European Ceramic Society*, vol. 30, no. 15, pp. 3005–3011, 2010.

[109] E. Boccardi, F. E. Ciraldo, and A. R. Boccaccini, "Bioactive glass-ceramic scaffolds: Processing and properties," *MRS Bulletin*, vol. 42, no. 3, pp. 226–232, 2017.

[110] N. Arai, "Freeze casting of ceramics: Pore design from solidification principles," Ph.D. dissertation, California Institute of Technology, 2021.

[111] A. Feinle, M. S. Elsaesser, and N. Huesing, "Sol–gel synthesis of monolithic materials with hierarchical porosity," *Chemical Society Reviews*, vol. 45, no. 12, pp. 3377–3399, 2016.

[112] R. Zhang, D. Fang, Y. Pei, and L. Zhou, "Microstructure, mechanical and dielectric properties of highly porous silicon nitride ceramics produced by a new water-based freeze casting," *Ceramics International*, vol. 38, no. 5, pp. 4373–4377, 2012.

[113] K. H. Zuo, Y.-P. Zeng, and D. Jiang, "Effect of polyvinyl alcohol additive on the pore structure and morphology of the freeze-cast hydroxyapatite ceramics," *Materials Science and Engineering: C*, vol. 30, no. 2, pp. 283–287, 2010.

[114] S. Großberger, "Tortuous membranes produced by vacuum-induced surface directional freezing," Ph.D. dissertation, Friedrich-Alexander-Universität Erlangen-Nürnberg (FAU), 2017.

[115] R. Liu, T. Xu, and C.-a. Wang, "A review of fabrication strategies and applications of porous ceramics prepared by freeze-casting method," *Ceramics International*, vol. 42, no. 2, pp. 2907–2925, 2016.

[116] A. Kumar, S. Kargozar, F. Baino, and S. S. Han, "Additive manufacturing methods for producing hydroxyapatite and hydroxyapatite-based composite scaffolds: a review," *Frontiers in Materials*, vol. 6, p. 313, 2019.

[117] U. G. Wegst, M. Schecter, A. E. Donius, and P. M. Hunger, "Biomaterials by freeze casting," *Philosophical Transactions of the Royal Society A: Mathematical, Physical and Engineering Sciences*, vol. 368, no. 1917, pp. 2099–2121, 2010.

[118] M. Naviroj, P. W. Voorhees, and K. T. Faber, "Suspension-and solution-based freeze casting for porous ceramics," *Journal of Materials Research*, vol. 32, no. 17, pp. 3372–3382, 2017.

[119] Y. Tang, S. Qiu, C. Wu, Q. Miao, and K. Zhao, "Freeze cast fabrication of porous ceramics using tert-butyl alcohol–water crystals as template," *Journal of the European Ceramic Society*, vol. 36, no. 6, pp. 1513–1518, 2016.

[120] N. Nayak, N. Vitorino, J. R. Frade, A. V. Kovalevsky, V. D. Alves, J. G. Crespo, and C. A. Portugal, "Design of alumina monoliths by emulsion-gel casting: Understanding the monolith structure from a rheological approach," *Materials & Design*, vol. 157, pp. 119–129, 2018.

[121] S. Vijayan, P. Wilson, and K. Prabhakaran, "Processing of ceramic foams for thermal protection," *Handbook of Advanced Ceramics and Composites: Defense, Security, Aerospace and Energy Applications*, pp. 1105–1134, 2020.

[122] S. Barg, E. G. de Moraes, D. Koch, and G. Grathwohl, "New cellular ceramics from high alkane phase emulsified suspensions (hapes)," *Journal of the European Ceramic Society*, vol. 29, no. 12, pp. 2439–2446, 2009.

[123] B. Aldemir Dikici and F. Claeyssens, "Basic principles of emulsion templating and its use as an emerging manufacturing method of tissue engineering scaffolds," *Frontiers in Bioengineering and Biotechnology*, vol. 8, p. 875, 2020.

[124] M. J. Rosen and J. T. Kunjappu, *Surfactants and interfacial phenomena*. John Wiley & Sons, 2012.

[125] M. Wang, H. Du, A. Guo, R. Hao, and Z. Hou, "Microstructure control in ceramic foams via mixed cationic/anionic surfactant," *Materials Letters*, vol. 88, pp. 97–100, 2012. [Online]. Available: https://www.sciencedirect.com/science/article/pii/S0167577X1201138X

[126] X. Guo, Z. Zhou, G. Ma, S. Wang, S. Zhao, and Q. Zhang, "Effect of forming process on the integrity of pore-gradient al2o3 ceramic foams by gelcasting," *Ceramics International*, vol. 38, no. 1, pp. 713–719, 2012. [Online]. Available: https://www.sciencedirect.com/science/article/pii/S0272884211007048

[127] O. Lyckfeldt and J. Ferreira, "Processing of porous ceramics by 'starch consolidation'," *Journal of the European Ceramic Society*, vol. 18, no. 2, pp. 131–140, 1998. [Online]. Available: https://www.sciencedirect.com/science/article/pii/S0955221997001015

[128] R. Mouazer, I. Thijs, S. Mullens, and J. Luyten, "Sic foams produced by gel casting: Synthesis and characterization," *Advanced Engineering Materials*, vol. 6, no. 5, pp. 340–343, 2004. [Online]. Available: https://onlinelibrary.wiley.com/doi/abs/10.1002/adem.200400009

[129] A. Lemos and J. Ferreira, "The valences of egg white for designing smart porous bioceramics: as foaming and consolidation agent," *Key Engineering Materials*, vol. 254-256, pp. 1045 – 1050, 2003.

[130] B. P. Binks and T. S. Horozov, "Aqueous foams stabilized solely by silica nanoparticles," *Angewandte Chemie International Edition*, vol. 44, no. 24, pp. 3722–3725, 2005.

[131] U. T. Gonzenbach, A. R. Studart, E. Tervoort, and L. J. Gauckler, "Macroporous ceramics from particle-stabilized wet foams," *Journal of the American Ceramic Society*, vol. 90, no. 1, pp. 16–22, 2007.

[132] C. Chuanuwatanakul, C. Tallon, D. E. Dunstan, and G. V. Franks, "Controlling the microstructure of ceramic particle stabilized foams: influence of contact angle and particle aggregation," *Soft Matter*, vol. 7, no. 24, pp. 11 464–11 474, 2011.

[133] G. Busca, "Structural, surface, and catalytic properties of aluminas," in *Advances in catalysis*. Elsevier, 2014, vol. 57, pp. 319–404.

[134] J. T. García-Sánchez and V. G. Baldovino-Medrano, "Elements of the manufacture and properties of technical catalysts," *Industrial & Engineering Chemistry Research*, 2023.

[135] M. Bhasin and M. Tarrell, "Catalysts for treating exhaust gases from internal combustion and stationary source engines," *European Patent EP 0*, vol. 584887, p. A2, 1994.

[136] F.-C. Buciuman and B. Kraushaar-Czarnetzki, "Preparation and characterization of ceramic foam supported nanocrystalline zeolite catalysts," *Catalysis Today*, vol. 69, no. 1-4, pp. 337–342, 2001.

[137] A. Said, H. Nouali, L. Limousy, P. Dutournie, L. Josien, J. Toufaily, T. Hamieh, and T. J. Daou, "Synthesis of mono-and bi-layer zeolite films on alumina substrates," *Comptes Rendus Chimie*, vol. 19, no. 4, pp. 486–495, 2016.

[138] J. He, D. Mao, J. Hou, C. Zhong, C. Yin, Z. Zhao, and R. T. Yang, "Efficient one-pot synthesis of cu-sapo-34 catalysts for nh3-scr of nox," *Fuel*, vol. 339, p. 126927, 2023.

[139] S. Govender and H. B. Friedrich, "Monoliths: a review of the basics, preparation methods and their relevance to oxidation," *Catalysts*, vol. 7, no. 2, p. 62, 2017.

[140] E. M. Cepollaro, S. Cimino, L. Lisi, R. Botti, P. Colombo, and G. Franchin, "Cu-exchanged 3d-printed geopolymer/zsm-5 monolith for selective catalytic reduction of nox," *Chemical Engineering Transactions*, vol. 84, pp. 67–72, 2021.

[141] Y. Wei, M. Chen, X. Ren, Q. Wang, J. Han, W. Wu, X. Yang, S. Wang, and J. Yu, "One-pot three-dimensional printing robust self-supporting mnox/cu-ssz-13 zeolite monolithic catalysts for nh3-scr," *CCS Chemistry*, vol. 4, no. 5, pp. 1708–1719, 2022.

[142] U. De-La-Torre, B. Pereda-Ayo, M. Moliner, J. R. González-Velasco, and A. Corma, "Cu-zeolite catalysts for nox removal by selective catalytic reduction with nh3 and coupled to no storage/reduction monolith in diesel engine exhaust aftertreatment systems," *Applied Catalysis B: Environmental*, vol. 187, pp. 419–427, 2016.

[143] P. S. Dhillon, M. P. Harold, D. Wang, A. Kumar, and S. Y. Joshi, "Enhanced transport in washcoated monoliths: Application to selective lean nox reduction and ammonia oxidation," *Chemical Engineering Journal*, vol. 377, p. 119734, 2019.

[144] L. Olsson, H. Sjövall, and R. J. Blint, "A kinetic model for ammonia selective catalytic reduction over Cu-ZSM-5," *Applied Catalysis B: Environmental*, 2008.

[145] P. S. Metkar, N. Salazar, R. Muncrief, V. Balakotaiah, and M. P. Harold, "Selective catalytic reduction of no with nh3 on iron zeolite monolithic catalysts: Steady-state and transient kinetics," *Applied Catalysis B: Environmental*, vol. 104, no. 1-2, pp. 110–126, 2011.

[146] G. I. Garrido, F. Patcas, S. Lang, and B. Kraushaar-Czarnetzki, "Mass transfer and pressure drop in ceramic foams: a description for different pore sizes and porosities," *Chemical Engineering Science*, vol. 63, no. 21, pp. 5202–5217, 2008.

[147] A. Kołodziej, J. Łojewska, J. Tyczkowski, P. Jodłowski, W. Redzynia, M. Iwaniszyn, S. Zapotoczny, and P. Kuśtrowski, "Coupled engineering and chemical approach to the design of a catalytic structured reactor for combustion of vocs: cobalt oxide catalyst on knitted wire gauzes," *Chemical engineering journal*, vol. 200, pp. 329–337, 2012.

[148] L. Giani, G. Groppi, and E. Tronconi, "Mass-transfer characterization of metallic foams as supports for structured catalysts," *Industrial & engineering chemistry research*, vol. 44, no. 14, pp. 4993–5002, 2005.

[149] F. C. Patcas, G. I. Garrido, and B. Kraushaar-Czarnetzki, "Co oxidation over structured carriers: A comparison of ceramic foams, honeycombs and beads," *Chemical Engineering Science*, vol. 62, no. 15, pp. 3984–3990, 2007.

[150] G. Groppi, L. Giani, and E. Tronconi, "Generalized correlation for gas/solid mass-transfer coefficients in metallic and ceramic foams," *Industrial & engineering chemistry research*, vol. 46, no. 12, pp. 3955–3958, 2007.

[151] R. M. Barrer, *Hydrothermal chemistry of zeolites*. Academic press, 1982.

[152] D. Chatterjee, T. Burkhardt, M. Weibel, E. Tronconi, I. Nova, and C. Ciardelli, "Numerical simulation of no/no2/nh3 reactions on scr-catalytic converters: model development and applications," SAE Technical Paper, Tech. Rep., 2006.

[153] A. Pant and S. J. Schmieg, "Kinetic model of nox scr using urea on commercial cu-zeolite catalyst," *Industrial & Engineering Chemistry Research*, vol. 50, no. 9, pp. 5490–5498, 2011.

[154] L. Olsson, H. Sjövall, and R. J. Blint, "A kinetic model for ammonia selective catalytic reduction over cu-zsm-5," *Applied Catalysis B: Environmental*, vol. 81, no. 3-4, pp. 203–217, 2008.

[155] T. J. Wang, S. W. Baek, H. J. Kwon, Y. J. Kim, I.-S. Nam, M.-S. Cha, and G. K. Yeo, "Kinetic parameter estimation of a commercial fe-zeolite scr," *Industrial & Engineering Chemistry Research*, vol. 50, no. 5, pp. 2850–2864, 2011.

[156] P. Metkar, "Experimental and kinetic modeling studies of selective catalytic reduction of nox with nh3 on fe-and cu-zeolite monolithic catalysts," Ph.D. dissertation, 2012.

[157] D. Wu, Q. Zhang, and R. Gao, "Mechanical stability of zsm-5 zeolite washcoated cordierite monoliths," *Chemical Engineering Research and Design*, vol. 168, pp. 426–434, 2021.

[158] L. Landong, C. Jixin, Z. Shujuan, Z. Fuxiang, G. Naijia, W. Tianyou, and L. Shuliang, "Selective catalytic reduction of nitrogen oxides from exhaust of lean burn

engine over in-situ synthesized cu- zsm-5/cordierite," *Environmental science & technology*, vol. 39, no. 8, pp. 2841–2847, 2005.

[159] L. Li, F. Zhang, and N. Guan, "Ir/zsm-5/cordierite monolith for catalytic nox reduction from automobile exhaust," *Catalysis Communications*, vol. 9, no. 3, pp. 409–415, 2008.

[160] S. Vijayan, R. Narasimman, C. Prudvi, and K. Prabhakaran, "Preparation of alumina foams by the thermo-foaming of powder dispersions in molten sucrose," *Journal of the European Ceramic Society*, vol. 34, no. 2, pp. 425–433, 2014.

[161] S. Lai, D. Meng, W. Zhan, Y. Guo, Y. Guo, Z. Zhang, and G. Lu, "The promotional role of ce in cu/zsm-5 and in situ surface reaction for selective catalytic reduction of no x with nh 3," *RSC advances*, vol. 5, no. 110, pp. 90 235–90 244, 2015.

[162] B. Dou, G. Lv, C. Wang, Q. Hao, and K. Hui, "Cerium doped copper/zsm-5 catalysts used for the selective catalytic reduction of nitrogen oxide with ammonia," *Chemical Engineering Journal*, vol. 270, pp. 549–556, 2015.

[163] D. He, H. Zhang, and Y. Yan, "Preparation of cu-zsm-5 catalysts by chemical vapour deposition for catalytic wet peroxide oxidation of phenol in a fixed bed reactor," *Royal Society open science*, vol. 5, no. 4, p. 172364, 2018.

[164] J. Zhou, Q.-H. Xia, S.-C. Shen, S. Kawi, and K. Hidajat, "Catalytic oxidation of pyridine on the supported copper catalysts in the presence of excess oxygen," *Journal of Catalysis*, vol. 225, no. 1, pp. 128–137, 2004.

[165] A. M. Vijayakumari, A. R. Oraon, S. Ahirwar, A. Kannath, K. Suja, and P. K. Basu, "Defect state reinforced microwave-grown cuxo/nio nanostructured matrix engineered for the development of selective co2 sensor with integrated micro-heater," *Sensors and Actuators B: Chemical*, vol. 345, p. 130391, 2021.

[166] X. Xing, N. Li, Y. Sun, G. Wang, J. Cheng, and Z. Hao, "Selective catalytic oxidation of n-butylamine over cu-zeolite catalysts," *Catalysis Today*, 2018.

[167] J. A. Sullivan, J. Cunningham, M. Morris, and K. Keneavey, "Conditions in which cu-zsm-5 outperforms supported vanadia catalysts in scr of noxby nh3," *Applied Catalysis B: Environmental*, vol. 7, no. 1-2, pp. 137–151, 1995.

[168] J. Despres, M. Koebel, O. Kröcher, M. Elsener, and A. Wokaun, "Adsorption and desorption of no and no2 on cu-zsm-5," *Microporous and mesoporous materials*, vol. 58, no. 2, pp. 175–183, 2003.

[169] A. Grossale, I. Nova, and E. Tronconi, "Study of a fe–zeolite-based system as nh3-scr catalyst for diesel exhaust aftertreatment," *Catalysis Today*, vol. 136, no. 1-2, pp. 18–27, 2008.

[170] L. Yuejin and J. Armor, "Temperature-programmed desorption of nitric oxide over cu-zsm-5," *Applied Catalysis;(Netherlands)*, vol. 76, no. 2, 1991.

[171] A. Grossale, I. Nova, and E. Tronconi, "Ammonia blocking of the "fast scr" reactivity over a commercial fe-zeolite catalyst for diesel exhaust aftertreatment," *Journal of Catalysis*, vol. 265, no. 2, pp. 141–147, 2009.

[172] S. Mulla, N. Chen, L. Cumaranatunge, W. Delgass, W. Epling, and F. Ribeiro, "Effect of potassium and water vapor on the catalytic reaction of nitric oxide and dioxygen over platinum," *Catalysis today*, vol. 114, no. 1, pp. 57–63, 2006.

[173] D. Bhatia, M. P. Harold, V. Balakotaiah, and R. W. McCabe, "Experimental and kinetic investigations of no oxidation on model pt catalysts."

[174] E. Tronconi and I. Nova, "The role of no 2 in the nh 3–scr catalytic chemistry," in *Urea-SCR Technology for deNOx After Treatment of Diesel Exhausts*. Springer, 2014, pp. 247–270.

[175] I. Nova and E. Tronconi, *Urea-SCR technology for deNOx after treatment of diesel exhausts*. Springer, 2014, vol. 5.

[176] P. S. Metkar, V. Balakotaiah, and M. P. Harold, "Experimental study of mass transfer limitations in fe-and cu-zeolite-based nh3-scr monolithic catalysts," *Chemical engineering science*, vol. 66, no. 21, pp. 5192–5203, 2011.

[177] J. Shao, S. Cheng, Z. Li, and B. Huang, "Enhanced catalytic performance of hierarchical mnox/zsm-5 catalyst for the low-temperature nh3-scr," *Catalysts*, vol. 10, no. 3, p. 311, 2020.

[178] Z. Shi, C. Wu, Y. Gu, Y. Liang, G. Xu, H. Liu, J. Zhang, H. Hou, J. Zhang, and Z. Guo, "Preparation and characterization of mesoporous cuo/zsm-5 catalysts for

automotive exhaust purification," *Science of Advanced Materials*, vol. 11, no. 8, pp. 1198–1205, 2019.

[179] M. Ulla, R. Mallada, J. Coronas, L. Gutierrez, E. Mir, and J. Santamarıa, "Synthesis and characterization of zsm-5 coatings onto cordierite honeycomb supports," *Applied Catalysis A: General*, vol. 253, no. 1, pp. 257–269, 2003.

[180] Z. Wang and Y. Yan, "Oriented zeolite mfi monolayer films on metal substrates by in situ crystallization," *Microporous and mesoporous materials*, vol. 48, no. 1-3, pp. 229–238, 2001.

[181] A. Aranzabal, D. Iturbe, M. Romero-Saez, M. Gonzalez-Marcos, J. Gonzalez-Velasco, and J. Gonzalez-Marcos, "Optimization of process parameters on the extrusion of honeycomb shaped monolith of h-zsm-5 zeolite," *Chemical Engineering Journal*, vol. 162, no. 1, pp. 415–423, 2010.

[182] J.-C. Wang, T. Dong, L.-N. Han, L.-P. Chang, and W.-R. Bao, "In situ synthesized cu-zsm-5/cordierite for reduction of no," *Transactions of Nonferrous Metals Society of China*, vol. 21, no. 2, pp. 353–358, 2011.

[183] M. Colombo, I. Nova, and E. Tronconi, "No2 adsorption on fe-and cu-zeolite catalysts: The effect of the catalyst red–ox state," *Applied Catalysis B: Environmental*, vol. 111, pp. 433–444, 2012.

[184] M. Colombo, I. Nova, and E. Tronconi, "A comparative study of the nh3-scr reactions over a cu-zeolite and a fe-zeolite catalyst," *Catalysis Today*, vol. 151, no. 3-4, pp. 223–230, 2010.

[185] T. V. Janssens, H. Falsig, L. F. Lundegaard, P. N. Vennestrøm, S. B. Rasmussen, P. G. Moses, F. Giordanino, E. Borfecchia, K. A. Lomachenko, C. Lamberti *et al.*, "A consistent reaction scheme for the selective catalytic reduction of nitrogen oxides with ammonia," *ACS catalysis*, vol. 5, no. 5, pp. 2832–2845, 2015.

[186] F. Gao and C. H. Peden, "Recent progress in atomic-level understanding of cu/ssz-13 selective catalytic reduction catalysts," *Catalysts*, vol. 8, no. 4, p. 140, 2018.

[187] A. Grossale, I. Nova, E. Tronconi, D. Chatterjee, and M. Weibel, "The chemistry of the no/no2–nh3 "fast" scr reaction over fe-zsm5 investigated by transient reaction analysis," *Journal of Catalysis*, vol. 256, no. 2, pp. 312–322, 2008.

[188] N. Katada, H. Igi, J.-H. Kim, and M. Niwa, "Determination of the acidic properties of zeolite by theoretical analysis of temperature-programmed desorption of ammonia based on adsorption equilibrium," *The Journal of Physical Chemistry B*, vol. 101, no. 31, pp. 5969–5977, 1997.

[189] H. J. Chae, S. T. Choo, H. Choi, I.-S. Nam, H. S. Yang, and S. L. Song, "Direct use of kinetic parameters for modeling and simulation of a selective catalytic reduction process," *Industrial & engineering chemistry research*, vol. 39, no. 5, pp. 1159–1170, 2000.

[190] M. P. Ruggeri, T. Selleri, I. Nova, E. Tronconi, J. A. Pihl, T. J. Toops, and W. Partridge, "New mechanistic insights in the nh3-scr reactions at low temperature," *Topics in Catalysis*, vol. 59, no. 10, pp. 907–912, 2016.

[191] S. A. Stevenson, J. C. Vartuli, and C. F. Brooks, "Kinetics of the selective catalytic reduction of no over hzsm-5," *Journal of Catalysis*, vol. 190, no. 2, pp. 228–239, 2000.

[192] M. Iwasaki, K. Yamazaki, and H. Shinjoh, "Transient reaction analysis and steady-state kinetic study of selective catalytic reduction of no and no+ no2 by nh3 over fe/zsm-5," *Applied Catalysis A: General*, vol. 366, no. 1, pp. 84–92, 2009.

[193] B. Roduit, A. Wokaun, and A. Baiker, "Global kinetic modeling of reactions occurring during selective catalytic reduction of no by nh3 over vanadia/titania-based catalysts," *Industrial & engineering chemistry research*, vol. 37, no. 12, pp. 4577–4590, 1998.

[194] M. Devadas, O. Krocher, and M. Elsener, "a wokaun, n. soger, m. pfeifer, y. demel, l. mussmann," *Applied Catalysis B: Environmental*, vol. 67, p. 187, 2006.

[195] M. Zhou, A. A. Rownaghi, and J. Hedlund, "Synthesis of mesoporous zsm-5 zeolite crystals by conventional hydrothermal treatment," *RSC Advances*, vol. 3, no. 36, pp. 15 596–15 599, 2013.

[196] C. Colella and W. S. Wise, "The iza handbook of natural zeolites: A tool of knowledge on the most important family of porous minerals," *Microporous and mesoporous materials*, vol. 189, pp. 4–10, 2014.

[197] E. Urquieta-Gonzalez, L. Martins, R. Peguin, and M. Batista, "Identification of extra-framework species on fe/zsm-5 and cu/zsm-5 catalysts typical microporous

molecular sieves with zeolitic structure," *Materials Research*, vol. 5, no. 3, pp. 321–327, 2002.

[198] A. Bhan and W. Nicholas Delgass, "Propane aromatization over hzsm-5 and ga/hzsm-5 catalysts," *Catalysis Reviews*, vol. 50, no. 1, pp. 19–151, 2008.

[199] H. Wang, J. Jia, S. Liu, H. Chen, Y. Wei, Z. Wang, L. Zheng, Z. Wang, and R. Zhang, "Highly efficient no abatement over cu-zsm-5 with special nanosheet features," *Environmental Science & Technology*, vol. 55, no. 8, pp. 5422–5434, 2021.

[200] K. Leistner, F. Brüsewitz, K. Wijayanti, A. Kumar, K. Kamasamudram, and L. Olsson, "Impact of copper loading on nh3-selective catalytic reduction, oxidation reactions and n2o formation over cu/sapo-34," *Energies*, vol. 10, no. 4, p. 489, 2017.

[201] J. Cejka, A. Corma, and S. Zones, *Zeolites and catalysis: synthesis, reactions and applications*. John Wiley & Sons, 2010.

[202] J. Jiao, J. Kanellopoulos, W. Wang, S. S. Ray, H. Foerster, D. Freude, and M. Hunger, "Characterization of framework and extra-framework aluminum species in non-hydrated zeolites y by 27 al spin-echo, high-speed mas, and mqmas nmr spectroscopy at b 0= 9.4 to 17.6 t," *Physical Chemistry Chemical Physics*, vol. 7, no. 17, pp. 3221–3226, 2005.

[203] S. Sklenak, J. Dvedevcek, C. Li, B. Wichterlova, V. Gabova, M. Sierka, and J. Sauer, "Aluminium siting in the zsm-5 framework by combination of high resolution 27al nmr and dft/mm calculations," *Physical Chemistry Chemical Physics*, vol. 11, no. 8, pp. 1237–1247, 2009.

[204] Y. Itho, S. Nishiyama, S. Tsuruya, and M. Masai, "Redox behavior and mobility of copper ions in nazsm-5 zeolite during oxidation," *The Journal of Physical Chemistry*, vol. 98, no. 3, pp. 960–967, 1994.

[205] S. K. Das, S. Mukherjee, L. M. Lopes, L. M. Ilharco, A. M. Ferraria, A. M. B. do Rego, and A. J. Pombeiro, "Synthesis, characterization and heterogeneous catalytic application of copper integrated mesoporous matrices," *Dalton Transactions*, vol. 43, no. 8, pp. 3215–3226, 2014.

[206] M. W. Anderson and L. Kevan, "Study of copper (2+)-doped zeolite nah-zsm-5 by electron spin resonance and electron spin echo modulation spectroscopies," *Journal of Physical Chemistry*, vol. 91, no. 15, pp. 4174–4179, 1987.

[207] G. Lei, B. Adelman, J. Sarkany, and W. Sachtler, "Identification of copper (ii) and copper (i) and their interconversion in cu/zsm-5 de-nox catalysts," *Applied Catalysis B: Environmental*, vol. 5, no. 3, pp. 245–256, 1995.

[208] N. Kovacev, S. Li, S. Zeraati-Rezaei, H. Hemida, A. Tsolakis, and K. Essa, "Effects of the internal structures of monolith ceramic substrates on thermal and hydraulic properties: additive manufacturing, numerical modelling and experimental testing," *The International Journal of Advanced Manufacturing Technology*, vol. 112, no. 3, pp. 1115–1132, 2021.

[209] S. Yashnik and Z. Ismagilov, "Control of the no–nh 3 scr behavior of cu-zsm-5 by variation of the electronic state of copper," *Topics in Catalysis*, vol. 62, no. 1, pp. 179–191, 2019.

[210] L. Xuesong, W. Xiaodong, W. Duan, and S. Lei, "Modification of cu/zsm-5 catalyst with ceo2 for selective catalytic reduction of nox with ammonia," *Journal of Rare Earths*, vol. 34, no. 10, pp. 1004–1009, 2016.

[211] M. Bendrich, A. Scheuer, R. Hayes, and M. Votsmeier, "Unified mechanistic model for standard scr, fast scr, and no2 scr over a copper chabazite catalyst," *Applied Catalysis B: Environmental*, vol. 222, pp. 76–87, 2018.

[212] L. Wang, W. Li, G. Qi, and D. Weng, "Location and nature of cu species in cu/sapo-34 for selective catalytic reduction of no with nh3," *Journal of Catalysis*, vol. 289, pp. 21–29, 2012.

[213] E.-Y. Choi, I.-S. Nam, and Y. G. Kim, "Tpd study of mordenite-type zeolites for selective catalytic reduction of no by nh3," *Journal of Catalysis*, vol. 161, no. 2, pp. 597–604, 1996.

[214] R. Raju, N. Gomathi, K. Prabhakaran, K. Joseph, and A. Salih, "Selective catalytic reduction of no over hierarchical cu zsm-5 coated on an alumina foam support," *Reaction Chemistry & Engineering*, 2022.

[215] P. N. Vennestrøm, T. V. Janssens, A. Kustov, M. Grill, A. Puig-Molina, L. F. Lundegaard, R. R. Tiruvalam, P. Concepción, and A. Corma, "Influence of lattice stability on hydrothermal deactivation of cu-zsm-5 and cu-im-5 zeolites for selective catalytic reduction of nox by nh3," *Journal of catalysis*, vol. 309, pp. 477–490, 2014.

[216] E. Borfecchia, K. Lomachenko, F. Giordanino, H. Falsig, P. Beato, A. Soldatov, S. Bordiga, and C. Lamberti, "Revisiting the nature of cu sites in the activated cu-ssz-13 catalyst for scr reaction," *Chemical science*, vol. 6, no. 1, pp. 548–563, 2015.

[217] C. Paolucci, A. A. Parekh, I. Khurana, J. R. Di Iorio, H. Li, J. D. Albarracin Caballero, A. J. Shih, T. Anggara, W. N. Delgass, J. T. Miller *et al.*, "Catalysis in a cage: condition-dependent speciation and dynamics of exchanged cu cations in ssz-13 zeolites," *Journal of the American Chemical Society*, vol. 138, no. 18, pp. 6028–6048, 2016.

[218] F. Gao, E. D. Walter, M. Kollar, Y. Wang, J. Szanyi, and C. H. Peden, "Understanding ammonia selective catalytic reduction kinetics over cu/ssz-13 from motion of the cu ions," *Journal of catalysis*, vol. 319, pp. 1–14, 2014.

[219] I. Nova, C. Ciardelli, E. Tronconi, D. Chatterjee, and M. Weibel, "Unifying redox kinetics for standard and fast nh3-scr over a v2o5-wo3/tio2 catalyst," *AIChE Journal*, vol. 55, no. 6, pp. 1514–1529, 2009.

[220] M. Wallin, C.-J. Karlsson, M. Skoglundh, and A. Palmqvist, "Selective catalytic reduction of nox with nh3 over zeolite h–zsm-5: influence of transient ammonia supply," *Journal of Catalysis*, vol. 218, no. 2, pp. 354–364, 2003.

[221] C. Paolucci, A. A. Verma, S. A. Bates, V. F. Kispersky, J. T. Miller, R. Gounder, W. N. Delgass, F. H. Ribeiro, and W. F. Schneider, "Isolation of the copper redox steps in the standard selective catalytic reduction on cu-ssz-13," *Angewandte Chemie International Edition*, vol. 53, no. 44, pp. 11 828–11 833, 2014.

[222] L. SHI, T. YU, X.-Q. WANG, J. WANG, and M.-Q. SHEN, "Properties and roles of adsorbed nh3 and no x over cu/sapo-34 zeolite catalyst in nh3-scr process," *Acta Physico-Chimica Sinica*, vol. 29, no. 7, pp. 1550–1557, 2013.

[223] T. Günter, H. W. Carvalho, D. E. Doronkin, T. Sheppard, P. Glatzel, A. J. Atkins, J. Rudolph, C. R. Jacob, M. Casapu, and J.-D. Grunwaldt, "Structural snapshots of the scr reaction mechanism on cu-ssz-13," *Chemical Communications*, vol. 51, no. 44, pp. 9227–9230, 2015.

[224] F. Gao, J. H. Kwak, J. Szanyi, and C. H. Peden, "Current understanding of cu-exchanged chabazite molecular sieves for use as commercial diesel engine denox catalysts," *Topics in Catalysis*, vol. 56, no. 15, pp. 1441–1459, 2013.

[225] A. Savara, M.-J. Li, W. M. Sachtler, and E. Weitz, "Catalytic reduction of nh4no3 by no: effects of solid acids and implications for low temperature denox processes," *Applied Catalysis B: Environmental*, vol. 81, no. 3-4, pp. 251–257, 2008.

[226] U. Deka, A. Juhin, E. A. Eilertsen, H. Emerich, M. A. Green, S. T. Korhonen, B. M. Weckhuysen, and A. M. Beale, "Confirmation of isolated cu2+ ions in ssz-13 zeolite as active sites in nh3-selective catalytic reduction," *The Journal of Physical Chemistry C*, vol. 116, no. 7, pp. 4809–4818, 2012.

[227] S. A. Bates, A. A. Verma, C. Paolucci, A. A. Parekh, T. Anggara, A. Yezerets, W. F. Schneider, J. T. Miller, W. N. Delgass, and F. H. Ribeiro, "Identification of the active cu site in standard selective catalytic reduction with ammonia on cu-ssz-13," *Journal of catalysis*, vol. 312, pp. 87–97, 2014.

[228] P. I. Chigada, T. C. Watling, J. P. Cleeton, M. Gall, and J. A. Wylie, "Experimental and modelling study of cold start effects on a cu-zeolite nh 3 selective catalytic reduction catalyst," SAE Technical Paper, Tech. Rep., 2015.

[229] M. Iwasaki and H. Shinjoh, "A comparative study of "standard","fast" and "no2" scr reactions over fe/zeolite catalyst," *Applied Catalysis A: General*, vol. 390, no. 1-2, pp. 71–77, 2010.

[230] X. Auvray, W. P. Partridge, J.-S. Choi, J. A. Pihl, A. Yezerets, K. Kamasamudram, N. W. Currier, and L. Olsson, "Local ammonia storage and ammonia inhibition in a monolithic copper-beta zeolite scr catalyst," *Applied Catalysis B: Environmental*, vol. 126, pp. 144–152, 2012.

[231] G. C. Dhal, D. Mohan, and R. Prasad, "Preparation and application of effective different catalysts for simultaneous control of diesel soot and no x emissions: An overview," *Catalysis Science & Technology*, vol. 7, no. 9, pp. 1803–1825, 2017.

[232] K. Kamasamudram, N. W. Currier, X. Chen, and A. Yezerets, "Overview of the practically important behaviors of zeolite-based urea-scr catalysts, using compact experimental protocol," *Catalysis Today*, vol. 151, no. 3-4, pp. 212–222, 2010.

[233] Y. Wei, M. Chen, X. Ren, Q. Wang, J. Han, W. Wu, X. Yang, S. Wang, and J. Yu, "One-pot 3d printing robust self-supporting mnox/cu-ssz-13 zeolite monolithic catalysts for nh3-scr," *CCS Chemistry*, pp. 1–29, 2021.

[234] S. Ni, X. Tang, H. Yi, F. Gao, C. Wang, Y. Shi, R. Zhang, and W. Zhu, "Novel mn–ce bi-oxides loaded on 3d monolithic nickel foam for low-temperature nh3-scr de-nox: Preparation optimization and reaction mechanism," *Journal of Rare Earths*, vol. 40, no. 2, pp. 268–278, 2022.

[235] S. Lawson, A. Farsad, B. Adebayo, K. Newport, K. Schueddig, E. Lowrey, F. Polo-Garzon, F. Rezaei, and A. A. Rownaghi, "A novel method of 3d printing high-loaded oxide/h-zsm-5 catalyst monoliths for carbon dioxide reduction in tandem with propane dehydrogenation," *Advanced Sustainable Systems*, vol. 5, no. 3, p. 2000257, 2021.

[236] Y. Wang, Y. Tang, A. Dong, X. Wang, N. Ren, W. Shan, and Z. Gao, "Self-supporting porous zeolite membranes with sponge-like architecture and zeolitic microtubes," *Advanced Materials*, vol. 14, no. 13-14, pp. 994–997, 2002.

[237] Y. Liu, C. Yan, Z. Zhang, L. Li, H. Wang, and S. Pu, "One-step fabrication of novel porous and permeable self-supporting zeolite block from fly ash," *Materials Letters*, vol. 196, pp. 328–331, 2017.

[238] P. Colombo, C. Vakifahmetoglu, and S. Costacurta, "Fabrication of ceramic components with hierarchical porosity," *Journal of materials science*, vol. 45, no. 20, pp. 5425–5455, 2010.

[239] J. Ding, X. Huang, Q. Yang, L. Wang, Y. Peng, J. Li, and J. Huang, "Microstructured cu-zsm-5 catalyst on aluminum microfibers for selective catalytic reduction of no by ammonia," *Catalysis Today*, vol. 384, pp. 106–112, 2022.

[240] S. Vijayan, R. Narasimman, and K. Prabhakaran, "Freeze gelcasting of hydrogenated vegetable oil-in-aqueous alumina slurry emulsions for the preparation of macroporous ceramics," *Journal of the European Ceramic Society*, vol. 34, no. 16, pp. 4347–4354, 2014.

[241] H. Li, J. Li, C. Li, M. Fu, and C.-A. Wang, "Near net shape fabrication of porous cordierite by combination of foam gel-casting and freeze-drying," *International Journal of Applied Ceramic Technology*, 2021.

[242] D. W. Stanton and C. J. Rutland, "Modeling fuel film formation and wall interaction in diesel engines," *SAE transactions*, pp. 808–824, 1996.

[243] E. Abu-Ramadan, K. Saha, and X. Li, "Modeling of the injection and decomposition processes of urea-water-solution spray in automotive scr systems," SAE Technical Paper, Tech. Rep., 2011.

[244] K. Jyothis and R. Vikas, "Study of conversion of ammonia from urea water solution droplets using cfd," in *IOP Conference Series: Materials Science and Engineering*, vol. 243, no. 1. IOP Publishing, 2017, p. 012011.

[245] M. Karlsson, U. Wallin, S. Fredholm, J. Jansson, G.-O. Wahlström, C. M. Schär, C. H. Onder, and L. Guzzella, "A combined 3d/lumped modeling approach to ammonia scr after-treatment systems: application to mixer designs," SAE Technical Paper, Tech. Rep., 2006.

[246] H. Ström, A. Lundström, and B. Andersson, "Choice of urea-spray models in cfd simulations of urea-scr systems," *Chemical Engineering Journal*, vol. 150, no. 1, pp. 69 – 82, 2009.

[247] A. Frobert, Y. Creff, S. Raux, C. Charial, A. Audouin, and L. Gagnepain, "Scr for passenger car: the ammonia-storage issue on a fe-zsm5 catalyst," SAE Technical Paper, Tech. Rep., 2009.

[248] T. Paramadayalan and A. Pant, "Selective catalytic reduction converter design: The effect of ammonia nonuniformity at inlet," *Korean Journal of Chemical Engineering*, vol. 30, no. 12, pp. 2170–2177, 2013.

[249] R. Ragab and T. Wang, "An investigation of liquid droplet evaporation model used in multiphase flow simulation," in *ASME International Mechanical Engineering Congress and Exposition*, vol. 45233. American Society of Mechanical Engineers, 2012, pp. 485–497.

[250] S. Sazhin, T. Kristyadi, W. Abdelghaffar, and M. Heikal, "Models for fuel droplet heating and evaporation: comparative analysis," *Fuel*, vol. 85, no. 12-13, pp. 1613–1630, 2006.

[251] W. Ranz, W. R. Marshall *et al.*, "Evaporation from drops," *Chem. eng. prog*, vol. 48, no. 3, pp. 141–146, 1952.

[252] F. Birkhold, U. Meingast, P. Wassermann, and O. Deutschmann, "Analysis of the injection of urea-water-solution for automotive scr denox-systems: modeling of two-phase flow and spray/wall-interaction," SAE Technical Paper, Tech. Rep., 2006.

[253] H. Vömel, "Saturation vapor pressure formulations," *CIRES, University of Colorado, Boulder, http://cires. colorado. edu/voemel/vp. html*, 2016.

[254] J. Y. Kim, S. H. Ryu, and J. S. Ha, "Numerical prediction on the characteristics of spray-induced mixing and thermal decomposition of urea solution in scr system," in *ASME 2004 Internal Combustion Engine Division Fall Technical Conference*. American Society of Mechanical Engineers Digital Collection, 2004, pp. 165–170.

[255] H. Dong, S. Shuai, and J. Wang, "Effect of urea thermal decomposition on diesel nox-scr aftertreatment systems," SAE Technical Paper, Tech. Rep., 2008.

List of Publications

Refereed Journals

1. Raju, Risha, Jishnu Chandran, A. Salih, and Kuruvilla Joseph. "Numerical analysis of mixing chamber non-uniformities and feed conditions for optimal performance of urea SCR." Reaction Chemistry & Engineering 5, no. 12 (2020): 2236-2249.

2. Raju, Risha, N. Gomathi, K. Prabhakaran, Kuruvilla Joseph, and A. Salih. "Selective catalytic reduction of NO over hierarchical Cu ZSM-5 coated on an alumina foam support." Reaction Chemistry & Engineering no 7 (2022): 929-942.

Refereed Conferences

1. Risha Raju, Jishnu Chandran R, and A. Salih. (2019). "Numerical Modelling of NO_x Reduction on Cu-ZSM 5 Monolith Reactor", 25th National and 3rd International ISHMT-ASTFE Heat and Mass Transfer Conference,IHMTC-2019, IIT Roorkee, December 28-31.

2. Kaisare, Niket S., Preeti Aghalayam, Sruti Dammalapati, and Risha Raju. "Modeling of NO_x reduction By Urea-Based Selective Catalytic Reduction in a Monolith Reactor." In 2019 AIChE Annual Meeting. AIChE, 2019.

Appendix A

Reaction Kinetics for SCR Simulation

A.1 Gas Kinetics

ELEMENTS
C N O H Cu
END
SPECIES
NO N2 NO2 CO2 O2 N2O NH3 H2O
END
THERMO
END
REACTIONS
END

A.2 Surface Kinetics

SURFACE MECHANISM FOR SCR REACTIONS
Kinetic data:
k = A * T**b * exp (-Ea/RT) A b Ea
(cm,mol,s) - kJ/mol
SITE/SURFACE/ SDEN/9.046e-10/
Cu(S) NH3(S)
END
THERMO ALL

300.0 1000.0 3000.0
Thermodynamic Data
Cu(S) Cu 1 S 300.0 3000.0 1000.0 1
0.00000000E+00 0.00000000E+00 0.00000000E+00 0.00000000E+00 0.00000000E+00 2
0.00000000E+00 0.00000000E+00 0.00000000E+00 0.00000000E+00 0.00000000E+00 3
0.00000000E+00 0.00000000E+00 0.00000000E+00 0.00000000E+00 4
NH3(S) N 1H 3Cu 1 I 300.0 3000.0 1000.0 1
0.00000000E+00 0.00000000E+00 0.00000000E+00 0.00000000E+00 0.00000000E+00 2
0.00000000E+00 0.00000000E+00 0.00000000E+00 0.00000000E+00 0.00000000E+00 3
0.00000000E+00 0.00000000E+00 0.00000000E+00 0.00000000E+00 4
END
NH3-SCR SURFACE MECHANISM
REACTIONS KJOULES/MOL
NH3 + Cu(S) => NH3(S) 6.82 0.0 0.0
NH3(S) => NH3 + Cu(S) 7.334E5 0.0 181.5
COV/NH3(S) 0.0 0.0 -177.87/
2NH3(S) + 1.5O2 => N2 + 3H2O + 2Cu(S) 8.8E11 0.0 162.4
FORD/NH3(S) 1.0/
FORD/O2 1.0/
NO + 0.5O2 <=> NO2 0.0058672 0.0 48
4NH3(S) + 4NO + O2 => 4N2 + 6H2O + 4Cu(S) 1.6868E9 0.0 84.9
FORD/NH3(S) 1.0/
FORD/NO 1.0/
FORD/O2 0.0/
2NH3(S) + NO + NO2 => 2N2 + 3H2O + 2Cu(S) 1.3935E19 0.0 85.1
FORD/NH3(S) 1.0/
4NH3(S)+ 3NO2 => 3.5N2 + 6H2O + 4Cu(S) 8.0674E7 0.0 72.3
FORD/NH3(S) 1.0/
FORD/NO2 1.0/
2NH3(S) + 2NO2 => N2 + N2O + 3H2O + 2Cu(S) 264024 0.0 43.3
FORD/NH3(S) 1.0/
FORD/NO2 1.0/
END